Engineering nano-scale diamond quantum devices and their applications to neuroscience

Liam Hanlon

A thesis submitted for the degree of
Doctor of philosophy
The Australian National University

September 2022

Draft Copy – 15 September 2022

Except where otherwise indicated, this thesis is my own original work.

Liam Hanlon
15 September 2022

Acknowledgments

"Sometimes I really have no idea what you are trying to say"

Dr. Marcus Doherty. After I eloquently explained a physics concept to him.

This thesis is the culmination of many years of work and has taken many unexpected changes in its form and direction to find its way here. But life never really goes in accordance with anyone's plans; this can mean that you change your nature intrinsically to adapt to life's changes, but it also means changing your nature based on the advice and experiences of those around you. This section is an acknowledgement and appreciation of the latter, of how those in my life have shaped me for the better and by extension, how it has affected this thesis.

Firstly thanks go to my family: my parents, Nell and Brendan Hanlon, my older brother and sister, Tim and Elise Hanlon, my younger sister Bethany Hanlon, and a very long list of extended family including new additions in my brother's wife, Ruth Brown, and their children, Victoria, Lilah and Celeste. More so than anyone in my life, these people shaped my morality and my desire to do good in the world which is what ultimately lead me down the path of pursuing physics to assist medical science. Special thanks go to my father, I hope it pleases him to know that in a household of people interested in arts and social sciences there was one person who got into physics like himself.

My next acknowledgment is a little obscure, a person who I didn't really know very well and will likely never read this thesis. When I got out of high school, my first degree was in Nuclear Medicine at Newcastle University. Whilst I miss the patient interactions, I found the work was not entirely suited to me and I eventually ended up leaving to study physics. During a student placement at a hospital in Sydney, I met Dr Michael Lin. When I was borrowing one of his textbooks for an assignment he asked if I ever wanted to be a doctor, to which I replied that I didn't think I was smart enough. His reply has stayed with me ever since:

"You don't have to be smart to be a doctor, you just have to apply yourself."

I later learned that this advice applies to almost anything in life, what you might lack in skill and talent you can always make up for with hard work. There was no harm in me attempting to become a physicist and I could always make up for my shortfalls by working hard to learn concepts and skills. It seems like very simple advice in hindsight, but I was always a bit of a slow learner.

During my ANU days, I has the good fortune of being taught by award-winning,

highly talented and good-natured people, both professional lecturers and fellow students. The ones I would like to thank in particular are the long term members of the diamond quantum science and technology group: Michael Barson, Prithvi Reddy, Lachlan Oberg, YunHeng Chen, Neil Manson and Sophie Stearn. There are also a long list of temporary members that I would like to mention, but my supervisor was very keen on students and the list gets very long if I name them individually. I would also like to thank those who I met during my time overseas, in particular Ou Wang and Fedor Jelezko of Ulm University in Germany. The pandemic meant that my time with them was limited but their effect on my education was just as important as anyone else. But of all the people I have mentioned I do want to give special thanks to Sophie Stearn, I would not have gotten through my undergraduate degree without her. Her sharp intellect was only ever matched by her good nature and endless patience for my silliness.

Finally, special thanks need to go to my supervisor, Marcus Doherty. At the end of my undergraduate degree, I was searching for someone at the ANU with whom I could undertake a biophysics project with. Unfortunately, there was a distinct lack of biophysics going on at the ANU, the best idea I got was a footnote of a possible project with Marcus Doherty. So I did the next best thing, I went to Marcus and asked him to help me make a neuroscience project out of his work with the nitrogen-vacancy (NV) center in diamond. I think most physicists would be hesitant to form a 4-year PhD project on a subject area they know little about. Marcus is highly skilled in quantum mechanics and less knowledgeable in neuroscience. However, he was keen on the idea of helping me develop this project and make it my own. Whilst the project did not go completely as planned, the things I learned along the way has helped me develop into a more independent scientist, comfortable with developing my own ideas and using scientific methods to develop the ideas into usable concepts and technologies for both neuroscience and a range of other fields.

Whilst I believe I have become a capable scientist because of the efforts of those around me, I know that there is still a lot for me to learn, which is why I have kept the quote from Marcus which I put in my Honours thesis as I still believe it applies to me every now and then. I look forward to a future of new experiences, successes and failures, knowing that the direction I take will be due to my personal preferences, circumstances out of my control, but most importantly, the influences of those closest to me.

Abstract

As modern neuroscience improves, our understanding of neuronal systems and the human brain improves as well. This includes a practical understanding of neurological diseases and how to treat them as well as a more general understanding of how humans and animals think and understand the world around them. One key mechanism for understanding neuronal systems is in experimental measurements. Being able to sense the electromagnetic signalling system that neurons produce in a network is essential for understanding their function; so much so that a lack of useful means of measuring neuron signals severely limits any new information neuroscience research can provide. Measuring and imaging neuronal signals, however, can be a difficult process, when measuring signals there is a requirement for a highly sensitive device that can measure the smallest electromagnetic signal of a neuron at particular regions of the cell as well as across a dense neuron network. Furthermore, measurements must be performed in such a way as to not alter the normal function of the cell. Whilst many technologies for measuring and imaging neuron networks exist, they all have distinct advantages and disadvantages that limit their effectiveness or applicability.

The nitrogen-vacancy (NV) center is an atomic defect in a diamond lattice whose unique quantum properties gives the defect great potential to be an extremely sensitive device for measuring electromagnetic signals. Coupled with its placement in the biocompatible diamond lattice, the NV center can potentially be used as a novel sensor of neuron signals in a way that would be vastly superior to current technologies. However, there are issues with design implementations that limits the potential benefits of the NV as a neurosensor.

In this thesis, a detailed exploration of the NV as a neurosensor is undertaken including a unique approach that places the defects in an array of diamond nano-pillars to improve the capacity to sense neuron signals at specific locations. In this study, the anatomy and physiology of the neuron are outlined and the current state of neuron imaging is presented including the role NV neurosensing would play in the field. The capacity of NV neurosensing is assessed with detailed theoretical modelling as well as a proof-of-principle growth study of neurons on an array of diamond nano-pillars.

The results of the growth study and modelling suggest that the NV would be inappropriate as a magnetic field sensor, but would be useful as an electric field sensor for neuronal systems. Whilst further study of the NV in its capacity as a neurosensor is required, the results motivate a more general study of the NV and the various means that can improve its performance. This includes two separate spin-to-charge conversion protocols for improved optical contrast, a study of NV photoionisation spectroscopy for a better understanding of the NVs energy structure and a study of diamond fabrication techniques for improved optical collection efficiency in the NV.

This research into NV performance enhancement allows for further consideration of the NV as a sensor for non-biological applications as well as a qubit for quantum computing and networking applications. As all the quantum operations in sensing and computing rely on the same spin-dependent dynamics of the NV itself, any improvement to NV performance can improve the NV viability in a number of fields including, but not exclusive to neurosensing.

The primary goal of this thesis is to present the potential of the NV as a novel sensor for neuron networks. The additional work in improving NV performance helps the NV function as a better sensor but also improves its capacity to function as a qubit in a quantum computer. This process leads to the consideration of NV quantum computing for neuroscience and the development of an algorithm that utilises quantum computation to better understand the dynamics of large scale neuron networks. Whilst this research is conceptual only, its research potential is significant and it widens the scope of this thesis to diamond quantum devices and their applications to neuroscience.

Contents

List of Figures

List of Tables

Chapter 1

Introduction

1.1 Motivation

The study of neuroscience is a growing concern, especially in the modern world. According to the World health organization's (WHO) global burden of disease study from 1990 to 2015, neurological disorders are the second leading cause of death worldwide after heart disease and the number one cause of disability worldwide [28]. To make matters worse, whilst the study can outline precautions to help prevent some neurological diseases (such as lifestyle changes to reduce the chance of stroke), many neurological disorders have little to no preventative measures or treatments that can be made. The reason for this is that the mechanisms for many neurological disorders are poorly understood. Imaging and measuring the electromagnetic fields of nerve cells (neurons) has been the hallmark of understanding modern neuroscience [88]. Advancements in this field have led to a better understanding of how the human brain operates which leads to improvements in the diagnosis and treatment of neurological disorders. This means understanding neurons from the perspective of a single cell and the nanoscopic structures within it as well as the larger-scale perspective of multiple neurons in a network. Sensing neuron electromagnetics is however a challenging task because, in order to fully understand neuron excitability and the neuron signal, the action potential (AP), there are a variety of requirements that must be met. These requirements can be presented in four major areas.

The first requirement is millisecond or sub-millisecond temporal resolution, this allows for the measurement of AP changes over fast timescales. Neuron APs are typically only ms in duration with many APs occurring in quick succession after one another [88]. It is also important to be able to resolve the timings of multiple signals correlated in a network. Signal timing is an important factor for understanding physiological responses [18]. The second requirement is nanoscale resolution across a field of view that is large enough to encompass multiple neurons in a network [88]. This includes the imaging of individual neuron compartments, such as dendritic spines or ion channels [78]. Singular nanoscale neuron structures can have a profound effect on microscale neuron networks so it is important to be able to measure this nanoscale process and observe its effect on a larger microscale network [129]. Thirdly the sensitivity of the probe must be exceptional, a sensor must be able to resolve millivolt changes in potential within sub-millisecond timescales in order to sense

the smallest signals produced by neurons [87]. Whilst most neuron sensors measure the larger amplitude signal of a neuron (the AP), being able to measure the smaller signals that build into the AP is an important factor in neurophysiology that is often overlooked due to the lack of suitable technology [96]. Finally, the last major requirement is the compatibility and stability of the sensor, the sensor must be able to probe a neuron without altering its behaviour. The sensor must also be able to make many measurements without it failing or having toxic effects on the neuron. These requirements allow for imaging of neuron changes over a long period of time, which is important for the study of neuroplastic effects [70]. An ideal sensor would be biocompatible when measuring neurons within a living subject (in vivo) or neurons that are cultured externally from a living subject (in vitro).

There are a growing number of different techniques which can meet one or more of these requirements. Improvements in patch-clamp techniques have pushed to cross-sectional nanoscale electrophysiology for investigating nanoscopic heterogeneities in ionic concentrations and local electric fields [105]. Coupled with scanning ion conductance microscopy, it can perform wide-field imaging of neurons in a resting state [78]. Voltage-sensitive fluorophores come in a variety of forms, some of which have been shown to be able to image nano-scale structures such as dendritic spines with high sensitivity [92]. Microelectrode arrays (MEA's) come in a variety of forms from large scale arrays which can measure signals from large networks all the way to in vivo full brain recordings and nanoelectrodes which can measure signals from individual cells [111]. However, no single device has the capacity to meet all the listed requirements at the same time. The patch-clamp technique can only measure APs at a single point on a neuron, removing the capacity of imaging propagation effects [88]. Voltage-sensitive dyes can be difficult to use, requiring careful tailoring of the correct dye to a specific cell [88]. In addition to this, any type of fluorophore that could be injected into a cell has an inherent time limit before photobleaching renders the sensor inoperable or phototoxicity kills the cell being imaged [88]. MEA's on a large scale can only measure the combined signal of multiple neurons at once, reducing spatial resolution and nanoelectrodes suffer from a lack of electrode density and difficulties making neuron/electrode contact, reducing sensitivity [111].

Another often overlooked detail to consider when probing neurons at the nanoscale is how to best theoretically simulate and interpret neuron nano-electromagnetics. Most spatial predictions of electromagnetics rely on variations of core conductor (CC) theory [105, 126]. The central assumption of this theory is that the density of ions inside and outside the neuron remains stationary during an AP. At micron distances from the membrane, where the ions can form a stable equilibrium this assumption is true, making CC theory viable. At these length scales, the CC model has been experimentally verified by measuring the magnetic field of large neurons (200μm in radius) [126]. However, at nanoscale distances from the membrane, ions flowing in and out of the neuron is precisely what generates the AP, making the assumption invalid [105]. The key to obtaining a full understanding of neuron electromagnetics is to apply a model which accounts for the full motion of charged ions and how they affect the electric potential both inside and outside the neuron, this is achieved using

the Poisson-Nernst-Planck theory of neuron electromagnetism [19, 67, 91]. With such a theory, external probes such as a diamond pillar can be added to the model to understand how a sensor might affect the natural neuron ion flow as well as assess whether a sensor can measure the signals being produced by the neuron.

In this thesis, a potential solution to the problem of neuron signal measurement is presented with the application of the nitrogen-vacancy center (NV) [12, 45]. The NV is a defect in a diamond lattice consisting of a substitutional nitrogen atom with a nearest neighbour vacancy [99]. The NV has unique spin-dependent photo-dynamics that allow its electronic spin to be optically initialized and read out using quantum protocols. This allows for the NV's electron spin resonance (ESR) to be measured using a protocol known as optically detected magnetic resonance (ODMR). The ODMR resonances shift with perturbations from external electric and magnetic fields [27] and magnetic fields [99]. Combining this with its atom-like size the NV can perform highly sensitive nanoscale measurements of electric and magnetic fields.

The NV has been shown to have some of the best sensitivities and spatial resolutions for a room temperature sensor. For DC sensing, single NVs have been able to measure 2.8×10^9 mV/m [27] electric fields and 1.26 μT [99] magnetic fields in a 1 ms acquisition time. In addition to its sensitivity, the NV has been shown to have sub-millisecond temporal resolution as well as spatial resolutions well into the nanometre scale [116]. The NV itself is also a very stable atomic system, which does not suffer from photobleaching, allowing for long term imaging of a single sample [12]. In addition to its physical capabilities, the NV is situated in a diamond structure. Diamond has been shown to be biologically compatible, having been successfully utilized in the past as a substrate to grow biological samples [72]. They have also been proven to support functioning neurons via growth on unstructured nano-diamond mono-layers which are assessed with calcium imaging [118]. With these characteristics, the NV has the potential to revolutionise neuron sensing as they have the capacity to meet all of the requirements listed before at the same time, something no other sensor to date can achieve. In fact, Barry et al. have successfully measured neuronal signals along axons of marine fan worms by placing the axon on a flat diamond substrate with embedded NVs [12]. In addition, work by Karaveli et al. have demonstrated NV sensing of 20 mV changes in potential by utilizing it as a charge state sensor [62]. The major issue with the previous work is that it focuses on the magnetometry of larger neuron structures such as marine fan worm axons which are microns in size. As sensing moves away from larger worm neurons towards the sensing of smaller mammalian neuron axons (nanometres in size), the signal will also decrease. It is this reduction in signal size which is the major barrier to NV neurosensing of mammalian neurons such as those found in the human brain. The next step in this research process and the major work of this thesis is to study the NVs performance for neurosensing and how to improve NV performance to achieve this goal.

The main solution to this problem presented in this thesis was inspired by work done with diamond nano-optics [8, 73, 74] as well as neuron growth studies on Indium phosphate pillars by Gautam et al. [35]. The idea is to sense neuron signals with the fabrication of diamond nanopillars, each with an NV sensor embedded within it.

The pillar geometry yields three advantages. Firstly, the shape of the pillars and the diamond's high refractive index guides the excitation and emission light in and out of the diamond without significantly illuminating the neurons themselves [74]. This light coupling phenomenon improves the sensitivity of the NV by up to 5 times [74] and reduces the phototoxic effect on the neurons from extended illumination. The second advantage comes from the growth of the neurons on the pillars themselves. It has been demonstrated using other materials that pillar geometries act like a scaffold for neuron growth, guiding neurites in a single direction along the tips of the pillars [35, 110]. This enhances the signal at the NV by coordinating neuron growth near the NVs themselves. In addition, the coordinated growth places a larger number of neurons structured in close proximity to the NVs. This provides more sites for experiment compared to an unstructured diamond. The third advantage lies in removing the Debye layer of the neuron; the key element that is absent in CC theories are the effects of the Debye screening layer [105]. The Debye layer is the build-up of ions on either side of the membrane due to the electrochemical forces acting on individual ions [51]. The Debye length is typically around 1 nm [51, 113], and is understood to greatly screen the electric potential external to the neuron [51, 97, 105], reducing its magnitude to zero over the course of a few nm. A diamond pillar placed in contact with the neuron could remove the screening ions, increasing the propagation of the external electromagnetic field. The assumption is that as long as the surface area where the nanopillar contacts the neuron membrane is small compared to the surface area of the enclosing cylindrical segment of the neuron, the removal of screening ions is unlikely to significantly alter the neuron's natural function. Based on the Ca^{2+} studies on an unstructured diamond [118] as well as Ca^{2+} studies performed on similar nanopillar arrays formed from other materials [35, 43, 44, 111], this assumption should be valid.

To assess the NVs potential in mammalian neurosensing two major initial steps are undertaken, neuromodelling and a proof-of-principle growth study. With the neuromodelling, the external electromagnetic fields of a simple neuron structure are simulated in order to assess whether the NV can sense the fields produced by a small mammalian neuron. With the growth study, a proof-of-principle demonstration of the diamonds biocompatibility is performed and a study of how diamond nano-pillar structures aid in sensing is undertaken. The results of these initial studies suggest that the NV is viable but requires further work to fully realise the technology. Improving NV sensitivity can make the neurosensing process more robust and easier to use and there are a variety of different improvement methods available. This motivates further research in which various techniques are studied to improve NV performance.

Whilst ODMR is a common and robust strategy for NV sensing, it is not the only method available. In conventional ODMR the ESR is measured as a change in fluorescence from the NV. Thus the key to measuring a spin resonance and subsequent electric or magnetic field lies in the optical contrast obtained from the measurement process. From this logic comes a method for improving optical spin contrast with the spin-to-charge conversion (SCC) technique. With SCC, the NV spin information is readout by optically ionizing the defect when it is in a particular spin state. Thus, the spin of the electron is mapped to the charge state of the NV and spin information is

obtained by measuring the charge state. This technique has been shown to have a larger optical contrast compared to conventional intrinsic photo-luminescence cycling techniques [58, 109, 131], which in turn increases the sensitivity of the NV.

The main approach to SCC in this thesis that is different to other works is with the use of an external electrode, which can have a variety of advantages in different settings. At cryogenic temperatures, SCC is not practical for biological sensing as the cells will die in such conditions, however, electrode-based, cryogenic SCC has the potential to immensely improve NV based cryogenic sensing as well as quantum computation. At cryogenic temperatures, the electrode creates a potential well within the diamond which has the effect of spectrally confining the density of low lying conduction band states in the diamond. This discretized conduction band has a two-fold effect. Firstly, it increases the photoionization probability at frequencies resonant to a discrete transition whilst reducing the probability of photoionization at other frequencies. Secondly, the electrode creates energy level separation in the conduction band which is much larger than the separation of levels in the NV ground state spin triplet. These two factors allow for an SCC protocol where the NV electron is resonantly ionized out of the ground state into a discrete conduction band state with a higher probability compared to conventional photoionization. The wide separation of the conduction band states means that the individual triplet transitions can be addressed. These factors create a highly selective spin to charge protocol with very high optical spin contrast. The technique promises to vastly improve the fidelity of spin readout which has applications for NV based quantum sensing, communications and computation. The design also creates a discrete three-level system for stimulated Raman adiabatic passage (STIRAP) experiments [83].

In addition to improving NV performance at cryogenic temperatures, photoionization at cryogenic temperatures has an additional advantage in that it allows for an in-depth study of fundamental NV physics. The key to NV spectroscopy and its many applications lies in its unique energy structure that allows for spin selective readout. Whilst much of the NV energy structure is known, there are still some energy level splittings that remain mysterious. One key method of understanding these energy levels is with photoionization. At cryogenic temperatures, an electron in the NV can be initialised into a particular state then ionized into the diamond conduction band. By using a laser that can sweep frequencies with a high spectral resolution, the energy of the transition from an NV state into the conduction band can then be found by performing the ionization pulse and checking if the electron was ionized by performing an NV charge state readout. By repeating this process where the NV electron is initialised into a different state, the energy difference in the two photoionization processes can be directly related to the energy splitting between the two energy states in the NV using Koopman's theorem [114]. This mechanism allows for a greater understanding of fundamental NV physics which in turn can help improve the overall performance of the defect as its photodynamics are better understood. In addition to this, the experimental techniques considered in this section can be applied to other defects to help understand their structure and function, potentially developing quantum defects that are superior to the NV. The results gained

from this experiment also permits an SCC readout mechanism that can be performed with the electrode at ambient conditions.

One key result of the photoionization experiment is the discovery that the energy for photoionization from the NV singlet states is almost the same as the energy for the zero phonon line (ZPL). This causes a significant issue with cross-talk where a single laser pulse will drive two transitions at the same time, creating noise in the readout when ionizing from the NV singlet state. One solution to this problem is to use an electrode to provide an electric field that will raise the energy levels in the NV without significantly affecting the diamond conduction band states. This will alter the photoionization energy relative to other transitions in the NV and allow for a unique room temperature SCC protocol that can, among other possibilities, allow for improved room-temperature readout and sensitivity of the NV for biological sensing. Whilst the electrode can be utilised in an SCC protocol at both cryogenic temperatures and at ambient temperatures, it is important to note that the SCC protocol and the application of the electrode are very different in the two approaches, requiring a very different approach to their theoretical modelling as well as their potential applications. The results of this study also have a wide range of potential improvements to the NV charge state control as well as spin coherence time.

If SCC improves the NV performance via increasing optical contrast, then improving the overall light obtained from the NV will also improve NV performance. The NV is a dipole emitter [57, 125] which emits in all directions from the defect. Placing a detector in one plane away from the NV will only collect some of the light emitted from the defect. Additionally, the high refractive index of diamond causes a large amount of reflection at the diamond/air interface which also limits the light collected during a measurement. Thus, another means of improving NV performance can be achieved by shaping the diamond structure itself around the NV. This changes the emission pathway in order to maximise the amount of light entering the detector. There are a number of known ways to achieve this including solid immersion lenses (SILs) [57], parabolic mirrors [125] and the nano-pillars already mentioned [74]. New methods of creating diamond structures can be developed and tested to observe the improvement in optical collection efficiency.

The main focus of this thesis is the development of the NV as a neurosensor, however, it has many other applications. Outside of sensing, information can be encoded onto the NV nuclear spin state as a quantum bit or qubit and the information extracted via a non-demolition readout of the NV electron spin [16, 90]. Information can also be encoded via entangling the NV nuclear spins with nearby carbon 13 nuclear spins [16, 90]. This makes the NV a viable candidate for the design of a quantum computer or quantum network. Whilst the majority of the work in this thesis is designed to improve the NV as a sensor, most of the work can also improve the NV as a qubit for computation. This motivates a study of quantum computing as a potential tool for simulating large scale networks of neuron systems. In this approach, a digital quantum simulation is studied and applied to a well-known differential equation for understanding neuron networks [36]. The potential speed-up of this algorithm can be assessed and the viability of its implementation on a diamond-based

quantum computer can be considered.

1.2 The nitrogen-vacancy center

The nitrogen-vacancy (NV) center is an atomic defect within a diamond carbon lattice. The defect consists of a substitutional nitrogen atom in place of a carbon atom and an adjacent empty lattice site (vacancy). Whilst the defect exists naturally in diamonds, for active use in research they are often engineered either en masse during chemical vapour deposition (CVD) growth [122] or in small numbers/singular sites with ion implantation [85]. With the vacancy in place, the carbon and nitrogen unbound electrons around the vacancy fill the space to create a unique molecular structure. Five electrons come from the adjacent atoms to create the neutral charge NV^0 state. An extra electron will create the negatively charged NV^- state which comes from a nearby donor in the diamond lattice, often a nitrogen defect. As long as the donor is close to the NV, the NV^- charge state will be relatively stable, however, active processes can ionize the NV^- back into the NV^0 state. This is most often achieved through photoionization, conversely, photoionization can ionize an electron in the diamond valence band or from another defect to the NV^0, returning it to the NV^- charge state. The electronic structure that allows for spin selective readout used in all NV quantum protocols only occurs in the NV^- state. Thus, all further uses of the term NV will be in reference to the NV^- charge state for simplicity. A more detailed study of the photoionization process is done in chapter 3.

The electronic structure of the NV consists of two orbitals with a well defined optical zero phonon line transition (ZPL) of 637 nm (1.945 eV) [25]. These orbital levels are spin triplets labelled $^3A_2$ (ground state) and ^3E (excited state). In between the triplet levels, there are intermediate ground and excited singlet levels labelled ^1E and $^1A_1$ respectively which have a ZPL transition of 1042 nm (1.190 eV) [25]. The triplet states naturally have fine structure splitting from spin-orbit interactions which split the levels into a singlet level ($m_s = 0$) and degenerate doublet levels ($m_s = \pm 1$). These levels have a zero-field magnetic resonance of 2.87 GHz in the ground state and 1.42 GHz in the excited state. The $m_s = \pm 1$ states can be further split into single levels with the application of an external magnetic field.

Along with the ZPL is a broad phonon sideband, this occurs as exciting vibrational modes in the diamond interact with the electronic transitions. During the excitation from the ground state to the excited state in the triplet manifold, the vibrational overlap with the electronic transition allows for a broad spectrum of absorption and emission in the NV. Whilst the resonant electronic transition in the NV triplet is 637 nm, the phonon sideband allows for excitation from a higher energy photon where the excess energy is released as phonons. This allows for off-resonant excitation at 532 nm with high probability, which is a common excitation laser in NV spectroscopy. Conversely, the phonon sideband allows for a range of emission energy when decaying from the excited state triplet back to the ground state. This emission spectrum is broad, with light emissions from 637 nm to 1000 nm, where the excess energy in the lower

energy transitions are released as phonons. At room temperature the ZPL emission only accounts for about 4% of the total emission spectrum, requiring a broadband detection window to measure NV fluorescence (see figure 1.1).

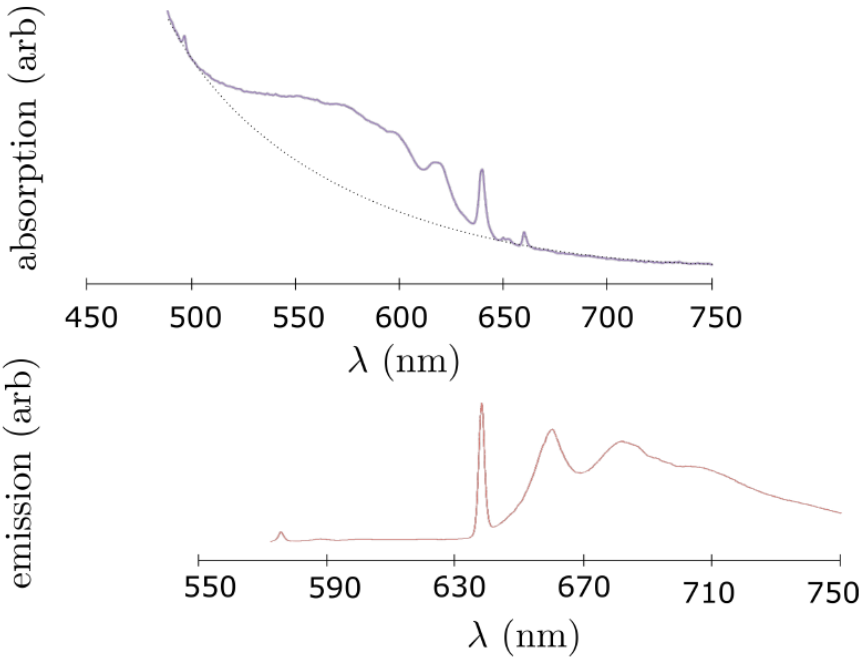

Figure 1.1: NV absorption a) and emission b) spectrum at ambient conditions. The broad phonon side-band allows for absorption and emission far outside the triplet ZPL of 637 nm. Image is taken from Michael Barson [103].

Upon excitation from the $^3A_2$ ground state to the ^3E excited state, the electrons can decay via two separate pathways. The first pathway is a spin conserving radiative transition back down the $^3A_2$ ground state, the second is a non-radiative transition from the ^3E excited state to the excited state singlet $^1A_1$. From this singlet state, there is a radiative transition to the ^1E ground state which can then reach the original $^3A_2$ state via a secondary non-radiative transition (see figure 1.2). The non-radiative transitions are called inter-system crossings (ISC's), unlike the radiative transitions which are spin conserving, these transitions can cross from triplet spin states to the singlet spin state via a spin-orbit interaction (see figure 1.2).

The ISC's are the key mechanism for spin readout using ODMR. In the excited state triplet, the ISC for the $m_s = 0$ is much slower compared to the $m_s = \pm 1$. This means that electrons in the $m_s = 0$ state are much more likely to decay via the radiative transition instead of the ISC compared to electrons in the $m_s = \pm 1$. Thus, when measuring the triplet ZPL emission (600 to 1000 nm), there will be much more fluorescence when the electron is in the $m_s = 0$ compared to the $m_s = \pm 1$ state, mapping the NV spin state to its fluorescence. In addition to this, the ISC from the

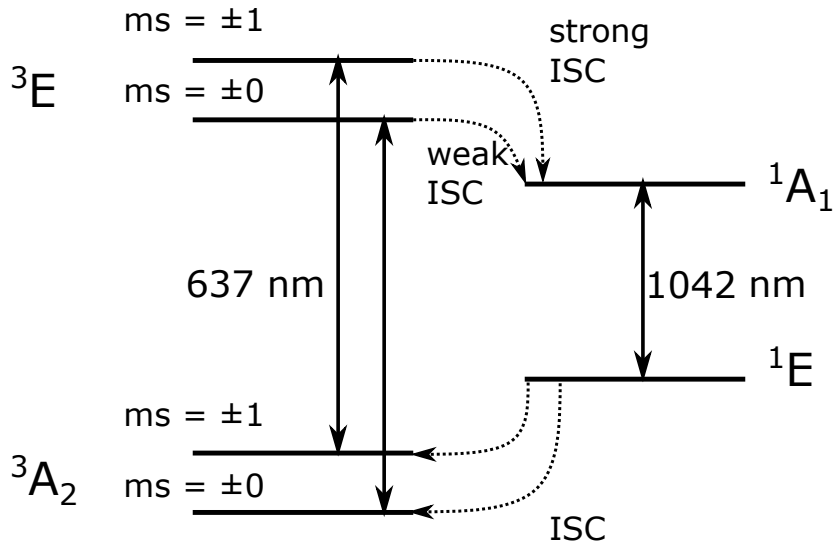

Figure 1.2: Electronic levels of the negatively charged NV center. The straight lines indicate the radiative ZPL transitions whereas the dotted lines indicate the non-radiative intersystem crossings (ISCs).

ground state singlet (^{1}E) to the ground state triplet (^{3}A$_2$) is roughly the same for both spin states in the ground state triplet. This process allows for spin initialisation. By applying a green laser to the NV for a few optical cycles, the electron is statistically much more likely to stay in the $m_s = 0$. This is due to the high probability of spin conserving radiative decay rather than spin altering ISC and the fact that the $m_s = \pm 1$ has a roughly 50% chance of converting to $m_s = 0$ during the ISC from the singlet to the ground state. Over time this means that the NV electron spin can be initialised into the $m_s = 0$ with about 70% probability. Initialising into the $m_s = \pm 1$ state is then achieved by initialising into the $m_s = 0$ state and applying a 2.87 GHz microwave pulse to make the zero-field magnetic resonance transition to the $m_s = \pm 1$.

ODMR is the basic process by which the NV acts like a sensor or a qubit. In quantum sensing, the zero-field resonances can be altered by external fields such as electric and magnetic fields, temperature and pressure. ODMR is a process where a microwave field is applied which sweeps over a range of frequencies and the fluorescence is measured at each frequency. Most microwave frequencies will be off-resonant to the spin-triplet transition, so the NV will remain in the $m_s = 0$ state and the fluorescence will be high, but when the frequency is resonant, the electron will be more likely to take the non-radiative transition from the $m_s = \pm 1$ state, causing a drop in fluorescence. Thus, by sweeping the microwave field over a range of frequencies and measuring the fluorescence, the drops in fluorescence at particular microwave frequencies can be attributed to the strength of the external field. For example, in NV magnetometry, the magnetic field splits the degenerate $m_s = \pm 1$ state due to the Zeeman effect[99], allowing for two microwave transitions from $m_s = 0$ to $m_s = 1$ and $m_s = 0$ to $m_s = -1$. Furthermore, the resonances split further and further apart with a stronger magnetic field. In an ODMR spectrum, this presents as two distinct

drops in fluorescence at the two separate resonant frequencies where the splitting of the resonances are linearly proportional to the external magnetic field [99] (see figure 1.3a). In NV electrometry, there is no splitting in the degenerate $m_s = \pm 1$, however the resonances shift in the presence of an electric field due to a Stark effect [27] (see figure 1.3b).

In quantum computation, there is an added complexity as the spin state being read out is the nuclear spin of the nitrogen or nearby carbon-13 atoms. The nuclear spin is mapped to the measurement of the NV electronic spin due to a hyperfine interaction. This allows for a projective non-demolition readout process where the nuclear spin state is readout via the NV electronic spin state in such a way that preserves the nuclear spin state [25]. In a quantum computer, various quantum gates are being applied to alter the nuclear spin states and by extension, the electronic spin states. However, the process of initialising the spin state and reading the electronic spin state with ODMR is the same for quantum computing and quantum sensing. This means that any process which improves electronic readout process has applications in both fields.

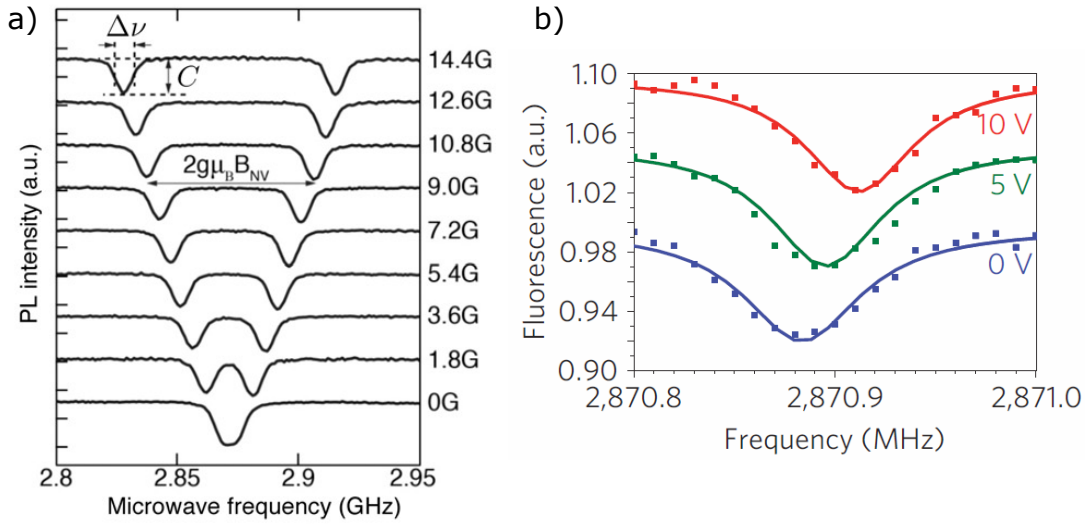

Figure 1.3: a) ODMR image of NV magnetometry from Rondin et al. [99]. As the magnetic field increases, the NV resonances split further and further apart due to Zeeman splitting. b) ODMR of NV electometry from Dolde et al. [27]. As the voltage (and subsequent electric field) changes, the resonance changes due to a Stark shift. Both processes allow for the NV to act as a sensor for magnetic and electric fields.

1.3 Thesis Outline

The aim of this thesis is to study the NV and its potential applications to neuroscience. The study begins with the neurosensing project in chapter 2. In section 2.1, a detailed overview of neurophysiology is performed, including the anatomy and physiology of neurons as well as the action potential (AP), how it is created and its associated electromagnetics. The current state of neuron imaging is described in section 2.2, where the strengths and weaknesses of a variety of technologies are considered including the potential impact of the NV. In section 2.3, established neuron modelling techniques are studied with the core conductor (CC) theory as well as the Hodgkin-Huxley (HH) theory, the strengths and weaknesses of these theories are addressed which leads to the application of a more fundamental theory of neuron modelling. In section 2.4, the more basic Poisson-Nernst-Planck (PNP) is applied in a unique way to simulate the Debye layer of the neuron and how an external sensor interacts with it. It is in this section that the NV diamond pillar is assessed for its capacity to measure a neuron signal. The final part of chapter 2 is the growth study in section 2.5, in this section an experiment was performed of neuron growth on a bed of diamond nano-pillars to demonstrate how structured diamond can alter the growth pattern of a neuron network to make sensing of the network much easier.

The result of the neurosensing study is that the NV can theoretically sense the electric fields of the neuron, however, efforts to improve NV sensitivity will make the

experimental process considerably easier. Chapters 3, 4 and 5 focus on understanding and improving the NV performance through photoionization and the spin-to-charge conversion (SCC) technique. In chapter 3, a unique SCC protocol is introduced with the application of an electrode and cryogenic temperatures via extensive theoretical modelling. In section 3.1, the photoionization concept in the NV is introduced in detail. In section 3.2, the mechanism for electrode-based discretization of the low lying diamond conduction band is extensively modelled with effective mass theory. In section 3.3, the major sources of linewidth broadening are considered and in section 3.4, the SCC protocol is detailed along with a calculation of the optical spin contrast and readout fidelity.

In chapter 4, the photoionization technique is applied to better understand NV, an experiment was performed in which the ground state energy splitting between the triplet and singlet manifolds of the NV are measured. In section 4.1, the photoionization experiment is introduced, with its aims and technical considerations for the experiment. In section 4.2, the diamond vibronic structure is studied to understand the effects of electron-phonon broadening on the experiment at different temperatures and in section 4.3, the preliminary results are analysed which motivate the future direction of the research.

The results of this experiment have a direct relation to the electrode-based ambient SCC protocol detailed in chapter 5. In this chapter, a new electrode-based ambient SCC protocol is introduced which relies on using the electrode to shift the energy levels of the NV relative to the diamond conduction band. In section 5.1, the SCC mechanism is outlined along with the method for calculating optical contrast using rate equation modelling. In section 5.2, the rate equation modelling is used to optimise the electrode-based SCC readout and in section 5.3, the same rate equation modelling is used to compare and contrast the electrode-based SCC protocol with another established methods of ambient SCC readout [58]. Finally, in section 5.4, a range of conceptual applications and advantages of the electrode-based SCC readout are considered and the future direction of the research is outlined.

In chapter 6, NV performance is considered via the study of optical collection efficiency. The issues with the standard readout of NV fluorescence is detailed and solutions are introduced with the shaping of diamond structures around the NV into solid immersion lenses (SILs) or parabolic mirrors using a focussed ion beam (FIB). In section 6.1, some basic concepts of diamond optical reflection and transmission are presented. In section 6.1, the FIB process for creating a parabolic mirror with a deep NV placement is detailed. In section 6.3, the quality of the FIB process is analysed with characterisations of the parabolic structure and simulations of how NV placement and parabolic structure affects the optical collection efficiency. Then in section 6.4 the results are analysed to guide future experiments.

Whilst these methods help improve NV sensitivity, most of the results have greater applications to readout fidelity in quantum computing and understanding basic NV physics. The improvements to NV quantum computing leads the research down the path of using NV quantum computing for simulating large neuron networks. In chapter 7, the mathematical model for studying large scale neuron networks using a

quantum computer is conceptualized. In section 7.1 a known mean-field model for simulation large networks of connected neurons is introduced [36]. In section 7.2 the computational complexity of this model is analysed and an alternative method for simulation using quantum computers is introduced. Some basic means of quantum encoding in the problem are addressed along with a short analysis on the potential quantum computer hardware requirements for a useful speed-up are considered.

Chapter 2

Neurosensing with the NV

The NV has immense capacity to sense neuronal electromagnetic fields, creating applications in neuroscience medical research. To understand this concept fully, a study of neuroscience and the NVs application to it must be performed. In this chapter, a new approach to NV based neurosensing is studied by engineering NV quantum sensors in diamond nanopillar arrays (figure 2.1) and switching their sensing mode to detect the changes in the electric fields instead of the magnetic fields which have the potential to greatly improve signal detection. This proof-of-principle approach allows for the change from sensing the magnetic field of larger worm axons performed by Barry et al. [12], to the electric field of smaller mammalian neurons. Allowing for a much wider range of neuroscience studies to be performed.

Apart from containing the NV quantum sensors, nanopillars also function as waveguides, delivering the excitation/emission light to improve sensitivity. The more light that can be collected from the NV during a measurement, the more information gathered which improves sensitivity. The nanopillars also improve the amplitude of the neuron electric field sensed by the NV by removing screening charges. When the nanopillar array is used as a cell niche, they act as cell scaffolds, which make the pillars function as biomechanical cues that facilitate the growth and formation of neuronal circuits. Based on these growth patterns, numerical modelling of the nano-electromagnetics between the nanopillar and the neuron was also performed.

In section 2.1 the neuron anatomy and physiology is studied in order to understand how and why a neuron creates an electromagnetic signal. This includes a brief study of the neuron anatomy, the charge distribution inside and outside the neuron, how ion channels alter this charge distribution to produce a signal and some basic mathematical theory of the transmembrane potential and Debye layer. In section 2.2 the current state of imaging neuronal signals is addressed and the advantages and disadvantages of each technology are assessed. This includes patch clamps, voltage-sensitive dyes, calcium indicators, genetically altered proteins, microelectrode arrays and a brief analysis of the potential of the NV nanopillar array in comparison to the other modalities.

Section 2.3 focuses on the established theory of neuromodelling for assessing the NVs capacity to sense a signal. In particular, the core conductor (CC) theory, and why it is inappropriate for our purposes. The CC theory leads into the highly

celebrated Hodgkin Huxley (HH) theory for modelling an AP. Section 2.4 applies the HH theory as a boundary condition along with the Poisson-Nernst-Planck theory or ionic charge distribution in a unique way in order to create the first model of the full external neuron electromagnetics (electric potential, electric field, magnetic field as well as charge and current densities). The solutions to this model are then applied to understand how external electromagnetics interact with a nanodiamond pillar.

Finally, in section 2.5 the growth study experiment is performed. Some basic understanding of how neurons grow in relation to the pillars is introduced. An experiment is undertaken to understand how pillar geometries are affected by growth, a detailed analysis of how to quantify coordinated growth is performed and an analysis is performed about how the neurons grow on diamond nanopillars and how the results can be considered for further experiments.

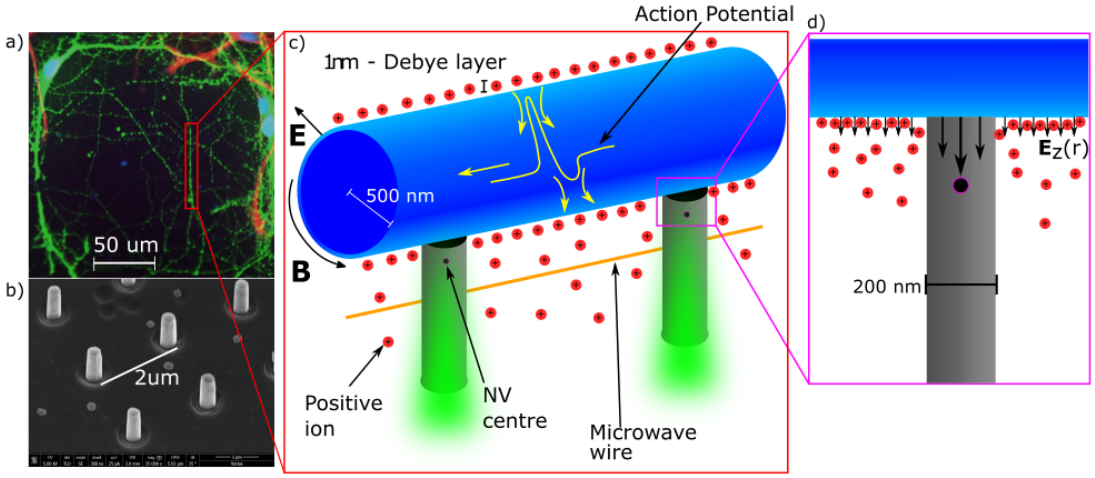

Figure 2.1: a) Confocal image of the stained neurons (green) grown on a bed of nanopillars. The cell labelling was performed using immuno-fluorescent dyes for the neurons and astrocytes and a Hoechst stain for the cell nuclei. b) scanning electron microscope image of one diamond nanopillar geometry. c) Cutout of a neurite grown on the pillars. The panel shows the cylindrical neurite with the surrounding positive ions that form a ≈1 nm thick Debye layer (negative ions not shown). Yellow arrows inside the cylinder indicate the current flow during an AP, which is depicted by the yellow line. The net ion charge and current densities generate the electric (**E**) and magnetic fields (**B**), respectively. These fields can be measured by the NVs situated in the grey diamond pillars. The sensing protocols use a green laser and microwaves to optically address the NV spin resonance. The pillars confine the laser light and direct the NV fluorescence. d) Illustration of how the pillar removes the Debye screening charges by making contact with the neurite membrane. This increases the radial electric field at the position of the NV.

2.1 Anatomy and Physiology

The Neuron is the basic cell type that exists in all nervous systems, its primary function is to connect to other cells in order to communicate signals across an organism. Neurons can connect from cell to cell in a line as well as to multiple cells is a neural network. Neurons can form connections to any type of cell to transmit a signal but primarily connect to other neurons in the large information network of the brain [3, 51, 61, 93].

The method of signal transmission is an electrical impulse, the way the neuron achieves this is via the movement of charged ions across the cell membrane. Neurons establish an electric potential across the cell membrane which encourages ions to pass through specific membrane channels under particular conditions. The process of ion channels opening and closing in succession across a neuron allows ion flow. This process creates longitudinal electric signal propagation in the form of a transverse wave [3, 51]. In order to understand the specific mechanism for this signal propagation, it is then important to understand the anatomy of the neuron, the structure of the membrane, its ion channels as well as the ion concentrations that establish the electric potentials.

Neurons have a variety of sub-structures that facilitate signal propagation (figure 2.2); they begin with dendrites where an external stimulus begins the propagation of a signal, the signal will then move to a cell body (Soma). If the signal is large enough to meet a threshold potential, it will then be amplified and broadcasted down the axon to an axon terminal where the signal is passed to another cell. This process of a signal being amplified and moved down an axon is called the action potential (AP). In the absence of an AP, the neuron maintains a constant potential known as the resting potential. The point where the cell connects to other cells (either at the dendrite or axon terminal) is a gap junction which is called the synapse [3].

The dimensions of each neuron can vary considerably; the size scale is typically in micrometres however some large axons can be millimetres in diameter and metres long [3]. In this thesis, the dimensions used are average values for mammalian cells such as those found in rats for experiments or people. The soma has a 15 μm radius [3], the axon and dendrite have a 0.5 μm radius [3], and the membrane itself has a 5 nm thickness [51]. The potentials generated by these types of cells, both the subthreshold events and the APs themselves can also vary in amplitude and duration, thus average values for mammalian neurons signals are what is primarily considered in this thesis [3, 51, 61].

Across the cell membrane, many different charged particles can travel, but only through specific channels, of which there are over 100 different types [3]. For the purposes of this study, only three major classes are considered, passive leak channels, active ion pumps and voltage-gated ion channels. Passive leak channels and the ion pumps work together to create a constant charge separation across the cell membrane which produces the resting potential. The voltage-gated ion channels work during electrochemical stimuli to create the AP. The three channel types apply two different means of allowing ion transport, passive or active. In passive transport, ions move

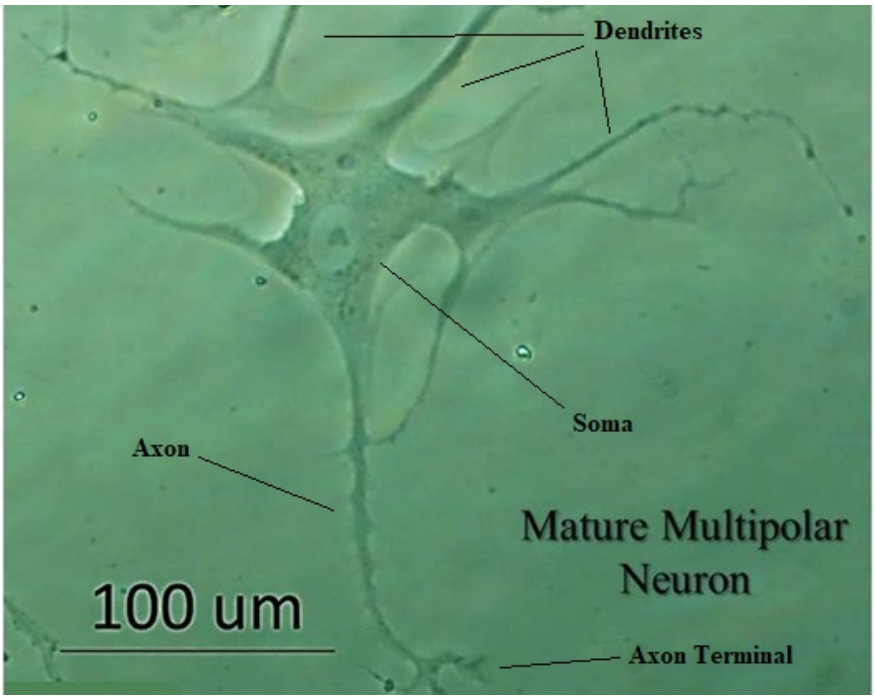

Figure 2.2: Photomicrograph of a neuron, note the central soma, with dendrite tendrils attached to it. The long rough tendril at the bottom of the image is the axon, which splits into the axon terminal at the very bottom of the image. Source Otify et al. [86].

across the membrane naturally via both their electrical and chemical potential. Electric potentials move ions to form a charge equilibrium, whereas chemical potentials move ions to form a concentration equilibrium. Active ion transport utilises cellular energy and chemical reactions to move ions against these electrochemical potentials [3].

Passive leak channels are protein pores that selectively allow ions to pass through the membrane per their electrochemical gradient (passive transport). Leak channels attract charged ions via charged amino acids in the entrance to the pore, the selectivity of the pore is created by the particular energy of molecular bonding. In solution, the various ions form complexes with water via weak intermolecular dipole interactions, each ion uses a different amount of energy when forming these bonds. The leak channels exploit this when applying their selectivity filter. The proteins for each type of pore have a similar weak intermolecular dipole bonding energy requirement which is exactly matched by the energy gained when the water molecules are removed as ions pass through the pore (fig 2.3). Since different ions have different bonding energy with water, ions that don't match the energy required to bond into the leak channel proteins will not pass through the membrane, thus creating a filter in which only a particular ion species can pass through. The selectivity of leak channels is extremely high, potassium leak channels conduct potassium 10,000 times better than sodium despite the two ions having the same charge and only 0.038 nm difference in diameter. In addition to this, leak channels can transport 100 million ions per second, as much as

10^5 times faster than any ion pump system, making the channel much faster and more efficient. Finally, it's important to note that there are typically many more potassium leak channels compared to any other ion leak channel, this helps create the passive equilibrium for the resting potential [3].

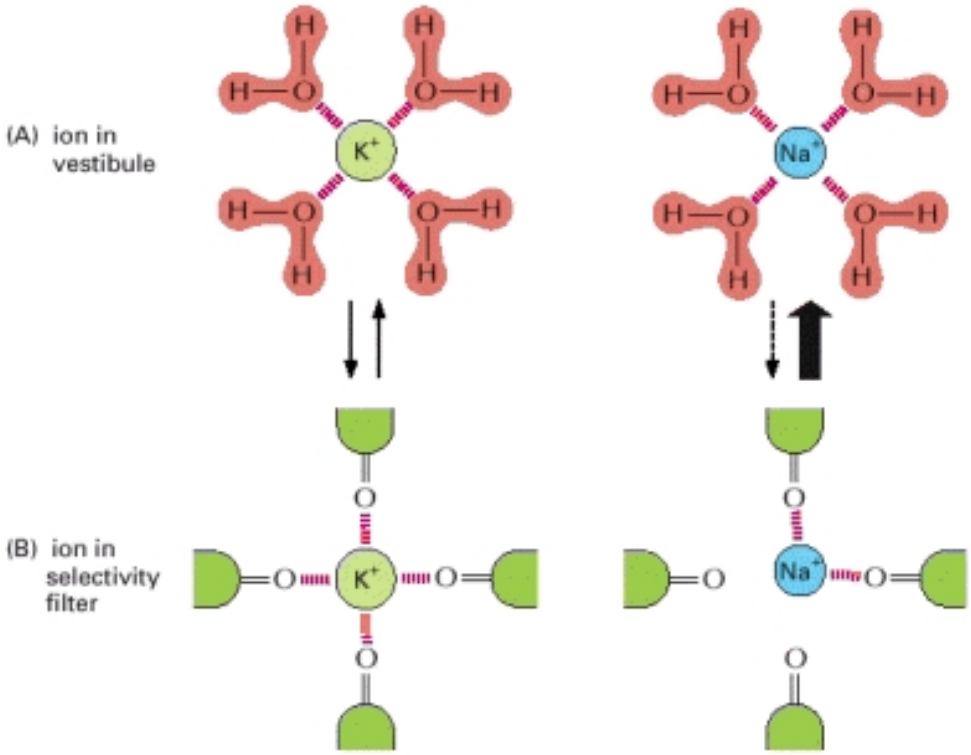

Figure 2.3: Diagram of the potassium leak channel. the above image (A), shows both potassium (left) and sodium (right) bound to water molecules via intermolecular forces. The bottom images in (B) show the ions interacting with the selectivity filter of the leak channel, the energy gained from removing water from potassium is exactly matched by the energy required to bind to the filter and pass through the channel. Sodium on the other hand is bound to water with less energy and thus does not meet the requirements to pass through the channel. Source: Alberts, Molecular Biology of the Cell [3].

The ion pump is a large complex of proteins that utilize the cellular energy, adenosine triphosphate (ATP) to create strong chemical bonds to ionic species. Upon binding, the proteins undergo a conformational change which exposes the protein from one side to the opposing side of the membrane and lowers the binding energy of the ion-protein bond, allowing the ions to break away into the opposing transmembrane space (fig 2.4). This active energy process allows a cell to pump ions in and out of the cell against the ions passive electrochemical gradient [3].

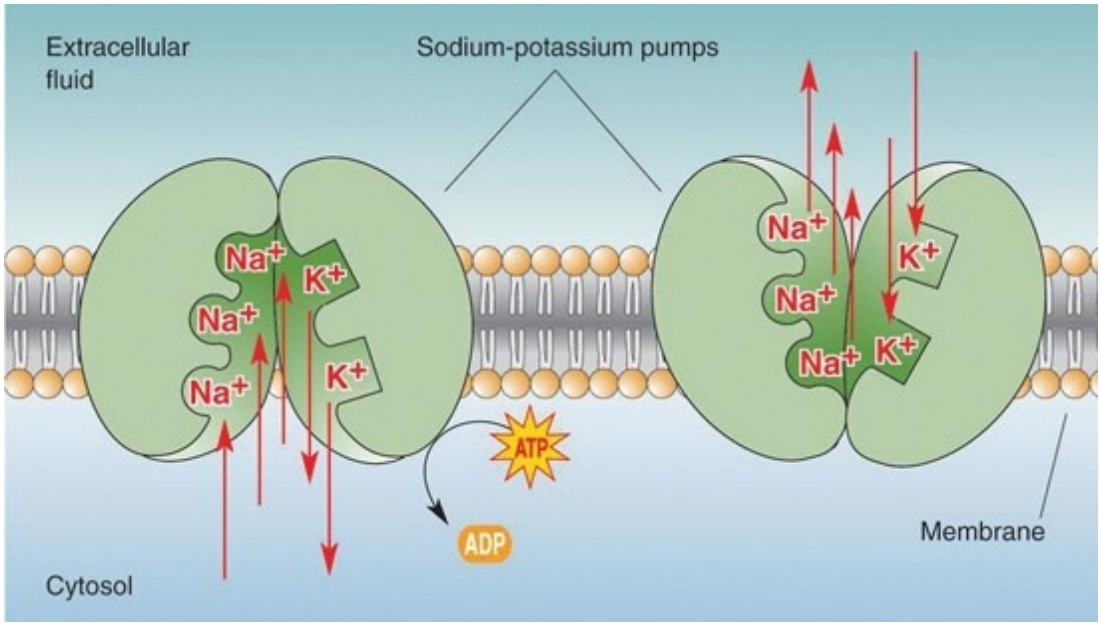

Figure 2.4: Diagram of the ion pump, the image shows the pumps two conformations. The left conformation allows intracellular sodium to bind to the pump whilst releasing potassium. ATP causes the pump to undergo a conformational change to the right image whereby sodium is released outside the cell and potassium binds to the pump. Source: Alberts, Molecular Biology of the Cell [3].

Ion pumps force intracellular sodium Na outside the cell whilst pumping extracellular potassium K into the cell. An important aspect of this transport system is the ratio of ion transport; from figure 2.4 it is clear that for every 2 potassium ions that are pumped inside the cell, three sodium ions are pumped out. This helps to create a charge separation which in part forms the resting potential [3].

The Voltage-gated ion channel is a channel that allows the flow of ions in and out of the membrane in response to a stimulus potential (often at approximately -55 mV). When the potential is below this threshold, the proteins in the channel are shaped in a way that closes the channel completely. During electrochemical stimuli, charged molecules enter via the dendrite and diffuse towards the voltage-gated ion channels in the soma, creating a local potential change. This sub-threshold signal is often called a postsynaptic potential (PSP) as it comes from a synaptic connection from another cell. If the PSP reaches the threshold value (often by combining with multiple PSPs), then that will activate the voltage ion channels. This causes a conformational change to open the channel which results in a rush influx of sodium ions, heavily depolarizing the cell. It is important to note that the PSPs can be excitatory, increasing the change of an AP or inhibitory, decreasing the chance of an AP. Structurally, the voltage-gated ion channel is similar to the leak channel in its speed of flow as well as its selectivity for sodium over other ions. However, the voltage-gated ion channel has additional structures which respond to the local potential to undergo the conformational change,

figure 2.5 [3, 5]. Although the principle is well understood, the physical mechanism which senses the gradient potential and causes the conformational change is not known. The main reason for this is that no current technique can measure changes in electric potentials next to the channel itself (within a few nm). The NV potentially can, giving it a distinct advantage as an imaging tool [27].

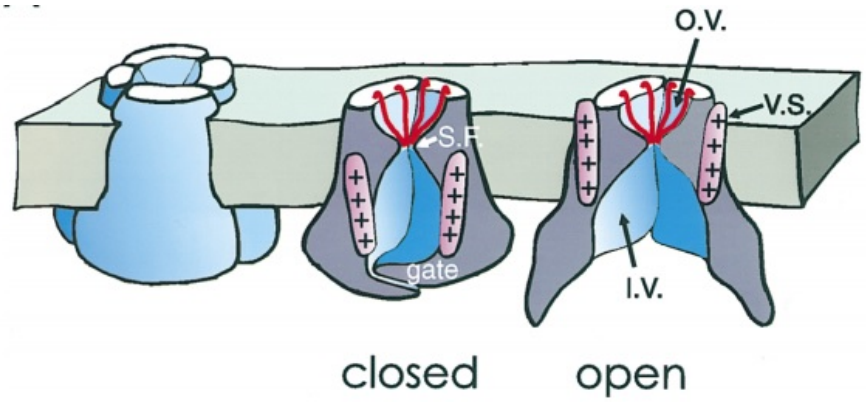

Figure 2.5: Diagram of the voltage-gated ion channel with the various protein subunits labelled (O.V, V.S, S.F). The middle image shows the channel in the closed conformation, preventing ion flow during the resting potential. The right image shows the lower protein subunits opening up to allow ion flow through the channel, although the concept is clear, the physical mechanism for how the channel opens is not well understood. Source: Armstrong and Hille [5]

The axon hillock is a region of the neuron where the soma meets the axon (see fig 2.7. In this region, the density of voltages gated ion channels increases from approximately 10 per μm to 100 per μm [61]. It is in this region where an external stimulus from the dendrite can activate the voltage-gated ion channels to begin the action potential. The principle is that if a stimulus activates one or two voltage-gated ion channels, the influx of sodium will change the local potential, activating the channels next to it. This causes a chain reaction that results in a large amount of sodium entering the cell, heavily changing the electrostatic equilibrium of the cell. As the sodium diffuses down the axon, more voltage-gated ion channels are activated, propagating the voltage signal as a transverse wave [3, 61].

Like all mammalian cell membranes, the neuron membrane is a complex structure primarily made up of phospholipids; along with phospholipids are galactolipids, as well as various proteins and cholesterol molecules embedded in the cell. The ratio of phospholipids to other molecules can vary from cell to cell and even across different parts of the cell. For example, the ratio of phospholipids would increase in parts of the cell where there is less molecular transport such as the axon but have increased proteins and ion channels in areas where there is high molecular transport, such as dendrites [3, 21]. Additionally, the density of phospholipids can change with changing curvature of the cell itself, densities tend to increase with increasing curvature (or reduced radius) [21]. Typical mammalian neurons approximate the phospholipid

density at approximately $5 * 10^6$ lipids per μm^2 [3]. The phospholipids themselves are a largely organic, hydrophobic carbon chain that can be saturated or unsaturated. At one end of the chain there are negatively charged, hydrophilic phosphate groups. These lipids come together in non-covalent bonding to form a lipid bilayer, a structure that consists of a double layer of phospholipids organized with the negatively charged heads pointing outwards, figure 2.6. This structure creates a hydrophilic membrane surface with a hydrophobic centre. The total thickness of the average cell membrane can vary from cell to cell, however from mammalian neurons, the thickness is typically placed at 5 nm [3, 51].

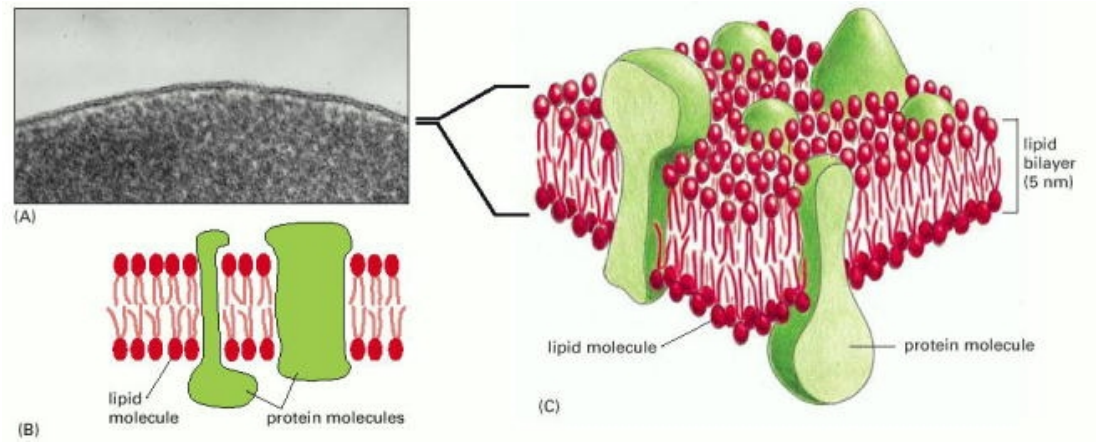

Figure 2.6: Typical cell membrane featuring the phospholipid bilayer with the charged heads pointing outwards from the membrane (red balls). The image also features various large proteins and other molecules which are often embedded in the cell (green). Source: Alberts et al., Molecular Biology of the Cell (2002) 4th Edition.

The primary role of the membrane is to create a wall that selectively allows various molecules in and out of the cell domain. In terms of electric potentials, the membrane has added importance as a charge separation across the inside and outside of the cell allows the membrane to become a capacitor, building up charges on either side of the membrane and creating the Debye layer across cell membranes.

With the Anatomy and physiology outlined, it is possible now to consider the microscopic nature of the cell in terms of ion flow. It is the ions moving in and out of the cell which generates the electric potentials across the cell. In this regard, there are three major potential environments to consider: the resting potential, the post-synaptic potential (PSP) and the action potential (AP).

The resting potential is created when the neuron is not transmitting an electrical signal, however, must maintain a charge separation in order to create APs when needed. The resting potential is generated by a steady-state equilibrium of ion flow. To create a resting potential, a difference of ion concentrations is created across the membrane of the neuron, this is initially mediated by the active ion pumps [3]. The pumps force intracellular sodium outside the cell whilst pumping extracellular

potassium into the cell. As the pump moves three positive charges outside the cell for every two going in, there will be a greater positive charge outside the cell. In addition to the active pumping, there are also negatively charged proteins produced by the cell which remain inside the cell. These two processes create an electric potential that encourages potassium to move inside the cell via the potassium leak channels [3].

It's important to note that sodium cannot enter the cell as easily as potassium as there are few sodium leak channels that allow it to move across the membrane and the voltage-gated pumps for sodium are closed. There is however a large amount of potassium leak channels to selectively allow potassium flow. Its also important to note that there are many other ions that exist across the cell membrane which can alter the potential (e.g. calcium and chlorine), however in mammalian cells, either their concentration is small or their ability to travel across the membrane is negligible, so their effect on the potential is minimal. A fuller description of the ionic concentrations for mammalian neurons is given in table: 2.1 [3, 51, 93].

As potassium flows into the cell along its electrical gradient, the buildup of the ion creates a concentration gradient which begins to encourage potassium flow outside the cell via the same leak channels. The potassium ion flow moves towards its electrochemical equilibrium, whereby the electric potential and the chemical gradient are equal and the flow of the ion stops. For potassium, its electrochemical equilibrium is at approximately -90 mV. However, the active ion pump forces potassium into the cell against its electochemical gradient, keeping the flow of ions across the membrane in a steady-state equilibrium. This steady-state system is the resting potential and is often measured at approximately -70 mV for mammalian cells. Note that there is a strong electric and chemical gradient for sodium to move into the cell, but largely cannot due to the lack of sodium selective channels, this gradient is utilized in the action potential [3, 51].

Mammalian Cell	Intra cellular concentration mM	Extra cellular concentration mM
K^+	139	4
Na^+	12	145
Cl^-	4	116
OA^-	138	9
Mg^{2+}	0.8	1.5
Ca^{2+}	<0.0002	1.8

Table 2.1: Table of ion concentrations inside and outside the cell in the neuron resting state. The OA^- term represents charged proteins produced by the cell. Note how overall there is still more overall positive charge inside and outside the cell. By neuroscience convention, the electric potential is defined as the inner concentration relative to the outer concentration, creating a negative potential [93].

In order to better understand and predict the resting potential, one can consider that during the resting potential, the ions are in thermal equilibrium. Thus it is

possible to model the ions using a Boltzmann distribution. Consider the relative probability of finding a particle in energy state 1 (P_1) or state 2 (P_2) as the energy difference between those two states in a Boltzmann distribution:

$$\frac{P_2}{P_1} = Exp(-\frac{u_2 - u_1}{k_b T}), \tag{2.1}$$

where u_1 and u_2 are the energies of state 1 and 2 respectively, k_b is the Boltzmann constant and T is the temperature. It is common to then re-express this equation in more chemical terms, where the probabilities are termed concentrations: $\frac{c_2}{c_1}$ and the energies are termed as molar energies: $U_2 - U_1$. This changes the Boltzmann energy to RT where R is the universal gas constant:

$$\frac{c_2}{c_1} = Exp(-\frac{U_2 - U_1}{RT}), \tag{2.2}$$

rearranging for the energy difference gives:

$$U_1 - U_2 = RTln(\frac{c_2}{c_1}), \tag{2.3}$$

in equation 2.3 the electrical molar energy difference $U_1 - U_2$ of a particular ion is a direct cause of the electrical potential difference $\Delta V = V_1 - V_2$ acting on an ion with charge e, a valency z, and multiplied by Faraday's constant F. Substituting these terms in and rearranging:

$$\Delta V = \frac{RT}{ezF} ln(\frac{c_2}{c_1}), \tag{2.4}$$

equation 2.4 is well known as the Nernst equation [51]. It describes the electric potential in terms of the concentration of the ions inside the cell (c_1) and the concentration of ions outside the cell (c_2). However, the Nernst equation is limited in that it only considers ions of a single species in equilibrium. The equation can be expanded to include terms from all contributing ion species:

$$\Delta V = \frac{RT}{F} ln\left(\frac{\sum_{i=1}^{M} P_{i+} c_{i+} \sum_{j=1}^{N} P_{j-} c_{j-}}{\sum_{k=1}^{O} P_{k+} c_{k+} \sum_{l=1}^{P} P_{l-} c_{l-}}\right), \tag{2.5}$$

Where P is the permeability of a particular ion species largely governed by the ion channels. The sums in i, j, k and l represent the ion concentrations of positive and negative species outside the cell (i and j respectively) as well as the ion concentrations of positive and negative species inside the cell (k and l respectively) [51].

The constant term: $\frac{RT}{F}$ is 26.7 mV at human body temperature (310.15 K); meaning that the sign of the potential is determined by the charge of the ions. The permeabilities are often described as a ratio relative to potassium; at resting for the major contributing ions they are given as: $P_K : P_{Na} : P_{Cl} = 1 : 0.05 : 0.45$ [51]. With these constants and the concentrations from table 2.1, the Goldmann equation can accurately predict the resting potential of mammalian neurons at approximately -70 mV, which can be confirmed experimentally [3, 51]. The model however has no spatial or temporal

component. This implies that the Goldmann equation cannot describe dynamic systems, nor can it describe a system whereby the potential changes with radius. The equation assumes a situation whereby the electric potential doesn't change when approaching the membrane. Section 2.3, describes a model in which the electric potential can be vastly different at the level of the membrane (PNP model).

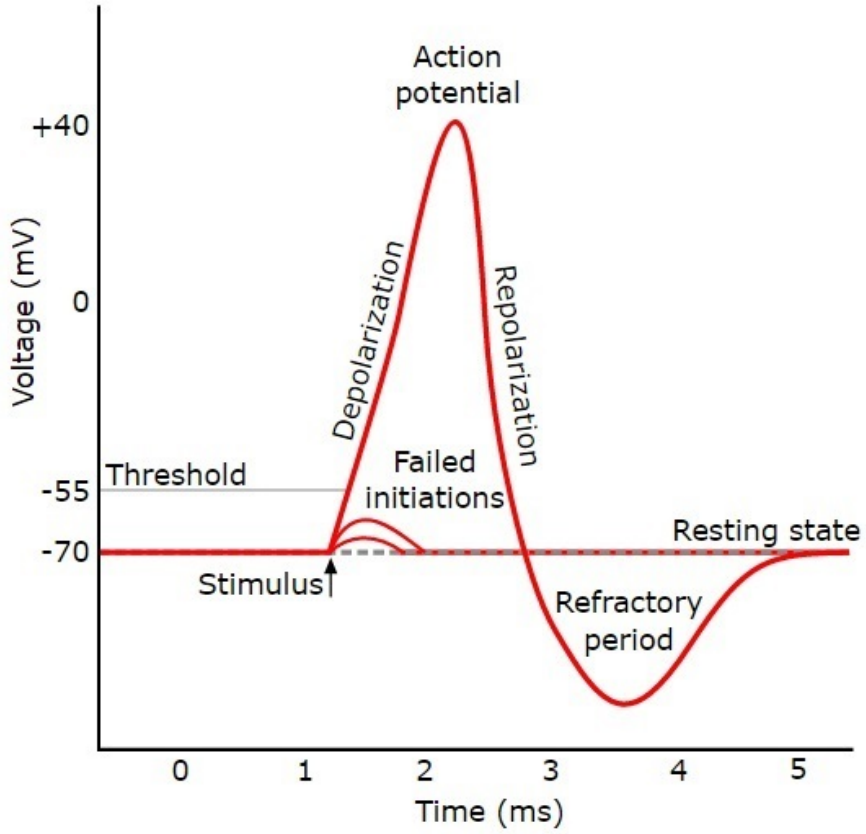

Figure 2.7: Graph of an electric potential as a function of time during an AP. The small hills are the PSPs that are not large enough in amplitude to meet the threshold for opening the voltage-gated ion channels (-55 mV). If a PSP makes the threshold potential, then the voltage-gated ion channels open, causing a large depolarising increase in signal, i.e. the large middle peak. The final drop in potential is the refractory period. Right image source: Purves et al., Neuroscience [93].

When an AP from a primary cell reaches an axon terminal at the synaptic connection to another secondary cell, chemical processes release small amounts of molecules called neurotransmitters into the synapse. Neurotransmitters come in a variety of forms and chemically bind to ion channels in the secondary neuron to open them and increase ion flow. The type of channel the neurotransmitter binds to will change the outcome of the ion flow. If the neurotransmitter binds to ion channels that selectively allow positive ion flow (e.g. Na^+ or K^+), then there will be an increase in positive ions in the secondary neuron increasing the potential from -70 mV towards 0 mV,

depolarising it. If this increase in potential reaches a threshold at the axon hillock where the voltage-gated ion channels are, then the synaptic event will cause an AP in the secondary neuron which will transmit a signal to another cell. If however, the neurotransmitter is a type that binds to ion channels that selectively allow negative ion flow (e.g. Cl^-), then the secondary neuron will experience a decrease in potential, hyperpolarising it which decreases the chances of an AP occurring. The neurotransmitter event causing a local potential change in another cell is called a postsynaptic potential (PSP), if the PSP causes a depolarisation, then the PSP is excitatory (EPSP), if the PSP causes a hyperpolarisation then the PSP is inhibitory (IPSP) [93]. In complex neuron networks, EPSPs and IPSPs work together to change the probability of a neuron firing which affects the network. It is important to note that in a network a synapse can be a connection of multiple neurons. So whilst a neuron might receive an EPSP from one neuron, increasing the chances of generating an AP, it might also receive an IPSP from a different neuron at the same time, reducing the chances of generating an AP. The amount and type of neurotransmitter released by neurons at a synapse can also change in time as neurons grow and change with response to various stimuli which in turn alters the probability of neurons firing. This changing nature of neuron chemistry and structure is known as neuroplasticity [93]. Understanding how PSPs operate in a complex and changing neuron network is one of the main goals of neuroscience and is the reason why understanding a nanoscopic structure such as ion channels at a synapse can have a profound effect on the neuron network as a whole.

When the neuron experiences a stimulus at the dendrite synapse which creates an EPSP that is large enough to activate the voltage-gated ion channels the AP begins. During this process, the chain reaction of voltage-gated ion channels causes a rush influx of sodium ions which depolarizes the membrane potential towards sodium's electrochemical equilibrium (approximately +50 mV, figure 2.7) [3, 51]. Once the action potential has begun, the influx of ions will diffuse inside the axon in all directions. This has the effect of dispersing the potential wave created by the action potential activating other nearby voltage-gated sodium ion channels, propagating the signal in the longitudinal direction. After the depolarization, ion pumps will begin to work to repolarise the cell by expelling the excess sodium ions. In addition to this, the voltage-gated potassium channels will pump out potassium from the cell for a short while during this repolarisation process, this has the effect of shortly hyperpolarizing the cell after the action potential. This is shown in figure 2.7 as the refractory period on the voltage graph. This process prevents the local potential from reaching sodium's electrostatic equilibrium (maxing out the potential at +40 mV). The purpose of the refractory period is to drop the local potential around voltage-gated ion channels to well below the threshold limit; this allows the ions to diffuse in all directions in a way that activates new voltage-gated ion channels without reactivating the old ones which have already opened up, unnecessarily recreating the AP. After the AP, the leak channels and ion pumps will begin to work in order to re-establish the resting potential, allowing a further action potential to occur if the stimulus persists [3, 51].

As the ions diffuse in the axon, the signal is propagated via the myelin sheath and the nodes of Ranvier (figure 2.8). The myelin sheath, is simply an insulating

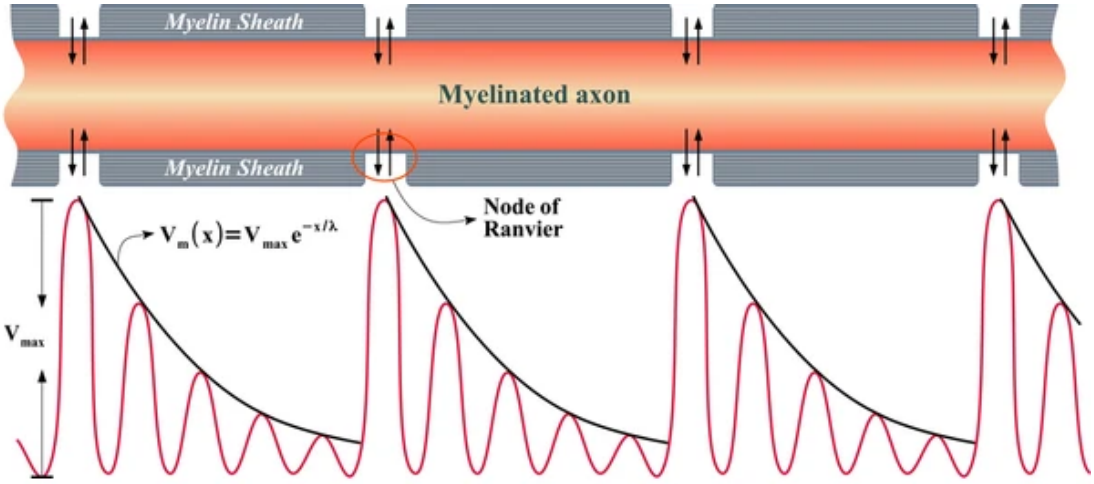

Figure 2.8: Diagram of the neuron focusing on the axon. The potential moves faster in the myelinated axon but loses signal strength due to dispersion. At the node of Ranvier, the signal slows down but is boosted by the voltage-gated ion channels.

membrane, wrapping the axon in segments, the purpose is to cause charge separation of ions, lowering capacitance on the membrane, and thus reducing the number of ions in the axon which might impede the ion diffusion of the action potential ions. This has the effect of increasing the speed of the travelling AP wave. As the ions creating the signal diffuse, the potential wave will shrink in amplitude due to dispersion. In between the myelin, sheath segments are nodes of Ranvier, which have voltage-gated channels. When the AP reaches a node, it causes a further influx of sodium ions into the axon. The influx has the effect of increasing the density of sodium, thus increasing the potential, preserving the wave. This process of both boosting the speed of the wave as well as maintaining its amplitude in 2 part steps is called saltatory conduction, propagating an electric signal in the form of a transverse wave [3, 51]. Myelin sheaths and saltatory conduction can increase the speed of an action potential from 2 m/s to approximately 200 m/s for an axon of the same size. Alternatively, it can allow for conduction speeds of a large unmyelinated axon to be equivalent to a much smaller myelinated axon. For example, the conduction speed of an unmyelinated giant squid axon is approximately the same as a myelinated frog axon (25 m/s) despite the almost 30-fold reduction in axon diameter, allowing for a much more energy-efficient process [49]. It's important then to note that not all neurons are myelinated, however, most are, the neurons being studied in this thesis are unmyelinated as they are simpler to consider. However, future work would likely lead to studies on myelinated neurons, necessitating this understanding.

It has been established that the difference in ion concentration across the membrane creates a charge separation which creates the electric potential. When considering the electric potential, its important to recognize that with the exception of bound

molecules on the membrane, all other charges (the ion concentration) aren't fixed. The ions can move freely to form an electrostatic equilibrium. During the resting potential, the negatively charged ions in the cell are built up along the interior of the membrane due to electrostatic forces. At the outer surface of the cell membrane, the negatively charged interior, as well as the negatively charged membrane itself, will encourage the formation of a layer of polar water molecules as well as divalent positive ions, often calcium and magnesium, although their bulk concentration is negligible, in this layer their concentration can increase by up to 10^4 times the bulk amount [51]. The positive and negative charges on either side of the membrane together will partially screen the electric potential, causing an exponential decay of the potential away from the cell membrane, the physical mechanism for this is described in more detail in section 2.3. At greater distances, the remaining ion concentrations experience a lower electric potential and continue to screen the potential until the ions reach an equilibrium. Outside the cell, the equilibrium of positive and negative charges can become equal, forcing the potential to go to zero. However, inside the cell, the ion concentrations cannot perfectly equilibrate and will go towards a constant potential. This is the transmembrane potential (or resting potential in steady-state equilibrium). This screening layer of ions which creates the exponential decay of electric potential is often called the Gouy-Chapman or Debye layer, the exponential decay has a characteristic length scale $\kappa = \frac{1}{D}$ where D is the Debye length often placed at 1 nm [51, 88, 91, 98, 113]. This means that the Gouy-Chapman layer of ions is typically no larger than 1 to 2 nm away from the membrane before reaching an equilibrium.

This model of electrical screening is called the Guoy-Chapman-Stern (GCS) model, it is important to note that the GCS model is purely theoretical as there are no current experimental techniques that allow probing of the electric potential within nanometres of a cell membrane. The Goldmann equation describes the electric potential in the absence of screening produced by the GCS model. At the large radial limit, (nanometres away from the exterior membrane), it will correctly describe the resting potential. However, in the limit close to the membrane where all the ions pass in and out of the cell, the model will fail to predict electric potentials. In this regard, the diamond NV's are unique in that they potentially have the ability to measure the potential of the Debye layer, providing important information about how the cell membrane functions as an electrical device. If however, the NV can measure the Debye layer potential, then modelling this effect is important in order to understand the signal being measured by the NV. To achieve this properly two concepts need to be understood. The first is the mathematical model of the Debye layer which is considered in using the PNP model of ion flow in section 2.3. The other is the understanding of the current state of neuron signal measurements and imaging which is considered in section 2.2.

2.2 Current imaging methods

There are many different methods of imaging electromagnetic fields in neurons, each with their own set of advantages and disadvantages, the more prominent methods are outlined in this thesis which includes electrode patch clamps, voltage-sensitive dyes, calcium imaging, genetic marker protein imaging and microelectrode arrays (MEAs). The NV is also described in more detail in the context of imaging. Its preliminary sensing capabilities are comparatively considered in this section. To re-iterate from chapter 1, the ideal neuro-sensor must have the following characteristics:

- Susceptibility - must be able to resolve the smallest possible change in a potential or electromagnetic field, ideally without the need for signal averaging. The smallest changes occur during PSPs, which can be as low as 20 mV in magnitude [93], so the ideal system should be able to sense in this range.
- SNR - must be able to resolve signals with a high signal to noise ratio (SNR). The combining of susceptibility and SNR creates the overall sensitivity of the system.
- Spatial resolution - an image must be able to resolve micron-scale areas for typical imaging and nanoscale areas for measuring a screening field or some sub-cellular structures.
- Wide-field imaging - there must be a capacity to measure single neurons as well as multiple neurons at the same time in a large network.
- Temporal resolution - action potentials occur over millisecond timescales, so ideal systems should have sub-millisecond resolution.
- In vivo capacity - must be able to image neurons in a lab sample (in vitro) environment as well as in an active organism (in vivo).
- Non-toxic - The system must be able to image neurons over a long period of time without killing the neuron itself.

Realistically no current imaging technique can achieve all these points, it is likely the NV's won't be the perfect modality either. Additionally, different methods have multiple brands and types which operate differently and have different strengths and weaknesses. For simplicity, most techniques have a representative brand which is described in greater detail than the overall technique itself. Although many systems can come close on their own to satisfying all the points in the list above, the ideal method is likely to use multiple imaging tools together [88]. Another important characteristic that is not directly to do with sensing is the capacity to generate neuron signals. Good neurosensors can measure neuron signals and also have the capacity to induce a signal from a neuron which can be subsequently measured. There are a few different ways to achieve this which are also detailed in this section.

Patch clamps are well known and operate by physically placing electrodes on the desired part of a cell in the form of a micro or even nanopipette. The pipette uses suction and heating techniques to form a resistive seal (giga ohm seal) around a section of the membrane. Once the seal is formed, any ion flow through the pipette will create a small current which can then be amplified and converted into a voltage measurement [34, 46]. Improvements in patch-clamp techniques have pushed to cross-sectional nanoscale electrophysiology for investigating nanoscopic heterogeneities in ionic concentrations and local electric fields [105]. Coupled with scanning ion conductance microscopy, it can perform wide-field imaging of neurons in a resting state [78] by utilising the pipette as a scanning probe.

There are many different techniques for patch-clamp measurements; including conventional cell-attached, whole-cell, inside out and outside out measurements (figure 2.9) [34]. Each method is used for specific types of experiments, in vivo, whole-cell, extracellular and intracellular studies respectively. The patch-clamp method is highly sensitive and allows voltage measurements to be made of specific areas of the cell in real-time, such as an individual ion channel. The sensitivity can be measured to pico-amp values with the ability to resolve at a sub-millisecond resolution [46].

Patch clamping is so sensitive that it is often considered the gold standard by which any other method is tested, in addition to its sensing capacity, patch clamps can also inject a current into the cell, which can alter the cellular potential and create action potentials which can then be measured by other techniques. The method can resolve single-shot action potentials as well as sub-threshold events. The drawbacks to this technique lie in its physical constraints; the patch-clamp often results in physical perforations of the cell, making the technique invasive and damaging for the cell. In addition to this, the technique can only be applied to a single micro-scale point on the outer membrane of a cell, making large scale and/or studies of signal propagation difficult if not impossible [88].

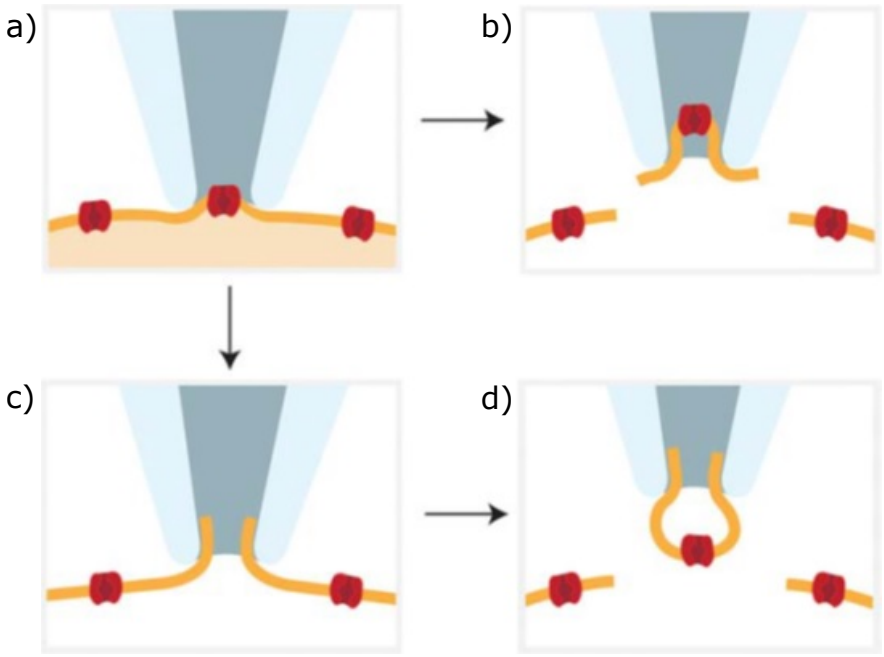

Figure 2.9: Different configurations of the patch-clamp technique. a) is the conventional cell-attached clamp technique for in vivo studies and b) is the inside out excised patch technique for intracellular studies. c) is the whole-cell technique for entire cell studies and d) is the outside out technique for extracellular studies. All methods demonstrate the clamps versatility; however, all these methods have some level of risk to cell mortality. Source: Gandini et al. [34]

Voltage-sensitive dyes are dyes that have a potentiometric part of their molecular structure which under optical excitation will change its fluorescence in response to an external electromagnetic field. They can be injected en mass into a sample of single or multiple neurons and the electromagnetic field can be measured as a function of the fluorescence of the dye [88]. One type of dye commonly used is the ANNINE series dyes. The ANNINE dye was developed in 1996 and has been iterated many times since its original inception [31, 64]. One of the more recent versions of the dye is ANNINE-6plus; this dye is a water-soluble, membrane binding chromophore that measures changes in electric potential via optical excitation and emissions [31] (figure 2.10). The fluorescent emissions are altered in the presence of an external field by the linear Stark effect [31, 64]. ANNINE-6plus has a voltage susceptibility measured as a 30% change in intensity per 100mV ($(\Delta F/F)/100$ mV where F is the emission intensity) with a quantum yield of 0.7 [31].

Voltage imaging can in principle measure sub-threshold electrical excitations in a variety of different cells as well as sub-millisecond and micron-sized measurements of neuronal activity in vivo as well as in vitro. The technique can image specific areas of a single neuron as well as large scale networks of neurons and certain dyes have even been able to measure single-shot neuronal activity for particular dyes without the need for signal averaging [31, 88]. The disadvantages of the dyes are however numerous, the

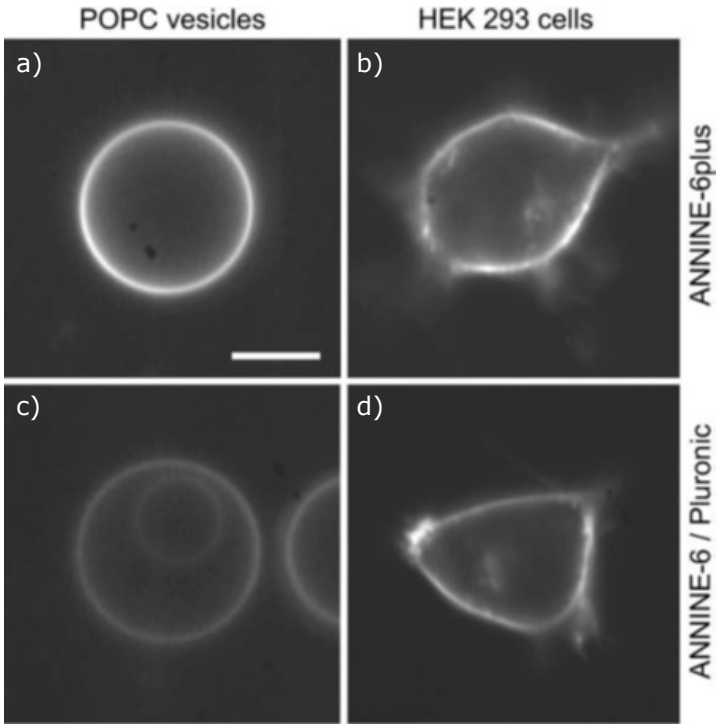

Figure 2.10: Example images of the ANNINE dye; a) and c) are POPC vesicles (artificial cells), b) and d) are live HEK-293 cells. All cells are labelled with a voltage-sensitive dye that allows visualisation under optical fluorescence. As the voltage change is most dramatic across the cell membrane, the dyes are chemically designed to bind to the cell membranes to maximise fluorescence. The level of fluorescence in the ANNINE-6plus labelled cells of a) and b) is improved from the older ANNINE-6 dye labelled in c) and d). Source: Fromherz et al. [31].

principle of these are the chemical constraints. Voltage-sensitive dyes must be water-soluble with the ability to permeate and ideally bind to the membrane of neurons all while having high levels of fluorescence to make measurements. However, the dyes chemical and optical response will often change from cell to cell, requiring extensive studies to be performed to optimize the right dye for the right experiment [88]. In the case of ANNINE-6plus, its solubility/binding and voltage susceptibilities are good, however, its highest susceptibility value occurs at large wavelength excitation. As the absorption in this regime is low, it results in poor signal to noise ratio's, lowering sensitivity. This effect can be alleviated by high-intensity studies, however, if the intensity is too high, then the neuron will begin to suffer from phototoxicity [64]. This trade-off of signal to noise ratio optimization to cell mortality is very common amongst voltage-sensitive dyes.

Calcium imaging is a technique that involves genetically or chemically engineering molecules or proteins into a cell that fluoresce in response to calcium binding to it, in this sense it is chemically driven fluorescence under optical excitation. During action potentials, calcium ions are transported in and out of cells; the calcium concentrations

at parts of the cell can change up to 100-fold during action potentials. Calcium can then bind to these markers, allowing imaging of electric fields indirectly via calcium concentrations [39, 115]. One example of this is the indicator CAL-520; this optically driven molecule is based on BAPTA chemistry (1,2-bis(o-aminophenoxy)ethane-N,N,N′,N′-tetraacetic acid). CAL-520 can be loaded into neurons via direct injection into the cell or by sample staining, where the indicator permeates a cell membrane with chemical assistance. Upon diffusion into the cell or extracellular space, calcium can then bind the indicator which causes it to undergo a conformational change, this results in a considerable change in the fluorescence of the indicator which can be imaged. Calcium molecules typically fluoresce much more brightly than voltage dyes; in the case of CAL-520, it has a fluorescence susceptibility change of 70% per action potential ($\Delta F/F/AP$) with a quantum yield of 0.75, considerably better than voltage dyes [115]. This increase in fluorescence, as well as high excitation energy, allows for two-photon imaging microscopy techniques. Two-photon microscopy is a technique in which two photons of approximately half the excitation energy of a fluorophore are used together to create an excitation. The half energy photons have increased wavelengths which are more penetrating, reducing phototoxicity as well as scattering noise [23]. Two-photon microscopy requires a bright and sensitive fluorophore as well a high-energy excitation level. Whilst this can be achieved with voltage-sensitive fluorophores, these factors are common and more effective in calcium indicators. The technique allows for a much greater resolution without the need for count averaging. For CAL-520, it improves the signal to noise ratio to 6.63 for in vitro imaging and allows for wider scale in vivo imaging [23]. Despite this increase in optical attributes, calcium imaging has several shortcomings which prevent it from being clearly superior to voltage imaging. The principle of these is in the fact that the binding, conformational change and resultant fluorescence of calcium imaging is a time-consuming process, the timescales of action potentials are often faster than this chemical process, resulting in poor temporal resolution of 200 ms, at least 100 times longer than the action potential time itself (see figure 2.11) [39, 88]. In addition to this, calcium imaging struggles to image low voltage events such as subthreshold voltages as it requires calcium-binding during low calcium concentration events. It also typically requires signal averaging as the poor temporal resolution does not allow for single-shot measurements [88].

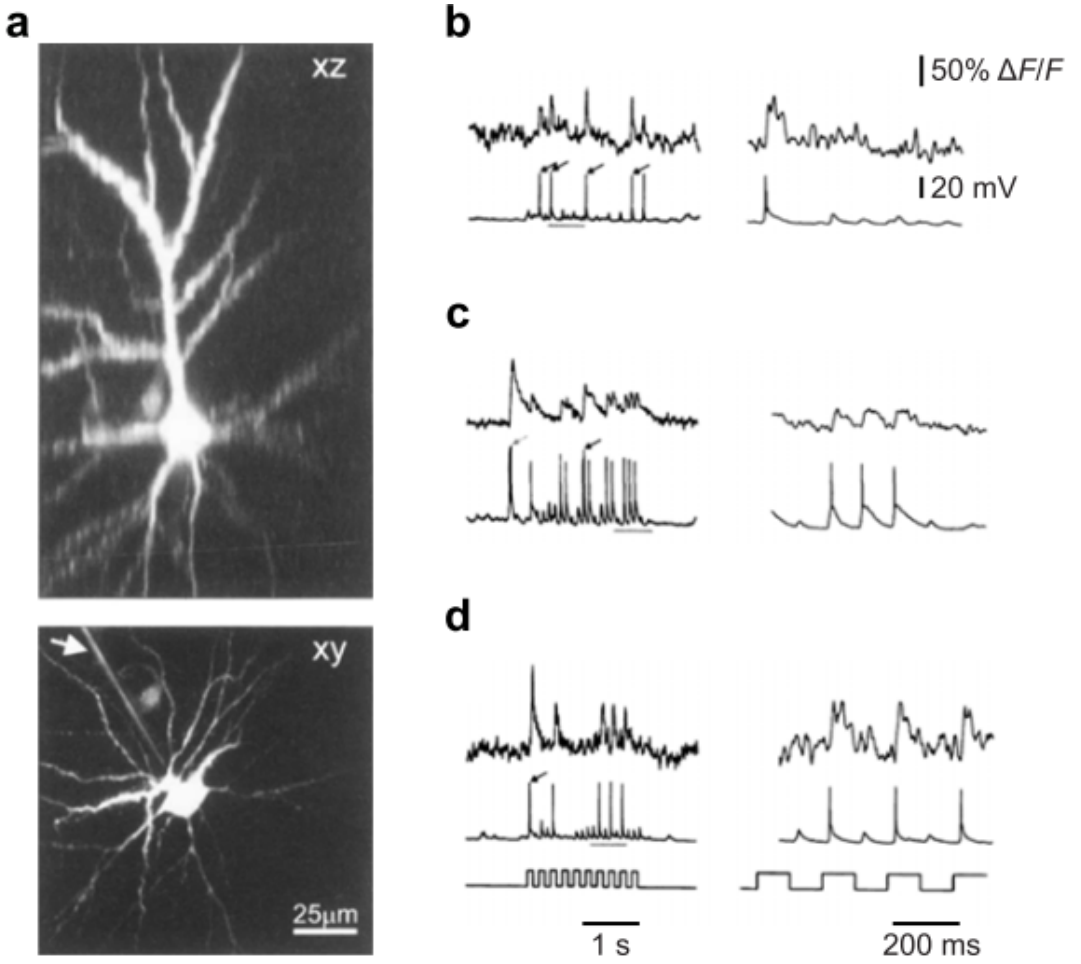

Figure 2.11: Example of in-vivo calcium imaging. Rat pyramidal neurons were loaded with the indicator calcium green-1 that respond to whisker stimulation. The black and white images a) are slices of a 3D reconstruction of a neuron from two-photon fluorescence imaging. The line plots in b), c) and d) show the recordings of three separate neurons which are being stimulated via two different whisking patterns that are the square wave functions at the bottom of d). The top trace is the calcium fluorescence and the trace below it is the direct voltage measurement performed by a sharp micro-electrode. whilst the whisking does not necessarily produce a neuron response every time, it is clear that the electrode records more spike events than the dye due to the poor time response of the calcium indicator. Source: Grienberger et al. [39].

Another technique is to genetically engineer proteins that will bind to specific sites of a neuron and fluoresce under certain conditions, this could be in direct response to an electric field or an indirect response such as a molecular binding (similar to calcium imaging) [88]. One example of genetically engineered voltage-sensitive proteins is the

Ace mNeon class of protein pairs, this system consists of two proteins: the rhodopsin protein, Acetabularia acetabulum (Ace) and an mNeon green fluorescent protein [38] (figure 2.12). The Ace mNeon pair operate via Förster resonance energy transfer (FRET). The principle of FRET is to combine two optically driven fluorophores together; in the case of Ace mNeon, the Ace component is a voltage-sensitive dye which under optical excitation and electrical stimuli will resonantly transfer its excitation energy non-radiatively to the mNeon protein via a dipole interaction. The excited mNeon will then produce an optical emission which is then detected. Using this method, the detection system will sense a drop in the donor fluorescence (Ace) as well as an increase in the acceptor emission (mNeon) [9, 38]. FRET-based imaging is designed to couple the sensing capacity of a voltage-sensitive dye with a much more optically efficient fluorophore. In the case of Ace mNeon, the mNeon component has good optical characteristics with a quantum yield of 0.8 and a radiative lifetime of 3 ns, and the Ace component allows for sub-threshold imaging with less than 0.4 ms temporal resolution and in vivo imaging with low phototoxicity [9].

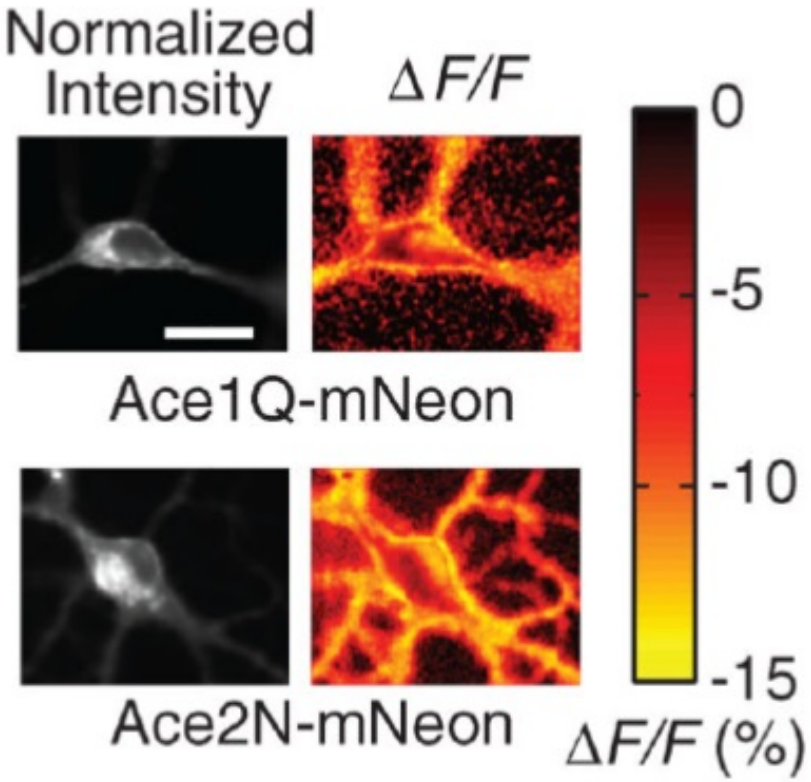

Figure 2.12: Fluorescence signals from neurons loaded with Ace1Q-mNeon (top) and Ace2N-mNeon (bottom). The black and white images show the baseline fluorescence of the mNeon protein and the colour images show the fluorescence response for a voltage change of 100 mV. The image also includes a legend for fluorescence susceptibility. Source: Gong et al., [38].

In general, genetic engineering can be highly specific as it's designed to bind to explicit sites, this can allow measurements of specific areas of cells as well as specific types of cells in a network [88]. FRET-based imaging is especially promising as it can in principle combine the ideal imaging characteristics of a good fluorophore with a molecule that is highly sensitive to electric fields in a way that is much faster than typical Calcium imaging [9]. There are however several drawbacks to this technique, mainly in protein design. Genetically engineering proteins to permeate, bind then sense fields can be a challenging process, for FRET imaging, finding a pair of proteins that will undergo resonance transfer can be difficult and the efficiency of the transfer can be quite poor [9, 38, 88]. In the case of Ace mNeon, the transfer rate is relatively low, creating a poor fluorescence sensitivity ($\Delta F/F$ of 12% per 100 mV) and lacks the capacity to perform single-shot imaging [38].

Micro-electrode arrays (MEAs) are a broad field of electrode technologies that are applied to a variety of neuroscience experiments as well as in a clinical setting. MEAs are essentially an array of electrodes where the conductive part of the electrode transduces a neuronal voltage signal (moving ion concentrations) into an electrical current within the electrode that is then measured [84, 111]. One immediate advantage of this technology is that an electrode can transduce a signal for measurement or it can provide a current in the electrode which alters the local potential in the neuron, opening voltage-gated ion channels and inducing an AP. Thus, like a patch-clamp, MEAs can stimulate neuron activity as well as measure it [84].

MEAs come in a variety of forms, planar microelectrodes can measure the combined signal from a group of neurons in a lab setting (e.g. in vitro cell studies) all the way to a clinical setting where electrode arrays form electroencephalography (EEG) that can measure the signal from an entire human brain. Alternatively, the arrays can be made into micro or even nanostructured pillars or other shapes which directly connect to a single neuron or neuronal structure to sense individual neuronal signals [84] (figure 2.13). Some connect via a contact mechanism on the outside of the neuron membrane whilst others can penetrate the neuron membrane itself to measure intracellular signals. With the ability to transduce a field in the neuron, MEAs can also measure using electroporation, where the electric field generated by an electrode temporarily alters the membrane permeability creating a local means of measuring the intracellular potential by allowing interior ion flow to pass into the local region where the electrode is [44].

MEAs have been reported to have sensitivities and resolution that is equivalent to patch clamps in a way that allows multiple recordings along with a network by utilising an array of electrodes on a single chip (up to 4096 simultaneous sensors in one device) [84]. The major difficulties in electrodes are the chip design and the contact of electrodes with the neurons. In planar MEAs, the number of sensing sites is large, but the resolution is poor as you are measuring the combined signal from multiple neurons. By utilising smaller, structured electrodes, the resolution improves, however, there is difficulty in creating a network of electrodes that are nanoscopic in size whilst being densely packed as each electrode must have an accompanying wire system to send signals to a detection system. This means that there is often a

trade-off of electrode size and density of the array (40 μm pitch between electrodes). In addition to this, the contact of the electrode to the neuron is not consistent. If an electrode does not make physical contact with the neuron, then Debye screening will stop the electrode from sensing a signal unless it is the combined signal of multiple neurons [84].

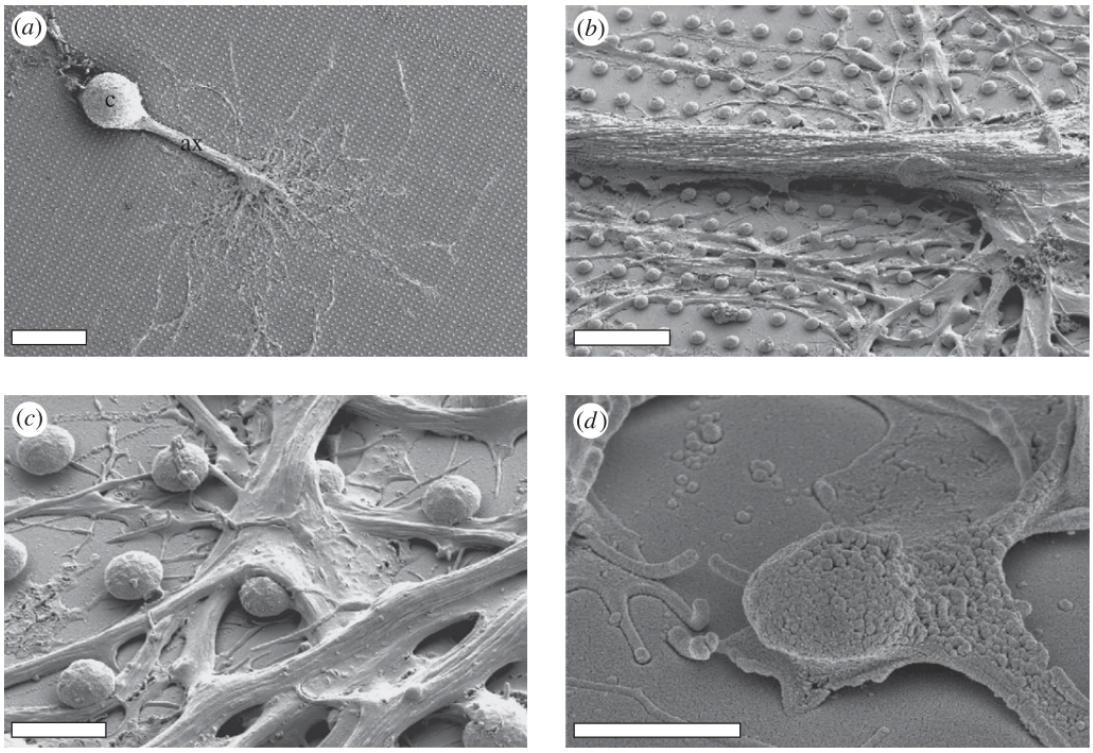

Figure 2.13: Scanning electron microscope (SEM) image of neurons growing on an array of gold-spine micro-electrodes. The images from a) through d) are of the same array but with different magnifications: 100, 20, 5 and 2 μm for a), b) c) and d) respectively. The labels c and ax in a) label the soma and axon respectively. Source: Hai et al., [43].

Diamond based quantum microscopy using the NV is a substantial change from the other technologies in that it is a quantum device used to sense neuronal signals, however, there are a lot of similarities between the different technologies. The NV can be used in a variety of ways for biological applications; as the NV resonances are sensitive to external electric [27] and magnetic fields [99], either can be used to sense neuronal signals. Additionally, the NV has been considered for applications as a sensor for thermal changes in a cell [106] as well as force changes from actively moving cells [14]. The NV has been applied like an MEA where neurons are grown on an array of fixed NV sensors [12] but can also be applied like a dye by injecting a dose of nanodiamond particles into a cell [62].

In this thesis, we focused on a novel way of sensing neuron signals by shaping the

diamond structure itself into an array of nanopillars similar to an MEA whilst sensing the field from the neurons using optical microscopy similar to a dye. As mentioned in chapter 1, the NV has exceptional sensitivity and resolution, as it is able to, in theory, measure sub-threshold signals with nano-scale spatial resolution and microsecond temporal resolution. This would make the NV as good as patch clamps (the gold standard) in terms of sensing capacity. In addition to this, the nano-pillar array would allow for wide-field imaging like an MEA, the NV won't suffer from bleaching like a dye, and the diamond substrate is biocompatible, allowing for high-quality neuron sensing in a way that is non-perturbing to the neurons natural function.

The NV does have its own inherent drawbacks, unlike MEAs, the NV has no known way of stimulating a neuronal signal and its optical emissions limits its capacity to perform in vivo imaging. However, it is likely that the biggest drawback is the lack of theoretical or experimental proof of the NVs capacity to perform neuron sensing. The only theoretical study of how the NV interacts with a neuronal signal was performed by Hanlon et al. [47] (section 2.3). The only experimental proof of NV-based neuron sensing was performed by Barry et al., successfully measuring neuronal signals along axons of marine fan worms by placing the axon on a flat diamond substrate with embedded NVs [12]. However, as mentioned in chapter 1, this experiment was a magnetometry experiment performed on large worm axons instead of smaller mammalian neurons. As the neurons get smaller, the magnetic field will get smaller as well, potentially beyond the sensitivity of the NV for magnetic fields. As a result, without theoretical and experimental proof, a lot of the potential benefits of the NV may not be true at all, thus necessitating an in-depth study of NV based neurosensing and its comparison to other technologies including the other NV neurosensing experiments already performed.

The first step in assessing the NV for neurosensing is to perform theoretical modelling of the NV pillar geometry and study how a neuron might interact with the pillar and what electromagnetic fields from the neuron will be sensed by the NV. Whilst this modelling is important for assessing the NV specifically, understanding neuron electromagnetics is useful for assessing a variety of sensing technologies. As a result, the work performed in section 2.3, whilst being NV specific, has the capacity to be generalised to a variety of different technologies, helping the wider neuroscience field.

2.3 Neuromodelling - CC and HH theory

There are a variety of ways to model individual neurons and neuron networks, however, most theories can be grouped into two major classes of models based on their underlying assumptions. The Core Conductor (CC) theory is a well established mathematical model of the electromagnetic fields produced by neurons [17, 94, 101, 126]. The key assumption of the CC model is the idea of a stationary charge density. This stationary assumption states that although charges move in and out of the neuron, its overall charge density remains largely static. In other words, the amount of charges

moving in and out of the neuron is small compared to the total charge of the neuron. If the charge density is static, then a change in potential can be presented in the absence of any charges. In stark contrast to the CC model is the Poisson-Nernst-Planck (PNP) is a model of direct ionic flow [19, 67, 91]. The PNP equation couples an equation modelling the concentration of ions in solution via the Nernst-Planck drift-diffusion equation with the Poisson equation for modelling electric potentials from charge concentrations. Both models can be altered in a variety of ways to suit particular situations and both models have been successful in simulating real neuron systems in particular conditions. However, both have drawbacks that limit their applicability which are largely based on the underlying assumptions that are used to derive them.

The CC model presents a neuron as a structure with one constant conductivity inside the neuron and another constant conductivity outside the neuron. If the conductivities are considered static, then Ohm's laws can be applied. The electric potential difference across the membrane is then modelled via a circuit theory in lieu of charge densities. The idea is to consider the membrane of the neuron as a series of infinitesimally small RC circuits (see figure 2.14). The RC circuits create the transmembrane potential at the membrane which propagates away from the neuron and acts on the charges, rather than the charges themselves creating electric potential.

The stationary assumption requires that the charge density remain constant even during an AP. The rationale for this lies in the premise that during an AP, the speed of the travelling potential wave is so fast that ions have no time to move or form an equilibrium. Thus the constant charge density is preserved and Ohms laws will still apply. If the effect of the charges can be ignored, then the electric potential can be solved using the Laplace equation. The CC model is based on a theory for understanding electric potentials being produced by underwater trans-Atlantic cables created by Lord Kelvin in the 1850s. In this sense, the model is applying assumptions that allow for a neuron to be treated like a cable, whose solutions are known. For this reason, the model is often called Cable Theory [126].

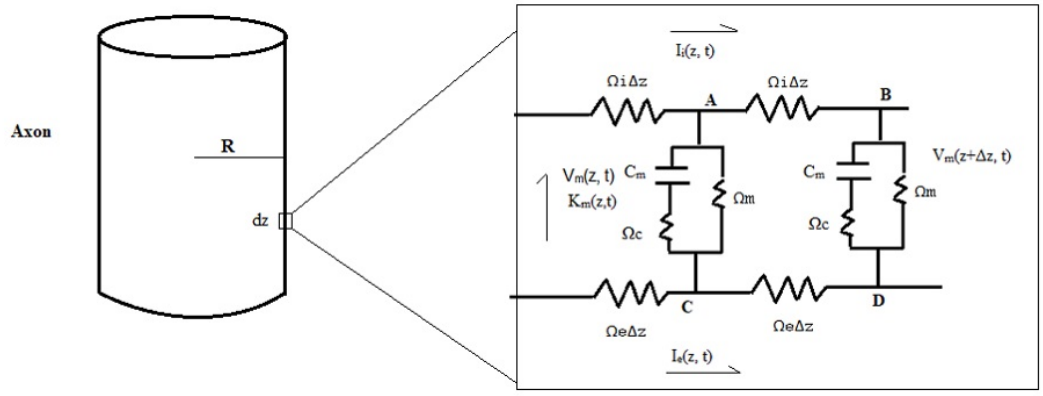

Figure 2.14: Diagram of the circuit modelling of the Core Conductor neuron. Each infinitesimally small portion of the membrane is modelled as an RC circuit which creates the transmembrane potential in the absence of any charges. Ω is the resistance, V is the potential, C is the capacitance, I is the axial current and K is the membrane current (radial current). The subscripts i e and m refer to the internal, external and membrane respectively.

One example of the CC model can be derived from Woosley et al. [126], where Laplace's equation is applied to calculate the neuronal electric potential. The electric field can then be calculated from the derivative of the potential and the current density can be solved using Ohms laws which then can be substituted into the Biot-Savart or Ampere's law in order to obtain an expression for the magnetic field. As a result, once the electric potential is solved, all other fields can be calculated as a function of the potential. The equations are solved for a cylindrical axon undergoing an AP and the system is considered to be in a quasi-DC state, whereby there is no self-inductance from the electric and magnetic fields.

It is important to note that in the Woosley paper, the electric potential is simply stated and not derived. In order to fully understand where the electric potential comes from; a derivation is done as a part of this thesis. The remaining current density and magnetic fields are however derived in the Woosley paper [126]. Beginning from the Laplace equation for the electric potential:

$$\nabla^2 V(r,z) = 0, \tag{2.6}$$

Woosley et al. specifically solve for a potential created by an AP, hence there is a resting potential as well as a wave travelling in the axial direction along the cylinder (z coordinate), created by the RC circuit. The result is a potential which is a function of two separate coordinates, if however, the only axial dependence of the potential lies in the travelling wave, the solutions can be made separable by taking the Fourier transform of the potential:

$$V(r,z) = V(r,k)e^{ikz}, \tag{2.7}$$

where the axial part of the potential is modelled as a travelling wave in Fourier space, e^{ikz} and k is the wavenumber or the spatial frequency of the wave. Substituting equation 2.7 into the Laplace equation and simplifying gives the following separable expression:

$$\frac{1}{r}\frac{\partial}{\partial r}(rV(r,k)) - k^2V(r,k) = 0, \tag{2.8}$$

in order to solve equation 2.8 some boundary conditions are required. The first is the boundary at the outer edge of the solution: as $r \to \infty$ the potential will go to zero ($V(\infty,k) = 0$). The second boundary condition can be calculated by requiring the normal component of the radial current density to be continuous across the boundary:

$$\vec{J}_{int}|_{r=R} = \vec{J}_{ext}|_{r=R}, \tag{2.9}$$

where the subscripts *int* and *ext* refer to the solution inside or outside the neuron. The R term refers to the full radius of the axon. Note that in this particular derivation the potential change across the membrane itself is negligible so the membrane thickness is neglected. The current densities themselves can be expressed by applying Ohm's law:

$$\vec{J} = \sigma\nabla_r V(r,k), \tag{2.10}$$

where σ is the conductivity of the medium begin solved for (inside or outside the neuron). Applying Ohm's law to equation 2.9 gives the following expression:

$$\sigma_{int}\nabla_r V_{int}(r,k)|_{r=R} = \sigma_{ext}\nabla_r V_{ext}(r,k)|_{r=R}, \tag{2.11}$$

equation 2.11 is a charge conservation equation. It essentially states that the amount of charge going through the membrane must be equal to the amount of charge going out, whereby the charge can be expressed in terms of the potential and the conductivity. In addition to this boundary condition, in a stationary environment, there is no screening layer along the membrane, as the potential is constant from $r = 0$ up to the membrane itself. This means that the potential jump across the membrane is equal to the transmembrane potential:

$$V_{int}(r,k)|_{r=R} - V_{ext}(r,k)|_{r=R} = V_t(k), \tag{2.12}$$

where $V_t(k)$ is the transmembrane potential, which will also be the same as the potential at $r = 0$. Solving equation 2.8 for the inner and outer neuron potentials gives the solution as a set of Bessel functions:

$$V_{int}(r,z,k) = AI_0(kr), \tag{2.13}$$

$$V_{ext}(r,z,k) = BK_0(kr), \tag{2.14}$$

where I_0 and K_0 are the modified Bessel functions of the first and second kind

respectively (to the zeroth-order). The K_0 function satisfies the boundary conditions as the solution will go to zero as $r \to \infty$. As $r \to 0$ on the interior solution, I_0 goes to a constant and the solution should approach the transmembrane potential $V_t(k)$. The Core Conductor boundary conditions can now be applied in order to find the unknown constants. Re-writing equation 2.11 in terms of the potential solution:

$$\sigma_{int} \nabla_r A I_0(kr)|_{r=R} = \sigma_{ext} \nabla_r B K_0(kr)|_{r=R}, \tag{2.15}$$

applying the gradient as a derivative in r and solving for the constant A:

$$A = \frac{-\sigma_{ext} B K_1(kR)}{\sigma_{int} I_1(kR)}, \tag{2.16}$$

substituting solved potentials and equation 2.16 into the second boundary equation, 2.12 gives an expression for B in terms of a single unknown constant and the transmembrane potential:

$$\frac{-\sigma_{ext} B K_1(kR)}{\sigma_{int} I_1(kR)} I_0(kr) - B K_0(kr) = V_t(z,k), \tag{2.17}$$

solving for B:

$$B = V_t(z,k) \left(\frac{1}{K_0(kR)} + \frac{\sigma_{int} I_1(kR)}{\sigma_{ext} K_1(kR) I_0(kR)} \right), \tag{2.18}$$

substituting A and B into the solutions 2.13 and 2.14 gives the final expression for the potential in Fourier space. Woosley et al. perform some simplifications on the solutions to obtain them in the following form:

$$V_{int}(r,k) = \frac{1}{\beta(|k|)} \frac{I_0(|k|r)}{I_0(|k|R)} V_t(k,z), \tag{2.19}$$

$$V_{ext}(r,k) = \frac{1}{\alpha(|k|)} \frac{K_0(|k|r)}{K_0(|k|R)} V_t(k,z), \tag{2.20}$$

where β and α are given by:

$$\beta(|k|) = 1 + \frac{1}{\frac{\sigma_{ext} K_1(|k|R) I_0(|k|R)}{\sigma_{int} K_0(|k|R) I_1(|k|R)}}, \tag{2.21}$$

$$\alpha(|k|) = -\left(1 + \frac{\sigma_{ext} K_1(|k|R) I_0(|k|R)}{\sigma_{int} K_0(|k|R) I_1(|k|R)} \right), \tag{2.22}$$

as previously stated in equation 2.7, the potential solutions are separable, all the axial dependence lies in the transmembrane potential and the radial dependence lies in the Bessel functions. As $r \to \infty$ on the external side, the solution still goes to zero. As $r \to 0$ on the interior side, the solution becomes $V_t(k,z)$, to an approximation, which is what was expected.

With the electric potential derived in Fourier space, the radial electric field can also be derived by applying the following Maxwell's equation:

$$\vec{E} = -\nabla V(r), \tag{2.23}$$

taking a derivative in the radial coordinate will give the electric field, whereas taking the derivative in the axial coordinate (z) with the conductivity will give the axial current density (Ohm's law, equation 2.10) which can be used with Biot-Savarts law for the magnetic field:

$$\vec{B}(r) = \frac{\mu_0}{4\pi} \int \frac{\vec{J}(\vec{r'}) \times (\vec{d} - \vec{r'})}{|\vec{d} - \vec{r'}|^3} d^3\vec{r'}, \tag{2.24}$$

where r' denotes the vector from the origin to the source point (membrane) and d denotes the distance from the origin to the measurement point, making $|d - r'|$ the vector distance from the source to the measurement point. Woosley et al. solve this equation by applying a vector identity and simplifying the distance term $|d - r'|$ with a Greens function. The solution is given in Fourier space as:

$$\vec{B}_{int}(r,k) = \frac{1}{2\pi} \int_{-\infty}^{\infty} \frac{i\mu_0 R\sigma_{int} k}{\beta} \frac{K_1(|k|r) I_1(|k|R) I_0(|k|r)}{I_0(|k|R)} V_t(k) dk, \tag{2.25}$$

$$\vec{B}_{ext}(r,k) = \frac{1}{2\pi} \int_{-\infty}^{\infty} i\mu_0 R k I_1(|k|R) K_1(|k|r) \Big(\frac{\sigma_{int}}{\beta} + \frac{\sigma_{ext}}{\alpha} \Big) V_t(k) dk. \tag{2.26}$$

it's important to note that the external magnetic field comes from the addition of the solutions to the magnetic fields from both the internal and external current densities. The other important point is that all these solutions are in Fourier space, in order to solve for a real potential, the solutions must undergo an inverse Fourier transform. This is achieved in this paper by applying a numerical integral to the solutions.

Roth et al. tested the Woosley model by comparing the theoretical data to an experiment on a crayfish medial giant axon [101, 126], this particular axon was chosen for both its ease of access as well as its size: 0.107 mm in radius. The large radius makes for greater ease of making experimental measurements. The transmembrane potential was measured using a glass micro electrode clamp. The Magnetic field was measured using a toroidal pickup coil, which uses magnetic induction to sense a magnetic field by converting it into a current. The general experimental setup is shown in figure 2.15.

The experiment produced a transmembrane potential which was approximated qualitatively using a two Gaussian function (figure 2.16a):

$$V_t(t) = A_1 e^{-\frac{(t-t_1)^2}{2\sigma_1^2}} + A_2 e^{-\frac{(t-t_2)^2}{2\sigma_2^2}} - 70, \tag{2.27}$$

the parameters in equation 2.27 were determined to be: A_1 = 64.4 mV A_2 = 56.0 mV σ_1 = 0.082 ms σ_2 = 0.156 ms, t_1 = 0.93 ms, and t_2 = 1.065 ms. The -70 mV on the end

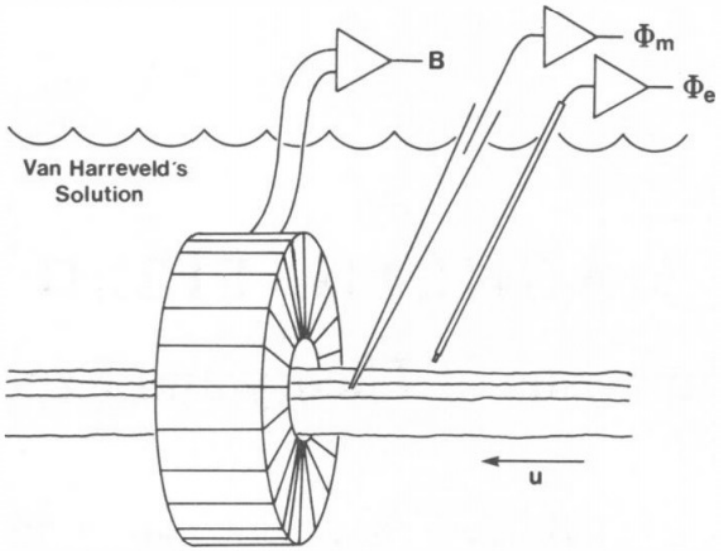

Figure 2.15: Experimental setup, the axon is placed in a crustacean saline called Van Harreveld's solution. The electrode clamps can then be placed within 1 mm of the toroid in order to obtain both transmembrane potential and magnetic field measurements. The distance from the membrane to the toroid is given as 1.48 mm and u is the current direction. Source: Roth and Wikswo, [101].

of the equation accounts for the resting potential of the neuron. As the measured transmembrane potential was performed as a function of time (ms); in order to achieve a function in space (mm) the time coordinate was multiplied by the speed of the action potential wave which was stated to be 16.5 m/s. Additionally, as the Core Conductor model is presented in Fourier space, equation 2.27 must also be Fourier transformed using equation 2.28; note the use of an asymmetric Fourier transformation:

$$V_t(k) = \int_{-\infty}^{\infty} V_t(t) e^{ikt} dt, \tag{2.28}$$

$$V_t(k) = \sqrt{2\pi}\sigma_1 A_1 e^{ikt_1 - \frac{k^2\sigma_1^2}{2}} + \sqrt{2\pi}\sigma_2 A_2 e^{ikt_2 - \frac{k^2\sigma_2^2}{2}} - 140\pi\delta(k), \tag{2.29}$$

where the $\delta(k)$ indicates a Dirac Delta function in k. The remaining parameters were defined from Woosley [126]. The internal and external conductivity's are given as: σ_{int} = 1.7 $\Omega^{-1}\text{m}^{-1}$ and σ_{int} = 2.06 $\Omega^{-1}\text{m}^{-1}$ respectively. The axon radius and action potential speed has been previously stated in the previous section to be 0.107 mm and 16.5 m/s respectively.

Figures 2.16a) and 2.16b) show the electric potential and magnetic fields outside the neuron as a function of the z-axis (axially along the neuron). Although the transmembrane potential is Gaussian in nature, the solution outside the neuron shows a derivative in the wave. What is interesting to note is the lack of any serious analysis of the radial component of the various fields. Woosley et al. derived and solved

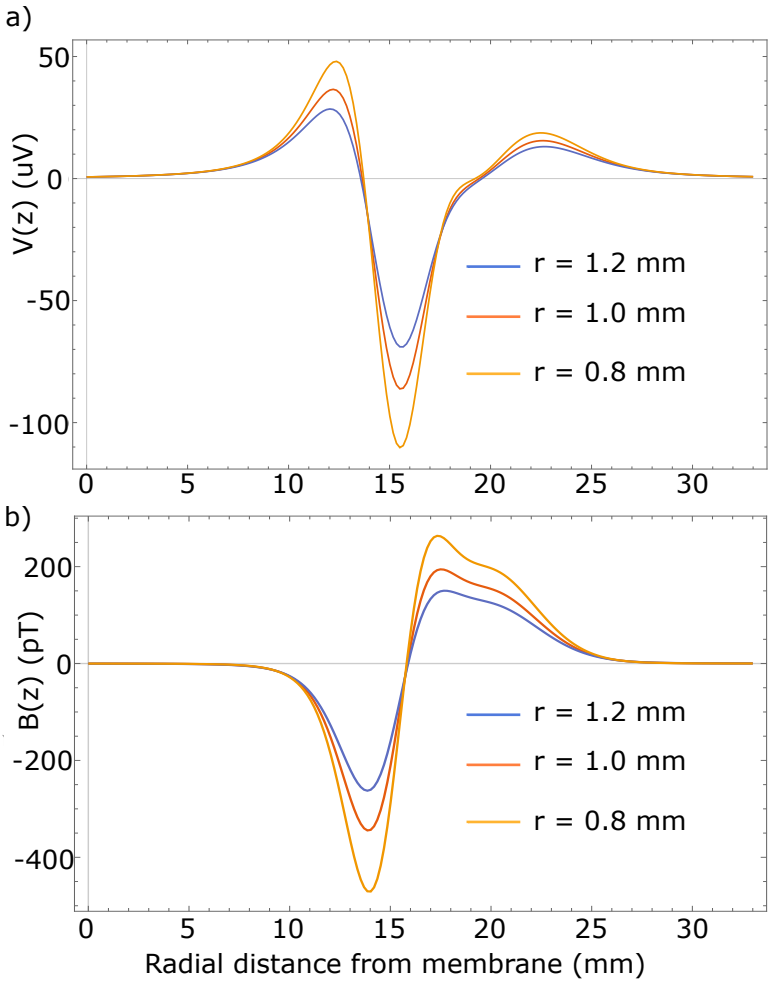

Figure 2.16: Plot of the a) external electric potential and b) external magnetic fields. The orange, red and blue in the legend indicates the strength of the fields at r = 0.8mm, 1mm and 1.2mm from the membrane respectively. Note that the wave drops in amplitude as r increases. Also note that the measurements are done millimetres from the membrane, so effects of nanoscopic ion concentrations are not measured. Reproduced from Woosley et al., [126].

the equations for use in an experiment where the sensing tool was placed at a fixed position, far from the neuron (figure 2.15). In addition to this, the effect of screening is not considered at all in this neuron compared. With Debye screening, the expectation is that the external potential will be effectively zero at the distances predicted in the plots. Whilst the magnetic field Woosley predicted is experimentally verified [101], the electric potential is not and the electric field isn't considered at all.

Whilst the CC theory does have success, we seek to understand how close an NV needs to be against a neuron in order to sense an external field, the distances being considered are nanometres in length. As mentioned at the start of this section, the main assumption in the CC theory is that the amount of charges moving in and out of

the neuron is small compared to the total charge of the neuron. If the charge density is largely static, then a change in potential can be presented in the absence of any charges. This theory can only work on large length scales, where the overall charge is larger than the change in charge due to an active process like an AP. However, at nanometre length scales near the membrane and Debye layer of the neuron, the local change in charge density cannot be ignored. Given that the goal for the NV is a nano-scale spatial measurement of local neuron electromagnetic field changes, the CC theory will not give accurate predictions of NV measurements. This logic means that a theory that explicitly models ion concentrations must be applied for understanding nanoscopic neuron electrodynamics e.g. the PNP theory. However, some of the underlying assumptions in the CC theory can be applied to understand what the current across the membrane might be. Understanding this allows for a model of the active membrane currents that are created during an action potential, which can then be applied to the PNP theory to predict how the membrane current changes the ion concentrations and subsequent electromagnetic fields. The theory that is applied to understand membrane currents is the Hodgkin-Huxley (HH) theory [52].

The HH model is a well known and experimentally verified set of coupled equations that describe the transmembrane potential, $V_m(t)$, and radial membrane currents in terms of the ion flow across the membrane-mediated by ion channels opening and closing [52]. Whilst the charge density is changing in the HH theory, both the HH theory and the CC theory share the concept of treating the neuron membrane as a series of infinitesimally small RC circuits. An RC circuit piece of the membrane will have the following currents based on Kirchhoff's laws of current conservation:

$$C_m \frac{\partial V_m(t,z)}{\partial t} + I_{\tilde{\xi}}(r,z,t) + I_r(R,t) = 0, \tag{2.30}$$

the first term is the capacitive current where C_m is the membrane capacitance and $V_m(t,z)$ is the transmembrane potential. The capacitive current is created by the passive diffusion of ions on and off the membrane in response to a stimulus (i.e. the dynamic motion of the Debye layer). The second term, $I_{\tilde{\xi}}(r,z,t)$, is an initial current that drives the system (e.g. from a clamp or a PSP). The third term, $I_r(R,t)$, is the ionic current at the membrane radial boundary ($r = R$). This is the major source of the AP and it is caused by the opening and closing of ion channels along the membrane. The HH models the radial current in terms of the three most prominent ion channel types in a given neuron and their respective currents:

$$I_r(R,t) = I_{Na}(R,t) + I_K(R,t) + I_{Cl}(R,t), \tag{2.31}$$

where the subscripts indicate the three major ions crossing the membrane during an AP (sodium, potassium and chlorine respectively) and can be expressed with the

following:

$$\begin{aligned} I_{Na}(R,t) =& g_{Na} m(t)^3 h(t)(V_m(t) - V_{Na}) + g_{NaL}(V_m(t) - V_{Na}) \\ I_K(R,t) =& g_K n(t)^4 (V_m(t) - V_K) + g_{KL}(V_m(t) - V_K) \\ I_{Cl}(R,t) =& g_{ClL}(V_m(t) - V_{Cl}). \end{aligned} \tag{2.32}$$

where g_x is the maximum conductance for a particular ion species, g_{xL} is the leak conductance of the same species and V_x is the Nernst potential of an ion species given by equation 2.4 with the ion concentrations from table 2.1. The maximum conductance describes the ion flow when voltage-gated ion channels are fully open and the leak conductance describes the ion flow when these channels are fully closed, allowing only passive channel ion flow. The $m(t)$, $n(t)$, and $h(t)$ terms are parameters that describe the opening and closing of ion channels and are described with the following equations:

$$\begin{aligned} \frac{dm(t)}{dt} &= \phi(\alpha_m(t)\big(1 - m(t)\big) - \beta_m(t) m(t)) \\ \frac{dh(t)}{dt} &= \phi(\alpha_h(t)\big(1 - h(t)\big) - \beta_h(t) h(t)) \\ \frac{dn(t)}{dt} &= \phi(\alpha_n(t)\big(1 - n(t)\big) - \beta_n(t) n(t)), \end{aligned} \tag{2.33}$$

these equations are dependant on the factors α_x and β_x, which are found through experimental fitting. Equations 2.30 and 2.33 can be coupled together to solve for the transmembrane potential across the neuron. Alternatively, these equations can be solved and input into equation 2.31 to find the membrane current (figure 2.17). Both of these solutions can be experimentally verified using patch clamps or microelectrode clamps [52]. This Nobel prize winning work is commonly used in neuroscience to understand the neuron signal spike and can be altered to understand how changes in ion channel conductance affects the overall signal [19, 52].

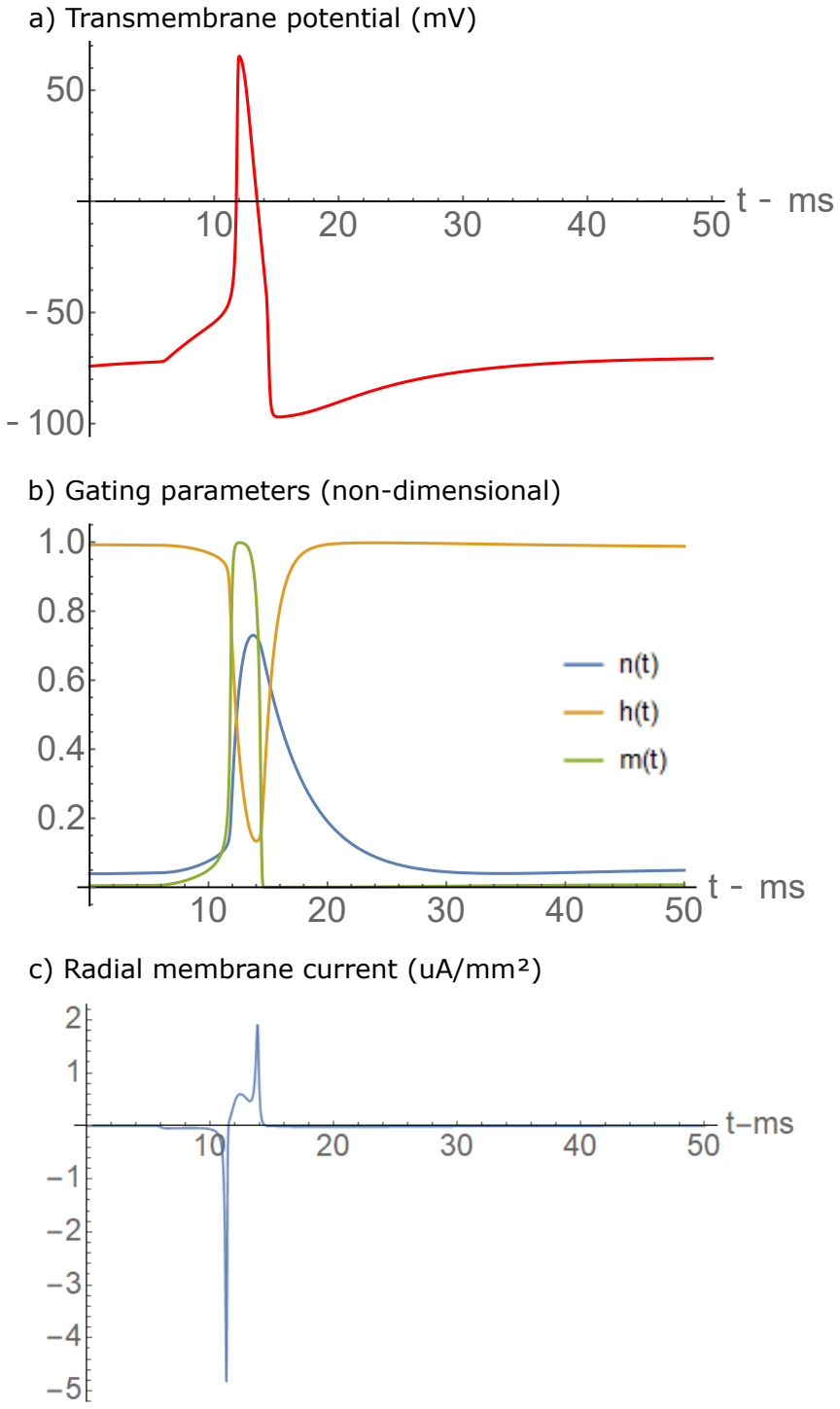

Figure 2.17: Plots of the a) Hodgkin-Huxley solutions (equation 2.30) for the potential, b) gating parameters (equation 2.33) and c) the radial current derived from equation 2.31.

2.4 Neuromodelling - Debye modelling and PNP theory

The key concept being considered in nano-scale neuron electromagnetics is the Debye layer, this charged layer is not modelled in the CC theory but can be using the PNP theory. Debye screening is a concept often used in semiconductor physics as well as plasma physics in order to model electric potentials from mobile charge carriers such as ionized gases or fluids. The principle is that the presence of moving charges in response to an external field suppresses or screens the effective interaction between charges, reducing the spatial extent of the external field. In the case of the neuron, the build-up of negative charge inside the neuron attracts positive charges in the extracellular space outside the neuron. As the positive charges build up on the outside of the neuron, the electric potential far from the membrane will be given by the accumulated charge density from the positive and negative charges. If an equal number of positive charges to negative charges builds on the membrane, then the overall charge density becomes zero and the potential far from the neuron is also zero. In a typical neuron environment, the solution of charges outside the neuron is considerably larger than the charges inside the neuron, thus there is always enough positive charge to fully screen the field outside the neuron. The theory however requires that the mobile charges have ample time to respond to an external electric potential in order to form an equilibrium of charges.

As a mathematical example, consider a neutral solid at thermodynamic equilibrium with a density of electrons $n_i(V)$ occupying a given energy level E_i [97]:

$$n_i(0) = N_i f(E_i), \tag{2.34}$$

where N_i is the density of energy states, adding an external potential $V(r)$ changes the density in the following way:

$$n_i(V) = N_i f(E_i + ezV(r)), \tag{2.35}$$

where e is the electric charge constant and z is the valency of the charge. The electron density can be expressed as a charge density in space $\rho(r)$:

$$\rho_i(r) = ezN_i(f(E_i + ezV(r)) - f(E_i)), \tag{2.36}$$

with the charge density known, the electric potential can be solved using Poisson's equation:

$$\nabla^2 V(r) = \frac{-\rho}{\epsilon} = \frac{-e}{\epsilon}\sum_{i=1}(f(E_i + ezV(r)) - f(E_i)). \tag{2.37}$$

In the limit that the potential energy $V(r)$ is smaller than the energy of the states E_i, the right hand side of equation 2.37 can be approximated as a truncated Taylor series:

$$\nabla^2 V(r) = \frac{-e}{\epsilon}V(r)\sum_{i=1} N_i \frac{dF(E_i)}{dE_i}, \tag{2.38}$$

gathering the constants on the right hand side gives an expression for the density of charges which screens the potential:

$$q_0^2 = \frac{-e}{\epsilon} \sum_{i=1} N_i \frac{dF(E_i)}{dE_i}. \tag{2.39}$$

Substituting equation 2.39 into 2.38, creates a simple equation which in spherical coordinates has a simple analytic solution:

$$\frac{1}{r}\frac{d^2}{dr^2}(rV(r)) = q_0^2 V(r), \tag{2.40}$$

applying the boundary conditions $V(\infty) = 0$ and $V(0) = \frac{ze^2}{4\pi\epsilon r}$, i.e. the solution is zero far from the charge and is a point charge solution exactly at the charge itself. The final solution to this equation is:

$$V(r) = \frac{ze^2}{4\pi\epsilon r} e^{-q_0^2 r} \tag{2.41}$$

equation 2.41 describes how the presence of mobile charges causes the electric potential to decay at a much faster rate than without any screening. The electric potential of a point charge on its own will decay as $\frac{1}{r}$, however, with screening charges around it, its decay is exponential [97]. The constant q_0^2 describes the characteristic length scale in which the exponential decay occurs which is the reciprocal of the Debye length. In a neuron, the charges which create the electric potential are mobile ions, in this sense, it is expected that the charges can interact with an external field to create a screening layer which is analogous to this derivation of Debye screening, with exponential decay and a decay constant of 1 nm [51].

As the charges in Debye screening are mobile carriers in a solution, to model Debye screening explicitly, we will apply the PNP theory. As mentioned earlier in this section, the PNP equations couple a drift-diffusion equation of ion flow with a Poisson equation for obtaining electric potentials. As it explicitly models ion flow, it is a much more detailed and informative model compared to the CC theory, the major issue with the PNP equations is that it is highly non-linear and difficult to solve even in situations where there is geometrical symmetry (such as a cylindrical axon). Understanding explicit boundary conditions is essential for this theory. In this thesis, the PNP equations are solved in a novel way in order to obtain external neuron electromagnetics and how they will be altered in the presence of a diamond pillar. Particular assumptions are made in order to obtain these solutions, so the advantages and disadvantages of the PNP model are largely made within the context of the specific model used.

To model neuron electrophysiology, we are applying the coupled Poisson-Nernst-Planck (PNP) equations [19, 67, 91] to a cylindrical axon with a radial coordinate r and an axial coordinate z. In this model we apply a quasi-DC approximation where

the effect of a time varying vector potential is negligible:

$$\epsilon \nabla^2 V(r,z) = -\rho(r,z) = -e \sum_{i=1}^{M} z_i c_i(r,z) \tag{2.42}$$

$$\frac{\partial c_i(r,z)}{\partial t} = -\vec{\nabla} \cdot [D_i(\vec{\nabla} c_i(r,z) + \frac{1}{k_b T} z_i e c_i(r,z) \vec{\nabla} V(r,z))], \tag{2.43}$$

the Poisson equation (2.42) utilises the charged ion concentration to solve for the potential and the Nernst Planck equation (2.43) utilises the electric potential to model ion concentrations in terms of the electrostatic and chemical forces that act on them. In this model, $c_i(r,z)$ is the ionic concentration which is proportional to its charge density $\rho(r,z)$, and $V(r,z)$ is the electric potential, k_b is the Boltzmann constant, T the temperature, e the electric charge, D_i is the diffusion constant and z_i the ion valency. The increment i denotes which ionic species is being studied (e.g. sodium or potassium), so the total potential will be the solution to the coupled equation, summed over all the participating ion species (up to the total, M). Equations 2.42 and 2.43 are very difficult to solve even in a cylindrical case where the azimuthal coordinate can be neglected due to symmetry. Thus we will apply the two key approximations to the PNP model in order to make solutions possible: reducing the number of participating ions and a travelling wave approximation. These approximations therefore also play a role in the derivation of the membrane boundary conditions.

The PNP model can in principle solve for any arbitrary number of ionic species, however, this is computationally difficult to achieve, so an approximation is made on the number of contributing species. Although there are many ions contributing to the electromagnetics of a neuron, the concentrations of many of them are small enough to be neglected such that we only consider four monovalent species in our model: sodium (Na^+), potassium (K^+), chlorine (Cl^-) and charged proteins produced by the cell (OA^-) [51, 67] (see table 2.2). These ions are considered individually when calculating the resting charge density and the HH solution, and are averaged when calculating the PNP solution such that the positive ion concentration is given by: $c_+ = \frac{Na^+ + K^+}{2}$ and the negative ions concentration is given by: $c_- = \frac{Cl^+ + OA^+}{2}$. As these ions are monovalent, their effect on the PNP solution should be the same, allowing us to re-write the PNP equations in the following way:

$$\vec{f}_\pm(r,z) = -D_\pm \vec{\nabla} c_\pm(r,z) \mp \mu_\pm c_\pm(r,z) \vec{\nabla} V(r,z) \tag{2.44}$$

$$\rho(r,z) = e(c_+(r,z) - c_-(r,z)) \tag{2.45}$$

$$\vec{J}(r,z) = e(\vec{f_+}(r,z) - \vec{f_-}(r,z)), \tag{2.46}$$

where $\vec{f}_\pm(r,z)$ is the flux of the positive or negative ion species, $c_\pm(r,z)$ is the concentration of the positive or negative ion species, $\mu_\pm$ is the ion mobility ($\mu_\pm = \frac{D_\pm e}{k_b T}$) and $\vec{J}(r,z)$ is the current density.

We then assume that the AP is a travelling wave with constant velocity. This assumption is well verified in literature for non-myelinated neurons as any non-linearity that disrupts the travelling wave is small enough to be insignificant [112]. This allows us to make the following change of variables using the chain rule, removing the temporal dimension and reducing the problem to a 2D spatial one:

$$\begin{aligned} \xi &= z - vt \\ \frac{\partial}{\partial t} &= \frac{\partial \xi}{\partial t}\frac{\partial}{\partial \xi} = -v\frac{\partial}{\partial \xi} \\ \frac{\partial}{\partial z} &= \frac{\partial \xi}{\partial z}\frac{\partial}{\partial \xi} = \frac{\partial}{\partial \xi}. \end{aligned} \tag{2.47}$$

In order to solve the PNP equations in this formalism, we require explicit boundary conditions for both the electric potential and the ion concentrations far from the neuron as well as on the external surface of the membrane. In this model, we only solve the PNP equations external to the neuron, this is reflected in our choice of boundaries:

$$V(r,\xi)|_{r\to\infty} = 0 \tag{2.48}$$

$$c_{\pm}(r,\xi)|_{r\to\infty} = c_{b\pm} \tag{2.49}$$

$$\frac{\partial V(r,\xi)}{\partial \xi}|_{\xi\to\infty} = 0 \tag{2.50}$$

$$f_{\pm}(r,\xi)|_{\xi\to\infty} = 0, \tag{2.51}$$

where we expect the potential to be zero far from the neuron radially as the ions are in an electroneutral equilibrium. The term $c_{b\pm}$ is the sum of the bulk ion concentrations for the positive and negative ions respectively which will sum to a zero charge density outside the neuron (see table 2.2). Axially, far from the AP along the neuron, we expect the ion concentrations and the electric potential to reach a constant equilibrium corresponding to the resting potential (-68 mV), thus the derivative of the axial potential and flux must be zero in this region.

At the membrane, the value for the potential and ion concentrations are less clear as they are dependent on the current flowing in and out of the cell during an action potential. In order to solve for these values we apply Gauss' law which can be

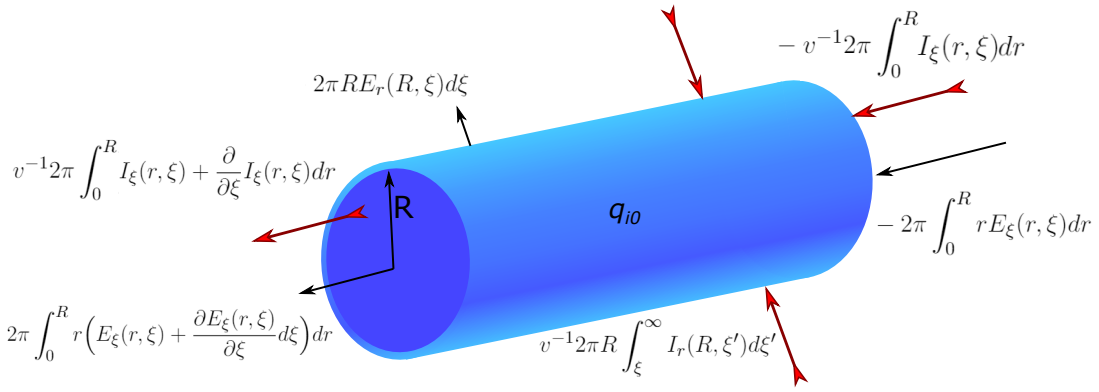

Figure 2.18: Plot of the Gaussian cylinder used in the calculations for the electric field at the membrane. The Gaussian cylinder is co-axial with the neuron with a radius R. The black arrows show the direction of the electric field components which are annotated by terms from the left-hand side of Gauss' equation 2.52. The red arrows show the direction of the current flow which are annotated from the right hand terms of the continuity equation 2.56. Note the radial currents are counter-propagating on opposite sides of the cylinder. The internal resting charge from equation 2.56 is also shown.

simplified in the following steps:

$$\begin{aligned}
\oint \vec{E}(r,\xi)\cdot dA &= \frac{Q_i(\xi)d\xi}{\epsilon_r} \\
\rightarrow 2\pi R E_r(R,\xi)d\xi + 2\pi\int_0^R r\Big(E_{\xi}(r,\xi)+\frac{\partial E_{\xi}(r,\xi)}{\partial\xi}d\xi\Big)dr - 2\pi\int_0^R rE_{\xi}(r,\xi)dr &= \frac{Q_i(\xi)d\xi}{\epsilon_r} \\
\rightarrow 2\pi R E_r(R,\xi)d\xi + 2\pi d\xi\int_0^R r\frac{\partial E_{\xi}(r,\xi)}{\partial\xi}dr &= \frac{Q_i(\xi)d\xi}{\epsilon_r},
\end{aligned} \tag{2.52}$$

where R is the radius of the Gaussian cylinder coaxial to the neuron which is the same as the radius of the axon (to the outer surface of the membrane). The first term on the left hand side of equation 2.52 is the integral for the electric field of the length of the Gaussian cylinder, and the second term is the solution for the electric field at end-caps of the cylinder (see figure 2.18). In the equations, $\epsilon_r = \epsilon_0\epsilon_w$ is the absolute permittivity of the medium made up of the relative permittivity of water (ϵ_w) multiplied by the absolute permittivity of free space (ϵ_0). The terms $E_r(r,\xi)$ and $E_{\xi}(r,\xi)$ are the radial and axial electric fields respectively and $Q_i(\xi)$ is the internal charge per axial unit length inside the neuron. Applying the relation $\vec{E} = -\vec{\nabla}V$, the above can be rewritten in terms of the electric potential:

$$\frac{\partial V(r,\xi)}{\partial r}|_{r\rightarrow R} = -\frac{1}{R}\int_0^R r\frac{\partial^2 V(r,\xi)}{\partial\xi^2}dr - \frac{Q_i(\xi)}{2\pi R\epsilon_r}, \tag{2.53}$$

To simplify the integral in equation 2.53 we will make the following substitution:

$$\frac{1}{R}\int_0^R r\frac{\partial^2 V(r,\xi)}{\partial\xi^2}dr = \frac{-\gamma R}{2}\frac{\partial^2 V(R,\xi)}{\partial\xi^2}, \tag{2.54}$$

where γ is a constant factor that describes the divergence of the axial electric field (as a function of r) from a radially uniform electric field. To effectively approximate γ we consider two extreme cases for the distribution of charge inside the neuron: the resting case and the peak of an AP. In the resting case near the membrane, the charge density (and the electric field) increases dramatically forming the Debye layer. In this case, the derivative of the axial electric field will be much larger than the integrated derivative of the axial electric field and γ will have to be very small in order to compensate ($\gamma \to 0$). This makes physical sense as in the resting condition we expect the change in the axial electric field to be negligible. In the other extreme case, an AP will cause a depolarizing influx of charge which will cause the interior charge density to become more radially uniform [67]. In this case, the derivative of the electric field will become radially constant and γ will become one. Thus, throughout the course of the neuron going from the resting condition, into the peak of an AP and returning to the resting condition the value of γ must fall between zero and one. However, even at its highest value, ($\gamma = 1$), this term has a negligible contribution to the overall electric field. This is due to the charge per unit length inside the neuron being mostly uniform across the length scales we use (microns), making the net surface integral of the end caps negligible similar to a line of charge.

The second term in equation 2.53 requires knowledge about the internal charge in the neuron, $Q_i(\xi)$. We can derive this quantity via the continuity equation for charge. The total internal charge is made up of the charge during the neuron resting condition plus the currents moving charge in and out of the neuron due to an AP:

$$\begin{aligned} Q_i(\xi) &= q_{i0}(\xi) - v^{-1}2\pi\int_0^R\int_{\xi}^{\infty}\Big(I_{\xi}(r,\xi) + \frac{\partial}{\partial\xi}I_{\xi}(r,\xi) - I_{\xi}(r,\xi)\Big)r\,dr d\xi - v^{-1}2\pi R\int_{\xi}^{\infty} I_r(R,\xi')d\xi' \\ &\to Q_i(\xi) = q_{i0}(\xi) - v^{-1}2\pi\int_0^R\int_{\xi}^{\infty}\frac{\partial}{\partial\xi}I_{\xi}(r,\xi)r\,dr d\xi - v^{-1}2\pi R\int_{\xi}^{\infty} I_r(R,\xi')d\xi' \\ &\to Q_i(\xi) = q_{i0}(\xi) - v^{-1}2\pi\int_0^R I_{\xi}(r,\xi)r\,dr - v^{-1}2\pi R\int_{\xi}^{\infty} I_r(R,\xi')d\xi', \end{aligned} \tag{2.55}$$

in this equation, $q_{i0}(\xi)$ is the total charge per unit length in the neuron resting condition, that is, the charge existing in the cell in the absence of an AP. The AP then alters the total charge by introducing radial membrane ($I_r(R,\xi)$) and internal axial ($I_{\xi}(r,\xi)$) currents which are currents per unit area. We then apply Ohm's law to turn the axial current into the integral of the axial electric field.

$$Q_i(\xi) = q_{i0}(\xi) + v^{-1}2\pi\int_0^R \sigma_{i0}E_{\xi}(r,\xi)r\,dr - v^{-1}2\pi R\int_{\xi}^{\infty} I_r(R,\xi')d\xi', \tag{2.56}$$

similar to the approximation we made in equation 2.54, we can re-express the second term on the right hand side of equation 2.56 by removing the integral and introducing a constant factor η, to represent the deviation from a uniform potential and conductivity. This results in a quasi-Ohm's law approximation where σ_{i0} is the total internal conductivity.

$$Q_i(\xi) \approx q_{i0}(\xi) - \eta\pi R^2\sigma_{i0}v^{-1}\frac{\partial V(R,\xi)}{\partial\xi} - v^{-1}2\pi R\int_{\xi}^{\infty} I_r(R,\xi')d\xi'. \tag{2.57}$$

Approximating η is a little more difficult than γ as we need to consider the conductivity as well as the electric field. The conductivity is a function of the total concentration of ions which we know will change with radius due to the Debye layer. During the peak of an AP, we expect the ion concentration (and conductivity) to be mostly uniform along with the axial electric field so η will be one in this instance. During the resting case, the conductivity will be mostly uniform with an increase at the Debye layer where the concentrations increase. However, increases in the concentration in the Debye layer have to be dramatic to have an effect on the overall fields due to the fact that the Debye layer is a very small region of charge compared to the overall volume of the interior neuron. For this reason, we will approximate η to one for all times during an AP.

Substituting equation 2.57 into equation 2.53 gives the following:

$$\frac{\partial V(r,\xi)}{\partial r}|_{r=R} = -\frac{q_{i0}(\xi)}{2\pi R\epsilon_r} + \frac{1}{2\pi R\epsilon_r}\Big(\eta\pi R^2\sigma_{i0}v^{-1}\frac{\partial V(R,\xi)}{\partial\xi} + v^{-1}2\pi R\int_{\xi}^{\infty} I_r(R,\xi)d\xi'\Big) - \frac{\gamma R}{2}\frac{\partial^2 V(R,\xi)}{\partial\xi^2}, \tag{2.58}$$

this equation requires the radial membrane current as well as the axial derivative of the electric potential. To find these quantities we apply the Hodgkin-Huxley (HH) equations [52, 67, 130]. In the classic HH model, however, the neuron is clamped during the experiment and in our case, it isn't so we will need to consider an axial current as well:

$$\frac{\partial V_m(t,z)}{\partial t} = \frac{1}{C_m}\Big(I_r(R,t) + \frac{1}{R}\int_0^R \frac{\partial I_{\tilde{\xi}}(r,z,t)}{\partial z}rdr\Big) \tag{2.59}$$

where the α_x and β_x terms of the gating parameters are found through experimental fitting which in this calculation is taken from Zandt et al. [130]. Also note that in our model, the effects of the Chlorine ion is negligible so it is removed in this version of the HH equations [67, 130]. As the AP wavelength is orders of magnitude larger than the radius of the neuron (mm vs μm respectively) [51], we expect the integrated derivative of the axial current to be much smaller than the radial current as the axial current will change slowly over the long wavelength of the AP. Therefore, the second

term on the right-hand side of equation 2.59 can be neglected.

We relate the HH equations to the terms in equation 2.58 by making the following substitutions from the travelling wave approximation:

$$\frac{\partial V_m(t)}{\partial t} = \frac{-1}{C} I_r(t) \rightarrow \frac{\partial V(R,\xi')}{\partial \xi} = \frac{v^{-1}}{C} I_r(R,\xi) \tag{2.60}$$

$$\begin{aligned} \int_t^{\infty} \frac{\partial V(R,t')}{\partial t'} dt' \rightarrow -v \int_{\xi}^{\infty} \frac{\partial V(R,\xi)}{\partial \xi'} d\xi' &= -v\big(V(R,\infty) - V(R,\xi)\big) \\ &= \frac{-1}{C} \int_{\xi}^{\infty} I_r(R,\xi') d\xi', \end{aligned} \tag{2.61}$$

where $V(R,\infty)$ is equivalent the resting potential V_{rest}. Equations 2.60 and 2.61 relates the HH transmembrane potential and radial current to $V(R,\xi)$ and $I_r(R,\xi)$ in equation 2.58 which we derived from Gauss' law. In this formalism, we describe $V(R,\xi)$ as the cross-sectional average of the potential which is effectively the transmembrane potential. This allows us to substitute these terms into equation 2.58 to obtain a simpler boundary condition whose potential and current terms can be added in from the HH solutions. We can also use the HH current solution to calculate the ion flux which can be used as a membrane concentration boundary condition. Putting all the equations together gives the membrane boundary conditions for the membrane electric fields as well as the ion flux:

$$\begin{aligned} -E_r(R,\xi) = -\frac{q_{i0(\xi)}}{2\pi R \epsilon_r} + \frac{1}{2\pi R \epsilon_r}\Big(\eta \pi R^2 \sigma_{i0} v^{-2} C^{-1} I_r(R,\xi) + 2\pi R C\big(V_{rest} - V(R,\xi)\big)\Big) \\ - \frac{\gamma R v^{-1}}{2C} \frac{\partial I_r(R,\xi)}{\partial \xi} \end{aligned} \tag{2.62}$$

$$\frac{\partial c_+(r,\xi)}{\partial r}|_{r=R} = \frac{N_A}{e} 2\pi R I_r(R,\xi) \tag{2.63}$$

$$\frac{\partial c_-(r,\xi)}{\partial r}|_{r=R} = 0, \tag{2.64}$$

where N_A is Avogadro's constant. Equation 2.63 simply states that the rate of change in the positive ion concentration is directly proportional to the radial current. Due to the assumption that there is only positive ion flow across the membrane [67, 130], the negative ion flux is zero.

To obtain the magnetic field boundary conditions we apply Ampere's laws where the axial current in the membrane boundary condition is treated in the same way as equation 2.57.

$$\vec{\nabla} \times \vec{B}(r,\xi) = \mu_0 \vec{J}(r,\xi), \tag{2.65}$$

where the external current density is given from equation 2.46 and the effect of a polarizing current is negligible (quasi-DC approximation). The boundary conditions are as follows:

$$\vec{B}(r \to \infty) = 0 \tag{2.66}$$

$$\vec{B}(\xi \to \infty) = 0, \tag{2.67}$$

the current densities are zero far from the AP axially and radially, so the magnetic field will be zero. At the membrane, the magnetic field is dependent on the axial and radial currents (I_ξ and I_r respectively). However, the radial current contribution to the magnetic field can be considered negligible as each radial current component on the cylinder would be cancelled out by the radial current component on the opposite side of the cylinder (see figure 2.18). This assumption is well established in the literature [126] and means that the magnetic field will be directly proportional to the axial current, similar to a current-carrying wire:

$$\vec{B_r}(r,\xi)|_{r=R} = -\frac{\mu_0}{2\pi R} I_\xi(R,\xi), \tag{2.68}$$

the axial current can be related to the derivative of the potential from Ohms law (equation 2.57):

$$\vec{B_r}(r,\xi)|_{r=R} = -\frac{\mu_0}{2}\eta R\sigma_{io}\frac{\partial V(R,\xi)}{\partial \xi}, \tag{2.69}$$

the potential derivative can be related to the radial current using the substitution equation 2.60:

$$\vec{B_r}(r,\xi)|_{r=R} = -\frac{\mu_0}{2}\eta R\sigma_{i0}C^{-1}v^{-1}I_r(R,\xi). \tag{2.70}$$

This means that despite the radial current contributing negligibly to the magnetic field, it is a driving force in the creation of the axial current which creates the magnetic field indirectly and can be derived using the HH equations.

The membrane boundary conditions derived above are all that is required to find the full electromagnetic quantities external to a neuron. Equations 2.62, 2.63 and 2.64 can be used with the PNP equations to solve for the electric potential and ion concentrations. The ion concentrations can then be used to derive the external current density which can be used with equation 2.70 and Ampere's law to find the external magnetic fields. The parameters used in these equations are given in Table 2.2. Included in the table are the dimensions of the cylindrical neuron used in the simulation. Although many of the values were obtained from literature, calculations of the conductivities, mobility's and resting potential were performed to ensure the values were self-consistent.

Figure 2.19 is the result of the membrane boundary condition derivations. Figure 2.19a) is the membrane electric field solution from equation 2.62, figure 2.19b) is the membrane magnetic field from equation 2.70 and figure 2.19c) is the membrane

Table 2.2: Table of Parameters used in the calculations, all other terms used (e.g. ion mobility's or Nernst potentials) are derived from these values. Values that are un-sourced were chosen by the to suit the model

	Description	Value	Source
K_i	Int Potassium Concentration	155 mmol/L	[67]
K_e	Ext Potassium Concentration	4 mmol/L	[67]
Na_i	Int Sodium Concentration	12 mmol/L	[67]
Na_e	Ext Sodium Concentration	145 mmol/L	[67]
Cl_i	Int Chlorine Concentration	4.2 mmol/L	[67]
Cl_e	Ext Chlorine Concentration	123 mmol/L	[67]
OA_i	Int Protein Concentration	162.802 mmol/L	[67]
OA_e	Ext Protein Concentration	26 mmol/L	[67]
g_{Na}	Total Sodium conductance	100 mS/cm^2	[130]
g_{NaL}	Sodium leak conductance	0.0175 mS/cm^2	[130]
g_K	Total Potassium conductance	40 mS/cm^2	[130]
g_{KL}	Potassium leak conductance	0.05 mS/cm^2	[130]
ϕ	HH time constant	3 ms^{-1}	[130]
C	Membrane Capacitance	1 μF/cm^2	[130]
T	Temperature	310^{o}K	-
D_K	Potassium Diffusion coefficient	1.957×10^{-9} m^2/sec	[102]
D_{Na}	Sodium Diffusion coefficient	1.334×10^{-9} m^2/sec	[102]
D_{Cl}	Chlorine Diffusion coefficient	2.032×10^{-9} m^2/sec	[102]
D_{OA}	Protein Diffusion coefficient	2.00×10^{-9} m^2/sec	[102]
ϵ_r	Absolute Permittivity of water	$80 \times 8.854 \times 10^{-12}$ C/Vm	-
μ_K	Potassium mobility	7.328×10^{-8} m^2 s^{-1} V^{-1}	[67]
μ_{Na}	Sodium mobility	4.995×10^{-8} m^2 s^{-1} V^{-1}	[67]
μ_{Cl}	Chlorine mobility	-7.609×10^{-8} m^2 s^{-1} V^{-1}	[67]
μ_{OA}	Protein mobility	-7.489×10^{-8} m^2 s^{-1} V^{-1}	[67]
V_{rest}	Resting Potential	-68 mV	[130]
R_n	Radius of neuron	500 nm	[66]
L_n	axial length of neuron	2 mm	-
R_n	Radius nano-mesh	10 nm	-
R_n	Radius of external solution	1.5 μm	-

positive ion flux taken from equation 2.63, which is simply the radial current, placed in units of ions per metre squared.

Surface plots of the PNP results are displayed in figure 2.20. In the plots, the 500 nm mark corresponds to the external membrane radius. The orange lines are the travelling wave signal moving axially along the neuron (the curves from figure 2.19). There are also radial line graphs of the solutions, which depict the electric and magnetic fields at the peak of the AP wave, as well as $1/r$ model, fits for the magnetic fields (figure 2.21). These plots also feature a CC solution calculated from the equations presented in Woosley et al. [126] but altered to match the parameters of the mammalian neuron considered in this study.

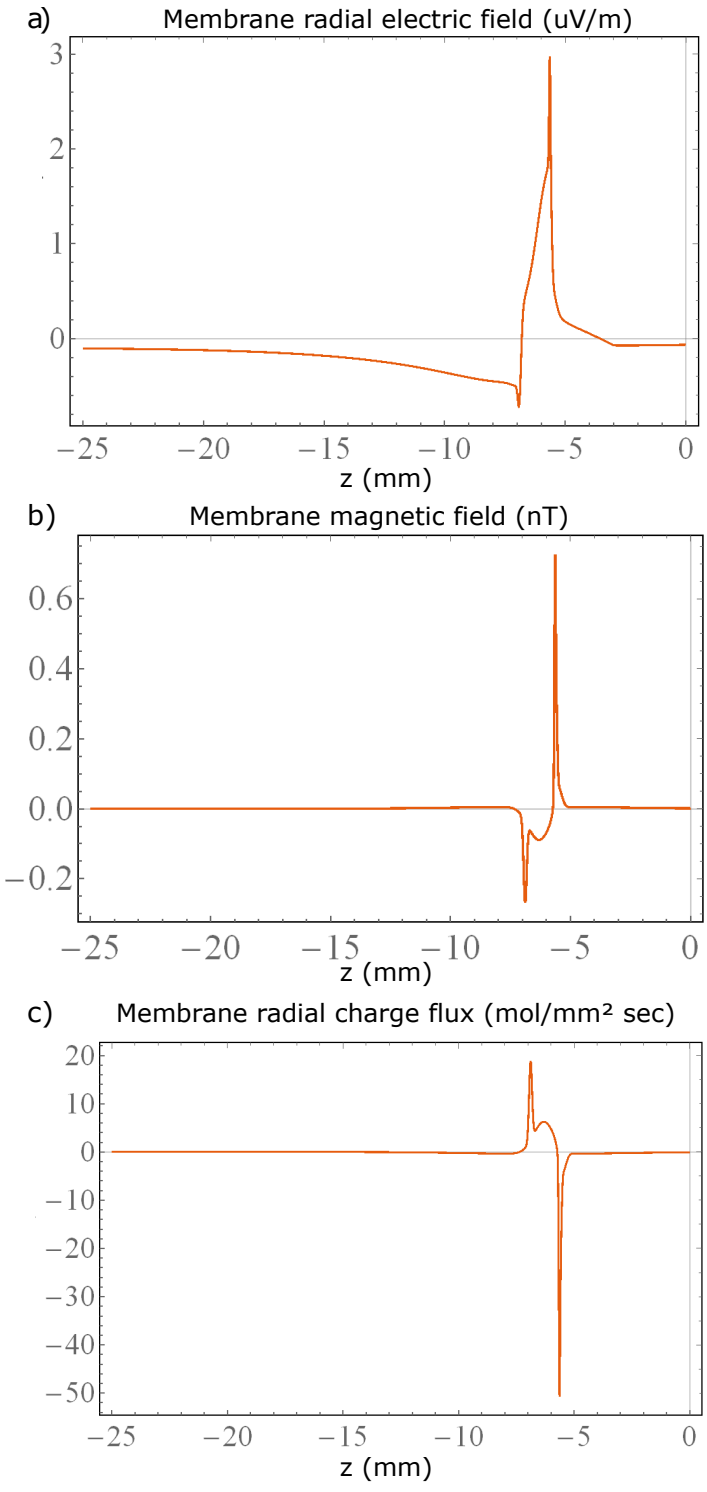

Figure 2.19: Plots for the a) membrane electric field, b) membrane magnetic field. The plots were derived from equations 2.62 and 2.70 respectively. c) Plot of the membrane flux derived from the HH equations. All three of these plots were used as the orange sketch lines in the 2D surface plots of figure 2.20

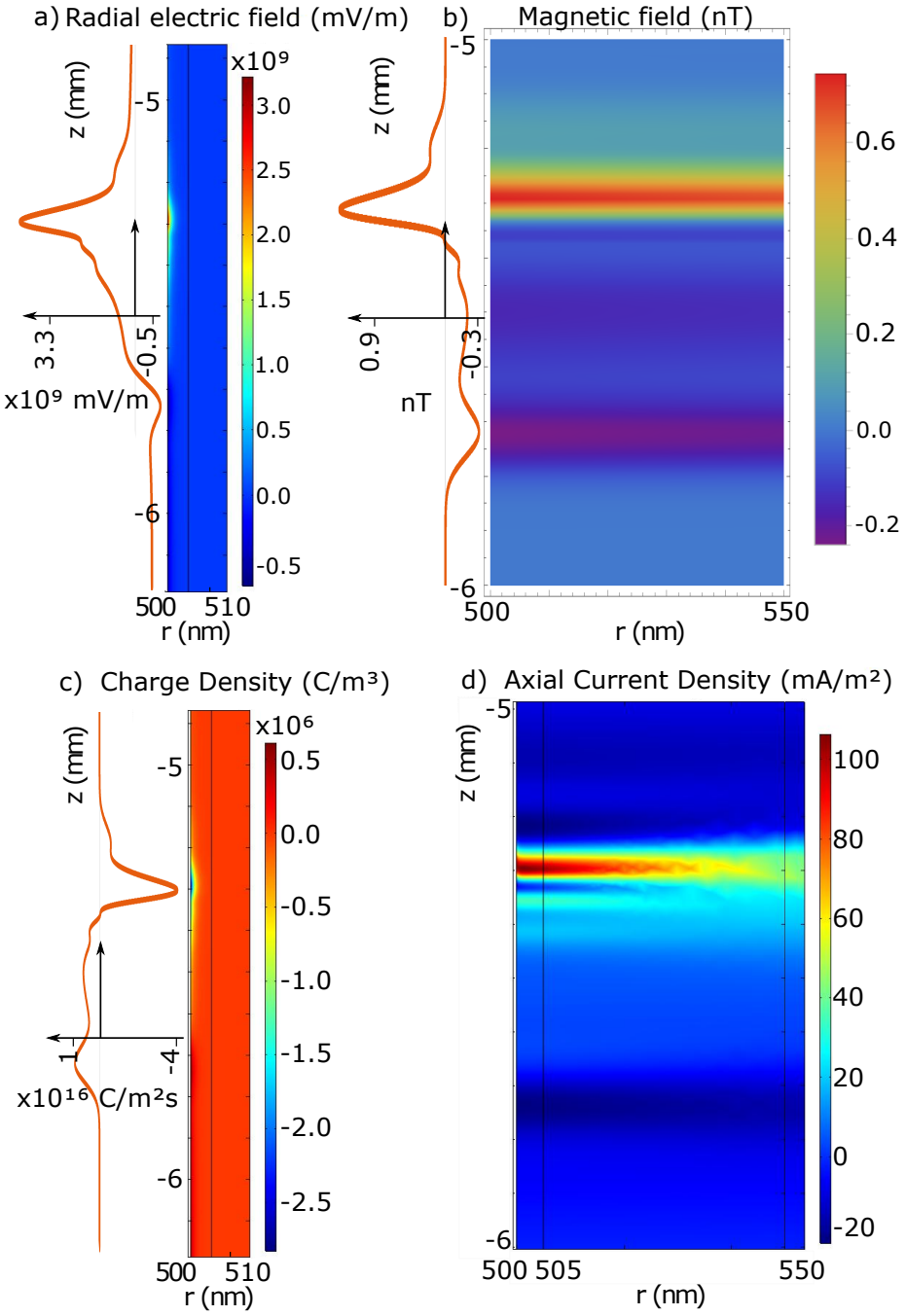

Figure 2.20: Simulation results for the a) electric field, b) magnetic field, c) charge density and d) axial current density. On the left of a), b) and c), the electric field, magnetic field and positive ion flux at the membrane are sketched respectively as orange lines which are plotted in greater detail in figure 2.19. The membrane solutions are derived from experimentally verified HH equations. These solutions demonstrate how these quantities longitudinally propagate with the neuron signal

As mentioned, the key result of the PNP calculation that is absent in CC theory is

the effects of the Debye screening layer [105]. The Debye screening is most evident in the electric field and charge density solutions. In figure 2.20a, the resting radial electric field at the membrane (ie where the AP wave has zero amplitude) is $\approx -0.5 \times 10^9$ mV/m. At the peak of the AP wave, this electric field at the membrane is significantly different $\approx 3.3 \times 10^9$ mV/m. However, despite this dramatic change at the membrane, the Debye screening reduces the change to zero over approximately 3 nm (solid blue line in figure 2.21b). Comparing our PNP and CC solutions, it is clear that the inclusion of Debye screening in the PNP model has resulted in a much larger electric field at the membrane, but also a much more rapid radial decay of the electric field. This result is also similar in the charge density solutions (figure 2.20c), where almost everywhere outside the neuron, the ion concentrations approach their bulk values, creating a zero net charge density. However, within the Debye layer and AP wave, the charge density decreases to as low as $\approx -3 \times 10^6$ C/m^3 due to the positive charge being transferred from outside to inside the axon, thereby increasing the potential and electric fields. Away from the AP wave, the charge density increases slightly to $\approx 0.5 \times 10^6$ C/m^3, re-forming the positive charge Debye layer in response to the internal negative charge present during the neuron resting conditions.

Debye screening has little effect on the magnetic fields (figure 2.20b). The current density external to the axon is aligned with the internal current density. Consequently, this external current density reinforces the magnetic field generated by the internal current density (figure 2.20d). However, the external current density is extremely small compared to the internal current density (≈ 100 mA/m^2 at its peak). Thus, the total magnetic field enhancement is negligible. The net magnetic field has a $1/r$ decay in both the PNP and CC models and so the magnetic field clearly decays radially much more slowly than the electric field (the magnetic field extending to over ≈ 2 μm, compared to the ≈ 3 nm of the electric field). Figure 2.21a) shows that there is only a small difference in magnitude between the magnetic fields of PNP and CC models. The similar radial decay, however, demonstrates how the PNP model can match the CC model at micron scales where the CC model is experimentally verified [126]. A notable outcome of the PNP results is that the axial current density is much smaller than the radial current density. This is in keeping with the radial current density being primarily responsible for the change in charge density that generates the AP.

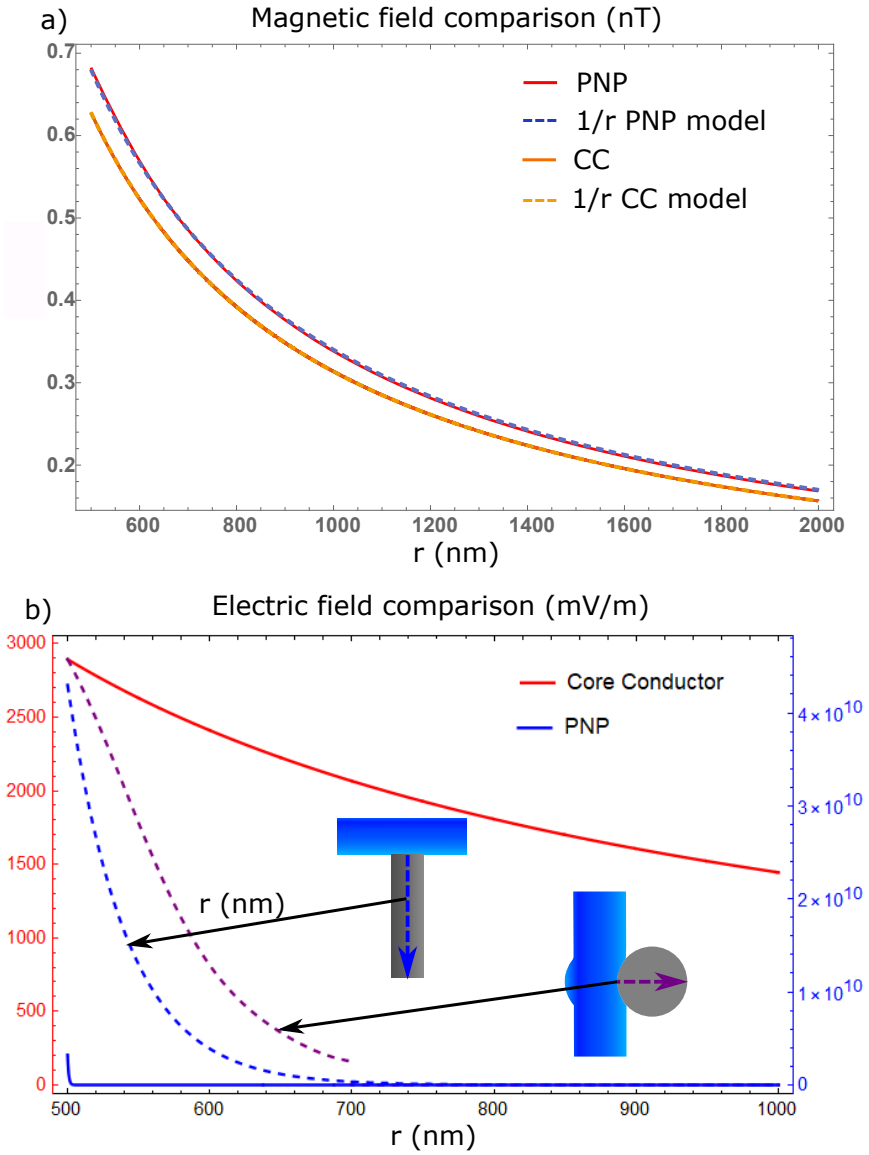

Figure 2.21: Radial 1D plots of the a) magnetic and b) electric fields taken from the peak of the AP wave. The magnetic field plots feature the PNP solution, the CC solution derived from Woosley [126] as well as $1/r$ model fits for both. The electric field plots contain solutions to the PNP, CC models and the Laplace solutions for the electric field in the diamond when the neuron is in contact along the tip as well as along the side of the diamond pillar. The red axis is for the CC model and the blue axis is for the other three.

Critically, the magnetic field reaches a maximum of 0.7 nT at the membrane boundary. Whether the calculation is done using a full PNP simulation, CC theory [126] or even by approximating the neuron as a current carrying wire [12], the results tend to suggest that a mammalian neuron can only produce a magnetic field that is less than a nT in magnitude. This signal is too small to be detected by an NV within

the millisecond timescale of the neuron signal [99]. Even with the light collection improvement from the pillar geometry, a 5-fold improvement to the magnetic field sensitivity still won't allow for mammalian neuron AP sensing [74]. For electric field sensing, although the magnitude of the field is larger than the minimum detectable electric field, the difficulty lies in placing an NV within the Debye layer external to the membrane. The closest range an NV can be placed to the surface of a diamond is ≈ 5 nm whilst maintaining reasonable coherence and stability [22]. In the simplest picture, if the diamond tip is in contact with the neuron, at this distance the field will have decayed to zero, thereby suggesting that NV sensing of both neuron electric and magnetic fields is impossible.

However, this reasoning is too simplistic and does not consider the effect of the diamond nanopillar on the screening charge and current densities. As shown above, the effects of external currents are small, and so the presence of the pillar will have a negligible effect on the magnetic field. However, the screening charge has profound effects on the electric field. By removing the screening charge between the neuron and the pillar tip (via good contact) and accounting for the much lower dielectric screening in the diamond ($\epsilon \approx 6$) compared to the surrounding water ($\epsilon \approx 80$), we expect the electric field inside the pillar to be much larger.

To model this enhancement, we solved Laplace's equation inside a 200 nm diameter pillar that is in contact with a neuron, such that the Debye screening layer is removed from the contact area. This simulation was done for two different co-ordinations of the pillar and neuron. One where the neuron is on top of the pillar and in contact with the pillar's complete circular top surface, and then another where the neuron is on the side of the pillar near its tip and has a square contact area of the same size.

Consider a geometry where a neuron runs over a single cylindrical diamond pillar where the tip of the pillar is in full contact with the neuron (figure 2.22). Assume that the charge inside the neuron is unperturbed by the presence of the pillar and that Debye screening fixes the electric potential on the sidewalls of the pillar to be zero. Note that this ignores the small region close to the neuron (i.e. within the Debye layer) where the potential is non-zero on the sidewalls. We expect these assumptions to be good as long as the diameter of the pillar isn't so large that affects the function of the neuron, but sufficiently large compared to the Debye length (1 nm) such that the non-zero potential within the Debye layer has negligible influence on the electric field in the region of the pillar's central axis. This is where it is desirable to implant the NV centers. Given these assumptions and adopting the local cylindrical coordinate system of the pillar depicted in figure 2.22, Laplace's equation yields the following electric potential within the nanopillar:

$$V(r,z) = \left(\frac{d}{k}\right) E_m J_0\left(\frac{rk}{(d/2)}\right) e^{(-k/(d/2))(z-R_{mem})}, \tag{2.71}$$

where J_0 is the zeroth Bessel function, d is the diameter of the diamond pillar (200 nm), R_{mem} is the radius of the neurite (500 nm) and $k \approx 2.4$, the first zero solution of the Bessel function. In addition there is E_m, the membrane electric field, i.e. the electric field at $z = R_{mem} = 500$ nm, the membrane boundary. This value is

calculated from equation 2.62 with the same parameters as used in table 2.2 but with a diamond permittivity ($\epsilon \approx 6$) instead of water. This yields a membrane electric field of 4.54×10^{10} mV/m. It then follows from $\vec{E} = -\vec{\nabla} V$, that the axial electric field inside the pillar is:

$$E_z = E_m J_0\Big(\frac{rk}{d/2}\Big) e^{(-k/(d/2))(z-R_{mem})}, \tag{2.72}$$

on the central axis of the pillar where $r = 0$, the Bessel function becomes 1 and the electric field propagation becomes:

$$E_z = E_m e^{(-k/(d/2))(z-R_{mem})}, \tag{2.73}$$

this axial field decays exponentially from the tip with a decay constant of $k/(d/2)$.

Figure 2.23 depicts a different modelled geometry, where the neurite runs along the side of the pillar towards the top. In this model, the surface of the pillar which is in contact with the neurite is the same area as in the case with the neurite running on top of the pillar. This contact area is considered small compared to the overall surface area of the enclosing cylinder segment. This small contact area is the basis for the assumption that the diamond pillar contact won't affect the natural function of the neuron. The contact area has the same surface electric field from the neuron as the previous case (4.54×10^{10} mV/m) and the rest of the pillar has its potential fixed at zero. With these boundary conditions, the electric field propagation inside the neuron can be solved numerically using COMSOL Multiphysics. The solution in this geometry is shown as a 2D slice density plot in figure 2.24.

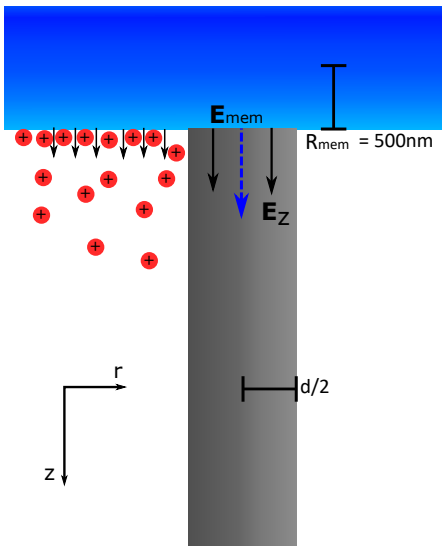

Figure 2.22: Image of the geometry considered for the electric field inside the diamond when the neurite (blue) runs over the top of the diamond pillar (grey). The image features the positive ions forming the Debye layer outside the neuron which doesn't exist inside the diamond as well as the coordinate system used to obtain the solution. The blue dashed line represents the 1D solution used in figure 2.21.

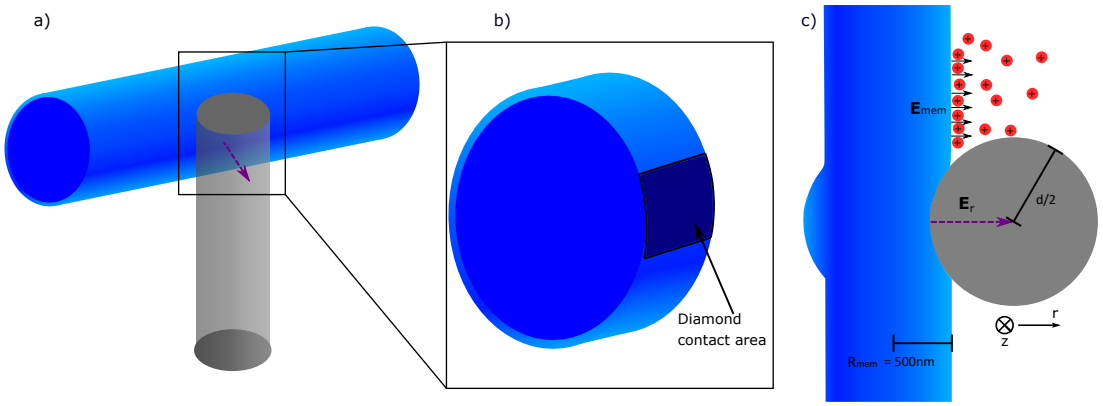

Figure 2.23: Image of the geometry considered for the electric field inside the diamond when the neurite (blue) runs across the side of the diamond (grey) towards the tip of the pillar. a) The diamond pillar the neurite makes contact towards the top of the pillar and the cutout of the neurite segment b) shows a dark shaded area where the pillar makes contact with the neuron segment. The contact area is small compared to the overall surface area of the enclosing cylinder segment. c) The top-down view of the same system in a)/b). The image features the positive ions forming the Debye layer outside the neuron which doesn't exist inside the diamond as well as the coordinate system used to obtain the solution. The purple dashed line represents the 1D solution used in figure 2.21.

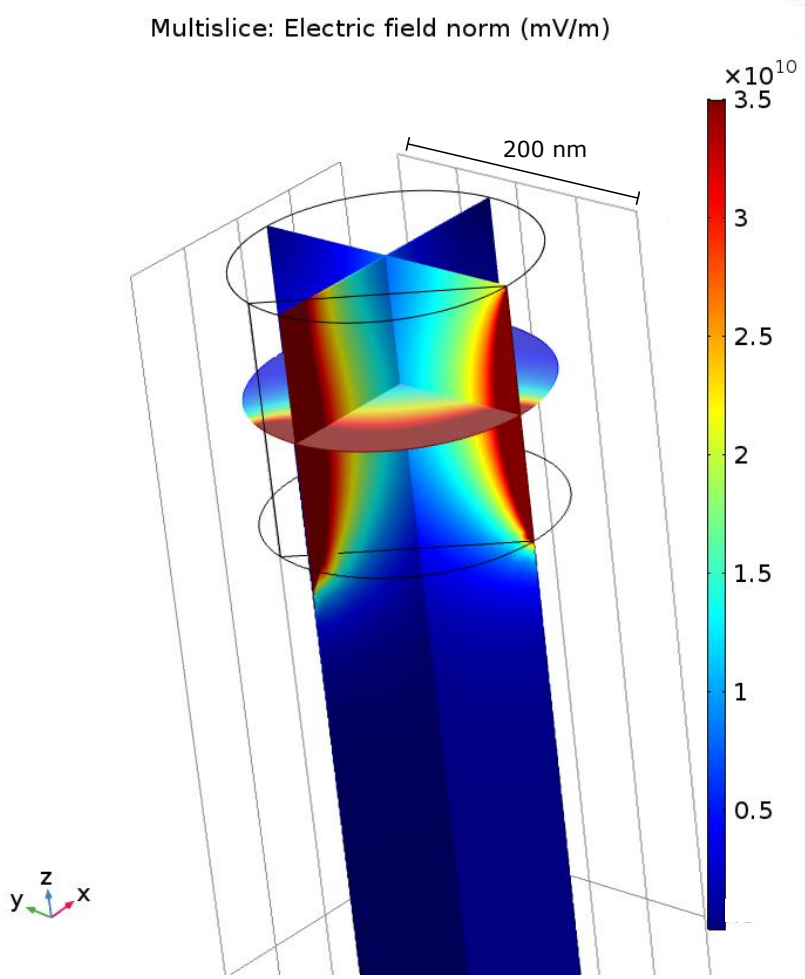

Figure 2.24: Solution for the electric field with a neurite in contact with the side of the pillar tip. The geometry with the neurite is shown in figure 2.23. The neurite contact area is marked by the surface of the tip cut out by the black wire-frame rectangle.

Plots of selected results are shown in figure 2.21b). Specifically, these results are for the electric field magnitude in the pillar along a line extending from the center of the contact area along/through the central axis of the pillar for the on-top (blue dashed line) and on-side (purple dashed line) co-ordination. The electric field of the on-top coordination has an analytic solution with an exponential decay determined by a decay constant of $\approx 4.8/d$. For an NV depth of ≈ 5 nm and a pillar diameter much larger than this depth, this implies that an electric field as high as $\approx 3.2 \times 10^9$ mV/m will occur at the NV. A value that is in the same order of magnitude as the maximum electric field measured by the diamond in literature [27]. For the on-side coordination, the electric field is predicted to be larger than for the on-top coordination at larger distances. Indeed, the results show that at 100 nm away from the neuron membrane (i.e. the central axis of the pillar) electric fields as high as $\approx 1.02 \times 10^{10}$ mV/m will occur. The larger field that arises when the neuron is on-side is due to the curvature of

the contact area. This curvature implies that the distance from a point in the pillar to a charge on the neuron surface is on-average smaller than for the flat contact area when the neuron is on top. This leads to a larger electric field for the on-side coordination.

Given the NV electric field sensitivity mentioned above and the geometries stated, the neuromodelling shows that the NV should easily be able to detect APs within the signal timescale when the neuron is in both on-top and on-side locations of a diamond pillar. However, it is important to note that only qualitative information can be drawn from this type of study. One thing that is not considered in this model is how internal charges will re-organise in response to the changing electric field the pillar provides. Although electric field enhancement is still predicted, the magnitude of such an enhancement cannot be accurately defined without a full model of internal and external neuron solutions in order to observe how the charges respond to the presence of the pillar. It should be noted that these simulations are far from trivial as both the scale of the neuron signal compared to the nanopillar makes approximations problematic and the presence of the nanopillar itself removes symmetry, making the full PNP calculations computationally challenging. These simulations will be one of the focus areas of future work.

One key result of the neuromodelling is that NV electric field sensing is possible as long as the neurons grow in such a way as to make consistent and close contact with the nano-diamond pillars, in the next section, this is investigated more thoroughly. The principle of neuron growth is discussed, and a preliminary growth study is undertaken in order to understand how neurons grow on diamond nanopillars to benefit sensing and how future work could improve upon this experimental concept.

2.5 Growth study

In this section, a general hypothesis is discussed for the neuron growth mechanism on a pillar substrate. The optical wavelengths used in the growth study microscopy are described, and a general description of the light collection efficiency provided by the diamond pillars is presented. Table 2.3, shows excitation and emission wavelengths used in the microscopy, table 2.4 shows the full results of the growth study, figure 2.25 shows the total and ordered growth as a function of averaged diameter, figure 2.26 shows the total and ordered growth as a function of averaged fractional separation factor and figure 2.27 shows the total and ordered growth as a function of pillar pitch.

Although the specific mechanism for the ordered growth is still unknown, a strong hypothesis is that ordered growth is centered around mechanosensitive structures in the neuron cytoskeleton [30]. During neuron growth on a protein layered substrate (e.g. laminin on a diamond pillar), neurons express proteins such as integrin molecules in all directions, which bind to the laminin in the extra-cellular matrix forming a new protein complex. This protein complex then binds to actin on the neuron cytoskeleton and mechanosensitive ion channels on the cytoskeleton initiate various mechanotransduction pathways, which encourages cellular growth at the point of the binding. As this process repeats itself, a regular line of pillar structures can encourage

the process to continue in a line, thus producing directionally ordered growth. In this way, external forces on mechanically sensitive ion channels direct neuron growth in response to physical cues such as a diamond nanopillar [30]. One result of this is that there is a distance in which, ordered growth is maximized. The protein complexes produced in the growth process have a finite size, creating a range where the neuron is mechanosensitive. If the distance between the pillars is larger than this, then there won't be a connection of growth between adjacent pillars. However, if the distance is too small, then the neurons could potentially grow in any direction towards an adjacent pillar (e.g. diagonally instead of vertically or horizontally) as long as it is within the range produced by the protein complex, thus producing no ordered growth at all similar to a flat substrate. This necessitates the need for a growth study to find the ideal pillar geometry that matches the growth mechanism.

Following the work of Gautam et al. and other neuron growth studies [30, 35, 110] on indium phosphide (InP) substrates, we fabricated arrays of cylindrical diamond nanopillars (see experimental section). We then cultured neurons on top of them, staining them and analysing their growth using fixed cell confocal microscopy. This confocal experiment is performed in a conventional upright setup, where the optical excitation and collection occurs from above the neurons in order to directly focus on the neuron dyes and their relation to the pillar arrays. In the NV sensing experiment, the confocal microscopy will be performed in an inverted confocal setup with laser emitting below the diamond substrate in order to take full advantage of the pillar waveguide effect. Each nanopillar array was 200×200 μm, separated by 400 μm, with flat diamond between the arrays. This geometry was suitable to grow a small network of neurons on top of, however much larger pillar arrays (centimetres in area) are possible in order to support larger neuronal networks. The pillar pitch and diameter was varied between the arrays. The pitch was varied from 1 to 4 μm in 1 μm steps and the pillar diameters were either 200 nm or 350 nm. In all arrays the pillar height was 1 μm. Each unique array geometry was fabricated twice (totalling 16 arrays) and we labelled the arrays 0-15. Growth was prevented on arrays 0, 9 and 12 by air bubbles and so these arrays did not contribute to our results (see table 2.4. Growth statistics were obtained for total growth and ordered growth (defined as being aligned with a pillar column or row) as functions of pitch, diameter and fractional separation factor ($(p-d)/p$). This statistical analysis was achieved by combining the results obtained from geometries with the same pitch, diameter or fractional separation, respectively. Together, the total growth and the ordering metric allow for an understanding of which diamond nanopillar geometries produce the ideal growth for sensing studies. The ideal growth being the geometries that maximise the overall amount of neuron growth as well as the amount of neuron growth that is coordinated in close proximity to the NVs in the diamond pillars.

The dyes used for the growth study are listed in table 2.3. The table also includes the excitation and emission wavelengths for the various dyes as well as the Raman line we used to image the diamond itself. There was some overlap between the diamond fluorescence and the Glia dye, however as the diamond imaging was only used to find the pillar patch neurons were growing on, this did not affect the overall results.

With the above exceptions, the cell labelling and confocal microscopy techniques were exactly the same as performed by Gautam et al. [35].

The pillar pitches were chosen following work from Gautam et al. [35], where distances between pillars were chosen to maximize the growth via the binding protein complexes. The diameters and heights were chosen by following work from Momenzadeh et al.[74]. In their work, they calculated the size and shape of pillars which maximizes light collection efficiency for shallow NV implantation. The general principle is that the pillar acts like a waveguide, whose size and shape match fundamental HE (hybrid electric) modes, guiding light out below the pillar into the detection system. Pillars 1 μm in height with 200 and 350 nm diameters are ideally shaped to maximize the number of fundamental modes guided in and out of the pillar.

Table 2.3: Table of fluorescent components used in the confocal microscopy and the structures being imaged with them.

Technique	Type Imaged	Laser Excitation (nm)	Emission band (nm)	Reference
Tuj1-Alexa	Neurons	488	525/50	Gautam et al[35]
GFAP-Alexa	Glia (Astrocytes)	561	595/50	Gautam et al.[35]
Hoechst stain	Cell nuclei	405	450/50	Gautam et al.[35]
Raman	Diamond	561	606	-

The total growth factor was performed by using a region of interest (ROI) image processing in order to measure the growth of neurons as a fraction of the diamond pillar patch. Calculating ordered growth required the design of a specific algorithm. The orientation and length of each neuron can be determined by calculating the center line of each neurite. A binary mask showing neurite center lines was calculated by applying a skeletonisation algorithm [65]. This algorithm reduces every neurite and cell body in the image to a single pixel line without changing the overall structure of the image. The binary mask was convolved by a 3x3 kernel, such that neurite ends, midpoints, and intersections can be uniquely identified. Treating the resulting image as an undirected graph, we can parameterize each neurite by searching the graph for connected lines of pixels. Our search algorithm starts from any endpoint or intersection and traverses connected pixels until it finds another endpoint. Each set of connected pixels is called a path. This process is repeated for each endpoint until all paths are identified. Each path parametrizes the centerline of a neurite. We perform the following line integral along these parameterized center lines to estimate how well the neurite aligns to a pillar line:

$$T_i = \sum_{i=1}^{L} \int_0^T |\frac{\partial}{\partial t}\vec{f}_i| dt \tag{2.74}$$

$$T_o = \sum_{i=1}^{L} \int_0^T \Theta(t) |\frac{\partial}{\partial t}\vec{f}_i| dt \tag{2.75}$$

Table 2.4: Table of the growth results, including patch label, total growth, ordered growth, fractional separation and volume ratios. Note that patches 0, 9 and 12 had problems with the growth, requiring their data results to be removed from the published results and analysis.

Patch	Pitch (p) (μm)	Width (d) (μm)	Distance ratio (p-d)/d	Volume ratio $\pi r^2/p^2$	Total Growth %Area	Total neurite T_i (μm)	Ordered neurite T_o (μm)	Ordered growth $\frac{T_i}{T_o}$(%)
0	1	0.2	0.8	0.031	0	0	0	0
1	1	0.2	0.8	0.031	15.9	3762.5	1116.4	29.7
2	1	0.35	0.65	0.096	13.7	5075.4	1494.5	29.4
3	1	0.35	0.65	0.096	0.7	331.7	116.3	35.1
4	2	0.2	0.9	0.008	12.8	3014.8	1148.4	38.1
5	2	0.2	0.9	0.008	21.1	4119	1593.3	38.7
6	2	0.35	0.825	0.024	2.2	796.4	315.0	39.6
7	2	0.35	0.825	0.024	0.8	475.1	169.9	35.8
8	3	0.2	0.933	0.003	0.3	341.8	95.2	27.9
9	3	0.2	0.933	0.003	0	0	0	0
10	3	0.35	0.833	0.011	6.9	1316.5	356.0	27.0
11	3	0.35	0.833	0.011	4.5	1503.7	433.2	28.8
12	4	0.2	0.95	0.002	0	0	0	0
13	4	0.2	0.95	0.002	10.1	1965.5	521.5	26.5
14	4	0.35	0.913	0.006	2.0	695.9	235.5	33.8
15	4	0.35	0.913	0.006	2.1	1052.5	294	27.9

where T_i is the total length of all the summed neurites (paths), T_o is the total length of the aligned (or ordered) neurites and $\vec{f}_i$ is the neurite's vector component parametrized by the length t:

$$\vec{f}_i = x(t)\hat{x} + y(t)\hat{y} \tag{2.76}$$

where the coordinate vectors $\hat{x}$ and $\hat{y}$ are chosen to coincide with the directions of the rows and columns of the nanopillar array.

The $\Theta(t)$ term represents a piece-wise function, which defines alignment by measuring the angle between the neurite vector component and the vector components of the pillar lines:

$$\Theta(t) = \begin{cases} 1, & arccos\left(\frac{\frac{\partial \vec{f}}{\partial t}\cdot\hat{u}}{|\frac{\partial \vec{f}}{\partial t}|}\right) \leq \frac{\pi}{36} \\ 0, & arccos\left(\frac{\frac{\partial \vec{f}}{\partial t}\cdot\hat{u}}{|\frac{\partial \vec{f}}{\partial t}|}\right) > \frac{\pi}{36} \end{cases}$$

where $\hat{u} = \hat{x}$ or $\hat{y}$. The principle is that the angle between a neurite vector components and a vertical ($\hat{y}$) or horizontal ($\hat{x}$) line of pillars is measured, if that angle is larger than our defined value ($\frac{\pi}{36}$) then the neurite is considered unaligned

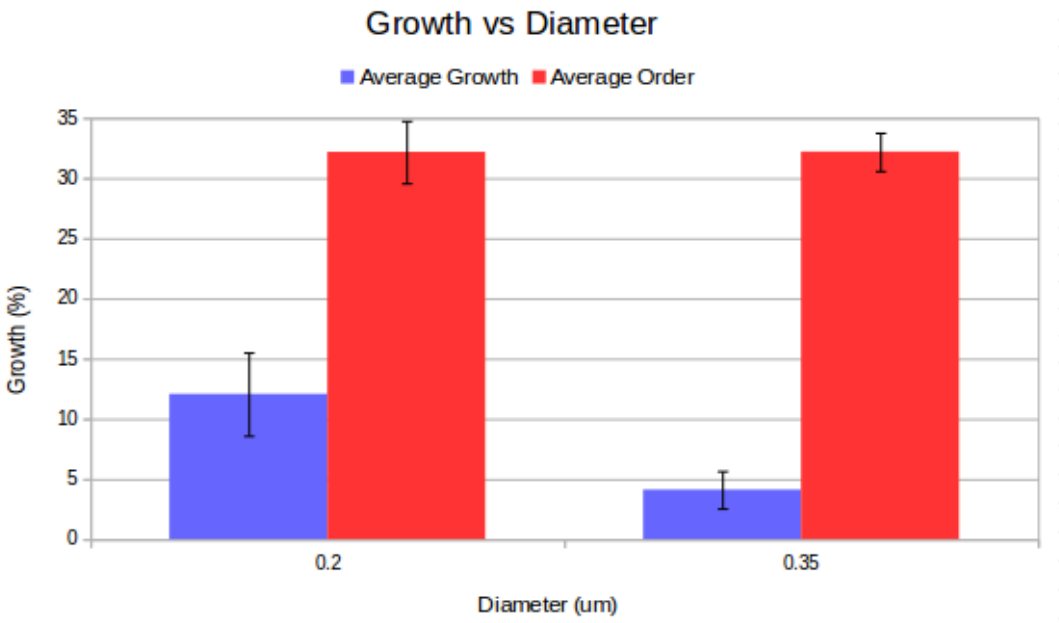

Figure 2.25: Table summary of growth as a function of diameter, averaged across all patches of the same diameters. Error bars indicate one standard error of the sample mean. There is no statistical dependence of diameter on ordered or total growth

with the pillars and discarded. This process is repeated and summed for all neurite vector components (T_o) and divided by the total integrated length of all neurites (T_i) to obtain our order ratio.

Before applying this procedure we preprocessed the raw confocal image of each patch to isolate the the neuron fluorescence. In particular, we started by masking large cell bodies, such as glial cells, either by hand or using a disk shaped structuring element. We then filtered in the colour space to extract the fluorescence from neuron neurites and applied an intensity threshold to filter out residual fluorescence from sources other than neurons. The resolution and quality of confocal scan is the most important factor determining the error in our alignment estimates as well as the ROI processing for total growth. Some factors are mitigated by preprocessing and denoising our image. For example, background fluorescence from other features is mitigated by our preprocessing steps. However, since we needed to apply an intensity threshold over the image, we also ignored low-intensity fluorescence from neurites. Another shortcoming of our approach is that it does not correct for discontinuities in the neurites. This is not a problem when the length of each segment of a neurite is longer than the gaps. If a neurite shows up as a line of disconnected dots it's alignment will not be measured correctly as the dots have no directionality, adding to the total neurite length as noise. This error can be quantified by measuring the number of short and singleton paths relative to the total length of the detected neuron.

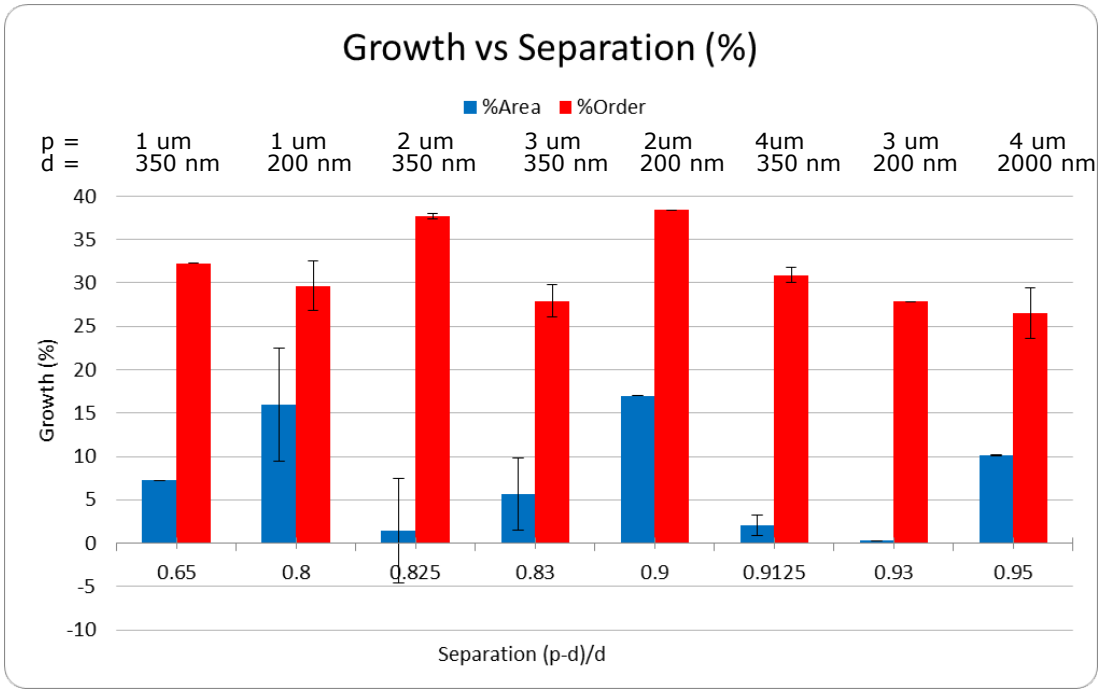

Figure 2.26: Table summary of growth as a function of the fractional separation, averaged across all patches of the same separation. The pitch and diameter for each separation are displayed above. Error bars indicate one standard error of the sample mean. The results show that high ordering occurs around 2 μm pitches which is a similar result when averaged over pitch alone.

A key observation is that all arrays showed non-negligible total growth. However, due to our small statistical sample size, the standard error is such that no single nanopillar geometry exhibited statistically significant advantage for total growth. However, particular geometries had significantly larger growth ordering when considering pitch or fractional separation. These geometries had 2 μm pitch and either 200 nm or 350 nm diameters. When sampling for pitch, these geometries achieved 38% ordering on average with a standard error of $\pm$0.8%. There was no significant dependence on pillar diameter. This is likely due to the small range of diameters that were sampled, which was chosen to approximately match the range of diameters where the nanopillars maximize optical collection efficiency [8, 74].

The analysis of the model also highlights the importance of having good contact between the neuron and the nanopillar in the region of the NV and that the location of this contact influences the electric field at the NV center. Previous neuron growth studies show that neurons tend to grow towards the tip of a pillar and can form contact with either the top or side, with contact on the side being more common [35, 48]. Future growth studies should seek to confirm this in a diamond substrate. In our results, it was not possible to determine the vertical position of the neuron in relation to the pillars nor the level of contact between the neuron and the pillar.

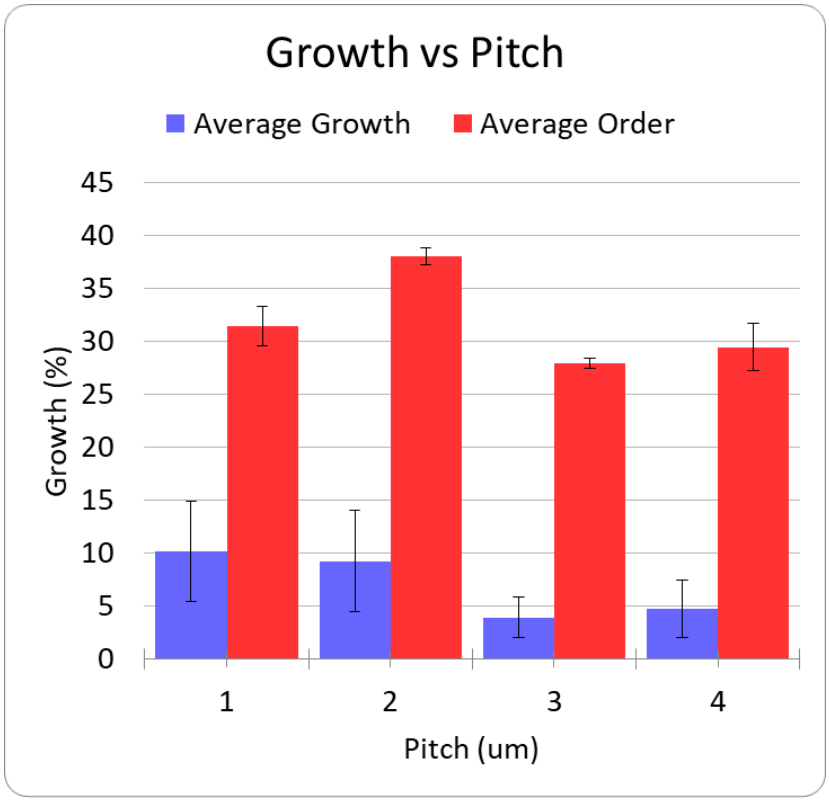

Figure 2.27: Table summary of growth as a function of pitch, averaged across all arrays of the same pitch. Error bars indicate one standard error of the sample mean. There is a general trend towards higher ordered growth for 2 μm pitch pillars.

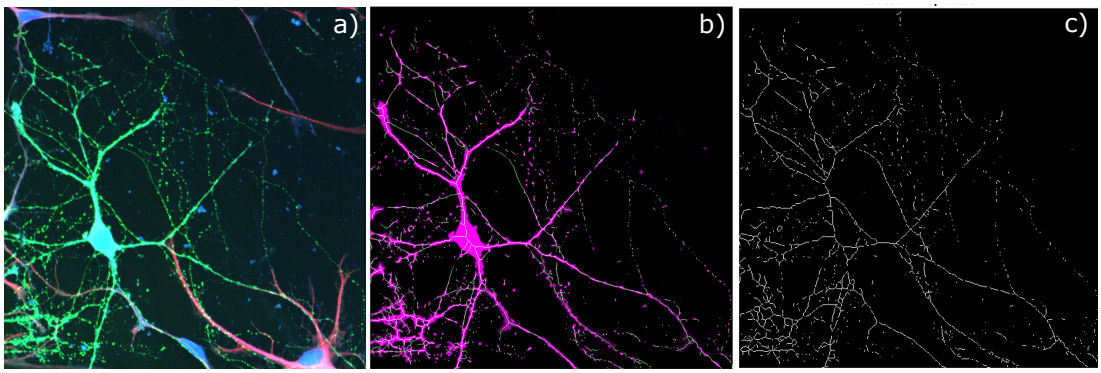

Figure 2.28: Example Images of the skeletonization process. a) The neuron confocal image, is processed to remove glia fluorescence and then 'skeletonized', b) where each neurite has a line drawn over it. The result is c) a list of lines which can be integrated to quantify neuron lengths

Super-resolution confocal microscopy or SEM studies should be performed in future to examine the precise vertical position of the neurons. One proposed means of

improving neuron to substrate contact is to utilise a peptide coating that has been demonstrated to promote close contact between neurons and a growth substrate. These coatings, known as "engulfment promoting peptides" (EPPs), come in a variety of forms such as poly-L-lysine (PLL), poly-D-lysine, extracellular matrix (ECM) gel and fibro-nectin [43, 44]. They have been shown to create to closer adhesion of cells than that of traditional enzyme substrates such as laminin and ornithin, which were used in this growth study experiment. The effectiveness of these coatings can be quantitatively assessed using TEM, in addition to this, TEM could also prove useful in determining the thickness and porosity of the protein coating used to promote neuron adhesion to the substrate. In this study, the coating was assumed to be dense enough such that ions couldn't penetrate the coating and thin enough that its effect on the propagating field from the neuron was negligible, however these assumptions weren't proven in any way and should be proven experimentally in order to be accurately factored into future simulations.

Finally, it is worth mentioning that whilst this work demonstrated a theoretical capacity to measure neuron signals, improving NV sensitivity to these signals is still worthwhile. Improving the range of signals that can be measured along with improving the simplicity of the measurement process with high sensitivity can make a future device easier to use in biological research labs. In chapters 3, 4, 5 and 6 different approaches to improved NV sensitivity are considered and their applicability to NV based neurosensing is addressed.

Chapter 3

Electrode based cryogenic SCC

The key result of the neurosensing project is that the NV has the capacity to sense the electric field of neuron signals with high sensitivity and resolution in particular conditions. However, improving NV sensitivity will always make the sensing protocol more effective and robust. For example, even if the NV can already sense the smallest signal the neuron is producing, improving sensitivity might allow for faster readout times which improves temporal resolution. Alternatively, high sensitivity might allow for a change in the sensing array; if smaller pillars produce better growth metrics but reduce optical collection efficiency, then having a method of improving sensitivity might help cover for this shortfall whilst maintaining good neuron growth.

The key to NV sensitivity is in the ability to measure the NV electronic spin state as its energy level will be directly related to an external field. Accurate readout of the NV electronic spin state is also a key factor in quantum computation, in an NV quantum computer or network, NV nuclear spins are initialised and readout by measuring the associated electronic spin state. In this sense, it could be argued that the readout of a nuclear spin state in the NV is itself, a sensing protocol. So any method which improves electronic spin state readout has applications in both NV quantum sensing and computation.

One such method of improving readout is by using the spin-to-charge conversion (SCC) technique. To re-iterate from section 1.1, in typical ODMR, the electron spin resonance (ESR) is readout as a drop in fluorescence when the electron is in a particular spin state. This change in fluorescence is known as the optical spin contrast. The larger the contrast, the better the confidence in the spin readout which in turn improves NV performance in sensing and computation. In SCC readout, the spin state is mapped to the NV charge state, the NV charge state can be readout with much higher contrast and fidelity compared to conventional NV readout protocols [58]. Thus, with good spin initialisation and mapping to the charge state, the readout of the NV spin state improves because the charge state readout performs better.

In this chapter we introduce a new SCC technique with the application of an external electrode to the surface of the diamond over a near-surface NV center at cryogenic temperatures. The electrode discretises the diamond conduction band for spin-selective resonant photoionization. We use effective mass theory to calculate the discrete eigenenergies in this new system and use them to formulate a new spin-to-

charge protocol that involves resonant photoionization out the NV ground state into the diamond conduction band. The major sources of broadening are also addressed which guide the design of the experiment.

In section 3.1 the concept of photoionization in the NV is detailed in the context of established SCC protocols as well as the photoionization experiments introduced in chapters 3, 4 and 5. In section 3.2 the electrode for cryogenic SCC is introduced, including a brief introduction on how it is fabricated and a detailed explanation of how the electrode potential discretises the diamond conduction band for improved photoionization using effective mass theory. In section 3.2 the potential issues with the protocol are considered as various sources of linewidth broadening are considered along with their effect on the spin readout protocol. Finally, in section 3.4 the work is put together to outline the SCC protocol and experimental design, in this section the overall optical contrast and readout fidelity are also calculated. With this mechanism, we theorise an optical spin contrast that and an associated spin readout fidelity of 85%. This significant improvement can be applied to a number of cryogenic quantum technologies.

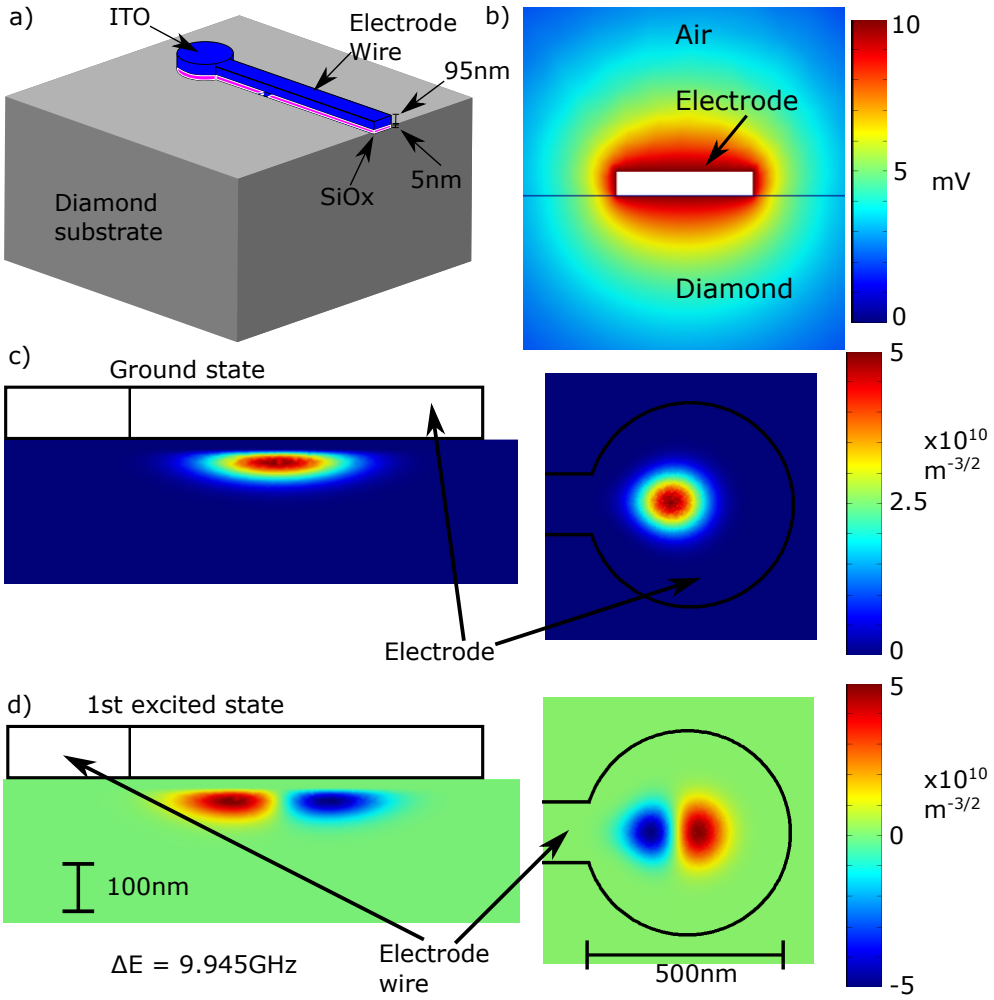

Figure 3.1: a) Image of the electrode setup. The grey diamond has an electrode fabricated onto it made of 5 nm SiOx and 95 nm ITO. The cylindrical section of the electrode sits over an NV center and a wire connects the electrode to a voltage source. b) Simulation of the potential well generated by the electrode. The white section is an electrode that sits on a diamond surface and carries a 10 mV potential. c) Plot of the simulated wavefunction for the ground state wavefunction viewed from the XZ (left) and XY plane (right image). d) Plot of the same simulation from c) but for the first excited state wavefunction. The ΔE term is the difference between the first and second eignenergies.

3.1 Photoionization in the NV

The key mechanism involved in both NV quantum sensing as well as computing is the ability to initialise and readout the NV electron spin state. The electronic structure that allows for spin selective readout is only available when the NV center is in the negatively charged state (NV^-), other charge states do not exhibit spin selective

properties. This presents a significant problem in NV physics as the center can ionize into the neutral NV^0 state under optical illumination where the electron is excited into the diamond conduction band. During this process, the spin information is lost and the NV center isn't usable until an electron repopulates the defect, converting it back into NV^-. The recombination process is most often achieved by optically exciting electrons into the NV center from the diamond valence band [7]. This ionization process limits NV charge state control and is an important issue in NV physics.

As mentioned in chapter 1, ODMR works by using lasers and microwaves to initialise the NV into a particular spin state and using the ISC to observe the NV spin state as a change in the NV fluorescence. In SCC, the principle is the same, however, once the NV is in a particular spin state, a powerful laser ionizes the defect, putting the electron in the diamond conduction band and the NV into the neutrally charges NV^0 state. One example of this is the room temperature SCC protocol from Jaskula et al. [58]. In this work, the NV electron is initialised into the $m_s = \pm 1$ in the same way as in conventional ODMR, however, with the $m_s = 0$ the electron is excited with a powerful red laser to ionise the electron and put the NV into the neutral charge state (figure 3.2). Thus the $m_s = \pm 1$ state is mapped to the negatively NV charge state and the $m_s = 0$ is mapped to the neutral NV charge state. The principle is that the NV charge state can be readout with much higher spin contrast and fidelity compared to the spin state in conventional ODMR, thus the contrast and fidelity improves.

The charge state can be measured optically with a laser maximally resonant to NV^-[58] or by measuring the photoelectric current induced by ionization [41, 109]. This technique has been shown to have a larger optical spin contrast compared to conventional intrinsic photo-luminescence cycling techniques [58, 109, 131], which in turn increases the readout fidelity of measuring a spin state. Whilst SCC methods improve contrast, the improvement is not very significant. For example, Jaskula et al. reported an SCC readout contrast of 36% compared to the conventional methods which have a readout contrast of 25% [58]. The primary reason for the limitation is that SCC protocols still require shelving the NV electron into the singlet state manifold via an inter-system crossing (ISC). The branching rate of the ISC is not 100% from the $m_s = \pm 1$ state nor is it 0% from the $m_s = 0$ state [37], this lowers the spin-selectivity and increases the probability of a false readout. Current methods also do not alter the probability of photoionization itself, the rate of photoionization is set by the intrinsic nature of the NV center in diamond. Being able to read out an electron spin state consistently without introducing noise from erroneous photoionization is essential in producing high fidelity spin measurements for quantum protocols.

We introduce a new mechanism of charge state control with the application of an external electrode to the surface of the diamond over a near-surface NV center. The electrode creates a potential well within the diamond which has the effect of spectrally confining the density of low lying conduction band states in the diamond. This discretized conduction band has a two-fold effect. Firstly, it increases the photoionization probability at frequencies resonant to a discrete transition whilst reducing the probability of photoionization at other frequencies. Secondly, the electrode creates energy level separation in the conduction band which is much larger than the

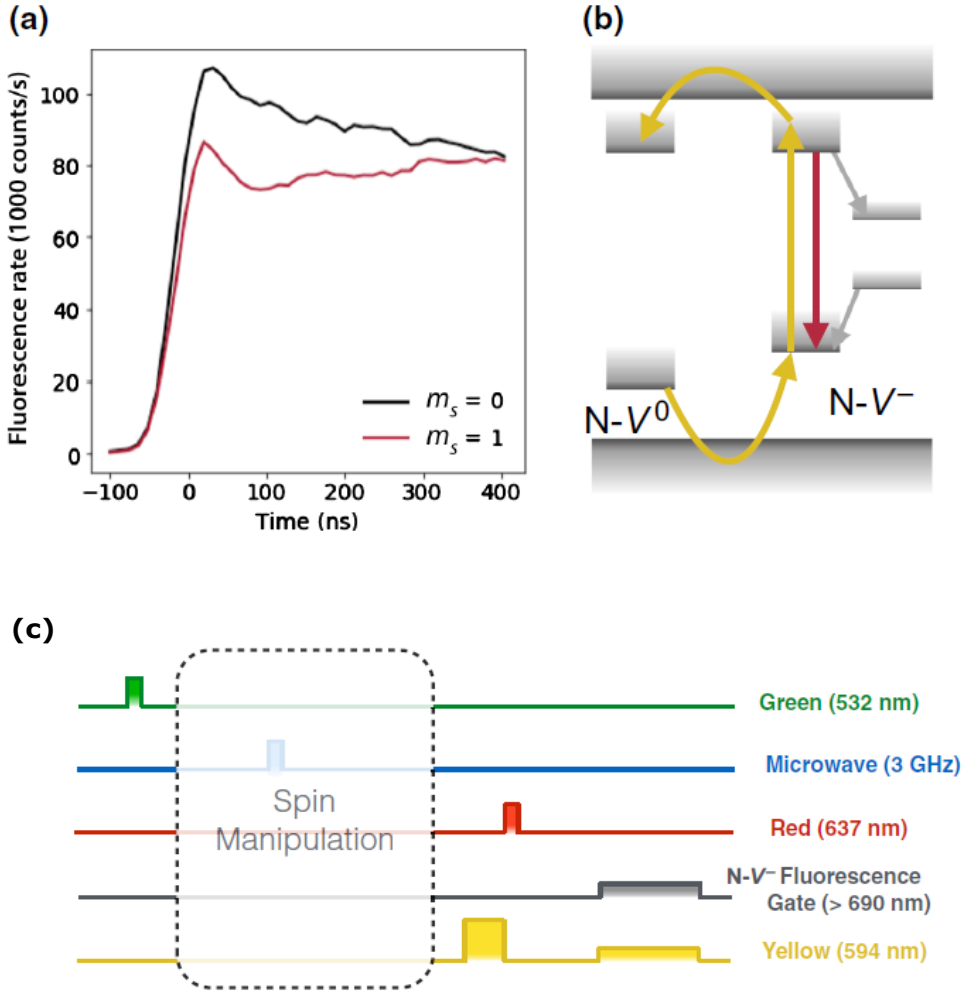

Figure 3.2: Image of the SCC protocol taken from Jaskula et al. [58]. a) An example of the fluorescence from a spin dependent charge state readout, the change in fluorescence for each spin state allows for spin selective readout. b) A simple model of the SCC protocol, the yellow lines indicate the excitation and ionization as a two-photon process. When the electron is in the singlet states via the grey ISC, it is shielded from the ionization pulses, allowing for spin selective ionization. c) The laser and MW pulse sequence for the SCC protocol, the green laser initialises the NV into the $m_s = 0$ state then the yellow laser excites and the red laser ionizes. A further yellow laser pulse reads the charge state of the NV.

separation of levels in the NV ground state triplet. These two factors allow for an SCC protocol where the NV electron is resonantly ionized out of the ground state triplet into a discrete conduction band state with a higher probability compared to conventional photoionization. The wide separation of the conduction band states means that the individual triplet transitions can be addressed. These factors create a

highly selective spin to charge protocol with very high optical spin contrast. The technique promises to vastly improve the fidelity of spin readout which has applications for NV based quantum sensing, communications and computation. The design also creates a discrete three-level system for stimulated Raman adiabatic passage (STIRAP) experiments [83]. The key to this process is ensuring that the spectral lines are narrow enough to be resolved. To achieve this the major sources of broadening need to be addressed.

3.2 Electrode application and effective mass theory

In our design, the cylindrical electrode is placed over an NV with a thin wire connecting to a voltage source. The electrode and wire have a thin, insulating silicon oxide (SiOx) layer to prevent charges from moving from the diamond into the electrode. On top of the SiOx is a transparent indium-tin-oxide (ITO) conductive layer which carries the electric potential and allows for optical illumination through the electrode. The dimensions of the electrode were chosen to maximise the energy splitting in the diamond conduction band (see figure 3.1). Smaller confinement volumes (from smaller electrodes) have larger energy splitting, making them easier to individually address. The limiting factor on size comes from the resolution of the nanofabrication process itself as the wire width must be smaller than the electrode to prevent wavefunctions occupying the space under the wire.

The electrode was designed to carry a potential that can create the confining well within the diamond substrate around the NV. Numerical calculations revealed that smaller confining regions produced larger conduction band splitting which is necessary for the high contrast spin-to-charge readout mechanism. The length and width of the electrode control the length and width of the potential well whereas the depth of the well is largely controlled by the magnitude of the potential at the electrode rather than its physical height. Stronger electrode potentials reduce the depth of the confining wavefunction, requiring the placement of NVs closer to the diamond surface in order to be affected by the electron confinement. This is undesirable as NVs close to the diamond surface exhibit charge instability[22]. The potential chosen was designed to create a wavefunction whose center is at the position of the NV which is approximately 50 nm from the diamond surface. This choice was made to maximise the eigenenergy splitting whilst maintaining NV stability.

The SiOx was applied to create an insulating layer between the electrode and the diamond surface and the ITO was chosen for its capacity to carry a potential as well as its optical transparency so laser illumination can occur over the diamond surface. The electrode is fabricated using a sputtering process. The diamond is cleaned using a three-acid boil (sulfuric, nitric and perchloric acid), after which approximately 100nm of polymethyl methacrylate (PMMA) is spin-coated onto the diamond to be used as a resist layer. The electrode shape is then etched into the PMMA along with the electrode wire using electron beam lithography (EBL). The resist is then exposed to methyl iso-butyl ketone (MIBK) for approximately 1 minute to etch away the PMMA

exposed by the EBL beam and is further exposed using a low dose oxygen plasma etch in a barrel etcher. This creates the hole in the resist layer which can be layered with 5 nm of silicon oxide (SiOx) and 95nm of indium-tin-oxide (ITO) using sputter deposition. The remaining PMMA layer is removed using a lift-off technique with acetone where only the SiOx and ITO layers remain. The wire connects to the end of the diamond which can be layered coarsely with a conductive material (for example silver paste) that can be more easily connected to a power supply for generating a potential using a wire bonding process.

In order to calculate the conduction band wavefunctions and eigenenergies which are confined by the electrode potential we apply effective mass theory. We begin by solving the Schrodinger equation in the absence of an external potential:

$$\left(\frac{-\hbar^2}{2}\vec{\nabla}\cdot\overleftrightarrow{\frac{1}{m}}\cdot\vec{\nabla}+V_c(\vec{k})\right)|F_n(\vec{r})\rangle = E_n^c\,|F_n(\vec{r})\rangle\,, \tag{3.1}$$

where E_n^c is the eigenenergy of the crystal system for a given energy level n, $V_c(\vec{k})$ is the crystal potential, m is the effective mass tensor of the electron and F_n is an envelope function which is related to the electron wavefunction by the following:

$$\psi_n = F_n(\vec{r})u_{\vec{k}}(\vec{r})e^{i\vec{k}\cdot\vec{r}}, \tag{3.2}$$

where $u_{\vec{k}}(\vec{r})$ is the Bloch function for the state of the conduction band minimum in the bulk diamond unit cell and $\vec{k}$ is its associated wavevector. The exponent describes the phase difference when going between unit cells and we are considering n conduction band minima as we expect new minima in different vector directions.

These equations are applicable due to three key assumptions that we apply in effective mass theory. The first is that for photoionization we only need to consider states that are energetically close to the conduction band minimum (CBM). This is due to the fact that we are only ionizing from the NV to the lowest lying states in the conduction band. This assumption allows us to approximate the electron energy as a free electron with an effective mass in a confining potential. The second assumption is that the envelope function varies on a distance much greater than the Bloch function, allowing it to be considered constant when calculating values over the Bloch function space. Finally, we assume that the electrode potential isn't strong enough or varying enough on the scale of the unit cell such that the Bloch function depends on the potential.

Expanding out equation 3.1 to include the Bloch function gives:

$$\left(T(\vec{r})+V_c(\vec{k})\right)F_n(\vec{r})\mu_{\vec{k}}(\vec{r})e^{i\vec{k}_n\cdot\vec{r}} = E_n^c F_n(\vec{r})\mu_{\vec{k}}(\vec{r})e^{i\vec{k}_n\cdot\vec{r}}, \tag{3.3}$$

where $T(\vec{r}) = \frac{-\hbar^2}{2}\vec{\nabla}\cdot\overleftrightarrow{\frac{1}{m}}\cdot\vec{\nabla}$, is the kinetic energy for a free electron with an effective mass m. For simplicity the Bloch function can be simplified to: $\mu_{\vec{k}}(\vec{r})e^{i\vec{k}_n\cdot\vec{r}} = |\phi(\vec{r})\rangle$. Expanding equation 3.3 as a product rule whilst multiplying both sides of the

equation by the complex conjugate $\langle\phi(\vec{r})|$ gives the following:

$$\begin{aligned}\langle\phi(\vec{r})|\phi(\vec{r})\rangle\, T(\vec{r})F_n(\vec{r}) + F_n(\vec{r})\,\langle\phi|\, T(\vec{r})\,|\phi(\vec{r})\rangle + \\ F_n(\vec{r})\,\langle\phi|\, V_c(\vec{k})\,|\phi(\vec{r})\rangle = E_n^c F_n(\vec{r})\,\langle\phi|\phi\rangle\,,\end{aligned} \tag{3.4}$$

note that the envelope function is not acting on the eigenstates. The envelope function varies on distances much larger than Bloch function between diamond unit cells. Thus when considering small length scales of the diamond unit cell, the approximation being made is that F_n is effectively constant and can be moved out of the inner product. Taking the inner product:

$$T(\vec{r})F_n(\vec{r}) + E_b F(\vec{r}) = E_n^c F_n(\vec{r}), \tag{3.5}$$

where E_b is the energy of the Bloch function for the conduction band minimum. The other key approximation being made in the above calculation is that an electrode confining potential isn't strong enough or varying enough on the scale of the unit cell such that the Bloch function depends on the potential. This means that the electrode potential can be added in a new Schrodinger equation as the Bloch function energy is independent of the electrode potential. Adding in the electrode potential gives the following equation:

$$\big(T(\vec{r}) + V(\vec{r})\big)F_n(\vec{r}) = E_n F_n(\vec{r}), \tag{3.6}$$

where $E_n = E_n^c - E_b$ so that E_n becomes the energy of the total wavefunction relative to the Bloch function.

Three separate solutions from equation 3.1 were obtained to account for the three effective masses in the separate Cartesian directions along the diamond. In each solution 6 eigenenergies/wavefunctions were obtained and added together to give a total of 18 conduction band energy levels. The eigenenergies can then be used to calculate the transition rate from the NV to a particular conduction band state by using Fermi's golden rule:

$$\Lambda_n(E) = \frac{2\pi}{\hbar}\sum_n |\mu_b C(E)\sqrt{A_e}F_n(r)|_{r=NV}\mathcal{E}(E)|^2\mathcal{L}(E-E_n), \tag{3.7}$$

where $\mathcal{L}(E-E_n)$ is a Lorentzian function whose peaks are at the energy levels of the conduction band states E_n, μ_b is the transition dipole moment in bulk diamond, $\mathcal{E}(E)$ is the electric field of the interrogating laser and $C(E)$ is the dimensionless Franck-Condon factor which describes the vibrational overlap of states under a Born-Oppenheimer approximation. The electron confinement envelope function is represented by $F_n(r)|_{r=NV}$ which is defined at the position of the NV and is normalised to the volume of the diamond with the constant A_e using the following equation:

$$\frac{A_e}{V_c}\int_V F_n^* F_n dV = 1, \tag{3.8}$$

where V_c is the volume of the diamond unit cell. Equation 3.8 is solved for A_e by using the results of equation 3.6 and numerically integrating the envelope function over the diamond volume directly.

For comparison purposes, it is important to derive the transition rates from the NV to both the diamond conduction band in bulk as well as to the conduction band in the confining electrode potential. To do this, the first step is to calculate the density of states for both cases. With the electrode, the density of states is simply the Lorentzian function with peaks at the given energies calculated from equation 3.1:

$$\rho_e(E) = \sum_n \mathcal{L}(E - E_n), \tag{3.9}$$

where the Lorentzian function can be explicitly written as:

$$\mathcal{L}(E - E_n) = \frac{\Gamma/\pi}{(E - E_n)^2 + \Gamma^2}, \tag{3.10}$$

and Γ is the total associated linewidth. In bulk diamond it is easier to express the density of states when the energy is in terms of a wavevector, $\vec{k}$:

$$\rho_b(E) = \sum_v \sum_{\vec{k}} \delta(E - E_{\vec{k}}), \tag{3.11}$$

where v denotes a sum over the valleys in the Bloch function. The sum of states can then be re-expressed as an integral of states over a sphere:

$$\rho_b(E) = \frac{4\pi V}{(2\pi)^3} \int_0^\infty \vec{k}^2 \delta(E - E_{\vec{k}}) d\vec{k}, \tag{3.12}$$

by taking an effective mass argument, the energy can be expressed as the energy for a free particle with an effective mass, m, such that $E_{\vec{k}} = \frac{\hbar^2}{2m}\vec{k}^2$. Rearranging the equation in terms of $\vec{k}$ and substituting it into the integral gives:

$$\rho_b(E) = \frac{V}{(2\pi)^2} \int_0^\infty \frac{2mE_{\vec{k}}}{\hbar^2} \sqrt{\frac{2mE_{\vec{k}}}{\hbar^2}} \frac{1}{2E_{\vec{k}}} \delta(E - E_{\vec{k}}) dE_{\vec{k}}, \tag{3.13}$$

which when solved gives the following:

$$\rho_b(E) = \frac{V}{2(2\pi)^2} \left(\frac{2m}{\hbar^2}\right)^{3/2} \sqrt{E}, \tag{3.14}$$

note the square root dependence on the energy, which carries into the transition rate calculation. The transition rate in the bulk diamond is then calculated using Fermi's golden rule:

$$\Lambda_b = \frac{2\pi}{\hbar} \left| \mu_b C(E) \sqrt{A_b} F_b(r)|_{r=NV} \mathcal{E}(E) \right|^2 \sum_{\vec{k}} \delta(E - E_{\vec{k}}), \tag{3.15}$$

where μ_b is the transition dipole moment in bulk diamond which is constant for all wavevectors close to the conduction band minimum and the $\sum_{\vec{k}} \delta(E - E_{\vec{k}})$ term

is the density of states in bulk diamond. The normalization constant is found by integrating the envelope function over the bulk diamond volume:

$$\frac{A_b}{V_c}\int_V F_b^* F_b dV = 1, \tag{3.16}$$

where V_c is the volume of the diamond unit cell. In bulk diamond, the envelope function encompasses all block wavefunctions so the probability of an electron existing in the envelope function will be unity: $F_b^* F_b = 1$, therefore: $A_b = V_c/V$. Substituting in the normalisation and the density of states gives the following:

$$\Lambda_b = \frac{1}{4\pi\hbar}\left(\frac{2m}{\hbar^2}\right)^{3/2}\sqrt{E}\left|\mu_b C(E)\sqrt{V_c}\mathcal{E}(E)\right|^2, \tag{3.17}$$

the transition rate in the electrode confined diamond is largely the same but with a different density of states and a different normalization:

$$\Lambda_e = \frac{2\pi}{\hbar}\sum_n \mathcal{L}(E-E_n)\left|\mu_n \mathcal{E}(E)\right|^2, \tag{3.18}$$

where the transition dipole moment in the electrode can be expressed in terms of the bulk dipole moment mediated by the envelope wavefunction for the confined electron: $\mu_n = \mu_b C(E)\sqrt{A_e}F_e(r)|_{r-NV}$:

$$\Lambda_e = \frac{2\pi}{\hbar}\sum_n \mathcal{L}(E-E_n)\left|\mu_b C(E)\sqrt{A_e}F_e(r)|_{r=NV}\mathcal{E}(E)\right|^2, \tag{3.19}$$

the normalization constant A_e found using equation 3.8.

The two transition rates calculated cannot be directly plotted as the dipole moment, laser electric field and Franck-Condon factor, whilst being common to both equations, are unknown factors. However, the important factor isn't the photoionization rates but the relative change in photoionization cross section from the bulk diamond to the diamond in the potential well. To understand this the transition rates in equations 3.17 and 3.19 are divided by the common factors mentioned and multiplied by: $1/\left(0.5n\sqrt{\frac{\epsilon_0\mu_0}{\hbar\omega}}\right)$ where n is the refractive index of diamond and ω is the wavelength of the photoionization laser. These extra factors places the dimensions of equations 3.17 and 3.19 into a photoionization cross section multiplied by the electric charge squared, divided by the dipole moment squared, which is a dimensionless quantity. With these changes, the transition rates can be plotted together, and the relative cross-sections can be compared.

Figure 3.3 shows the transition cross section for photoionization in a confined electrode (orange, equation 3.19) and bulk diamond (blue, equation 3.17) for the first 12 energy levels. Whilst the bulk diamond transition rate is a smooth function proportional to $\sqrt{E}$, the transition rate in the confined system shows clear Lorentzian peaks at each eigenenergy calculated using equation 3.1. When the electron is confined, the probability of resonant ionization to the first conduction band level is 2.4 times higher compared to bulk diamond, increasing charge state control.

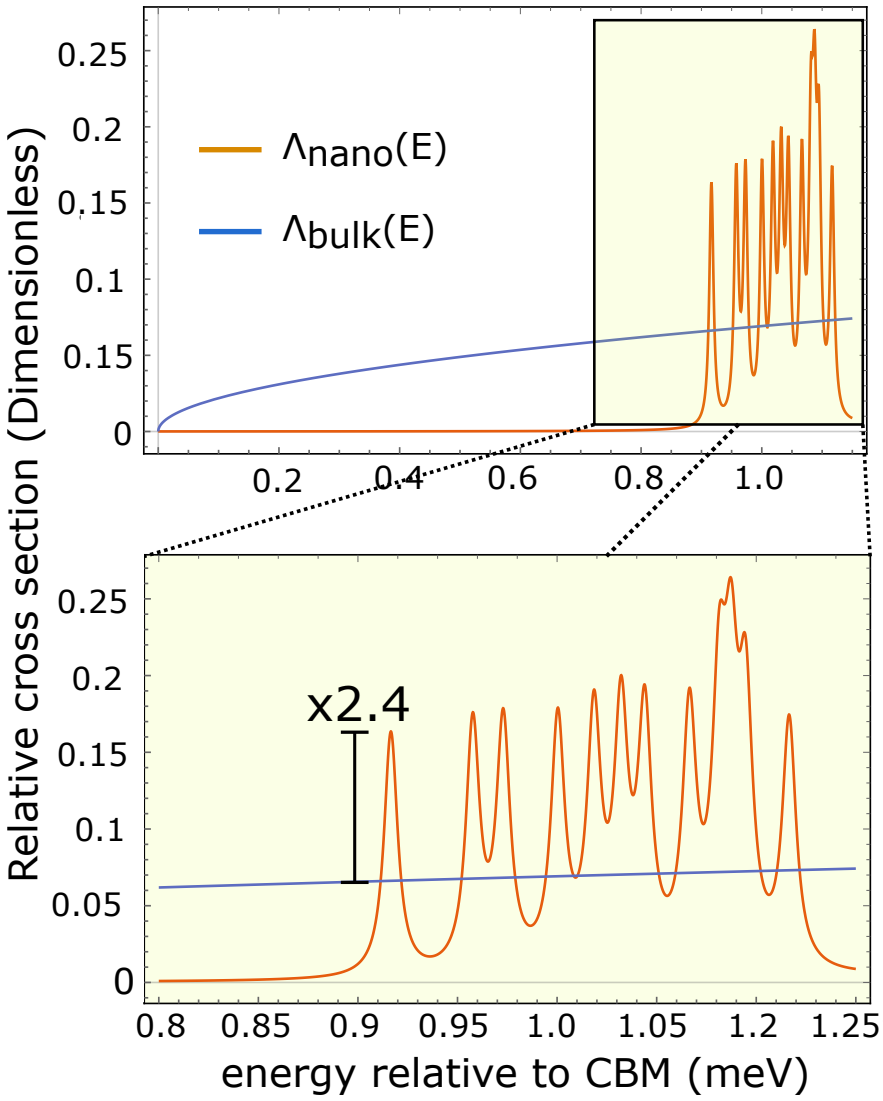

Figure 3.3: Plot of the transition cross section in both bulk diamond (blue) and in the confined region created by the electrode (orange). The cross section is proportional to $\sqrt{E}$ in bulk diamond whereas the confined electron has Lorentzian peaks at each eigenenergy calculated using equation 3.1. The linewidth: $\phi = 1$ GHz, is chosen based on the error modelling and shows how thin lines are easily distinguishable. Taking the ratio of the first peak with the equivalent bulk value gives a transition rate that is 2.4 times more likely for a confined electron.

Distinguishing between adjacent transitions is a key aspect of the SCC protocol. Broadening of the transition lines will increase the probability of an unwanted transition and will prevent accurate readout of the NV spin state. From figure 3.3, the transition linewidths are approximated to be about 1 GHz and the transitions are qualitatively distinguishable, however this needs to be considered in more detail. The three main sources of linewidth broadening are identified as: fluctuations in the

confining potential from the electrode, fluctuations in the confining potential due to surface charge traps and fluctuations in the conduction band energy levels from electron-phonon broadening. Analysing these major sources of broadening helps us understand what is possible in the SCC protocol, and what needs to be changed to fully realise this technology.

3.3 Linewidth Broadening

In order to create the potential well in the diamond, an electric potential must be applied to the electrode. If however, this potential is unstable, then it will cause a fluctuating shift in the discretized diamond conduction band energy levels which will present as linewidth broadening. To model this effect, the simulation can be performed with a 10 mV electrode potential and it can also be performed with an offset based on the expected noise in the signal generator: ± 0.001 mV. The change in the potential at the NV (50 nm from the surface of the diamond) can be measured and the change first conduction band eigenenergy levels can also be measured.

Figure 3.4 shows the electric potential as a function of distance from the diamond surface for all three electrode potential values. The figure also has the first conduction band eigenenergy levels labelled for each electrode potential. By taking these energy levels and plotting them the slope of the values can be calculated to be ≈ 15 GHz/mV which is shown in figure 3.5. The change in the transition energy (linewidth broadening) will then be the change in the conduction band energy as a function of potential ($\frac{\partial E_n}{\partial V} \approx 15$ GHz/mV), minus the change in the NV energy as a function of potential ($\frac{\partial E_{NV}}{\partial V}$), multiplied by the RMS uncertainty of the electrode:

$$\Gamma_{electrode} = \sigma_V \Big(\frac{\partial E_c}{\partial V} - \frac{1}{h} \frac{\partial E_{NV}}{\partial V} \Big), \tag{3.20}$$

where σ_V is the RMS uncertainty of the electrode which was assumed to be ± 0.001 mV and the change in NV energy with potential is linear ($\frac{\partial e_{NV}}{\partial V} = -eV$) which can be calculated and converted to -242 GHz/mV. Solving equation 3.20 gives the linewidth broadening mentioned in the main paper of 0.257 GHz broadening.

Electron-phonon (e-p) scattering is the process by which the energy of an electron is altered slightly by a phonon interaction. This will alter the transition energy of photoionization as the conduction band electron states are altered by phonon interactions, causing linewidth broadening. In bulk diamond, this can be an issue even at low temperatures (4 K). We can model this broadening with Fermi's golden rule:

$$\begin{gathered} \Gamma_{ep} = \alpha \sum_n \int |\langle n|\psi_k(\vec{r})|1\rangle|^2 \omega_k^3 n_B(\omega_k) \delta(\omega_n - \omega_k) d^3k \\ \alpha = \frac{\Theta^2}{2(2\pi)^2 \hbar \rho c_l^4}, \end{gathered} \tag{3.21}$$

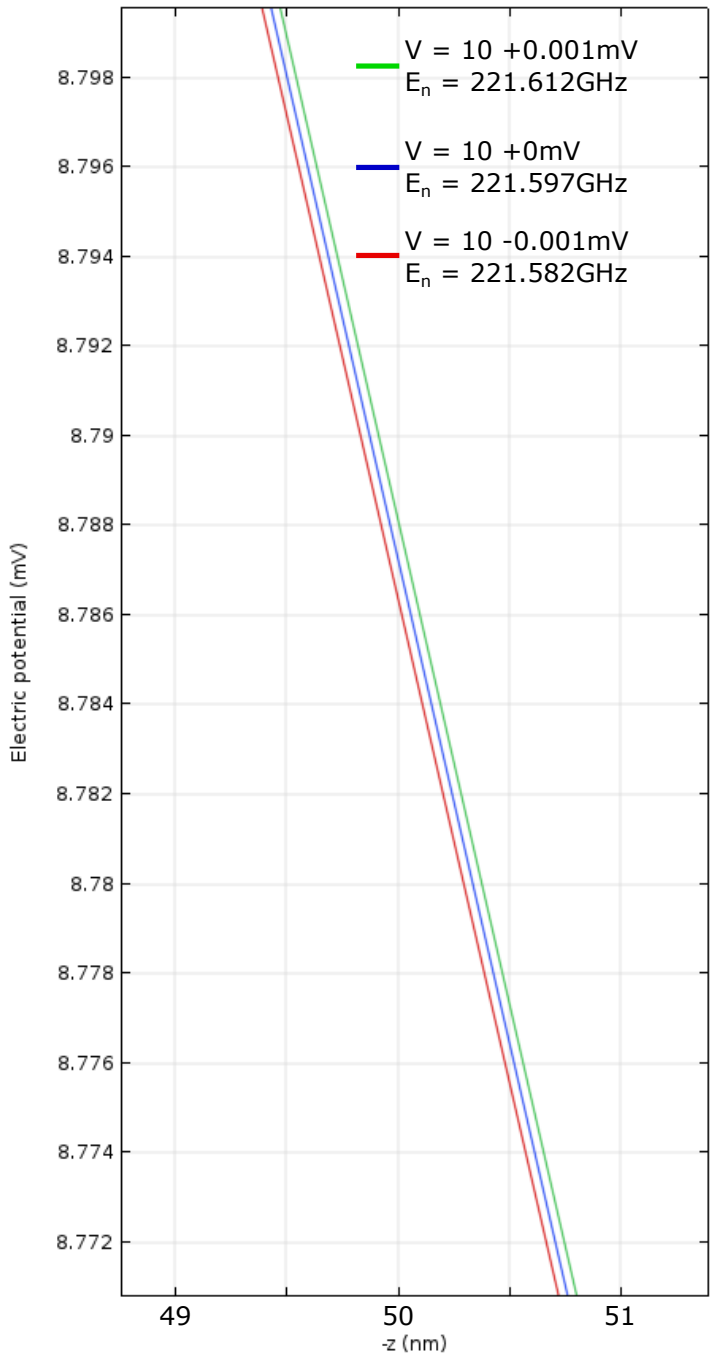

Figure 3.4: Plots of the electric potential as a function of the distance from the surface of the diamond where it meets the electrode. The 50 nm mark is where the NV is placed. The three curves designate the solution for the 10 mV potential as well as its offsets of ± 0.001 mV. Additionally, the plot legends show the first conduction band eigenenergy levels for each potential solution. Overall the change generated from the potential noise is very small.

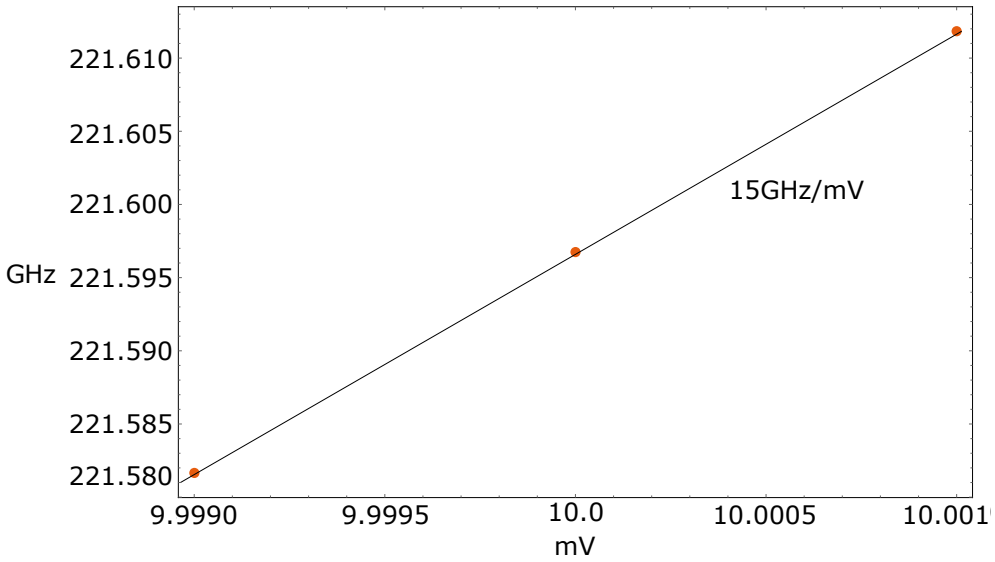

Figure 3.5: Plots of the first conduction band eigenenergy levels as a function of electrode potential. The change is roughly linear so a line can be drawn to connect the three data points and a slope can be calculated to be ≈ 15 GHz/mV which is labelled on the plot.

where Θ is the acoustic deformation potential, ρ is the density of diamond and c_l is the longitudinal speed of sound in diamond. The equation is a sum of all the interactions of the phonon modes $\psi_k(\vec{r})$ with the discretised energy levels of the conduction band minimum from 1 to n, integrated over the phonon k-space. The phonons have a wavelength ω_k and a temperature dependent distribution given by a Bose-Einstein distribution n_B [83]. The phonon modes can be calculated by understanding that e-p scattering only occurs with dilational modes as they are the only modes with a non-zero divergence. Deriving an expression for the dilational modes as:

$$\vec{u}(r) = \vec{\nabla}\psi(r), \tag{3.22}$$

the scalar potential is satisfied by the wave equation:

$$-\nabla^2\psi(r) = c_l^{-2}\omega^2\psi(r), \tag{3.23}$$

which has the following solution:

$$\psi(r) = A_k e^{i\vec{k}\cdot\vec{r}}. \tag{3.24}$$

In equation 3.24 the normalisation constant A_k can be found by integrating all the

dilational modes over the volume of the diamond:

$$\begin{aligned} V &= \int_V |\vec{u}|^2 d^3r \\ &= \int_V |\vec{\nabla}\psi|^2 d^3r \\ &= \int_V A_k^2 k^2 d^3r \\ A_k &= k^{-1} = c_l/\omega. \end{aligned} \tag{3.25}$$

To help solve equation 3.21 its easier to assume that confining potential is rectangular in shape rather than the Gaussian-like shapes they actually are as it allows for integrals to be solved in Cartesian coordinates whose solutions are similar to solutions to a finite square well:

$$G_n(k) = |\langle n|\psi_k(\vec{r})|1\rangle|^2 = \left| \int_0^{L_x}\int_0^{L_y}\int_0^{L_z} F_n \frac{c_l}{\omega_k} e^{i\vec{k}\vec{r}} F_1 \right|^2, \tag{3.26}$$

where L is the length of the confining potential in a Cartesian direction and F_n is the envelope wavefunction for an electron in a Cartesian box. This assumption shouldn't change the broadening by much as long the volumes of the approximate and actual confining potentials are roughly the same. A change in the potential shape will change the subsequent confining wavefunctions and eigenenergies, however, if the volume and potential well lengths are roughly the same, then the eigenenergies should also be roughly the same, so using the previously calculated eigenenergies should be valid. Substituting equation 3.26 into equation 3.21 and writing out the integral over k gives:

$$\begin{aligned} \Gamma_{ep} = \alpha \sum_n \int_0^\infty \int_0^\pi \int_0^{2\pi} k^2 \sin(\theta_k) \\ G_n(k)\omega_k^3 \eta_B(\omega_k)\delta(\omega_n - \omega_k) dk d\theta_k d\phi_k, \end{aligned} \tag{3.27}$$

substituting $k = \omega/c_l$ and simplifying gives:

$$\begin{aligned} \Gamma_{ep} = \frac{\alpha}{c_l^3} \sum_n \int_0^\infty \omega^5 \eta_B(\omega)\delta(\omega_n - \omega) G_n(\frac{\omega^2}{c_l^2}) \\ \int_0^\pi \int_0^{2\pi} \sin(\theta_k) d\omega^2 d\theta_k d\phi_k, \end{aligned} \tag{3.28}$$

which when solving the integral over the Dirac delta function gives:

$$\Gamma_{ep} = \frac{\alpha}{c_l^3} \sum_n \omega_n^5 \eta_B(\omega) G_n\left(\frac{\omega^2}{c_l^2}\right) \int_0^{\pi} \int_0^{2\pi} \sin(\theta_k) d\omega^2 d\theta_k d\phi_k. \tag{3.29}$$

The solution to equation 3.26 in Cartesian coordinates is effectively the solution to a three dimensional finite square well which can be analytically calculated to be:

$$\begin{aligned} G_n(k) = \frac{8}{L_x L_y L_z} \frac{c_l}{\omega} \\ \int_0^{L_x} \sin\left(\frac{n_x \pi}{L_x} x\right) e^{ik_x x} \sin\left(\frac{\pi}{L_x}\right) dx \\ \int_0^{L_y} \sin\left(\frac{n_y \pi}{L_y} y\right) e^{ik_y y} \sin\left(\frac{\pi}{L_y}\right) dy \\ \int_0^{L_z} \sin\left(\frac{n_z \pi}{L_z} z\right) e^{ik_z z} \sin\left(\frac{\pi}{L_z}\right) dz, \end{aligned} \tag{3.30}$$

where each integral in a Cartesian direction can be calculated to be:

$$\begin{aligned} \int_0^{L_m} \sin\left(\frac{n_m \pi}{L_m} m\right) e^{ik_m m} \sin\left(\frac{\pi}{L_m}\right) dm = \\ \frac{2i(1 + (-1)^{n_m} e^{ik_m L_m}) k_m L_m^2 n_m \pi^2}{k_m^4 L_m^4 - 2k_m^2 L_m^2 (1 + n_m^2)\pi^2 + (-1 + n_m^2)^2 \pi^4}. \end{aligned} \tag{3.31}$$

Using the solutions from equations 3.30 and 3.31 they can be substituted into equation 3.29 and solved for a given confining volume across the number of energy levels solved in the system (18). It is important to test the solution across a range of energy levels to observe when the sum of broadening values converges, 18 levels are sufficient for convergence in this case. This process was then performed multiple times over many confining potential sizes in order to understand how the broadening changes with volume.

In Figure 3.6 the broadening is calculated for a variety of confining potential volumes. The x and y coordinates are changed together for the length of the confining potential and the z coordinate is changed separately for the depth of the potential well. For the purposes of this work, the broadening for a potential well that is 250 nm in length and 100 nm in depth is required. Reading off of figure 3.6 a confining potential of roughly this size creates linewidth broadening which does not exceed 0.5 GHz.

Imperfections in the diamond structure as well as its surface termination allow for surface charge traps that can hold electrons [104]. Surface charge traps can be occupied briefly by electrons both from the NV as well as from defects in the bulk diamond. Charges from these surface traps can then ionize back into the bulk diamond or can

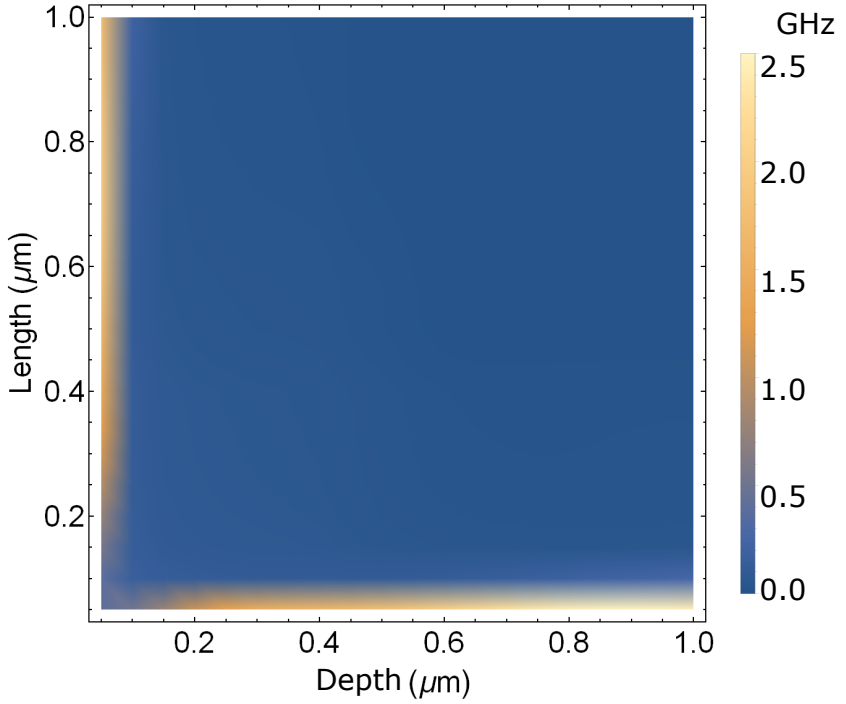

Figure 3.6: Plot of the e-p broadening in Hz as a function of confining potential volume. The length of the potential well is for both the x and y coordinate whereas the depth is from the z-coordinate only.

hop from trap to adjacent trap. The result is a continuous fluctuation of a local electric field from the constant change in the position of the charges relative to NV. This arises as noise which can affect both the NV and conduction band energy. Calculating this noise is more difficult compared to the other sources of broadening as the density of the charge traps on the diamond surface and the rate of their motion from trap to trap isn't well known. This concept is actually considered in more detail in chapter 7. To calculate the broadening we assume that the surface charge traps are uniformly distributed on the diamond and that the electrons occupying the traps can only move from trap to adjacent trap. In this picture, the charge motion acts like a two level fluctuator which can be modelled using Redfield theory [107] where the linewidth is given by:

$$\Gamma_{sc} = \frac{2\pi}{\hbar^2}\overline{|\delta E|^2}S(0), \tag{3.32}$$

where $S(\omega)$ is the noise spectrum which in a two level system is assumed to be Lorentzian and $\overline{|\delta E|^2}$ is the variance of the change in energy which is given by:

$$\overline{|\delta E|^2} = \eta e^2 \int_\Omega |\langle F_0| V(\vec{r},\vec{q}) |F_0\rangle - V(\vec{r}_{NV},\vec{q})|^2 d^2q, \tag{3.33}$$

where η is the surface density of acceptors (diamond surface trap density) and

$V(\vec{r},\vec{q})$ is the potential generated by an electron at position $\vec{q}$ on the surface of the diamond away from the NV which is at position $\vec{r}$. Equation 3.33 describes the energy variance as the change in the conduction band energy (first term in the integral) minus the change in the NV energy (second term in the integral). If the fluctuations are assumed to have a zero mean, then the rate of charge motion will follow Boltzmann statistics:

$$\gamma = \gamma_0 e^{-E_t/k_b T}, \tag{3.34}$$

where E_t is the electron energy and the noise spectrum can be described as:

$$S(\omega) = \int_{-\infty}^{\infty} e^{-\gamma|\tau|} e^{-i\omega t} = \frac{\gamma/\pi}{\omega^2+\gamma^2}, \tag{3.35}$$

note how equation 3.35 describes the spectral noise with a Lorentzian line shape with a width given by the charge hopping rate γ.

To get an understanding of the process and to solve equation 3.33 for the linewidth three separate regimes are considered. The first regime is when the Fermi level is equal to the trap energy level and the trap occupation is $\approx$ 50%, in this regime the electrons in the trap can hop to adjacent traps and we can model the system like a series of 2D dipoles where the dipoles can orient their direction as the electrons hop into adjacent traps in any direction. The second is when the Fermi level is below the trap energy and the trap occupation is less than 50%, in this regime the charges act like monopoles and can hop anywhere in the surface via other traps or through the diamond conduction band. In this regime the charges effectively appear and disappear in the traps as they have a larger freedom of movement compared to the dipole regime. The third regime is when the Fermi energy is above the trap energy level causing the traps to be mostly occupied. Charge hopping occurs in a similar mode to the monopole regime, but the effective trap density is considerably lower. This mechanism doesn't happen automatically, but it is something that can be engineered by reducing the trap density, or, adding an electron donor level in the diamond which preferentially donates electrons to the unoccupied traps.

The first regime is the dipole regime, in this approach, the potential term in equation 3.33 is modelled as a dipole charge:

$$V(r) = \frac{e\vec{p}\cdot(\vec{r}-\vec{q})}{4\pi\epsilon_d|\vec{r}-\vec{q}|^3}, \tag{3.36}$$

where $\vec{p}$ is the displacement vector between neighboring traps. The idea is that an electron can move from one trap to another, creating an electron/hole pair that is effectively a dipole. The electron motion to a trap is then modelled as the dipole moment flipping sign as the electron flips the direction of the dipole. The change in conduction band energy due to a single dipole is solved individually. This solution is then integrated over all possible charge traps (the diamond surface) to find out the

overall energy change. Beginning with the solution due to a single dipole:

$$\langle F_0|\, V(\vec{r},\vec{q})\,|F_0\rangle = \frac{e}{4\pi\epsilon_d}\int F_0^2(\vec{r})\frac{\vec{p}\cdot(\vec{r}-\vec{q})}{4\pi\epsilon_d|\vec{r}-\vec{q}|^3}d^3r, \tag{3.37}$$

in this instance, F_0 is modelled as a Gaussian. Mathematically this approach is actually equivalent to solving for the potential of an observer point far from a dipole charge distribution, however, the roles are reversed, F_0 acts like the charge distribution and the observer point is $\vec{q}$. In this formalism, the solution is obtained by using a multipole expansion. The key assumption in the expansion is that the observer point $\vec{q}$ is sufficiently far from the charge distribution F_0. This isn't entirely true for this system, so higher-order terms are added in the multipole expansion to make sure it is valid. Considering the charge distribution in terms of the electric displacement:

$$\vec{\nabla}\cdot\vec{D} = 0, \tag{3.38}$$

in equation 3.38, the solution is zero as the the charge density of a group of dipoles will be zero. Substituting in the displacement field with the electric field ($\vec{E}$) and polarization ($\vec{P}$) and rearranging gives:

$$\vec{\nabla}\cdot\epsilon_d\vec{E} = -\vec{\nabla}\cdot\vec{P}, \tag{3.39}$$

the polarization can be described in terms of the wavefunction size and the displacement vector between neighboring traps ($\vec{p}$). The electric field can also be described in terms of the electric potential, giving:

$$\epsilon_d\nabla^2 V = -\vec{\nabla}\cdot eF_0^2\vec{p}, \tag{3.40}$$

electrons on the diamond surface can only form dipoles on the 2D surface plane:

$$\nabla^2 V = \frac{-e}{\epsilon_d}\Big(p_x\frac{\partial}{\partial x}F_0^2 + p_y\frac{\partial}{\partial y}F_0^2\Big). \tag{3.41}$$

Using Maxwell's law, the electric potential can be re-written in terms of the effective charge density: $\nabla^2 V = \rho_{eff}/\epsilon_d$:

$$\rho_{eff} = -e\Big(p_x\frac{\partial}{\partial x}F_0^2 + p_y\frac{\partial}{\partial y}F_0^2\Big), \tag{3.42}$$

with an effective charge, an equation 3.37 be rewritten for the change in conduction

band energy due to a surface trap with a multipole expansion:

$$\begin{aligned}\langle F_0|\, V(\vec{r},\vec{q})\,|F_0\rangle &= \frac{e}{4\pi\epsilon_d}\int \frac{\rho_{eff}}{|\vec{r}-\vec{q}|}d^3r \\ &\approx \frac{ep_0}{4\pi\epsilon_d|\vec{r}-\vec{q}|} + \sum_i \frac{ep_{1i}(r_{0i}-q_i)}{4\pi\epsilon_d|\vec{r_0}-\vec{q}|^3} + \\ &\quad \frac{1}{2}\sum_{i,j}\frac{ep_{2ij}(r_{0i}-q_i)(r_{0j}-q_j)}{4\pi\epsilon_d|\vec{r_0}-\vec{q}|^5},\end{aligned} \tag{3.43}$$

where:

$$\begin{aligned}p_0 &= \int \rho_{eff} d^3r \\ p_{1i} &= -\int \rho_{eff}(r_{0i}-r_i)d^3r \\ p_{2ij} &= \int \rho_{eff}\Big(3(r_{0i}-r_i)(r_{0j}-r_j) - \delta_{ij}(r_{0i}-r_i)^2\Big)d^3r,\end{aligned} \tag{3.44}$$

in the above equation, r_0 is the position of the electron in the conduction band (which is set at the origin), and the sum over i and j are for the different dimensions of the problem (x,y,z). The first term then denotes an asymmetric solution which is the monopole term, the second is the dipole and the third is the octupole term. The expansion increases with higher orders of $\vec{q}$, thus higher-order terms should contribute less and less to the overall solution. Equation 3.43 will be the solution for the conduction band electron, and the solution to the NV electron can be written from equation 3.37 where $r = r_0$ as the origin is set at the centre of the confined wavefunction where the NV is. The solutions to a single dipole charge are then integrated over the diamond surface to account for the effects of all surface charges. Additionally, the equations are also integrated over all the possible orientations of the dipole, p_ϕ, where $p_x = p\cos(p_\phi)$ and $p_y = p\sin(p_\phi)$. The last thing to consider is the trap pair distance which will be estimated to be 1nm. This estimation comes from the density of traps, $p = \sqrt{1/\eta}$ where η is the density of traps on the diamond surface. From this derivation, equation 3.33 becomes:

$$\begin{aligned}\overline{|\delta E|^2} = \frac{\eta/2e^2}{2\pi}\int_0^{2\pi}\int_\Omega \frac{p_{dip}\cdot(\vec{r}-\vec{p})}{4\pi\epsilon_d|\vec{r_0}-\vec{q}|^3} - \\ \frac{ep\cdot(\vec{r}-\vec{p})}{4\pi\epsilon_d|\vec{r_0}-\vec{q}|^3} + \frac{p_{hex}\cdot(\vec{r}-\vec{p})}{4\pi\epsilon_d|\vec{r_0}-\vec{q}|^7}d^2q\,dp_\phi,\end{aligned} \tag{3.45}$$

where η has been halved as the dipoles effectively halve the number of contributing traps. Due to the fact that the charge density is Gaussian, an even function, equation 3.44 shows that the first order term in the expansion will be an odd function and will integrate to zero. In fact, all odd terms in the expansion will be odd functions, so

only the dipole (p_{dip}) and hexapole (p_{hex}) terms remain in the above equation which are derived from equation 3.45. When adding the dipole orientations in the integral, equation 3.45 becomes:

$$\begin{aligned}\overline{|\delta E|^2} = \frac{\eta/2e^2}{4\pi}\int_0^{2\pi}\int_\Omega \frac{e\big(p\cos(p_\phi)+p\sin(p_\phi)\big)\cdot(\vec{r}-\vec{p})}{4\pi\epsilon_d|\vec{r_0}-\vec{q}|^3} \\ -\frac{e\big(p\cos(p_\phi)+p\sin(p_\phi)\big)\cdot(\vec{r}-\vec{p})}{4\pi\epsilon_d|\vec{r_0}-\vec{q}|^3}+\frac{p_{hex}\cdot(\vec{r}-\vec{p})}{4\pi\epsilon_d|\vec{r_0}-\vec{q}|^3}d^2q\,dp_\phi,\end{aligned} \tag{3.46}$$

note how with the expansion of the dipole terms it becomes clear that the first two terms of the integral will cancel each other out, leaving just the hexapole term which has an analytic solution that will be referred to as $\overline{|\delta E|^2}_d$:

$$\begin{aligned}\overline{|\delta E|^2}_d &= \frac{15p^2e^4\eta(\alpha+\beta)}{8192\pi q_z^6\epsilon_d^2} \\ \alpha &= 3\sigma_x^4+2\sigma_x^2\sigma_y^2 \\ \beta &= 3\sigma_y^4-8(\sigma_x^2+\sigma_y^2)\sigma_z^2+8\sigma_z^4,\end{aligned} \tag{3.47}$$

where σ_n is the standard deviation in a Cartesian direction for the Gaussian approximation to the wavefunction and q_z is the distance from the diamond surface to the NV. Using the Lorentzian spectral noise density from equation 3.35 the linewidth broadening due to a dipole surface of charges will then become:

$$\Gamma_{dipole} = \frac{2\pi}{\hbar^2}\overline{|\delta E|^2}_d\frac{\gamma/\pi}{\gamma^2}, \tag{3.48}$$

the σ values are chosen for a wavefunction confined to a volume that is 250 nm in length/width and 100 nm in depth, the NV is 50 nm in depth (q_z) and the density of traps is 10^{18} m^{-2}. Whilst the charge hopping rate (γ) is unknown, a range of values from kHz to GHz can be tested to see its effect on the overall linewidth. Even when considering extremely fast charge motion on the surface (THz in order) the broadening can be as high as 10^{15} Hz for a typical trap density (10^{18} m^{-2}), as much as 6 orders of magnitude broader than the limiting requirement.

Calculating the broadening in the monopole regime is largely the same as the dipole regime but the potential and the subsequent expansion will be for a monopole

charge source. Following the logic from equation 3.43:

$$\begin{aligned}\langle F_0|\, V(\vec{r},\vec{q})\, |F_0\rangle &= \frac{e}{4\pi\epsilon_d}\int \frac{F_0^2}{|\vec{r}-\vec{q}|}d^3r \\ &\approx \frac{ep_0}{4\pi\epsilon_d|\vec{r}-\vec{q}|}+\sum_i \frac{ep_{1i}(r_{0i}-q_i)}{4\pi\epsilon_d|\vec{r_0}-\vec{q}|^3}+ \\ &\quad \frac{1}{2}\sum_{i,j}\frac{ep_{2ij}(r_{0i}-q_i)(r_{0j}-q_j)}{4\pi\epsilon_d|\vec{r_0}-\vec{q}|^5},\end{aligned} \tag{3.49}$$

where:

$$\begin{aligned}p_0 &= \int F_0^2 d^3r \\ p_{1i} &= -\int F_0^2(r_{0i}-r_i)d^3r \\ p_{2ij} &= \int F_0^2\Big(3(r_{0i}-r_i)(r_{0j}-r_j)-\delta_{ij}(r_{0i}-r_i)^2\Big)d^3r,\end{aligned} \tag{3.50}$$

and the octupole term can be rewritten as:

$$p_{2ij} = \frac{1}{2}\sum_i \frac{(2\sigma_i^2-\sum_{j\neq i}\sigma_j^2)(r_{0i}-q_i^2)}{|\vec{r_0}-\vec{q}|^5}. \tag{3.51}$$

Equations 3.49 and 3.50 are almost exactly the same as equations 3.43 and 3.44 with the exception of the substitution of F_0^2 for ρ_{eff} to account for the dipole nature of the charge distribution in the dipole regime. This will change the non-zero terms in the expansion as F_0^2 is an even function whereas ρ_{eff} is an odd function. This means that whilst in the dipole regime the odd terms in the expansion integrated to zero, in the monopole regime the even terms in the expansion will integrate to zero. Placing equations 3.49 and 3.51 into equation 3.33 gives:

$$\begin{aligned}\overline{|\delta E|^2} = \eta e^2\Big(\frac{e}{4\pi\epsilon_d}\Big)\int \Big|&\frac{1}{|\vec{r_0}-\vec{q}|}-\frac{1}{|\vec{r_{NV}}-\vec{q}|}+ \\ &\frac{1}{2}\sum_i\frac{(2\sigma_i^2-\sum_{j\neq i}\sigma_j^2)(r_{0i}-q_i^2)}{|\vec{r_0}-\vec{q}|^5}\Big|^2 d^2q,\end{aligned} \tag{3.52}$$

equation 3.52 has an analytic solution which will now be referred to as $\overline{|\delta E|^2}_m$:

$$\begin{aligned} \overline{|\delta E|^2}_m &= \left(\frac{\eta e^4}{4\pi\epsilon_d}\right)^2 \frac{3\pi(\alpha+\beta)}{128 q_z^4} \\ \alpha &= 3\sigma_x^4 + 2\sigma_x^2\sigma_y^2 \\ \beta &= 3\sigma_y^4 - 8(\sigma_x^2+\sigma_y^2)\sigma_z^2 + 8\sigma_z^4, \end{aligned} \tag{3.53}$$

substituting equation 3.53 into equation 3.32 with the Lorentzian noise spectrum gives the linewidth broadening in the monopole regime:

$$\Gamma_{monopole} = \frac{2\pi}{\hbar^2}\overline{|\delta E|^2}_m \frac{\gamma/\pi}{\gamma^2}, \tag{3.54}$$

where the parameters are chosen for the same simulation as the dipole regime. Even when considering extremely fast charge motion on the surface (THz in order) the broadening can be as high as 10^{17} Hz which is 2 orders higher than the dipole regime. This is likely due to the fact that the effective charge density is higher in the monopole case and that charges have a much higher freedom of movement across the diamond surface compared to the adjacent hopping in the dipole case. In both regimes, the broadening is too high for resolving conduction band states individually. So a new approach is needed to reduce the effective trap density. One option is to reduce the physical number of surface traps, which is difficult to achieve, and the other is to fill the traps with a donor layer in the diamond.

When adding a donor layer of nitrogen below the NV, the surface charges and the donor layer act like the plates of a capacitor. The donor layer nitrogen atoms will pass their electrons to the surface traps due to the fact that the donor nitrogen energy level is higher than that of the traps [82]. This encourages a passing of electrons from the nitrogen to the traps, resulting in a complete filling of the traps [82] (see figure 3.7). The filling of the traps will mitigate any opportunity for electrons to hop within the traps, thereby reducing the AC electric field they might produce. The electric field can also cause band bending within the diamond bulk which can further screen the electric field [15]. This occurs as a result of impurities in the diamond, however, this effect is mitigated by using high purity diamonds [13].

How much trap filling that occurs will depend on the donor layer as well as the trap density. This can be described by using an effective charge density with the following capacitor equation:

$$\rho_s = CV = e\eta \frac{1}{e^{\frac{E_T - E_N + V(\eta,N)}{k_b T}} + 1}. \tag{3.55}$$

Where C is the capacitance generated by the trap layer and the donor layer, E_T is the trap energy, E_N is the donor layer energy and $V(\eta, N)$ is the potential generated in eV. The exponential function is the Fermi-Dirac distribution which modulates the normal trap density η based on the energy of the system. As long as the density of donors is high enough, the Fermi energy will be pinned to the donor layer energy

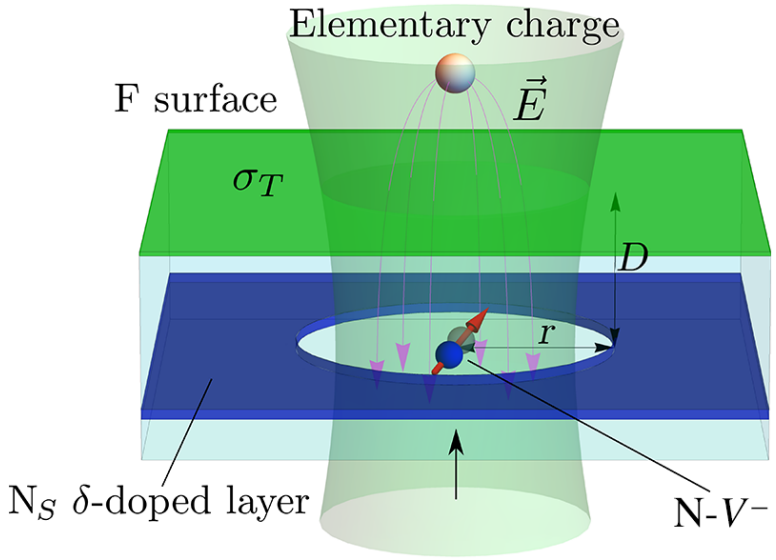

Figure 3.7: Example image of the nitrogen donor in diamond. In this case, the green layer is the surface of the diamond with a trap density of σ_T. Below the surface, at a depth, D is the NV along with a N_S δ dope layer of nitrogen atoms with a circular hole to prevent NV interactions with the donor layer and allow green laser illumination. This schematic is from Oberg et al. [82] and is designed to help sense elementary charges above the diamond with the NV. However, the design can also be used in our case to prevent surface charge trap broadening.

and can be removed from equation 3.55. Fermi pinning is a process where the surface charge density gets high enough that the energy of the surface pins the Fermi energy at the same point. In other words, higher dopant concentrations cause charges to go to the surface but the surface charges in equilibrium force the charges to move back into the bulk, pinning the energy at a point where there is only 50% occupation at a minimum no matter how dense the dopant concentration is compared to the trap density. Fermi pinning is in part what motivates a reduction of the trap density instead of just increasing the dopant concentration as pinning won't occur if the surface trap density is low. The only unknown in equation 3.55 is the potential, $V(\eta, N)$; to solve for it equation 3.55 is rearranged for the trap density and the capacitance is replaced by an equation with a capacitance per unit area for a parallel plate capacitor: $C = \epsilon_d / N$ where N is the distance from the diamond surface to the nitrogen donor layer:

$$\eta = \frac{eN}{\epsilon_d V(\eta, N)} \frac{1}{e^{\frac{E_T - E_N + V(\eta,N)}{k_b T}} + 1}, \tag{3.56}$$

equation 3.56 can then be solved to obtain the capacitor potential $V(\eta, N)$. The potential can be substituted into the following equation which mediates the effective

trap density by the occupation of traps created by the nitrogen donor layer:

$$\eta_{eff} = \eta(1 - Oc(\eta, N))$$
$$Oc(\eta, N) = 0.5\left(1 + \frac{1}{1 + e^{\frac{E_T - E_N + V(\eta,N)}{k_b T}}}\right), \tag{3.57}$$

where $Oc(\eta, N)$ is the occupation of the surface traps which is a function of the initial charge density as well as the distance the donor layer is from the diamond surface. Equation 3.57 can be used in place of η in the dipole regime linewidth equation 3.48.

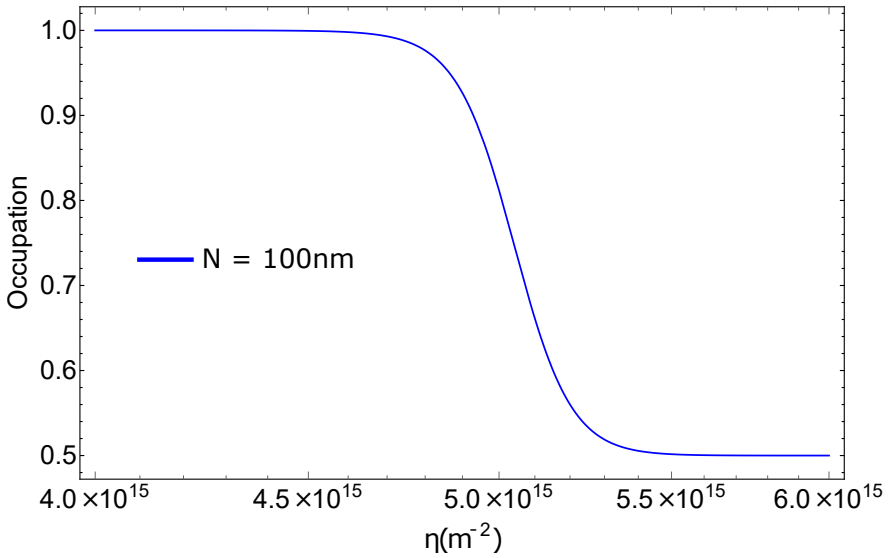

Figure 3.8: Plot of the trap occupation for a donor layer 100 nm below the surface of the diamond. At very low surface trap densities ($\eta <\approx 4.5 \times 10^{15}$ m^{-2}) the trap occupation is 100% however when the density is higher, then the occupation rapidly drops to 50%

Figure 3.8 shows shows the occupation as a function of the surface trap density for a donor layer that is 100 nm away from the diamond surface. From equation 3.57 it becomes clear that as the occupation increases, the effective density drops. If the traps are fully occupied, then the effective density is zero and the charge hopping will also go to zero, which occurs when the trap density is around 10^{15} m^{-2}. This means that the associated AC electric field from trap charge motion will be zero and the broadening from the surface charges will also be zero. If however, the charge density is too high, then the occupation will quickly drive towards 50% and the linewidth broadening will become similar in value to the dipole regime.

To ensure that there is full trap occupation there are three options: the first is to increase the capacitance by reducing the depth of the donor layer (N). This increases the ease of nitrogen donation. For example, when the donor layer is 50 nm instead

of 100 nm then the full occupation occurs at 5.5×10^{15} m^{-2}. There is a problem with this approach, nitrogen atoms too close to the NV center decreases coherence times and the higher capacitance will cause the NV to donate electrons to the surface traps, causing unwanted ionization. The second option would be to increase the Fermi level with an external potential such as the electrode positive potential, this will increase the Fermi level thereby increasing trap occupation for the traps located around the electrode. This can be modelled by adding the electrode potential to the Fermi Dirac distribution in equations 3.55, 3.56 and 3.57. Whilst this method will already be in effect, the potential from the electrode is relatively small (10 mV), which has a negligible effect on the occupation. If the electrode potential were to increase beyond 10 mV, then the potential well would get smaller to the point where it would be difficult to place an NV in the well volume. The third method would be to reduce the surface trap density which whilst being technically challenging, is possible and has the greatest overall effect on the occupation without affecting the NV performance. This theoretical approach motivates the final result that broadening from surface traps can be completely mitigated as long as there is a nitrogen donor layer approximately 100 nm below the surface of the diamond (with the NV at 50 nm below the surface of the diamond) and the surface trap density is reduced to $\approx 10^{15}$ m^{-2}.

With the major sources of broadening considered, it is clear that with some extra engineering, creating discrete diamond conduction band energy levels which can be individually addressed is entirely possible. In the next section, the SCC protocol is outlined, and the linewidths studied in this section are considered along with the discrete energy levels to work out what the optical spin contrast and readout fidelity could be in this project.

3.4 SCC protocol and fidelity

With the electrode and diamond design characteristics outlined, the spin-to-charge protocol is relatively simple. When the NV electron is in the ground triplet, an ionizing laser excites the electron from the ground state to the upper energy states which represent the ionized NV^0 ^2E state with an electron in one of the first two conduction band levels c_0 and c_i respectively (figure 3.9). The NV^0 charge state can then be read out either optically or through measuring the photoelectric current [58, 109]. The ionization will present as a drop in fluorescence from the NV^- or by an increase in current as the NV is ionized into the neutral charge state. This process can occur when ionizing from $m_s = 0$ to the conduction band or $m_s = \pm 1$ to the conduction band. The fine structure of the first two conduction band states is negligible due to the fact that there are no spin-orbit effects in the conduction band minimum [83].

In order to understand the improved performance of this SCC protocol, the optical spin contrast and readout fidelity is calculated to compare with other methods. Readout fidelity can be understood as the probability of getting the right answer in a process. Conversely, infidelity can be thought of as the probability of getting the wrong answer. The probability of getting the wrong spin state can be expressed as the

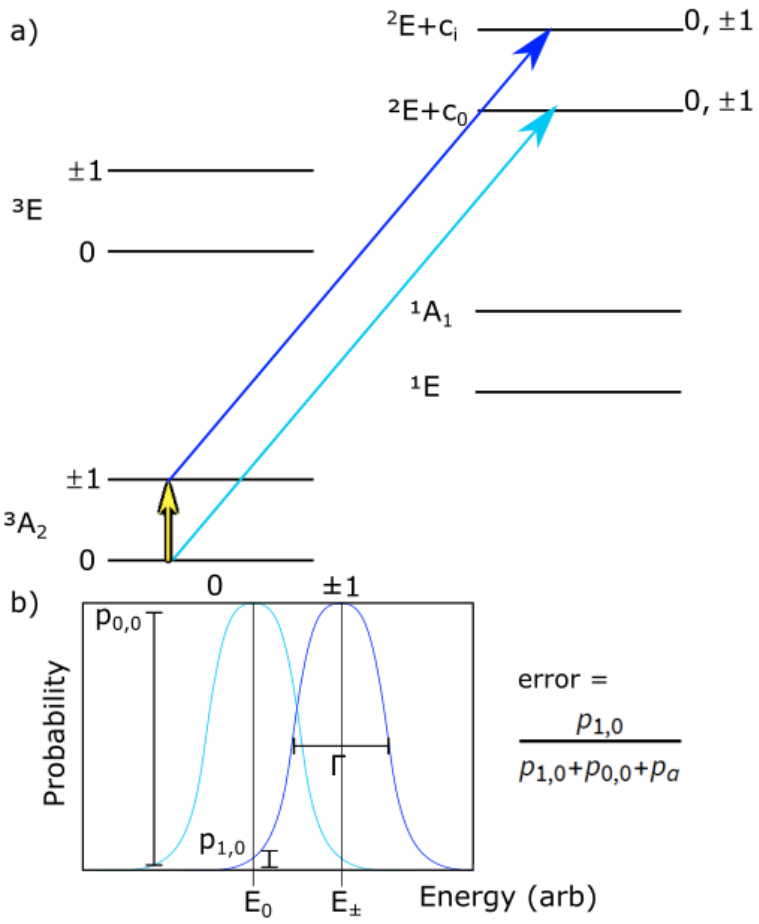

Figure 3.9: a) Diagram of the spin to charge readout protocol. With the electrode in place, the low lying conduction band states are discretized. This allows for resonant ionization into the upper energy states which represent the ionized NV^0 ^2E state with an electron in one of the first two conduction band levels c_0 and c_i respectively. Thus a laser (light blue) can be applied to ionize out of the ground state $m_s = 0$ and a microwave/laser (yellow/dark blue respectively) combination can be used to ionize out of the $m_s = \pm 1$. b) As long as the linewidth Γ is small and the energy difference between the two transitions is large then the two transitions can be distinguished. In the error equation, $p_{1,0}$ is the probability of ionizing from the wrong spin state when intending ionization from the other, $p_{0,0}$ is the probability of ionizing correctly from the correct spin state and p_a is the probability of absorbing instead of ionizing. Thus, the error is the ratio of erroneous photoionization compared to the total amount probability of other processes.

sum of the probabilities for wrong processes divided by the sum of the probabilities for all processes:

$$error = \frac{p_1 + p_0}{p_0 + p_1 + p_a}, \tag{3.58}$$

In the above equation, you are trying to get a particular spin readout p_0, but there is a chance you could get the wrong spin state, p_1, during photoionization or there is a chance you could get no photoionization at all, this is because for the expected photoionization energy (2.6 eV [7]), there is a non-zero chance of absorption which is given by p_a where the electron goes to the excited state in the NV instead of ionizing. The probability of the correct readout (p_0) is given by the cross section of photoionization at 2.6 eV in bulk diamond ($\sigma_{i,b}$), multiplied by a further factor, $f = 2.4$, which describes the increase in photoionization rate due to the discrete energy levels (see figure 3.3 of section 3.1). The rate of the wrong spin readout (p_1) can be expressed as the rate of photoionization, $\sigma_{i,b}$, multiplied by the same f factor as well as an error rate given as a Lorentzian function. The Lorentzian function describes how the energy levels and linewidth broadening affects the probability of getting the correct spin state in an ionization readout process. It is a function of the difference in energy separation between the ground state NV triplet and the conduction band energy levels as well as the total linewidth broadening:

$$\mathcal{L}(\Delta E) = \frac{\phi/\pi}{\Delta E^2 + \phi^2}, \tag{3.59}$$

where ϕ is the total linewidth broadening calculated by adding all the sources of broadening listed in this section 3.3 (0.757 GHz). The splitting of the NV ground state triplet ($m_s = 0$ and $m_s = \pm 1$ respectively) is known to be: $\Delta D \approx 2.87$ GHz [25, 69] and the splitting of the first two conduction band levels under the electrode is calculated to be: $\Delta C \approx 9.945$ GHz using equation 3.1. The ΔE term in the Lorentzian function is then the difference in energy separation between the conduction band energy levels and the ground state NV triplet energy levels ($\Delta E = \Delta C - \Delta D = 7.075$ GHz). The final term in equation 3.58 is the absorption probability p_a which can be expressed as the photoionization cross-section multiplied by the ratio of photoionization to absorption, $g = 0.4$, at the energy of photoionization (2.6 eV). This ratio can be found from the photoionization/absorption cross section data by Razinkovas et al. [95]. Substituting all the relevant terms into equation 3.58:

$$\begin{aligned} error &= \frac{f\sigma_{i,b}\mathcal{L}(\Delta E) + g\sigma_{i,b}}{f\sigma_{i,b} + f\sigma_{i,b}\mathcal{L}(\Delta E) + g\sigma_{i,b}} \\ &= \frac{\mathcal{L}(\Delta E) + g/f}{1 + \mathcal{L}(\Delta E) + g/f}, \end{aligned} \tag{3.60}$$

note that equation 3.60 gives the error rate or the infidelity (15%). To find the fidelity, the difference must be used (1-0.15), which gives the readout fidelity of 85%. To calculate the optical spin contrast, the same methodology is applied, but the contrast is given by the difference in probabilities for readout divided by the

probability for all processes:

$$\begin{aligned} C &= \frac{p_0 - p_1}{p_0 + p_1 + p_a} \\ &= \frac{1 - \mathcal{L}(\Delta E)}{1 + \mathcal{L}(\Delta E) + g/f}, \end{aligned} \tag{3.61}$$

solving equation 3.61 gives an optical spin contrast of 85%. Recall that the best reported optical spin contrast to date is 36% from Jaskula et al. [58]. This presents a significant improvement that benefits sensitivity and computation (via readout fidelity). The calculation of fidelity and contrast both dictate the requirements of the SCC protocol. The three main factors that improve fidelity and contrast include: smaller linewidth broadening, increasing photoionization probability and increasing the energy splitting in the low lying conduction band states.

Readout fidelity is one of the main limiting factors in NV performance for a variety of quantum technologies. Typically in the NV, spin readout occurs when the electron is pumped into the singlet levels from the triplet manifold via an ISC. The branching ratio in the ISC reduces the probability of electrons transitioning to the singlet from the $m_s = \pm 1$, reducing overall contrast [37]. This SCC protocol avoids this issue by performing a single transition photoionization that avoids the ISC altogether. It is only achievable with the electrode as the two spectral lines need to be distinguishable and this is only achieved with discrete, wide-gap conduction band energy levels. Achieving this high readout fidelity SCC using an external electrode is possible as long as the electrode remains stable, the diamond is at cryogenic temperatures and is engineered with a nitrogen donor layer with a surface trap density of 10^{15} m^{-2}. Future work would involve engineering the electrode, measuring confinement and then fully realising the design parameters for the SCC readout protocol. All these requirements are achievable, offering great potential for the future of NV technology.

Chapter 4

Photoionization spectroscopy of NV singlet levels

Whilst photoionization is the key mechanism in the SCC protocol, photoionization has additional uses for understanding the NV itself. Decades of research in various forms has been accumulated to understand the NV energy structure which in turn allows for the various spin readout protocols that are used routinely in quantum experiments and applications [25]. There are, however, still aspects of the NV energy structure that remain unknown, in particular, the precise nature of the NV inter-system crossing (ISC). From Goldman et al. the upper ISC rate from a purely spin-orbit interaction can be described using Fermi's golden rule [37]:

$$\Gamma_{ISC} = 4\pi\hbar\lambda_{\perp}^{2} \sum_{n} \left| \langle \chi_0 | \chi_\nu \rangle \right|^2 \delta(\nu - \Delta), \tag{4.1}$$

where $\lambda_\perp$ is the transverse spin-orbit coupling rate, $\langle \chi_0 |$ is the wavefunction of the vibrational state above the electronic triplet state and $|\chi_\nu\rangle$ is the wavefunction of the vibrational state that is ν in energy above the upper singlet state. In the spin-orbit interaction, the electron passes from the excited triplet state into an excited vibrational state of the upper singlet where it then decays into the upper $^1A_1$ state. The process in the lower ISC is largely the same and other ISC processes can occur where an electron-phonon interaction causes mixing of states in the triplet before undergoing the spin-orbit interaction. However, the spin-orbit interaction is the key to all ISC processes and one of the main values required to understand and properly quantify this process is the energy splitting, Δ, of the electronic states in the ISC. Whilst the splitting in the singlet states is well known at 1042 nm (1.2 eV) [25, 37] the position of the singlet energy levels relative to the triplet states is not very well known. Theoretical modelling places the energy gap from the triplet to the singlets from 344 to 430 meV [37]. Understanding this energy gap precisely helps complete the understanding of the NV and allows for improved NV experiments. One experiment that could see improvement is measuring and calculating the ISC rates from the triplet to the singlet states more accurately to improve spin contrast [37]. Another is understanding the energy gap for improved photoionization out of the NV singlet states into the diamond conduction band. This information can be used to create a room temperature SCC

technique which is considered in chapter 5. Finally, understanding the ISC process allows for a better understanding of other defects in other materials. Whilst the NV is a prominent and very useful defect in diamond, it is not necessarily the ideal defect for performing quantum operations. There are a number of defects in diamond and other materials which are largely unknown in their structure and properties. Understanding this non-radiative process allows for theoretical and experimental investigations to be performed to discover a variety of atomic defects which could create sensors or qubits that are comparable or higher quality compared to the NV.

In this chapter, a photoionization readout protocol is developed with the goal of understanding and quantifying the energy gap from the lower singlet ^{1}E to the ground state $^3A_2$. The basic principle is to discover the minimum energy required to ionise out of these states individually. The first step of the experiment would be to initialise the NV into the ground state and use a laser with a very high spectral resolution to sweep frequencies until the minimum energy to ionise out the ground state is achieved (figure 4.1a)/b)). The second step is to initialise the NV into the singlet ^{1}E state and perform the same ionisation sweep to find the minimum energy to ionise out of the singlet state (figure 4.1c)/d)). The difference in energy of the two ionisations is equal to the energy gap between the two states due to Koopman's theorem [114]. This experiment is initially performed at room temperature to get a rough idea of the energy levels and then repeated at cryogenic temperatures to reduce electron-phonon broadening and obtain a more accurate measurement.

In section 4.1, the experimental design is described. This includes an explanation for some of the technical equipment required as well as a basic description of Koopman's theorem and how it is applied to the experiment. In section 4.2 the high-temperature diamond vibronic band is studied to predict the effect of electron-phonon broadening on the ionisation measurements. Finally, in section 4.2 the preliminary setup and results are analysed and the future of the experiment is outlined. This includes the steps that remain to be undertaken as well as experimental additions that can improve the measurement.

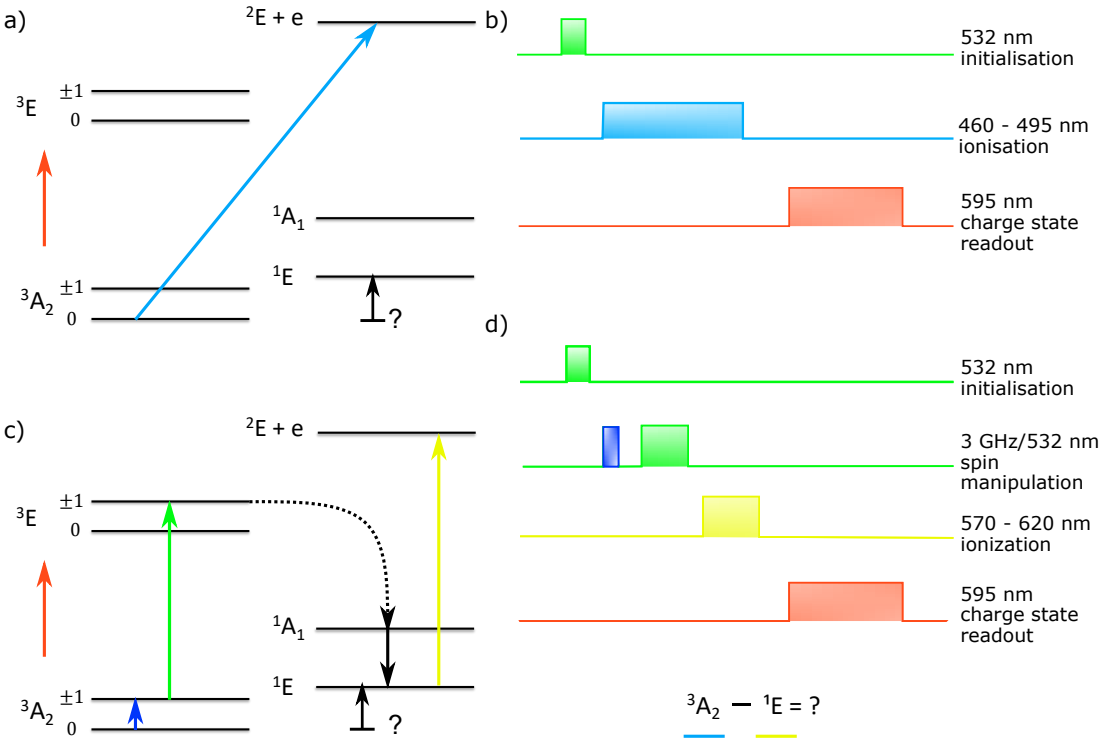

Figure 4.1: Image of the ionisation experiment. The first step is to find the ionisation energy of the ^{3}A$_2$ ground state to the ionised ^{2}E+e state by applying a laser that sweeps from 460-495 nm which is the range predicted which will ionise the NV from the ground state. The energy diagram a) shows the ionisation process and the pulse sequence, b), outlines the light blue laser used for ionisation along with the green 532 nm laser for charge state initialisation and the orange 595 nm laser for charge state readout. The second ionisation process is shown with the energy diagram c) and associated pulse sequence d). In this experiment, the NV electron is initialised into the ^{1}E singlet state with a dark blue microwave pulse, a green laser pulse and the black ISC process. Once initialised the yellow pulse ionises the laser. Similar to the first experiment, the charge state is initialised with a green laser and readout with the 595 nm orange laser. The difference in ionisation energies of the two processes is equal to the energy gap between the ^{1}E state and the ^{3}A$_2$ state.

4.1 Experimental design and aims

Figure 4.1 shows the ionisation experiment which is broken up into two separate pulse sequences. Figure 4.1a) shows the energy diagram for the first ionisation sequence and figure 4.1b) shows its associated pulse sequence. The goal of the first experiment is to find the ionisation energy from the ground state ^{3}A$_2$ level to the diamond conduction band which would ionise the NV into the neutral ^{2}E state with an electron in the conduction band. To achieve this, a number of laser pulses are required. The first

pulse is a green laser that initialises the NV into the negatively charged state with ≈75% probability [7], continuous cycling of the green laser will also initialise the NV into the ground state $m_s = 0$ (chapter 1, section 1.2). The second pulse in the sequence is the light blue ionisation pulse after which a 595 nm laser is used to measure the charge state of the NV which in turn, will measure if the ionisation has occurred. The 595 nm wavelength is chosen as it is maximally absorbed in the NV^- state compared to the NV^0 state, thus creating the highest level of optical contrast in the charge state readout [7]. This sequence is then repeated many times, where in each successive run, the wavelength of the ionisation process is altered by 1 nm from 460 nm to 495 nm. The range is chosen as the predicted range for the ionisation energy based on previous experiments [7].

Figure 4.1c) shows the energy diagram for the second ionisation sequence with the associated pulse sequence in figure 4.1d). In this part of the experiment, the goal is to initialise the electron into the lower singlet state and ionise from that state. To achieve this, the NV is initialised into the ground state $m_s = 0$ using the same green laser pulse and a combination of a microwave (dark blue) and green laser is used to pump the electron into the excited $m_s = \pm 1$ state. From there, the electron moves into the singlet states via the ISC process and is then an ionisation laser (yellow) is used to excite the electron into the conduction band and the NV charge state is measured with the same 595 nm charge state readout laser. Similar to the previous experiment, the ionisation laser is swept from 570 to 620 nm in increments of 1 nm to find the precise energy for the ionisation process. Once the ionisation energy is known for both experiments, the difference in energy can be taken to find the energy difference between the associated ^2E and $^3A_2$ states in the NV. With this knowledge, the difference from the upper ^3E and $^1A_1$ can also be calculated by simply taking the difference from the triplet ZPL (1.9 eV) from the combined ZPL of the singlet state and the energy difference of the lower ISC gap calculated in the experiment. The connection from the ionisation energy to the energy difference in the NV electronic states can be attributed to Koopman's theorem.

Koopman's theorem is a theory of ionisation that builds from the Hartree-Fock theory for describing the wavefunctions of multi-body systems. Koopman's theorem states that the first ionisation energy of a molecular system is equal to the negative of the orbital energy of the highest occupied molecular orbital (HOMO) [114]. In the context of the NV, it means that the energy of ionisation from an occupied orbital in the NV is equal to the negative of the energy of the orbital which is removed during the ionisation process. Thus, the energy difference of two separate ionisation events is equal to the energy difference of the two removed orbital states or the energy gap between them. Koopman's theory derives from Hartree-Fock theory and shares the same assumptions. In Hartree-Fock theory, multi-body wavefunctions can be calculated using the Schrodinger equation where each particle is described by its kinetic energy, potential energy and a single matrix of particle interactions called a Slater determinant where each correlation between particles can be described as an average of all the particle interactions together. In this formalism, the orbitals of the ionised state are identical (or close to) the orbitals of the neutral state. During

ionisation, the change in the energy structure can be described accurately using a new Hartree-Fock equation and the effects of individual electron correlations altering the energy structure (and by extension the ionisation energies) can be ignored. Hartree-Fock theory (and by extension, Koopman's theory) works in situations where the electron interactions can be described by a single Slater determinant in which all the electron interactions are described by a single averaged value. The theory breaks down in situations where the electron interactions are highly correlated and can't be averaged such as those found in Mott-insulators or superconductors, neither of which apply to the diamond in ambient conditions. The theory also breaks down when multiple Slater determinants are required to model a system such as excited systems where the excitation can come from many different lower-lying electron states. The ionisation in this experiment comes from the ground state as well as an excited singlet state that can only be populated from a single excitation pathway, so a single Slater determinant would still apply and Koopman's theory is applicable.

The ionisation laser used in the experiment is a C-Wave Vis OPO laser from Hübner photonics. The laser operates using the principles of an optical parametric oscillator (OPO). OPO lasers take an input laser (in this case a 532 nm green laser) and convert it into two output frequencies called a "signal" and "idler" whose frequencies sum to the input laser. The conversion occurs via a cavity with a non-linear optical crystal which converts the input laser via a second-order nonlinear optical interaction. By changing the temperature or the orientations of the crystal, the mixing of the input, signal or idle frequencies change. By out-coupling the signal laser and using the altering properties of the crystal the laser achieves the means of frequency sweeping for the experiment [120]. The C-Wave Vis OPO output has a wavelength range from 450 nm up to 3.5μm with a 1 nm resolution and a < 500 kHz linewidth.

All the excitation lasers are focused into the diamond sample via a single multi-mode fiber and an achromatic objective lens. This equipment helps to focus the laser power into roughly the same place regardless of the laser wavelength. The ionisation process is power dependent so it is important to be able to focus the laser energy into the same NV spot whilst changing the ionisation laser wavelength. If the changing wavelength alters the focal spot too much, then the reduction in laser power may not ionise the NV and cause a false readout. The microwave delivery system is achieved using copper wire over the diamond sample and the cryogenic cooling is performed using a flow cryostat. With the sweeping laser frequencies and extra equipment required to achieve good NV excitation, it is clear that this experiment is time-consuming and complex. The addition of the cryostat complicates the experiment further as all optical excitations and emissions are reduced when passing optical signals through the cryostat itself. It is for this reason that an extensive study at room temperature is undertaken. Whilst electron-phonon broadening will reduce the accuracy of the ionisation energies, the wide range of laser wavelengths required in the ionisation process means that the laser sweeping is time-consuming and prone to experimental error. This is especially true when using a cryostat where the optical quality is substantially reduced, due to the difficulty of getting optical pulses in and out of the cryostat itself. The idea is to obtain a rough idea of the

ionisation energies at room temperature then repeat the experiment at cryogenic temperatures with a reduced range of ionisation energies to obtain a more accurate readout. Future experiments which involve the electrode at cryogenic temperatures for even greater accuracy are considered in section 4.3.

In both experiments the charge state readout is performed in two parts, the initial sequence is the control experiment where the pulse sequence is performed without the ionisation pulses and the second sequence is performed with the ionisation pulse. Over a number of repetitions in the experiment, the repetitions will build statistics on the probability of the NV charge state, the two separate charge state readouts allow for a comparison that can be used to identify the charge state with high fidelity.

4.2 Diamond vibronic structure

Recall from section 3.2 the density of states for a bulk diamond at room temperature can be calculated to be:

$$\rho_b(E) = \frac{V}{2(2\pi)^2}\left(\frac{2m}{\hbar^2}\right)^{3/2}\sqrt{E}, \tag{4.2}$$

where V is the volume of the diamond, m is the electron effective mass, and E is the energy of ionisation from an NV state relative to the conduction band minimum. The key aspect of this equation is that the density of states is zero until the energy reaches the minimum ionisation energy and increases with $\sqrt{E}$. Recall also from the same section that the transition rate or probability of exciting into a particular state in the bulk diamond conduction band can be expressed in terms of the density of states:

$$\Lambda_b = \frac{2\pi}{\hbar}\rho_b(E)\left|\mu_b C(E)\sqrt{\frac{V_c}{V}}F_b(r)\mathcal{E}(E)\right|^2, \tag{4.3}$$

where μ_b is the transition dipole moment, $\mathcal{E}(E)$ is the electric field from the laser, V_c is the volume of the diamond unit cell, $F_b(r)$ is the conduction band envelope function (which in bulk diamond is one) and $C(E)$ is the dimensionless Franck-Condon factor which describes the overlap of vibrational states under a Born-Oppenheimer approximation. As shown in section 3.2, at room temperature, the transition probability for ionisation from the NV to the bulk diamond conduction band will increase with $\sqrt{E}$ (see figure 4.2). In an ideal case, if we are ionising from any state in the NV using a laser with a sweeping energy, then we would expect no ionization until we reach the minimum ionization energy to excite into the diamond conduction band. After that, there is a continuum of states to ionize into so we expect a rapidly rising ionization probability with energy that increases as $\sqrt{E}$, following the density of states.

In section 3.3 we considered how discretised conduction band ionisations are broadened by electron-phonon (e-p) scattering. In this section, we consider e-p scattering for bulk diamond and how it will broaden the ionisation threshold at high temperatures, creating a larger slope in figure 4.2 at the onset of ionisation and lowering the accuracy of the first ionisation energy. To achieve this, a detailed study

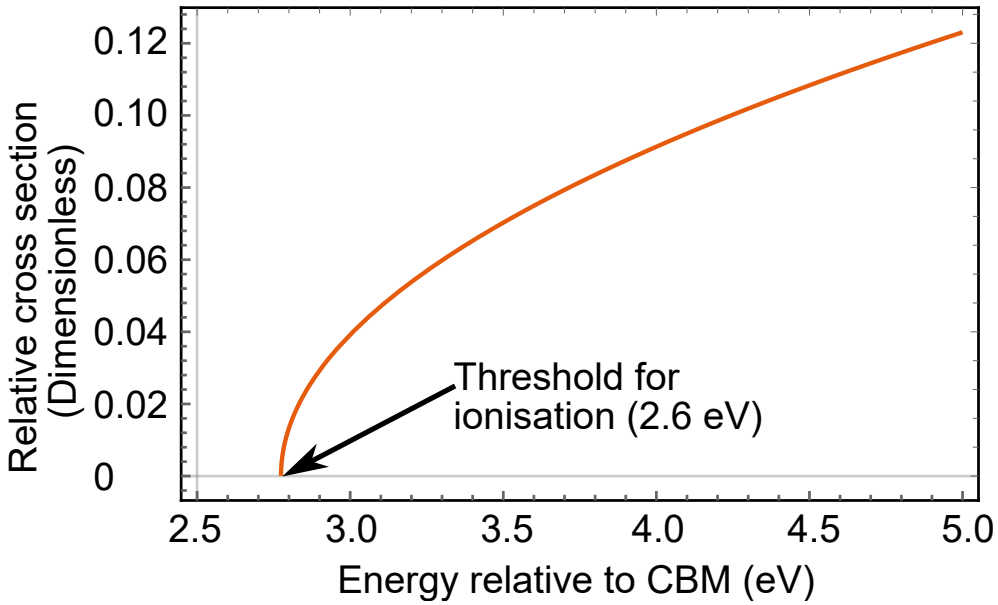

Figure 4.2: Plot of the transition rate as a function of energy taken from equation 4.3. Note the transition rate follows a $\sqrt{E}$ function from the density of states equation 4.2. Also note that the transition rate only begins at the minimum energy for ionisation out of the NV ground state, 2.6 eV [7].

of the NV-diamond absorption band is undertaken.

Figure 4.3 illustrates the concept of vibronic transitions in the NV. The two curves are the electronic levels of the NV ground and excited state labelled $E^{HR}_{^3A_2}(Q)$ and $E^{HR}_{^3E}(Q)$ respectively. These labels indicate electronic energy (E) level in the Huang-Rhys model and are a function of the effective nuclear displacement coordinates of the NV and diamond lattice, Q. Within each electronic level are a number of extra vibrational levels indicated by the horizontal lines where the Stokes and anti-Stokes shifted energies of the vertical transitions (solid lines) are indicated with the ΔS and ΔAS terms respectively. The key to e-p scattering is the transitions between the two electronic states. In a pure electronic transition, the excitation would occur from the 0th vibronic ground state to the 0th vibronic excited state (diagonal line). If there is an excitation from the first vibrational ground state to the first vibrational excited state then the energy gap would be the same. However, if the excitation occurs to different vibrationally excited states such as the ones shown by the vertical solid lines then the energy gap between them will be higher or lower than the pure electronic transition which has the effect of broadening the excitation energy linewidth. Excitations that create phonons, such as the long vertical line are Stoked shifted transitions and are known as cold-band absorptions. Excitations that remove phonons, such as the short vertical line are anti-Stoked shifted transitions are known as hot-band absorptions. These vibronic transitions create the broad absorption band of figure 1.1 in section 1.2. These transitions can occur in vibrational states of the ground and excited states within the NV such as those shown in the figure or they can occur in other states

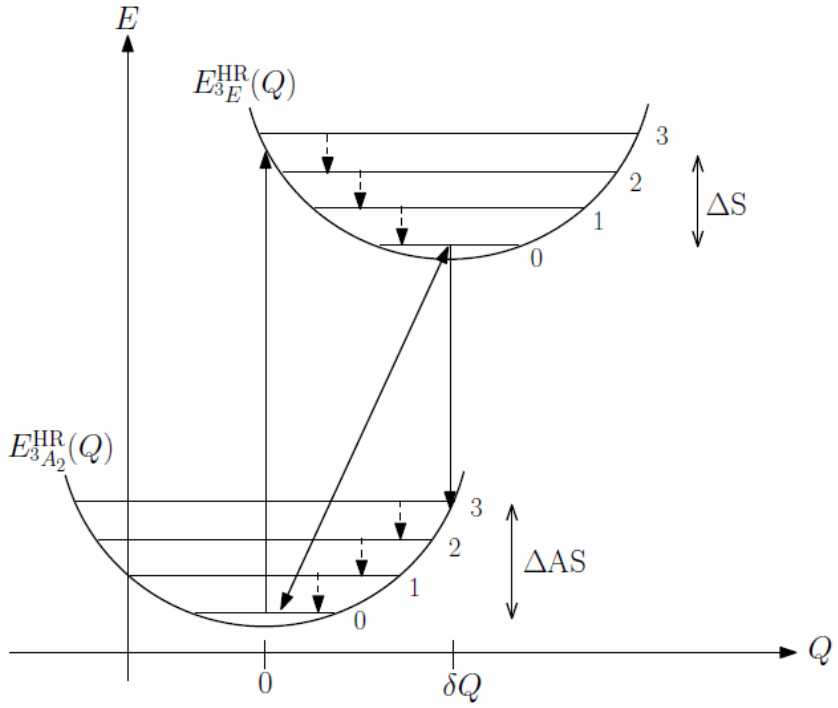

Figure 4.3: Diagram of the vibrational structure of the $^3A_2$ and ^3E levels in the NV as a function of the energy E and nuclear displacement coordinate Q. The electronic levels are represented by the curved line and within each curved line are a number of vibrational excited states. This energy structure allows for a number of transitions that correspond to the Stokes (ΔS) and anti-Stokes (ΔAS) shifted transitions where an electronic transition is accompanied by a process that either produced or annihilates a phonon. A transition that features no phonon interaction is represented by the diagonal arrow between electronic states. The long and short vertical arrows between electronic states represent the cold band (phonon producing) and hot band (phonon destroying) transitions.

such as an NV electronic state and a conduction band state in the diamond during ionisation.

Figure 4.4 is a reproduced plot of various cross-sections in the NV taken from Razinkovas et al. at 0 K [95]. The plot shows the absorption cross-section (green) which is similar to the room temperature values from figure 1.1 of section 1.2, however, at 0 K the ZPL at ≈1.9 eV is effectively infinite and broadens with temperature. The plot also shows the cross-sections for the stimulated emissions (orange) and photoionization (blue).

Calculating the e-p scattering in bulk diamond at high temperatures is impractical as there are an infinite number of vibronic wavefunctions from a continuum of conduction band states to consider. However, the scattering can be understood qualitatively by studying the diamond absorption band at different temperatures. To

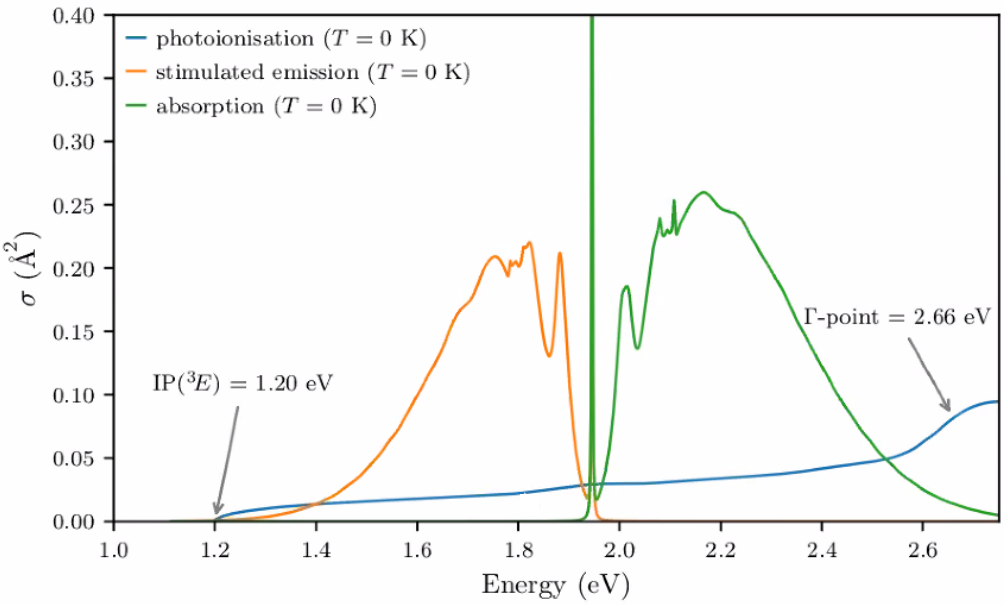

Figure 4.4: Image of the cross-sections for photoionization (blue), stimulated emission (orange) and absorption (green) at 0 K. At this temperature, the absorption at the ZPL (≈1.9 eV) is near unity, however, the photoionization is a smooth function at almost all until it approaches the band gap from the NV to the lowest level conduction band state (≈1.2 eV). The ratio of the photoionization cross-section to the absorption cross-section at a given excitation energy taken from this data can be used as the σ value in contrast calculations. Data reproduced from Razinkovas et al. [95].

calculate the absorption band we apply a similar approach from Davies et al. [20, 25] which uses the Frank-Condon theory of electronic and vibrational interactions during an electronic transition along with the Huang-Rhys model of transitions in a defect. Recall that we are calculating the broad spectrum of transitions that occur when an electronic transition interacts with phonon modes in a lattice. The theory states with a temperature-dependent electron-phonon coupling, the function that describes the vibrational overlap is given by:

$$F(\omega, T) = e^{-S} \sum_{i=1}^{\infty} \frac{S^i}{i!} F_i(\omega, T), \tag{4.4}$$

where S is the average Huang-Rhys factor. The Huang-Rhys factor is a measure of the interaction of defect electrons with phonons in a crystal lattice [55] and can be expressed with the following:

$$S = \int_0^{\Omega} \Big(2n(\omega, T) + 1\Big) f(\omega) d\omega, \tag{4.5}$$

where $n(\omega, T) = 1/(e^{E/k_b T} - 1)$ is the temperature-dependent Bose-Einstein distribution of phonons and $f(\omega)$ is the low temperature one-phonon sideband function. This function describes the single electronic transition that can either create or annihilate a single phonon. It can be approximated by deconvolving the 0 K absorption sideband given in figure 4.4 [95]. The temperature-dependent function describing the vibrational overlap of an electronic transition with one phonon can then be expressed as:

$$F_1(\omega, T) = \begin{cases} \big(n(\omega, T) + 1\big) f(\omega) & \omega > 0 \\ n(-\omega, T) f(-\omega) & \omega < 0 \end{cases}, \tag{4.6}$$

where the negative frequency $-\omega$ allows for the annihilation of phonons and sets ω as the transition frequency relative to the zero phonon transition frequency.

To obtain the function for a two phonon interaction equation 5.14 is then convolved with itself:

$$F_2[\omega, T] = F_1(\omega, T) * F_1(\omega, T) = \int_{\infty}^{\infty} F_1(\omega - x, T) F_1(\omega, T) dx, \tag{4.7}$$

then to obtain any arbitrary number of phonon interactions, equation 4.6 is simply convolved with itself the number of times required to obtain $F_i(\omega, T)$. By using the experimentally obtained Huang-Rhys factor of 3.49 [63], setting the temperature to 0 K and convolving the solution eight times the absorption spectrum shown in figure 4.4 can be reproduced. This equation predicts the absorption spectra for the electronic transition in the NV. However, we are more interested in the ionization spectra, in particular, the ionization onset to observe the effect of e-p broadening. To achieve this, we simply follow the same pattern we did before, but instead of overlapping electronic states of the NV, we are overlapping the NV electronic state and the ionization state of the conduction band minimum:

$$I_n[\omega, T] = F_n(\omega, T) * \rho(E)|_{E=E_t} = \int_{\infty}^{\infty} F_n(\omega - x, T) \rho(E)|_{E=E_t} dx, \tag{4.8}$$

where E_t indicates the threshold energy to ionise from an NV state to the conduction band minimum. The main assumption in this calculation is that the vibronic energy levels are the same as for the NV electronic states as we don't explicitly know the CBM vibronic levels. This assumption works for different NV energy levels (e.g. the 1E and the 3E vibronic states are mostly the same), but it is an assumption when comparing the vibronic levels of the NV to the CBM.

Figure 4.5 shows the results of the convolution equation 4.8 calculated over a variety of different temperatures. The energy has been shifted such that 0 meV corresponds to the onset of ionisation and the inset shows the region we are most interested in, which is the ionisation cross-section at a small range of energies around the ionisation threshold. At 0 to 100 K the onset of ionisation is sharp, with a zero cross-section value in the energies lower than the threshold and a sharp increase in ionisation rate for energies larger than the threshold. At higher temperatures (200 to 300 K) we can observe the onset of ionisation at energies below the threshold and

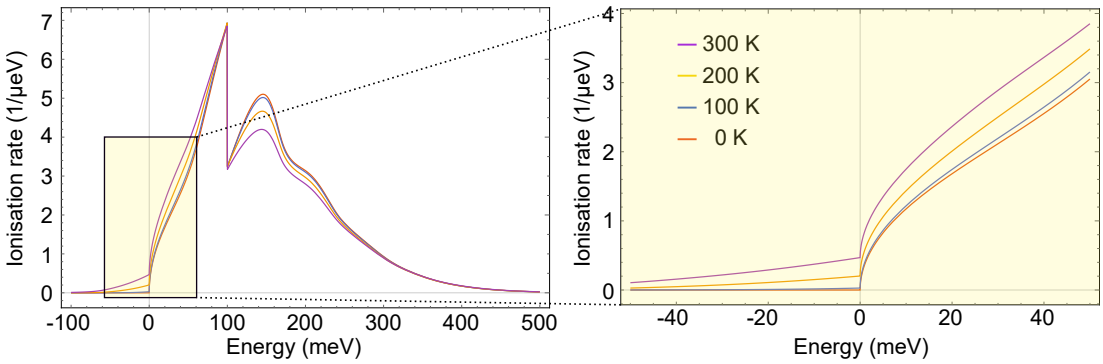

Figure 4.5: Ionization rate as a function of the energy of the ionization laser calculated for different temperatures. The left image is the full ionization spectrum and the right image is a closer look at the energies around the ionization threshold. The energy is shifted so that 0 meV corresponds to the minimum energy required to perform ionization from the NV to the diamond conduction band. At 0 K, there is no ionization until the 0 meV then a sharp increase in the ionization rate. At higher temperatures, the ionization curve becomes smoother with more ionization occurring below the threshold, this can obscure measurement of the ionization onset and is due to e-p broadening.

a broader ionisation curve for energies higher than the threshold. This corresponds to hot-band absorption and cold-band absorption respectively. Whilst this effect is measurable, it is important to note that the change in absorption cross-section is less than 1 μeV which is much smaller than the 1 nm changes to the laser output being performed in the experiment, so the effect of e-p scattering at high temperature will not be significant.

4.3 Discussion and future direction

From a purely theoretical perspective, this photoionization experiment requires lengthy consideration and calculations before even attempting an experiment. The process requires an understanding of NV energy structure and the ISC process, it requires an understanding of the ionisation process and its effect on the energy structure via Koopman's theorem and it requires a calculation of the diamond vibronic structure to make predictions of the effects of e-p scattering. From an experimental perspective, there are many additional considerations including the use of specialised optical equipment such as the high spectral resolution laser and cooling devices such as the cryostat. The work performed in this chapter lays the groundwork for the photoionization experiment and makes predictions on the future results which can be analysed.

Future work requires the completion of the experiment itself, this includes the initial experiments at room temperature followed by the higher accuracy experiments

performed at low temperature in the cryostat. Care will need to be maintained to ensure that the laser power for all the lasers remains constant throughout the experiment even when sweeping frequency in order to eliminate changing laser power as a variable for ionisation. The data analysis after the experiment will also require careful consideration; mainly in regards to defining the optical thresholding for each charge state. This will define the overall probability that an ionisation occurred for a given laser energy which will, in turn, define the overall energy gap in NV structure.

Future work can also include different means of improving the ionisation and readout process. In chapter 3 the photoionization rate was improved by performing resonant ionisation on a discretised conduction band. This concept can be applied to the experiment as increased ionisation rates will improve the charge state readout and subsequent readout of the energy splitting. The photoionization experiment will already be undertaken at cryogenic temperatures, the other additions required for resonant ionisation is the application of the electrode to the diamond surface and the treatment of the diamond to reduce surface charge noise which was discussed in section 3.3.

Optical spectroscopy is a key foundation in understanding atomic structure which drives all quantum operations. This is especially prevalent in defect spectroscopy as atomic defects can be difficult to understand, which affects their applicability. Photoionization spectroscopy provides a convenient way of understanding defect energy transitions that don't necessarily have radiative components such as the inter-system crossing. Photoionization of the NV allows for a better understanding of the defects themselves, allowing for a range of improved quantum applications in sensing and computing. The techniques used in this research can be verified and applied to a range of other atomic defects for better understanding. Whilst this chapter is still focused on NV physics, the results and techniques generated in this study can be generalised to many other spectroscopic experiments, making this chapter a foundational approach to optical spectroscopy.

Chapter 5

Electrode based ambient SCC

One of the major benefits of chapter 4 is an accurate value of the ionisation energy from the lower state singlet in the NV to the diamond conduction band. With this knowledge, an SCC protocol can be developed for ambient conditions in the NV. Recall that in chapter 3 a high contrast/fidelity SCC protocol was developed, but it was only possible at cryogenic temperatures, making the technique unusable in a variety of conditions (e.g. biological sensing). As spin readout fidelity is still an issue with the NV at ambient conditions, a means of improving this increases the sensitivity of the NV and increases its applicability in different conditions.

In this chapter, we develop an SCC protocol using the electrode at ambient conditions. In chapter 3 the role of the electrode potential was to discretise the diamond conduction band for resonant photoionization. In this work, we apply a larger electrode potential to shift the NV energy levels relative to the diamond conduction band in order to alter the photoionization probabilities and maximise charge state control. To understand this process we need to only refer to the effective mass equation derived in section 3.1:

$$\big(T(\vec{r}) + V(\vec{r})\big)F_n(\vec{r}) = E_n F_n(\vec{r}), \tag{5.1}$$

where $T(\vec{r})$ is the kinetic energy of a free electron, $F_n(\vec{r})$ is the envelope function of the diamond, $V(\vec{r})$ is the external potential from an electrode which will in turn, alter the total energy, E_n. This equation states that the position of the energy level relative to the NV energy levels can change in the presence of an external potential from the electrode.

It's important to note that discretisation of the diamond conduction band won't occur as at ambient conditions the electron-phonon broadening will be so large that individual states will not be distinguishable. So the goal is to non-resonantly ionise into the conduction band. The key to this method is to pump the NV electron into the singlet state via the spin selective inter-system crossing (ISC) and from there, ionise the electron into the diamond conduction band (figure 5.1c)). Thus this work follows from chapter 4 as the spin state initialisation process is the same and the ionization energy from the singlet state to the first conduction band states is required. The electrode creates shifts in the NV energy levels which prevent cross-talk where the ionization pulse excites a different transition in the NV (detailed in section 5.1). The electrode

can also be used to prevent unwanted two-photon ionization where ionization occurs in the NV triplet manifold instead of the singlet manifold, introducing noise in the charge state readout. The resultant spin optical contrast is lower than the reported values in chapter 3 (42% contrast vs 85% using the cryogenic method), however, the improvement is still significant compared to other techniques and the protocol can be used in ambient conditions, making them more widely applicable.

The SCC protocol is developed using extensive theoretical modelling. In section 5.1 the protocol is outlined and the concept of rate equation modelling is described which is the main methodology for calculating optical spin contrast. In section 5.2, the rate equation modelling is applied to calculate the spin contrast of the protocol where the electrode only affects the rate of cross-talk in the system. This calculation is performed in a way that optimises over a variety of conditions including laser power, pulse times, and wavelength. In section 5.3, the SCC protocol is critically compared to an experimentally proven alternative performed by Jaskula et al. [58] by applying an alternate rate equation. In both sections, the ratio of photoionization to absorption is calculated by studying the absorption phonon side-band in the NV. The final result made is that our SCC protocol can outperform the other method with a theoretical spin contrast of 42% compared to 37% (the experimentally realised value being 36%[58]), however, our method does require more equipment with the use of the electrode. This translates to a 1.6 fold improvement in DC magnetic field sensitivity compared to a 1.2 fold increase shown by Jaskula et al. Finally, in section 5.4, further considerations for improving spin contrast by altering the lasers used and/or the electrode potential during the SCC protocol are considered. In addition to this, a concept for using the electrode to increase NV charge state control is examined, which has been considered to improve NV optical collection efficiency and coherence time.

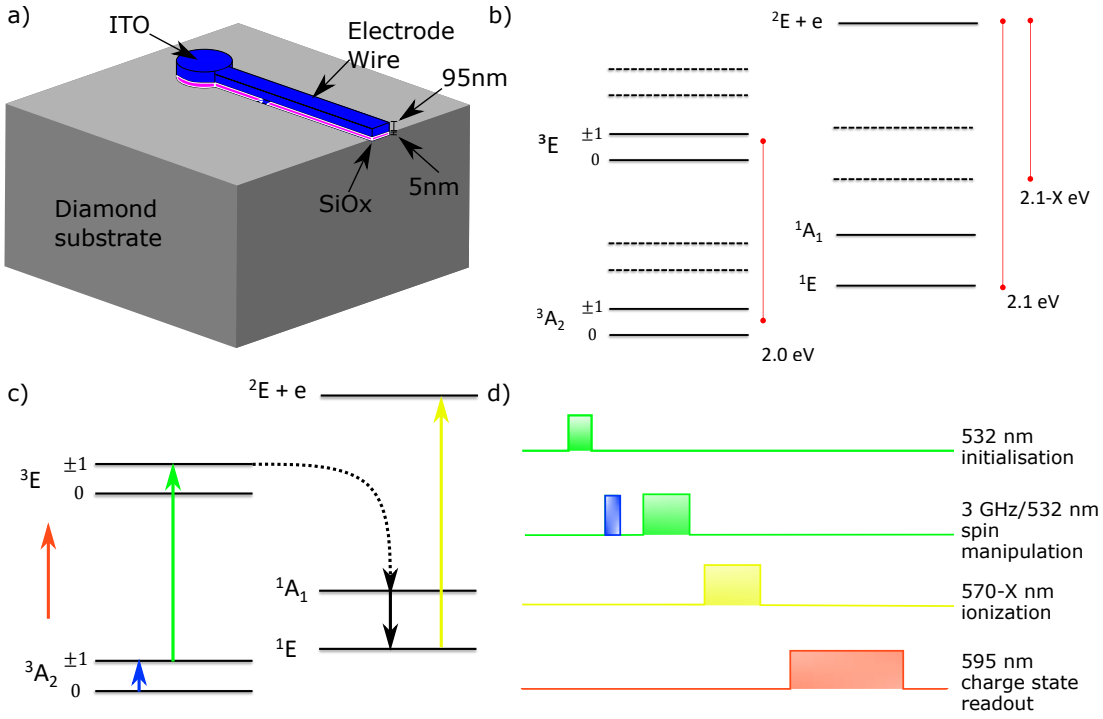

Figure 5.1: a) Image of the electrode over the diamond substrate where the main cylindrical electrode is over a near-surface NV and the electrode wire connects to a power supply which provides the electrode potential. b) Diagram of the NV energy level structure where a positive potential raises the NV levels to a new value (dashed lines). Note that the triplet splitting does not change (≈2.0 eV) as the ground and excited triplet levels rise by the same amount. The energy difference from the lower state ^{1}E raises from 2.1 eV to 2.1-X eV, where X is the energy provided by the electrode. This has the effect of separating the transition energy of the singlet ionization and the triplet excitation. c) Energy diagram depicting the SCC protocol. The NV is initialised into the ^{1}E singlet state with a green laser and microwaves (blue) where it is then ionised with a high power laser (yellow) into the NV^0 ^{2}E state with an electron in the diamond conduction band. The charge state of the NV is then readout with a 595 nm orange laser pulse. The Pulse sequence for the same SCC protocol in c) is shown in d).

5.1 SCC protocol and Rate equation theory

The SCC protocol presented in this work is largely inspired by Hopper et al. [53], in their work, near-infrared (1064 nm) lasers were used with conventional optics for two purposes. The first was to increase the rate of recombination to increase the probability of NV$^-$ in a charge state readout. This was successful, increasing the steady state NV$^-$ population from 77% (using conventional green optical cycling) to

91% [53]. The second purpose was to initialise an electron in the NV into the singlet state using conventional means and ionize the defect using the near infrared-laser with two-photon excitation, thus allowing for an SCC protocol very similar to the one considered in this thesis. This work was also somewhat successful with an experimentally realised optical spin contrast of 25%, equivalent to that of conventional optical spin cycling techniques [10, 58].

The major drawback to this method is the probability of ionisation with the near-infrared laser. From the paper, the probability of ionizing out of the singlet with a single ionization pulse is 6%, which raises to 32% with a pulse train (considered in section 5.2). This low ionization probability increases the probability of a false readout as the subsequent charge state readout registers NV^- when the desired outcome was ionisation, obtaining NV^0 (i.e. mapping the wrong spin state to the wrong charge state). One of the major issues with ionization from the singlet state and the reason for the near-infrared laser is the NV triplet absorption band. Recall from section 1.2, figure 1.1, the NV has a ZPL of 637 nm (2.0 eV) and can be excited by broadband of energies both higher and lower than the ZPL. The predicted energy gap from the singlet state to the first diamond conduction band states is ≈570 nm (2.1 eV) which from figure 1.1, has a higher absorption cross-section than the ZPL itself. This means that when ionizing from the singlet with an energy that has a high ionization cross-section, the probability of exciting the NV triplet energy is also very high. The solution in Hopper et al. was to choose an ionization laser that has effectively no absorption cross-section at the cost of a low ionization cross-section.

The solution in our work is to shift the photoionization energy level with the use of an electrode (figure 5.1a). At high electrode potentials, the energy levels in the NV will shift relative to the diamond conduction band (figure 5.1b). Positive potentials will shift the energy closer to the conduction band, increasing photoionization probability whereas negative potentials will have the opposite effect. This allows us to selectively change the ratio of photoionization to absorption cross-section in order to maximise or minimise ionization. By adding a potential that shifts the NV energies towards the diamond conduction band, the singlet ionization energy gap will go below 2.0 eV. If the energy gap is low enough, then the absorption cross-section will be effectively zero, allowing for a higher probability ionization, with low levels of cross-talk, resulting in a high optical spin contrast which we can calculate.

A successful SCC protocol is one in which the probability of an electron being in a particular state at the time of readout is at the highest possible value. In chapter 3, optical spin contrast is relatively straightforward to calculate as there was only one transition to optimise which was the resonant transition from the NV triplet ground state directly into the diamond conduction band for both spin states. The process for calculating optical spin contrast in this SCC method is a little different as the idea is to pump the NV electron into a particular state, then ionise. As a result, there are a number of steps to optimise both when considering the $m_s = 0$ pathway as well as the $m_s = \pm 1$ pathway. The overall optical spin contrast is calculated with the following:

$$C = p_1 - p_0, \tag{5.2}$$

where p_1 is the probability of the NV being in the neutral charge state when it is initialised into the $m_s = \pm 1$ state and p_0 is the probability of the NV being in the neutral charge state when it is initialised into the $m_s = 0$ state.

To calculate this contrast we will apply Einstein coefficients in the weak field limit to create a rate equation that describes the probability of the electron existing in a particular energy state in time [29]. To get an understanding of rate equation modelling, consider a two-level system with a probability for existing in the ground state given by P_1 and a probability for existing in the excited state given by P_2. When the electron is in the excited state, we can express the rate of its spontaneous emission with the following expression:

$$\frac{dP_2}{dt} = A_{21}P_2 \tag{5.3}$$

where A_{21} is the Einstein coefficient for the decay rate from the excited (2) to the ground (1) state. This equation can be solved to give an exponential decay rate with a decay constant $\tau = 1/A_{21}$ where τ is the radiative lifetime of the state. From the ground state, a similar equation can be made for the probability of absorbing a photon and exciting the electron out of the ground state:

$$\frac{dP_1}{dt} = -B_{12}P_1\mu(\omega), \tag{5.4}$$

where B_{12} is the Einstein coefficient for absorption and $\mu(\omega)$ is the spectral density of excitation source (e.g. a laser) with a mean frequency of ω. The B_{12} term is effectively the capture cross-section (i.e. the probability of absorbing a photon) and the $\mu(\omega)$ term is the rate of photons incident on the atom (i.e. the laser power). If one were to illuminate the two-level system such that the absorption and illumination reached a steady state then the system could be expressed in the following way:

$$\frac{d\vec{P}}{dt} = \begin{pmatrix} -B_{12}\mu(\omega) & A_{21} \\ B_{12}\mu(\omega) & -A_{21} \end{pmatrix} \vec{P}, \tag{5.5}$$

where $\vec{P}$ is a vector of P_1 and P_2. In this rate equation, spontaneous emission is ignored and the rate of absorption and emission creates an equilibrium. This can be solved to obtain the probabilities of the electron being in either of the two states.

This methodology can be applied to the NV, however, it is more complicated as there are multiple sources of excitation (green laser pumping, microwave sources and ionizing lasers) as well as multiple energy states with various forms of decay (e.g. radiative and non-radiative decay pathways). Thus, similar to the two-level system. The goal is to make a vector of all the NV energy levels we want to study, as well as their various decay pathways and the various pulses we want to apply to them. Once this is achieved, the probability vector is solved numerically using matrix exponentials.

Figure 5.2 shows the energy level diagram for the rate equation model being used in this simulation. The energy levels are mostly the same as shown in other parts of this thesis, with the degenerate ± 1 spin levels and the ^{2}E+e energy level representing

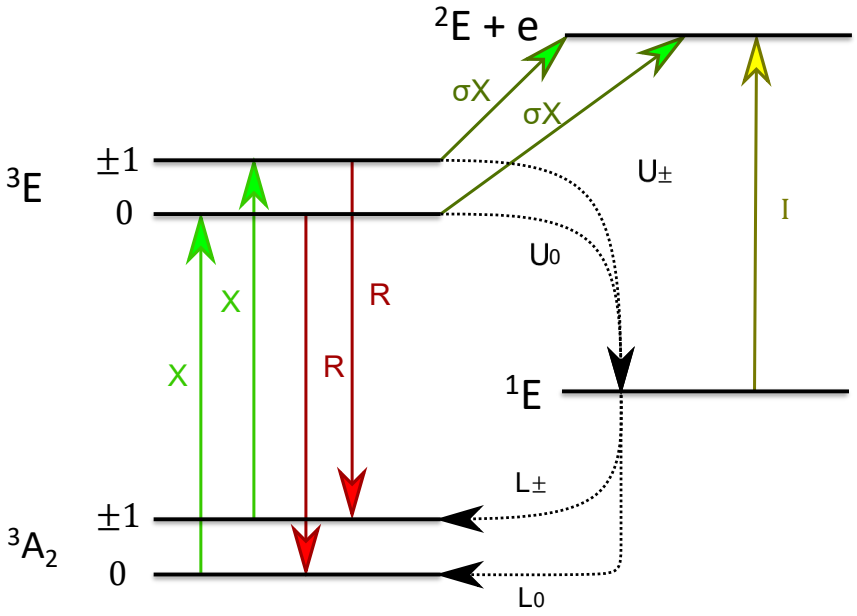

Figure 5.2: Image of the NV states considered in the rate equation model with the various transitions labelled including the ionised NV^0 ^{2}E state with an electron (e) in the conduction band. Note in the rate equation the excited singlet $^1A_1$ level is removed for computational simplicity. The solid arrows indicate radiative transitions for both excitations and emissions whereas the dotted lines indicate non-radiative ISCs.

the ionised NV^0 state with an electron in the diamond conduction band. This system features labels that represent the various excitations and relaxation pathways expected in the SCC protocol. The green X terms represent the spin selective excitation from a green laser which excites the triplet manifold but also excites from the $^3A_2$ to the ^{2}E state via two-photon ionization. The ratio of absorption in the triplet to the two-photon ionization is given by σ:

$$\sigma = \sigma_I / \sigma_A, \tag{5.6}$$

where σ_A is the absorption cross-section and σ_I is the photoionization cross-section. Note that the microwave pulse that performs the spin manipulation is implicit in this model and is assumed to excite with 100% probability [124]. Also, note that the excitations are a single constant representing both the photon capture Einstein coefficient as well as the energy spectral density. The red R terms represent the radiative emission pathway and the U/L terms represent the spin-orbit non-radiative inter-system crossing (ISC). Note that in this model the excited $^1A_1$ level is removed for computational simplicity, as the decay rate is so fast from the $^1A_1$ to the ^{1}E state compared to all levels that the pathway to the ^{1}E state is effectively instantaneous [119]. Finally, the yellow I terms represents the ionization pulse, which although is ≈570 nm without the electrode, should change in the presence of the electrode.

Each energy level has different sources/sinks that either populate or depopulate

an electron from the level. These levels can be placed into a 6 level vector for all the energy states and a 6x6 matrix that governs all the transitions between the states, creating a rate equation similar to equation 5.5:

$$\frac{d\vec{P}}{dt} = \begin{pmatrix} -X & 0 & R & 0 & L_0 & 0 \\ 0 & -X & 0 & R & L_\pm & 0 \\ X & 0 & -(R+U_0+\sigma X) & 0 & 0 & 0 \\ 0 & X & 0 & -(R+U_\pm+\sigma X) & 0 & 0 \\ 0 & 0 & U_0 & U_\pm & -(L_0+L_\pm+I) & 0 \\ 0 & 0 & \sigma X & \sigma X & I & 0 \end{pmatrix} \vec{P}, \tag{5.7}$$

if we call the matrix in equation 5.7 **M** and over some time period, **M** becomes constant (steady state approximation) then $\vec{P}$ can be solved using the following matrix exponential:

$$\vec{P}(t) = e^{\mathbf{M}t} \cdot \vec{P}(0), \tag{5.8}$$

which can be achieved numerically. The initial condition $\vec{P}(0)$ is the vector state representing where the electron population is at the beginning of the protocol. In this work, we assume that the electron in the NV can be initialised into a particular spin state with 100% fidelity. Whilst this isn't precisely true, it can be achieved with near-unity fidelity with careful manipulations [54]. As a result, The initial states in this system are the following:

$$\vec{P}(0)|_{ms=0} = \begin{pmatrix} 1 \\ 0 \\ 0 \\ 0 \\ 0 \\ 0 \end{pmatrix}, \vec{P}(0)|_{ms=\pm1} = \begin{pmatrix} 0 \\ 1 \\ 0 \\ 0 \\ 0 \\ 0 \end{pmatrix}, \tag{5.9}$$

where $\vec{P}(0)|_{ms=0}$ is the initial state with all the electron population in the first $m_s = 0$ state and $\vec{P}(0)|_{ms=\pm1}$ is the initial state with all the electron population in the second $m_s = \pm1$ state. The solution to equation 5.8 will give a vector of state probabilities based on the values in the matrix as well as the initial conditions. In this vector, the last entry corresponds to the probability of the electron existing in the ionised state at the end of the SCC process. Thus, the spin optical contrast is calculated to be:

$$C = P_6|_{ms=\pm1} - P_6|_{ms=0}, \tag{5.10}$$

where P_6 is the sixth entry in the vector which is calculated after the process has been solved for the spin zero case and the spin ±1 case.

The relaxation (R, U and L) rates are intrinsic properties of the NV that can be found experimentally. The radiative relaxation rate used in this study is R = 65.3 MHz

[117], the upper ISC rates are: U_0 = 6.7 MHz and $U_\pm$ = 53 MHz, and the lower ISCs are: L_0 = 2.38 MHz and $L_\pm$ = 0.35 MHz [60]. For the excitations rates, X and I can be expressed using the following:

$$X = \gamma_X \mu_X \quad , \quad I = \gamma_I \mu_I, \tag{5.11}$$

where $\gamma_{X,I}$ is the absorption cross-section for each laser and $\mu_{X,I}$ is the spectral density for each laser, equivalent to the Einstein coefficient and spectral density in equation 5.4. The cross-section is a constant factor dependent on the wavelength of the laser and the spectral density is a variable dependent on the laser power as well as the duration of the laser pulse, thus, these three factors are the main parameters that are altered to optimise the SCC protocol. The choice of these values can have dramatic effects on the overall optical spin contrast and so must be chosen carefully. For example, powerful green (X) excitation lasers will improve initialisation into the singlet state for ionization, however, it will also increase the two-photon ionization rate σX. Alternatively, longer ionization pulses (I) can increase the ionization rate but it is important to limit the pulse time to less than the lower singlet state lifetime of $\approx$200 ns [2] as further pulsing will have no ionization effect on an electron that has decayed back into the ground state triplet. In section 5.2 the rate equation 5.7 is solved in a variety of conditions and the ideal pulse rates and times are optimised to give the highest possible optical spin contrast.

5.2 Rate equation modelling of electrode protocol

In order to solve equation 5.7 we need the ratio of the absorption to photoionization cross-section (σ). This value tells us the probability of the electron being raised to the excited triplet state or ionised into the diamond conduction band during green excitation (X). Ideally, we want this value to be as low as possible as this will ionise electrons in the $m_s = 0$, lowering spin contrast. This value is typically set by the intrinsic properties of the NV but can be theoretically altered by the electrode. In this section, we solve for the optical spin contrast in the case where the electrode shifts the NV levels to prevent cross-talk but doesn't affect the two-photon ionization process. This would be achieved with a two-step electrode potential, where the electrode is off during the pumping phase but has a positive potential during the ionization phase. In section 5.4 we consider the alternative where the electrode has a negative potential during the pump phase, decreasing two-photon ionization and a positive potential during the ionization phase, reducing cross-talk. The main purpose of this study is to observe the SCC protocol in a regime where the effect of the electrode is relatively well known. Shifting the energy levels to the point where two-photon ionization is zero requires a very large electrode potential and may have unexpected consequences on the energy levels, thus it is only considered conceptually in section 5.4.

To work out σ, the ratio of the absorption cross-section and the photoionization cross-section is taken for a given excitation energy. To achieve this we need to calculate the absorption sideband of the NV in a similar way that was performed in section

4.2. Note that the ratio is the key data, not the cross-section itself, this means that the units are not important as long as they are the same across the two data sets. The idea is to re-create the NV absorption data from figure 4.4 for ambient conditions and take the ratio at the energy of the green laser excitation (≈2.3 eV). As phonons broaden the transition energies, the expectation is that at 300 K, the absorption cross-section will look also to broaden, however, the photoionization cross-section is already smooth and therefore isn't expected to change with temperature. Recall from section 4.2 we studied the absorption cross at room temperature by applying a similar calculation from Davies et al. [20, 25] which uses the Frank-Condon theory of electronic and vibrational interactions during an electronic transition along with the Huang-Rhys model of transitions in a defect. The theory states with a temperature-dependent electron-phonon coupling, the function that describes the vibrational overlap is given by:

$$F(\omega, T) = e^{-S} \sum_{i=1}^{\infty} \frac{S^i}{i!} F_i(\omega, T), \tag{5.12}$$

where S is the average Huang-Rhys factor. The Huang-Rhys factor is a measure of the interaction of defect electrons with phonons in a crystal lattice [55] and can be expressed with the following:

$$S = \int_0^{\Omega} \Big(2n(\omega, T) + 1\Big) f(\omega) d\omega, \tag{5.13}$$

where $n(\omega, T) = 1/(e^{E/k_b T} - 1)$ is the temperature-dependent Bose-Einstein distribution of phonons and $f(\omega)$ is the low temperature one-phonon sideband function. This function describes the single electronic transition that can either create or annihilate a single phonon. It can be approximated by deconvolving the 0 K absorption sideband given in figure 4.4 [95]. The temperature-dependent function describing the vibrational overlap of an electronic transition with one phonon can then be expressed as:

$$F_1(\omega, T) = \begin{cases} \big(n(\omega, T) + 1\big) f(\omega) & \omega > 0 \\ n(-\omega, T) f(-\omega) & \omega < 0 \end{cases}, \tag{5.14}$$

where the negative frequency $-\omega$ allows for the annihilation of phonons and sets ω as the transition frequency relative to the zero phonon transition frequency.

To obtain the function for a two phonon interaction equation 5.14 is then convolved with itself:

$$F_2[\omega, T] = F_1(\omega, T) * F_1(\omega, T) = \int_{\infty}^{\infty} F_1(\omega - x, T) F_1(\omega, T) dx, \tag{5.15}$$

then to obtain any arbitrary number of phonon interactions, equation 5.14 is simply convolved with itself the number of times required to obtain $F_i(\omega, T)$. By using the experimentally obtained Huang-Rhys factor of 3.49 [63], setting the temperature to 0 K and convolving the solution eight times the absorption spectrum shown in figure

4.4 can be reproduced. By keeping the same parameters but setting the temperature to 300 K we can obtain a new absorption side-band for the electron-phonon interactions at high temperature.

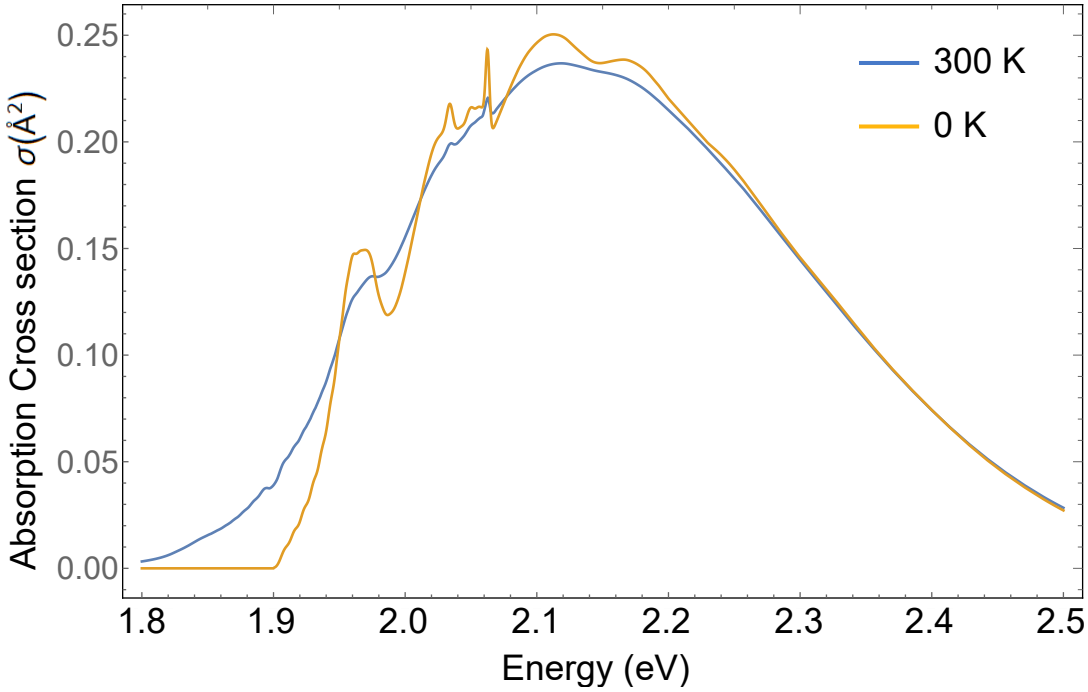

Figure 5.3: Plot of the absorption cross-section calculated using Huang-Rhys theory. The yellow curve is the solution at 0 K and is a match for the absorption cross-section data shown in figure 4.4. The blue curve is the same calculation performed at 300 K. At higher temperatures, the data broadens, and lowers slightly in amplitude which is expected.

Figure 5.3 shows the absorption spectrum for the NV across a range of electron energies. The yellow curve shows the calculated absorption spectrum at 0 K which is the same as the data taken from figure 4.4 without the ZPL. The blue curve shows the same absorption spectrum calculated at 300 K. As expected, the data is largely the same, but the higher temperature electron-phonon interactions broaden the absorption spectrum. Whilst the ZPL is missing from both data sets, even at 300 K, it is only about 1 THz in width [32]. Such a thin peak won't contribute significantly to the convolutions so the ZPLs are removed for computational simplicity. From this data, the cross-section for absorption can be compared to the cross-section for photoionization from figure 4.4 at 2.3 eV to obtain a ratio of ≈0.26. This ratio is then used as the σ value in the rate equation modelling.

The rate equations were initially solved under different laser excitations and pump times whilst keeping the other variables constant. The results of these studies help validate the model and also inform future simulations of the ideal bounds for the laser power and pulse times for optimisation studies. Figure 5.4 shows the transient

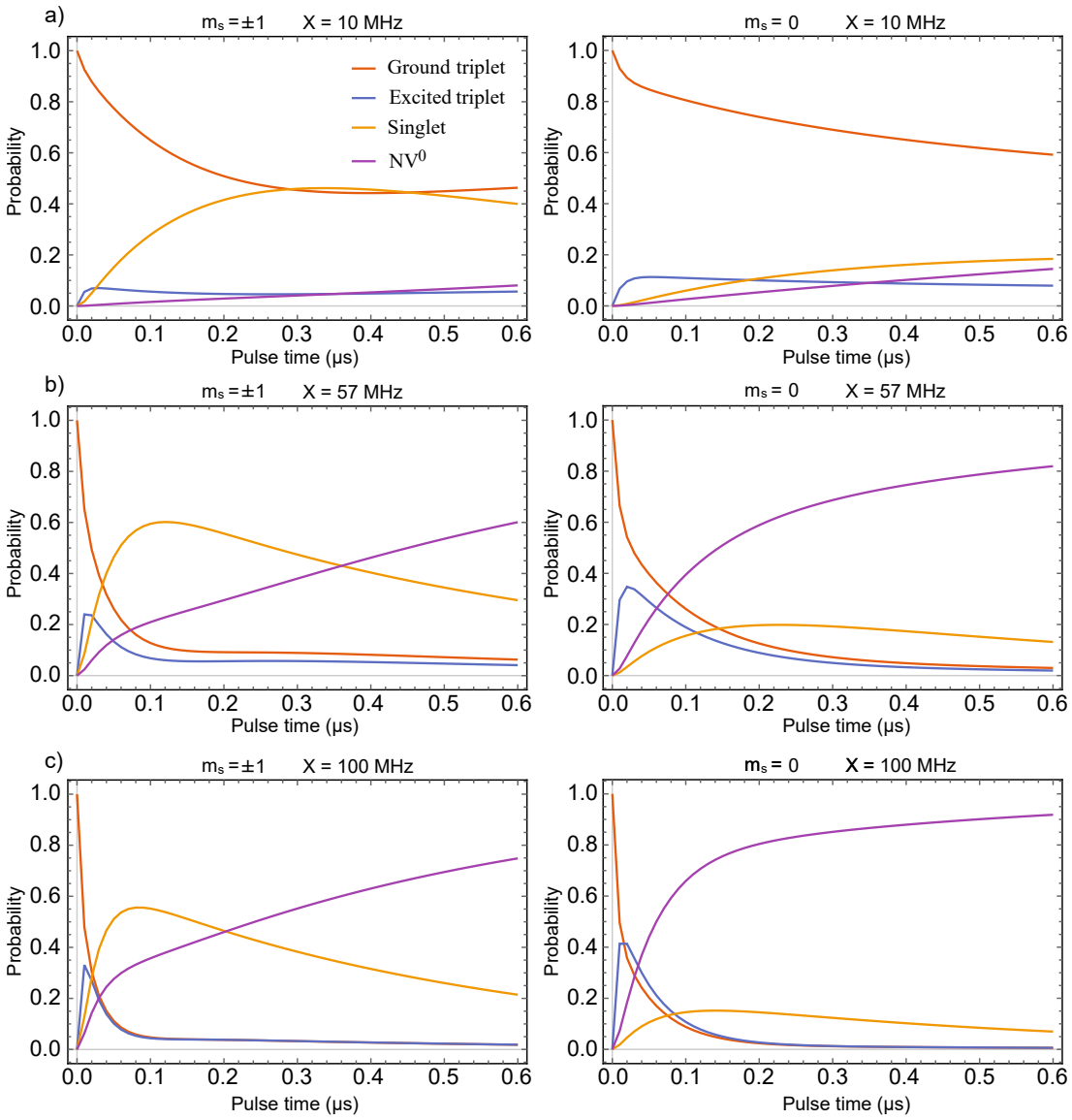

Figure 5.4: Plots of the electron state probability for different green (X) excitation powers are plotted over different pulse durations. The excitation powers used are a) 10 MHz, b) 57 MHz and c) 100 MHz and are plotted for the $m_s = \pm 1$ initialisation (left) and $m_s = 0$ initialisation (right). The figures validate the model as the populations follow an expected path, in addition, they also highlight how powerful green lasers increase excited state population as well as ionised state population. This motivates a choice of laser power and pulse time which maximises pumping into the singlet state without causing ionisation.

evolution of the ground state (orange), excited-state (blue), singlet state (yellow) and ionised state (purple) with changing green laser parameters. In this study, there is no ionisation pulse (I=0 in the rate equation 5.7), the pulse times are varied from

0 to 600 ns and the results are ordered in increasing intensity: 10 MHz (fig 5.4a)), 57 MHz (fig 5.4b)) and 100 MHz (fig 5.4c)). This study was done for the $m_s = \pm 1$ initialisation (left images) and the $m_s = 0$ initialisation (right images). The results show that over time, the green excitation will shift the populations in an expected way. The electron population begins in the ground state, in all simulations and decays in time with the fastest decay occurring at the highest intensity, where the population in the ground state becomes effectively zero. During this time, the excited state population will rise but decays as the population moves from the excited state to either the singlet state, the ionised state or back to the ground state. The singlet state also increases during this time but decays as the lower ISC process move electrons out of the singlet. Whilst the neutral state will decay eventually under optical illumination due to recombination, its lifetime under these conditions is long compared to any other state lifetime (on the order of milliseconds [7]). As a result, recombination is ignored in this study so the probability of occupying the ionised state will increase steadily during the whole process. The results also show the spin selectivity in the upper ISC, as the population in the singlet state is higher for the $m_s = \pm 1$ initialisation compared to the $m_s = 0$ initialisation which is expected. The results also show that this selectivity is altered with green laser power. At low power there is less population in the excited triplet state, thus reducing the amount of ISC, lowering the singlet state population. At very high power there is the population in the excited state is higher, but two-photon ionisation limits the excited state population and by extension, the singlet state population. This means that a middle ground must be applied to effectively pump electrons into the singlet state in a way that minimises two-photon ionisation. Additionally, the time when the ionisation should occur is also important as the maximum singlet state population only occurs at a particular point in time before decaying back into the triplet manifold, providing a rough idea of how long the excitation pulse should be as well as its power. Overall the results are expected and help apply upper and lower bounds in the optimisation process for both pulse power and pulse time.

To obtain an understanding of the effects of the ionisation laser a second study was performed. In this study, the green excitation was performed with constant values and an ionisation pulse was performed afterwards. To achieve a multiple pulse system, we to create two separate rate equation matrices and apply them together with a dot product:

$$\vec{P}(t) = e^{\mathbf{M}_{ion} t_{ion}} \cdot e^{\mathbf{M}_{pump} t_{pump}} \cdot \vec{P}(0), \tag{5.16}$$

where $\mathbf{M}_{pump}$ is the rate equation matrix from equation 5.7 with I=0, $\mathbf{M}_{ion}$ is the rate equation matrix where X=0 and each matrix is run for a specific amount of time, t_{pump} and t_{ion} (pulse duration). Figure 5.5 shows the solution of equation 5.16 under different conditions for the ground state (orange), excited-state (blue) and ionised state (yellow). In the plots, the excitation has already occurred and t=0 refers to the time when the ionisation pulse starts. Thus, the initial populations are different depending on the excitation conditions. Figure 5.5a) shows the ionisation dynamics

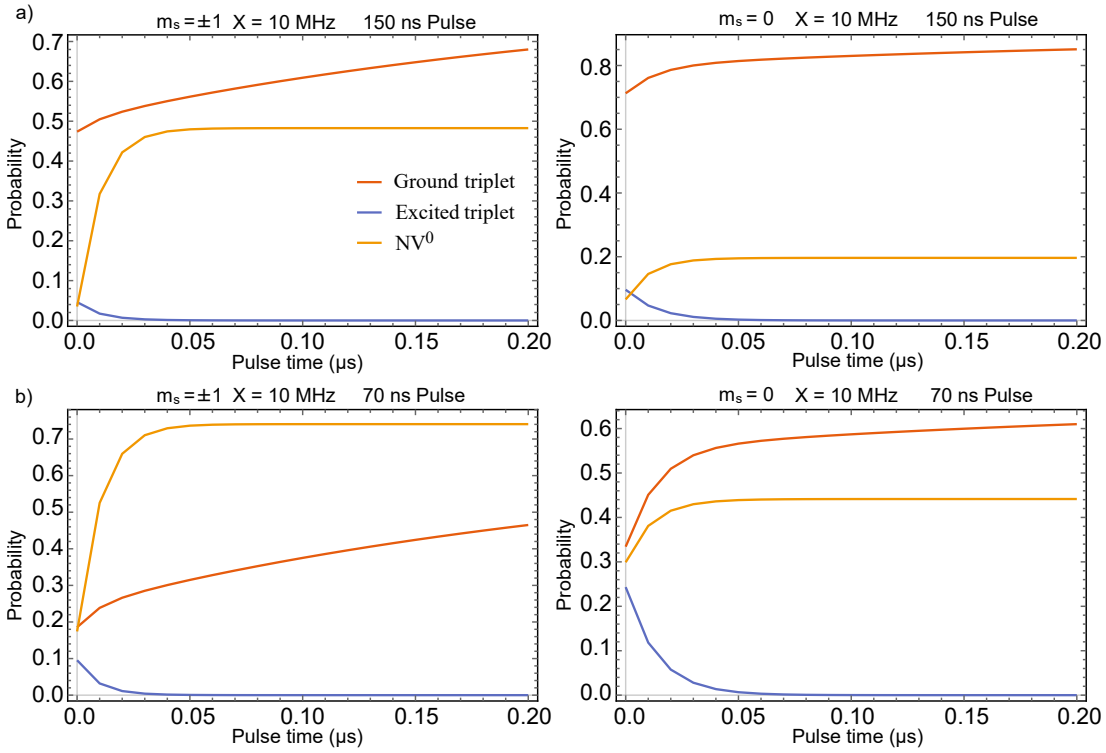

Figure 5.5: Plots of the NV probabilities with the addition of an ionisation pulse. In all the plots the ionisation is 100 MHz and pulses for up to 200 ns (x-axis). The top images a), show the probabilities for a low, 10 MHz laser power with a 150 ns green laser excitation. The bottom b) plots show the probabilities for the higher power, 57 MHz, with a 70 ns pulse. Both a) and b) are plotted for the $m_s = \pm 1$ (left) and $m_s = 0$ (right) initialisation.

after a 10 MHz green laser pulse for 150 ns, figure 5.5b) shows the same dynamics after a 57 MHz green laser excitation for 70 ns. Both simulations have an ionisation pulse that is 100 MHz in power and pulses for up to 200 ns (the singlet state lifetime). In the plots, relatively high ionisation laser ionises out of the singlet state, raising the ionised population quickly which then saturates. This is expected, unlike the green laser which can cause two separate transitions, with the electrode, the ionisation pulse only creates one transition so there is less need to optimise as the ideal ionisation rate is the maximum pulse power. At high power, the ionisation pulse ionises the singlet electron and the saturation occurs due to the probability of the electron being in the singlet state in the first place. In other words, if there is a 40% chance of the electron being pumped into the singlet state, then the high power ionisation will excite the electron into the conduction band with near 100% probability and the probability overall of being the ionised state depends solely on the probability of pumping the electron into the singlet state (40%). This is shown in the difference in ionised population from figures 5.5a) and 5.5b) despite the same ionisation laser parameters. The only other

path out of the singlet is the lower ISC, but if the ionisation pulse duration is much lower than the singlet state lifetime, then this process can be ignored. This assumption is valid as the speed at which the ionised state saturates happens within 50 ns in all the figures. The other limitation to this process is the singlet state population that occurs when the state is initialised into the $m_s = 0$. Whilst there is higher ionised population in the $m_s = \pm 1$ initialisation, it is clear that there is still ionised population in the $m_s = 0$ initialisation. From the rates used in this study, it is known that the branching ratio from $m_s = 0$ excited state to the singlet isn't 0%, thus there is always a source of erroneous ionisation. As this process comes from an intrinsic part of the NVs ISC, this factor will always affect the overall contrast and cannot be removed.

The results of these studies suggest that the key mechanism to achieving high contrast lies in the ability to pump the electron into the singlet state. With the electrode reducing cross-talk and allowing us to use a wavelength that is suitable for ionisation, the ionisation rate is near 100% with a powerful laser. Thus the green laser will be the key part of the optimisation process. Figure 5.6 shows the results of optimisation processes performed over a range of green laser excitations (figure 5.6a)) and pulse times (figure 5.6b)). In this simulation, the optimal spin contrast was calculated numerically by solving the two-step rate equation 5.16 and calculating the optical spin contrast using equation 5.10. This solution was then optimised over the following values in two separate simulations:

$$Opt(a) = \begin{matrix} 1 < I < 300 \\ 0.005 < t_{ion} < 0.2 \\ 0.005 < t_{pump} < 0.2 \end{matrix} \quad Opt(b) = \begin{matrix} 1 < X < 300 \\ 1 < I < 300 \\ 0.005 < t_{ion} < 0.2 \end{matrix}, \tag{5.17}$$

where $Opt(a)$ is the optimisation parameters with varying pulse power and $Opt(b)$ are the optimisation parameters with varying pulse duration. The plots show a steady increase which maximises at an optimum pulse power and pulse duration. These results make physical sense, as the optimum value follows the logic of the previous simulations with modest pulse power and short pulse duration. The overall optimal contrast occurs with the following parameters: $\mathbf{X} = 29$ MHz, $\mathbf{I} = 300$ MHz, $\mathbf{t}_{pump} = 100$ ns, and $\mathbf{t}_{ion} = 30$ ns, which give a contrast of 33%. These values make sense; the ionisation pulse improves contrast when it is maximal in its power but figure 5.5 shows that maximal pulse duration is unnecessary as the ionisation rate saturates quickly. The green laser required a modest power and low pulse duration to optimise the singlet state probability whilst minimising two-photon ionisation.

Whilst the results of this initial simulation makes intuitive sense, the overall contrast is lower than the contrast shown in Jaskula et al. with 36% [58]. This is likely due to the two-photon ionisation process. In Jaskula et al., the two-photon ionisation process is a feature of the protocol which is mediated by using two separate lasers to alter the ionisation-absorption ratios (considered in more detail in section 5.3). One way to limit two-photon ionisation in our SCC protocol would be to alter the ratio using the electrode which is considered in section 5.4. However, there is another method that can be applied immediately to improve the optical spin contrast. The technique which is applied in the next simulation was inspired by Hopper et al.

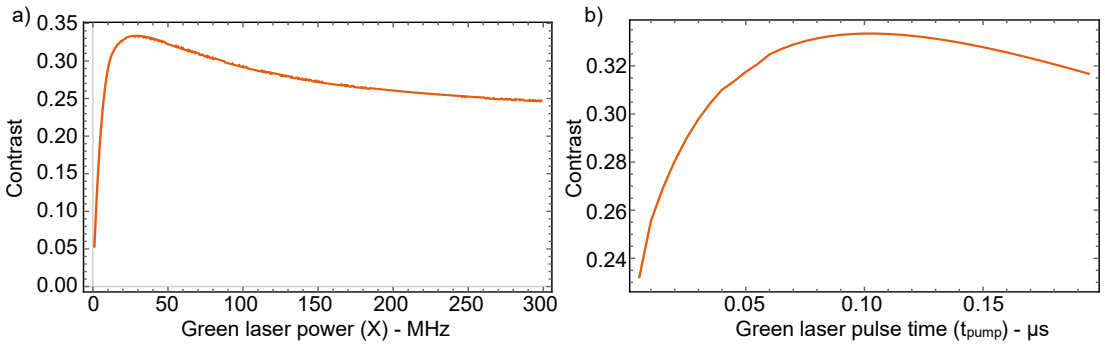

Figure 5.6: Plot of the optical spin contrast optimisation as a function of a) green laser excitation and b) green laser pulse duration. In both plots, the contrast steadily increases until reaching an optimum value of 33% before dropping in value.

[53]. In their work, they improve contrast by running the pulse sequence more than once and optimising the pulses for each run (figure 5.7). The idea is that during the pumping phase, when initialised in the $m_s = \pm 1$ state, the electron can be pumped by the green laser into the excited triplet state and decay via the non-radiative ISC or the radiative path back into the ground state. By running the SCC protocol multiple times for the same electron there is an extra chance at pumping the electron into the singlet which decayed to the ground state. In each pumping phase, the laser can have different values to optimise over to improve the process. Thus if the electron isn't in the singlet state in the first run, it might be in the second or third:

$$\vec{P}_p(t) = e^{\mathbf{M}_{ion1}t_{ion1}} \cdot e^{\mathbf{M}_{pump1}t_{pump1}} \cdot e^{\mathbf{M}_{ion2}t_{ion2}} \cdot e^{\mathbf{M}_{pump2}t_{pump2}} \cdot \vec{P}(0), \tag{5.18}$$

where the number in the subscript indicates a new rate matrix with a different laser power or a new pulse duration time. Equation 5.18 shows only two runs of the SCC protocol but in principle, any number of sequences can be made at the cost of the overall time of the protocol. The only limiting factor in the time would be the spin coherence time which is typically much longer than the nanosecond duration of the entire SCC protocol. In practice, as more sequences are added, the likelihood of pumping into the singlet increases which means that each subsequent run increases the contrast by smaller and smaller amounts as the probability of the electron remaining in the triplet state gets smaller. The simulation showed a reasonable increase when adding up to three runs of the SCC protocol and found that the increase in contrast for four or more runs is negligible. Another consideration in this process is optimising power; experimentally, changing the pulse duration is simple as it is applying a different voltage pulse to an acoustic-optic modulator (AOM) to change the laser pulse gates which can happen almost instantaneously. Changing the power of a laser takes a lot more time or requires coupling in two separate lasers into the system. For experimental simplicity, the pulsing simulations optimise over a single laser power for both the pumping and ionising lasers whilst optimising over a new pulse duration for each run of the protocol.

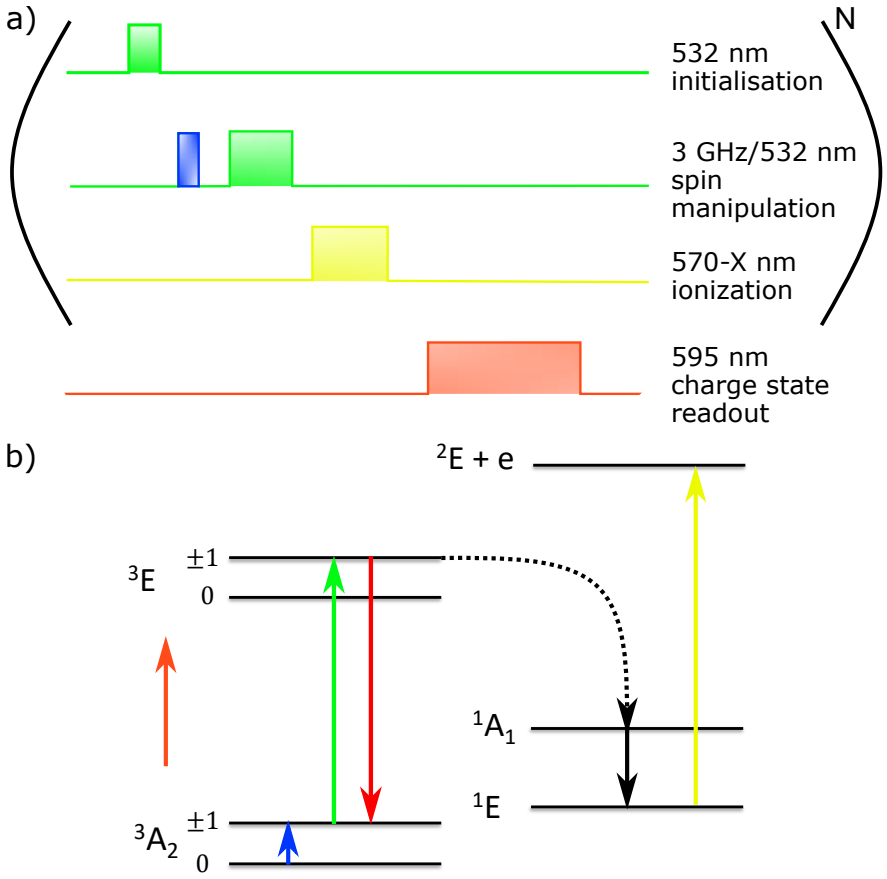

Figure 5.7: Image of the pulsing mechanism: a) is the standard pulse sequence used in figure 5.1 but the sequence is repeated N times before undergoing the orange charge state readout. This sequence is reflected in b) which is also the pulse sequence in figure 5.1 but with the red relaxation rate in the diagram. The idea is that when the NV electron is excited in the triplet, it might decay back into the ground state instead of the blue ISC. In that case, the repeat pulse sequence will be applied a second or third time to try and pump the electron into the singlet state for ionisation.

Using the pulsing system, a new protocol was developed where the SCC protocol was run three times for the one electron in an NV. Each new run of the simulation carried a new pulse duration to optimise over which gave an optical spin contrast of 42% with the following parameters: $\mathbf{X} = 15$ MHz, $\mathbf{I} = 294$ MHz, $\mathbf{t}_{pump1} = 65$ ns, $\mathbf{t}_{pump2} = 79$ ns, $\mathbf{t}_{pump3} = 100$ ns, $\mathbf{t}_{ion1} = 50$ ns, $\mathbf{t}_{ion2} = 50$ ns and $\mathbf{t}_{ion3} = 23$ ns. As mentioned in the introduction to this chapter, this contrast is about 6% higher than the experimentally realised spin contrast achieved in Jaskula et al. [58] however requires more experimental apparatus to achieve (the electrode). It is, however, important to note that the contrast reported in Jaskula et al. is experimental so the comparison is not an accurate one. In order to obtain an accurate comparison, the rate equation method used in these simulations should also be applied to the Jaskula protocol so

that two theoretical values which were derived from the same methodology can be critically compared.

5.3 Comparison to Jaskula et. al.

The SCC protocol applied in Jaskula et al. is in a lot of ways, the inverse of the protocol we present in this chapter. In our protocol, the idea is to ionise when the electron is in the singlet state, thus mapping the $m_s = \pm 1$ state into the NV neutral charge state. In the Jaskula protocol, a 594 nm laser shelves the $m_s = \pm 1$ into the singlet state and the $m_s = 0$ state is ionised with a powerful red 637 nm laser in a two-photon process. As a result of this, the $m_s = \pm 1$ is mapped to the negative NV^- state and the $m_s = 0$ state is mapped to the neutral NV^0 state, the opposite mapping of our protocol. At 595 nm, the ratio of ionisation to absorption is lower compared to the green 532 nm (0.16 compared to 0.26 respectively) which can be read off the same plot performed in the previous section (the ratio of absorption in figure 5.3 vs photoionization in figure 4.4). This means that the rate of two-photon ionisation when shelving into the singlet is lower compared to our method. The 637 nm is the resonant ZPL of the NV and the absorption rate is very high compared to ionisation in this limit, even at room temperature. However, 637 nm is lower in energy compared to the predicted 570 nm energy required to ionise out of the singlet state, so this choice of laser will reduce erroneous ionisation out of the singlet state. The ionisation out of the triplet occurs by using a very high power laser to re-excite if the electron decays back into the ground state and knowing that the chances of non-radiative ISC in the $m_s = 0$ state are low.

To obtain the optical spin contrast of the Jaskula method, rate equation modelling is used in a similar way as the previous section featuring the two-step pulse system from equation 5.16 with some adjustments:

$$\vec{P}_j(t) = e^{\mathbf{M}_{ionJ} t_{ionJ}} \cdot e^{\mathbf{M}_{pumpJ} t_{pumpJ}} \cdot \vec{P}(0), \tag{5.19}$$

where $\mathbf{M}_{ionJ}$ and $\mathbf{M}_{pumpJ}$ are the same matrices from equation 5.7 but with I=0 and with different σ values to reflect the change in the absorption to ionisation ratio for the different lasers. For $\mathbf{M}_{pumpJ}$, σ=0.16 which reflects the two-photon ionisation for the 594 nm laser designed to pump electrons into the singlet state. For $\mathbf{M}_{ionJ}$, the ratio needs to be found for the 637 nm laser used in ionisation which is the ZPL of the NV. Figure 5.8 shows the same room temperature absorption spectrum from figure 5.3 but with a ZPL added in as a Lorentzian whose linewidth at 300 K is 1 THz which is experimentally obtained from Fu et al. [32]. From this figure and the photoionization cross-section in figure 4.4, the ratio was calculated to be 0.1.

With the ratios for the different lasers found, equation 5.19 can be solved using the same parameters and optimising over the 594 nm pump laser as well as the 637 nm ionisation laser. Using this method we calculate an optical spin contrast of 37% with the following parameters: $\mathbf{X}_{pump} = 185$ MHz, $\mathbf{X}_{ion} = 300$ MHz, $\mathbf{t}_{pump} = 26$ ns, $\mathbf{t}_{ion} = 97$ ns. This value is 1% higher than the experimental value reported in Jaskula

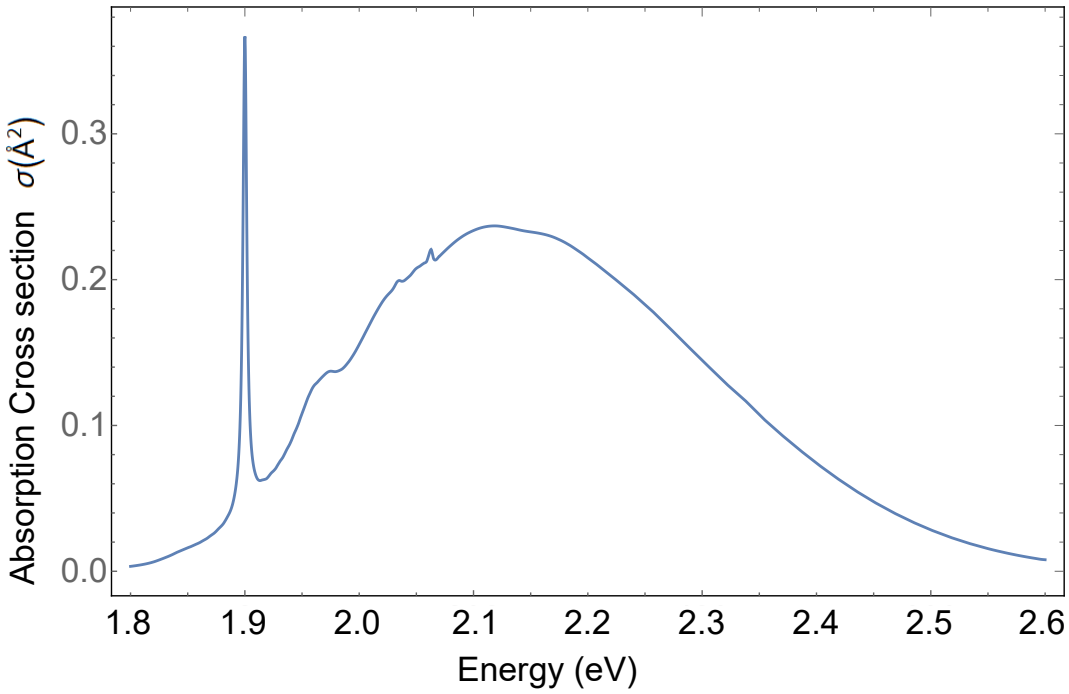

Figure 5.8: Plot of the same room temperature absorption cross-section used in figure 5.3, with the ZPL added in. The ZPL is added as a Lorentzian peak with a linewidth given by Fu et al. [32].

et al. [58] which is likely a reflection of imperfect experimental parameters.

It has been mentioned that the Jaskula method is simpler compared to the method presented in this thesis. The main reason for this is that the Jaskula method does not require the extra technical considerations of the electrode over the diamond. This also makes the method more suitable in instances where the electrode can be physically cumbersome. For example, in a sensing operation, the closer the source is to the NV probe, the larger the signal and the easier it is to sense. The presence of the electrode will improve optical contrast and by extension, sensitivity, but if it pushes the source further away from the NV then it might not be worthwhile. Additionally, the Jaskula method would be more suitable for sensing in conditions where fabricating an electrode might be difficult, for example, on top of diamond nano-pillars. The method introduced in this thesis does have its advantages.

The major advantage is that ionisation from the singlet allows for the extra pumping methods utilised in the last section which raises the contrast from 33% to 42%, a significant increase that allows the overall contrast to surpass the Jaskula method by up to 5%. We can relate the change in spin optical contrast to sensitivity by using the DC magnetic sensitivity from Rhondin et al. as an example [99]:

$$\eta_{dc} \sim \frac{1}{g\mu_B} \frac{1}{C\sqrt{nT_2^*}}, \tag{5.20}$$

where g is the g-factor for the magnetic moment, μ_B is the Bohr magneton, $n = t_l * P$ is the optical collection efficiency defined by the total counts obtained from the NV P_0 and the time of the readout t_l. T_2^* is the NV electronic spin dephasing time and C is the optical contrast. In principle, all the factors are constant except for the change in contrast, so the improvement in sensitivity is proportional to $1/C$. By subtracting the difference in the inverse contrast of one method to the other, we can predict that the Jaskula method offers an improvement in DC magnetic sensitivity of $\approx$1.2, compared to conventional optical cycling. The method in this thesis offers an improvement in sensitivity of $\approx$1.6. The main reason for the improvement is that the Jaskula protocol does not allow for re-pumping. The reason for this is that each ionisation phase of the SCC protocol occurs in the triplet manifold and thus would ionise the $m_s = \pm 1$ electron state erroneously. Overall, the technique in this thesis is much more suitable in situations where contrast is important and geometry is not. For example, in macro sensing where the variations in the field are much larger than the sensor or in the design of a quantum chip for quantum computation where there is no source to sense.

Whilst the method with the electrode does modestly improve optical spin contrast, the real advantage lies in its potential capabilities. In the section 5.4, various ways of improving the contrast using the electrode are considered. This includes simple additions such as using the same lasers applied in Jaskula et. al. to reduce the two-photon ionisation rate. It also includes the alternative of reducing the two-photon ionisation by shifting the NV energies relative to the diamond conduction band in a two-step electrode potential mentioned at the beginning of this section. Finally, the section ends with another potential use of the electrode which is altering the rate of two-photon ionisation and recombination, creating charge state control, which has the potential of improving the NV coherence time and optical collection efficiency.

5.4 Discussion and future direction

The two key concepts that were discussed in the previous section that can improve the optical spin contrast are changing the lasers used in the SCC protocol and changing the electrode potential. Recall that the effect of these two methods is the same, the goal is to change the ratio of absorption to ionisation in the triplet manifold to maximise the probability of pumping the NV electron into the singlet state for ionisation. When changing the laser power the idea is to take the ratio at a new energy for both absorption and ionisation, one where the ratio is much smaller for ionisation. When applying the electrode, the energy gap in the NV levels do not change and by extension neither will the absorption cross-section. However, the shift in the energy gap from the triplet to the conduction band will increase. This has the effect of moving the photoionisation cross-section in figure 4.4 to the right, increasing the minimum energy required to perform the two-photon ionisation. If the gap increases to the point where the minimum energy gap is larger than the excitation laser, then the two-photon ionisation rate will be zero. However, any shift in the

photoionization cross-section will cause a reduction in the cross-section as the curve is steadily increasing with energy.

In the previous work, the electrode was only activated during the ionisation phase of the protocol to change the energy gap of the singlet to the ionised state. To alter the two-photon ionisation process, the SCC protocol would involve a two-step electrode potential as opposed to the single potential used in the previous section. This concept is shown in figure 5.9, which shows the electrode potential, V and its effects on the excited state triplet ^{3}E and the singlet ^{1}E compared to the ionised state ^{2}E + e. Figure 5.9a) shows the effects of the single-step potential considered in the previous section and figure 5.9b) shows the two-step potential. In the two-step potential, the electrode would initially have a negative potential (blue) for the pumping phase, shifting the NV energy levels away from the conduction band and reducing the probability of two-photon ionisation. This is shown in figure 5.9 by the green laser arrow which can make the gap from the ^{3}E state to the ionised ^{2}E + e state in figure 5.9a) but cannot in figure 5.9b) as the negative potential shifts the energy level downward, increasing the energy gap. In the second step of the process, the ionisation phase, the electron is in the singlet state and the electrode would have its polarity reversed. This creates a positive potential (red), shifting the NV levels towards the conduction band and improving the rate of photoionisation from the singlet whilst reducing cross-talk. This is shown with the yellow ionisation laser which can more easily make the energy gap from the singlet to the diamond conduction band without exciting the NV triplet levels.

In order to quantify these techniques we apply the same rate equation modelling as in the previous section but change the σ value to reflect the change in the ratio achieved by one of the techniques. For example, when applying the 595 nm laser to excite the NV triplet instead of the 532 nm laser the σ value changes from 0.26 to 0.15. We can solve equation 5.18 with this new σ value whilst applying the electrode, applying the same three pulse system, calculating the contrast using equation 5.10 and optimising over the same parameter space as used in 5.17. With this change, the optical spin contrast rises to 45% with the following parameters: $\mathbf{X} = 25$ MHz, $\mathbf{I}_{ion} = 292$ MHz, $\mathbf{t}_{pump1} = 40$ ns, $\mathbf{t}_{pump2} = 47$ ns $\mathbf{t}_{pump3} = 68$ ns, $\mathbf{t}_{ion1} = 32$ ns $\mathbf{t}_{ion2} = 19$ ns and $\mathbf{t}_{ion3} = 46$ ns. This improvement would result in a 1.7 fold increase in sensitivity compared to the 1.6 improvement shown in the previous section. Whilst this is a small increase, it is far from insignificant. It is also worth noting that in this setup the voltage required to shift the NV energies to remove cross-talk in the system is less than when using the higher energy 532 nm laser, potentially increasing the experimental robustness of the system.

Quantifying the effects of the electrode is a little more difficult. Figure 5.10 shows the optical spin contrast as a function of σ where for each value of σ, the optimisation process is performed with the same parameters used in equation 5.17. The contrast is maximised when σ is zero, i.e. when there is no two-photon ionisation process out of the triplet states. When σ=0, the green laser pumping is maximised at 300 MHz along with the ionisation laser and its pulse duration is short. In figure 5.10a), there is no pulsing system and the contrast maximises at 58%, in figure 5.10b) there is a

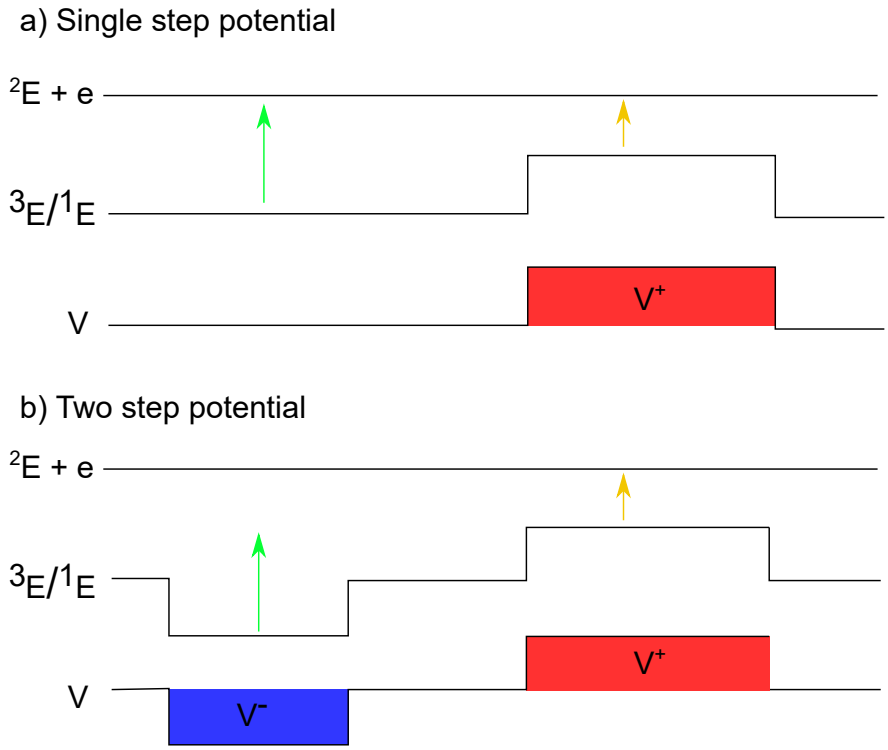

Figure 5.9: A simple diagram of the electrode pulsing effect. The diagram features the ^{2}E + e ionised state which does not alter appreciably with the electrode potential. It also features the ^{3}E excited triplet state and the ^{1}E singlet state which both shifts in the presence of the electrode potential by the same amount and are hence represented by the same line. In the single-step potential protocol a), there is only one potential applied, the positive potential (red) which shifts the NV energies towards the conduction band, allowing for easier photoionisation with a yellow laser (yellow arrow) in a way that does not cause cross-talk in the NV. In the two-step potential protocol b), there is an initial negative potential (blue), which shifts the NV levels downwards. This increases the energy gap to the conduction band so that the green laser (green arrow) does not have the energy required to drive the two-photon ionisation transition. After the green excitation, the same positive (red) potential is applied which alters the ionisation rate in the same way as in the previous protocol.

three pulse system and the contrast raises to 61%. Without two-photon ionisation, the main limitation of the optical spin contrast is the branching ratio at the ISC. This technique can be used in conjunction with a 595 nm laser, however, as long as the electrode potential is large enough to remove two-photon ionisation on its own, the process can be achieved with a more conventional 532 nm laser.

By using the same methodology as the previous section with the sensitivity equation 5.20, an optical spin contrast of 61% translates to a 2.36 fold improvement to the NV sensitivity compared to conventional ODMR optical cycling techniques.

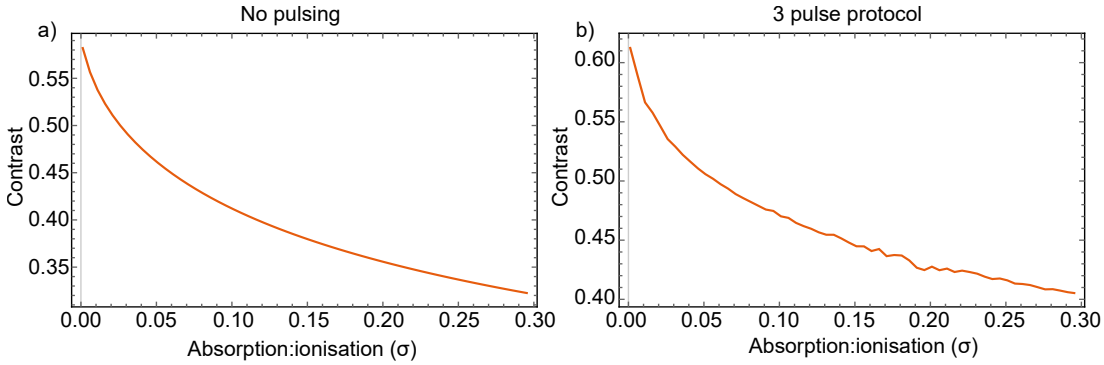

Figure 5.10: Plots of the optimisation processes as a function of changing absorption to photoionisation ratio σ. The left image a) is the optimisation process with no pulsing of the laser protocol, the right image b) is the same optimisation but with the pulsing sequence repeated and optimised three times. In both cases, the contrast is maximised when σ=0, i.e. no two-photon ionisation, with a steady decline in contrast with increasing σ. The pulsing system does, however, produce somewhat higher contrast rates.

However, using the electrode to alter the rate of two-photon ionisation has an added benefit. In a publication by Doi et al. [26], they postulate that improving the ratio of NV^- to NV^0 during optical illumination would improve the amount of photons the NV emits during a quantum operation. From equation 5.20, an improvement in photon counts will improve the NV sensitivity proportionally to $1/\sqrt{n}$, where n is the optical collection efficiency of the readout. To achieve this improvement, Doi et al. increase the amount of electron donors in the diamond with phosphorous doping during the chemical vapour deposition (CVD) process that grows the diamond samples. The higher density of donors would donate electrons to the NV more readily when it is ionised, thus increasing the average time the NV spends in the negatively charged state. Adding extra donors is detrimental during a SCC protocol as there would be less measurements of NV^0 in the charge state readout, reducing contrast. However, by using the electrode to selectively reduce two-photon ionisation, the NV charge state is preserved in cases where ionisation is unwanted. From Doi et al., with phosphorous doping and a 1 μW laser at 593 nm, the NV^- state increases to over 99% compared to the neutral state which translates to an almost five-fold increase in NV luminescence [26]. If we assume that the electrode can reduce two-photon ionisation to effectively zero, then the rate of NV^- and by extension, the increase in illumination would be the same. By adding a $1/\sqrt{5}$ increase to the optical collection efficiency to the sensitivity calculation (equation 5.20) along with the improvement to the optical spin contrast, then we can achieve a sensitivity that is 3.27 times better than traditional optical cycling techniques. This mix of techniques would by among the highest improvement to NV performance as it combines the improvement of optical collection with contrast all using the same technological addition of the electrode over the NV in the diamond at room temperature.

The major issue with using the electrode in this way is the unpredictable nature in which the NV energy levels react to such a large electrode potential. Whilst not explicitly calculated, it is assumed that the potential required to shift NV energy levels for removing cross-talk is small. From figure 4.4, the energy gap at which no ionisation occurs is at 1.2 eV, implying that the smallest energy gap from the excited state to the conduction band is 1.2 eV in the absence of an electrode potential shifting the levels. With the electrode, the idea is to shift the gap such that the minimum energy gap is larger than the energy being used to excite the NV during the pumping phase. With a green 532 nm laser, the energy of excitation is about 2.3 eV, this implies that the electrode would have to shift the NV energy levels about 1.1 eV away from the conduction band. Given that the diamond bandgap is 5.48eV [7], it is unclear what such a large potential would do to the NV energy levels or whether they would shift linearly with electric potential at such large values. This could be solved using density functional theory (DFT) calculations [80].

Finally, the last thing to consider when using the electrode for charge state control is the effect it might have on the coherence time of the NV. In most modern theories of the NV, decoherence occurs as the spin state in the NV interacts with nearby paramagnetic defects in the diamond which cause a spin-flip in the NV spin state [25, 50]. Thus, most efforts to improve NV coherence time involve engineering diamond samples that remove these paramagnetic defects. However, if the NV ionises due to an unwanted two-photon ionisation process, then the spin information of the NV is lost along with its charge state. Physically this could occur through an extended ionisation mechanism (figure 5.11). In a typical quantum operation in the NV, the spin state, as well as its charge state, is initialised and readout with optical pulses. During this time, the NV can undergo multiple photoionisations whereby the NV photoionises into the neutral state then returns to the negatively charged state through a recombination process (figure 5.11a)). The recombination process produces positively charged holes as an electron leaves a donor within the diamond lattice (or from a defect) to populate the NV. As a result, over some period of laser excitation, a number of ionisations, recombinations occur which produce a number of holes that exist within the local vicinity of the NV and diffuse with time (figure 5.11b)). This means that even during a period where there are no optical interactions, the NV can still combine with a hole to ionise into the neutral state once more. This process can affect the NV charge state and subsequent coherence time during a non-optical coherence readout process such as the spin echo period of a Hahn echo sequence [25]. An electrode could create charge control and increase coherence time by either reducing photoionisation using the shifting of the energy levels or simply applying a positive electrode potential which would repel positively charged holes that are nearby to the NV.

Theoretical modelling of this effect could be achieved by calculating the flux of holes produced by a typical optical process, their thermal velocity (or diffusion rate) as well as their capture cross-section both with and without an external electrode potential. The flux could in principle be solved using rate equations and the capture cross-section and thermal velocity has been experimentally verified in other work [68].

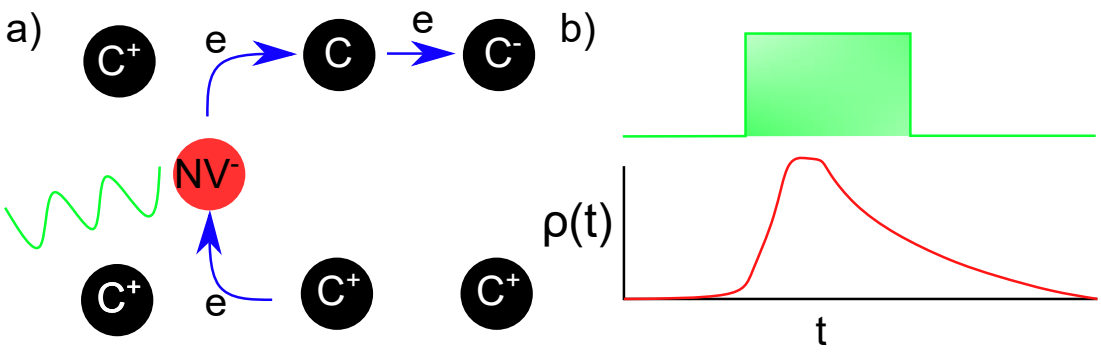

Figure 5.11: Diagram of the NV ionisation scheme a), the green laser pulse interacts with the red NV^- which causes ionisations into the diamond lattice. Over time, electrons will form recombinations, donating electrons from the lattice back into the NV, creating the negatively charged state and a positively charged carbon atom (hole). Over time the negative charges in the lattice are repelled from the NV and the positive holes will orbit the NV before diffusing themselves or interacting with the NV to ionise once more. This means that even if the laser is off, ionisation can still occur via holes interacting with the NV. This is shown in the diagram predicting the hole density $\rho(t)$ as a function of time b). After the green laser pulse, the hole density increases, but is predicted to orbit the NV for a time after the laser is turned off before fully diffusing away from the NV.

If the capture rate is roughly equivalent to the NV coherence time, then we could claim that ionisation is a significant limitation to NV coherence time. This would be complicated as in principle this calculation would need to be performed for both the NV and any number of donors and acceptors in the local diamond environment in a coupled manner. Experimentally this could be verified by measuring the NV coherence time and charge state relaxation time for NVs in diamonds with varying defect concentrations to observe if there is a correlation between charge state and coherence time.

The modelling performed in this thesis shows a relatively straightforward way to improve NV optical spin contrast in ambient conditions through careful manipulation of optical pulses in an SCC protocol. With the pulsing mechanism in place, the 42% contrast calculated promises a 1.6 fold increase in the NV DC magnetic field sensitivity which is a significant improvement on other mechanisms and has applications in quantum sensing, quantum computation and experiments to understand NV energy levels in a variety of conditions. The electrode itself has many other potential advantages such as improving optical collection efficiency and coherence time. As a result, there is a lot of future work to be done with the electrode. This includes the experimental realisation of the initial one step potential SCC work and experimental investigations of the possible two-step potential SCC protocol. Further theoretical modelling of the effects of high potentials on the NV energy levels is required as well as further experimental and theoretical investigations of the effects of the electrode on the NV

charge state stability and its effect on the NV fluorescence and coherence. The results shown so far show concrete theoretical evidence of NV performance enhancement that is applicable in a variety of quantum technologies and the future work has great promise for a variety of alternative means of NV performance enhancement.

Chapter 6

Micro-optical structures for enhanced collection efficiency

Recall from chapter 5 when calculating the DC magnetic field sensitivity of the NV we applied an equation from Rhondin et al. [99]:

$$\eta_{dc} \sim \frac{1}{g\mu_B} \frac{1}{C\sqrt{nT_2^*}}, \tag{6.1}$$

where g is the g-factor for the magnetic moment, μ_B is the Bohr magneton, $n = t_l * P$ is the optical collection efficiency defined by the total counts obtained from the NV, P_0, and the time of the readout t_l. T_2^* is the NV electronic spin dephasing time and C is the optical contrast. In chapter 5 the key variable being changed was the optical spin contrast C, however, from equation 6.1 it is clear that there are other variables that can be altered to increase sensitivity and by extension, the overall readout fidelity for a range of quantum operations. One variable, in particular, is the optical collection efficiency, n. Almost all NV readout operations are optical and as a result, the fluorescence from the NV is a key factor in reading out a spin state with high probability. In terms of contrast, this is measured as the difference in optical fluorescence when measuring different spin states. In terms of optical collection efficiency, it is measured as the overall optical fluorescence that is collected by the detection system. So, similar to the efforts of chapters 3, 4 and 5, the goal of this chapter is to improve NV performance, however the mechanism for this lies in diamond optical structures for improved optical collection as opposed to improved readout mechanisms for improved optical contrast.

The main problem with NV optical collection efficiency is the high refractive index of the diamond. Diamond has a refractive index of 2.42 which translates to a critical angle of 24^o [57] at a diamond/air interface (figure 6.1a)) which can be calculated using Snell's law [79]. For an NV emitting from inside a flat diamond block, the light that emits at an angle larger than the critical angle is reflected at the diamond/air interface and will not be collected by the detection system. One simple solution to this problem is altering the refractive index outside the diamond, the most common method is to use immersion oil with a refractive index of 1.6. This increases the critical angle to 42^o at the diamond/oil interface, however, this is still a relatively

small segment of the total NV fluorescence that could be detected.

The main method considered in this chapter for increasing NV optical collection efficiency is to shape the diamond itself to improve the optical emission profile. Common approaches in the literature include nanopillars [74] and the hemispherical solid immersion lens (SIL) [42, 57, 108], although there are a number of other ideas such as meta-lenses [56] and the parabolic mirror [125]. The two approaches considered in this chapter are singular micro-structures that can be fabricated in a focused ion beam (FIB), these are the SIL and the parabolic mirror. The SIL shapes the diamond into a hemisphere with the NV at its spherical centre (figure 6.1b)), with the NV at the centre of the hemisphere, all-optical emissions at the curved surface would be at normal incidence to diamond/air interface and would have maximal transmission through the diamond, increasing the optical emission to the detector. Parabolic mirrors make use of the high refractive index to purposefully reflect the light. The parabolic shape is designed with the NV at the parabola focal point such that all optical emissions are reflected downwards through the diamond to an inverted detection system (figure 6.1c)).

Parabolas have been demonstrated to have significantly higher photon collection efficiency compared to both unstructured diamonds and SILs. Parabolas have been experimentally confirmed to collect approximately 5×10^6 counts per second (cps) for a 48% or 20-fold improvement to the optical collection efficiency compared to unstructured diamond [125]. This could result in an almost 4.5-fold improvement to NV sensitivity. In addition to this, the parabolic mirror collimates the light as it is reflected below the diamond sample. This means that the light can be collected with a low numerical aperture (NA) objective lens or potentially without an objective lens at all, reducing experimental costs and complexity. Conversely, SILs have been demonstrated to collect up to 493×10^3 cps which can result in a 5 to 6 fold improvement in optical collection efficiency [42, 108]. Which would result in an approximately 2.3-fold improvement to sensitivity. The main reason for the improvement in parabolas is likely due to the fact that the parabola collects light emitting above the NV, via the parabolic reflection as well as below the NV as it emits directly downward to the inverted detection system. SILs on the other hand will only collect light that is being emitted above the NV, directly towards the detection system, and all light emitting in the opposite direction is not collected (see figure 6.1).

SILs however do have advantages compared to parabolic mirrors, mostly in experimental simplicity. When constructing the SILs or parabolas, the initial step is to locate the NV with high accuracy, then position the nanofabrication so that the NV resides in the structure focal point or spherical centre. The parabolic mirrors designed in Wan et al. [125] are near the surface of the parabola (approximately 100 nm from the surface) whereas the SIL NVs are typically microns deep [42, 57, 108]. If the alignment of the NV to the structure is off by a few hundred nanometres, the SIL will still perform well. The 5-fold improvement in the optical collection is an averaged value, but can be 3 to 10 times depending on the fabrication accuracy [42, 108]. For near surface parabolas, a 200 nm error in NV positioning can result in considerable optical losses or even the removal of the NV altogether in the etching process. It is

also important to note that the SILs created in previous work was achieved using FIB and the method for creating the parabolic mirrors was achieved using reactive ion etching (RIE). RIE is useful for the large scale creation of structures with the same parameters but is a lengthy process when creating single structures were each new structure is altered. This makes understanding and troubleshooting errors in the fabrication process much more time-consuming.

In this chapter, the parabolic mirror is designed and fabricated using a FIB process similar to a SIL fabrication where the focal point (and subsequent position of the NV) is much deeper at 500 nm compared to other work [125]. The deep NV will be more robust to fabrication errors and the FIB fabrication process can more easily be altered for troubleshooting purposes. In section 6.1 some basic concepts of optical reflection and transmission are considered and how they apply to the structures being designed. In section 6.2 the FIB process is detailed with the various means of improving the quality of the fabrication. In section 6.3 the quality of the structures is tested using fit models and simulations. This includes tests of the structure shape, its surface roughness and a simulation of its predicted optical collection efficiency. It is also in this section that the process of aligning NVs with a parabola is described and the effects of NV misalignment on the simulated optical collection efficiency is studied. Finally, in section 6.4 these preliminary results are discussed and the future direction is considered.

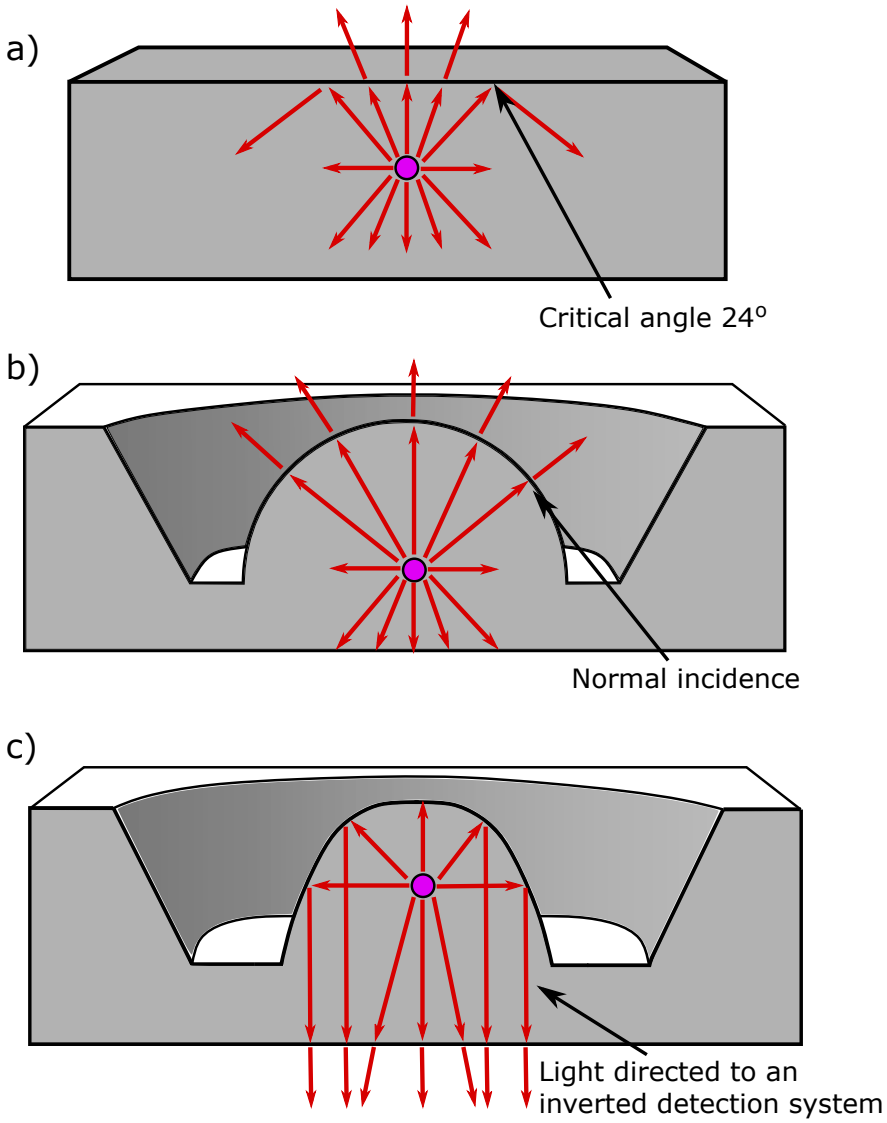

Figure 6.1: Images of various diamond structures and their effect on the NV (purple) optical emission (red lines). The first is the flat, unstructured diamond a), where the large refractive index between diamond and air create a critical angle of 24^o. All-optical emissions outside this angle are reflected and severely reduce the amount of light reaching a detection system. The second image is the SIL b), where the diamond is shaped into a hemisphere with the NV at its spherical centre. In this structure, all-optical emissions from the NV are at normal incidence to the diamond surface and have maximal transmission through the diamond, increasing the optical emission. The final structure is the parabolic mirror c), where the diamond parabolic curvature is designed such that optical emissions from the focal point are reflected and collimated downwards through the diamond to an inverted detection system. Note that the lines represent maximal reflections and transmission, but the reflections and transmissions shown is not 100%.

6.1 Optical reflection

When calculating how light passes through one medium into another, one simple formula for its refraction and reflection is Snell's law [79]:

$$\frac{n_1}{n_2} = \frac{sin(\theta_2)}{sin(\theta_1)}. \tag{6.2}$$

Snell's law simply relates the angle of the incident light, θ_1, through one medium with a refractive index, n_1, to the refracted light, θ_1, through a second medium with a refractive index, n_2. In this case, the refractive index of the first medium is diamond (n_1=2.4) and the refractive index of the second medium is air (n_2=1). For a light emission within the diamond, there is a critical angle where the angle of refraction is travelling parallel with the surface of the diamond and all emissions larger than this angle will result in total internal reflection (TIR). By setting θ_2 to ninety degrees and solving for θ_1, the result is the 24^o critical angle mentioned in the previous section. By solving the same equation where n_1=1.6, the refractive index of immersion oil, the solution is 42^0, also mentioned in the previous section. This critical angle calculation is what creates a clear understanding of the light losses to the detection system as light passes from diamond into the air towards a detector, as such, it motivates the diamond structures considered in this chapter. Whilst Snell's law is useful to predict the angle of light passing through mediums, it does not account for the power loss that can occur during reflection and transmission. Even when the emitted light is incident with the surface boundary, there can still be some reflection, resulting in losses to the detector. The ideal way to analyse this phenomenon is with the Fresnel equations of light transmission.

By considering the light propagation as an electromagnetic wave, the fraction of incident light power that is reflected at the boundary between two non-magnetic materials can be expressed as [79]:

$$\begin{aligned} R_s &= \left|\frac{n_1 cos(\theta_1) - n_2 cos(\theta_2)}{n_1 cos(\theta_1) + n_2 cos(\theta_2)}\right|^2 \\ R_p &= \left|\frac{n_1 cos(\theta_2) - n_2 cos(\theta_1)}{n_1 cos(\theta_2) + n_2 cos(\theta_1)}\right|^2, \end{aligned} \tag{6.3}$$

where R_s and R_p denote the s and p polarised reflected light respectively. Note that equation 6.3 considers the power loss at the boundary and does not consider losses from attenuation in the mediums. Whilst this is an important consideration for the overall measure of optical collection efficiency, it is not explicitly studied in this chapter. Equation 6.3 shows that there is some reflected light even within the critical angle of light emission. In an idealised SIL, the light emission is incident to the diamond/air boundary such that θ_1 and θ_2 are both zero, in this case, equation

6.3 simplifies to:

$$R = \left|\frac{n_1 - n_2}{n_1 + n_2}\right|^2, \tag{6.4}$$

where R is the reflected power regardless of polarisation. Equation 6.4 can be solved to give an reflected power of 17%, such that even in a perfect SIL, there are still some losses due to reflection at the diamond/air boundary. Parabolic mirrors exploit TIR at the curved boundary to air, meaning that losses through the parabola are minimal as the only source of loss would be from the near-field transmission [79], if the NV is placed far from the surface of the parabola (500 nm), the near-field transmission will be reduced, however the larger source of loss would likely occur from the reflection at the bottom of the diamond which is unstructured. This source of loss is only considered conceptually in section 6.4.

6.2 FIB nanofabrication

The design for the FIB nanofabrication of the parabolic mirror is based on a similar FIB nanofabrication for a SIL performed by Jamali et al. [57] FIB nanofabrication works by using a focused beam of gallium ions to etch away small pieces off of the diamond surface. Structures are made by generating a list of x-y coordinates, each with a milling time, that is read by the FIB software which then etches away the diamond in a point-wise fashion. The code is generated using Python and is parameterised in a way to allow for simple changes in the structure size and quality.

The points which generate the micro-structure (SIL or parabola) are designed to form an Archimedes spiral which starts at the centre of the structure and spirals outwards. The important property of the Archimedes spiral is that the distance between neighbouring lines in the spiral is constant. Whilst the overall structure size is parameterised by its radius, R_s, and the list points generated by the code are in Cartesian coordinates; the Archimedes spiral in the code is parameterised by a polar angle, θ and the distance between neighboring points in the spiral, dS, where the full arc length is given by S (figure 6.2).

The reason for the use of the Archimedes spiral is to mitigate charge buildup. Diamond is an insulating material, so charged particles such as those in a gallium beam get stuck in the diamond for long periods of time. If this charge builds up, then the electric field it produces can deflect the ion beam, causing errors in the structure. Prior to fabrication, the diamond is coated in 30 nm of gold and placed onto a metallic sample holder with silver paste to provide a conductive surface that removes the gallium charge. However, milling in the same region for a long period of time will still cause a buildup of charge before the conducting material can remove it. The Archimedes spiral allows for a milling procedure in which the beam does not stay in the same region for a long period of time. The beam will spiral out of the Archimedes spiral, then back in towards the centre of the structure and repeat this process many times.

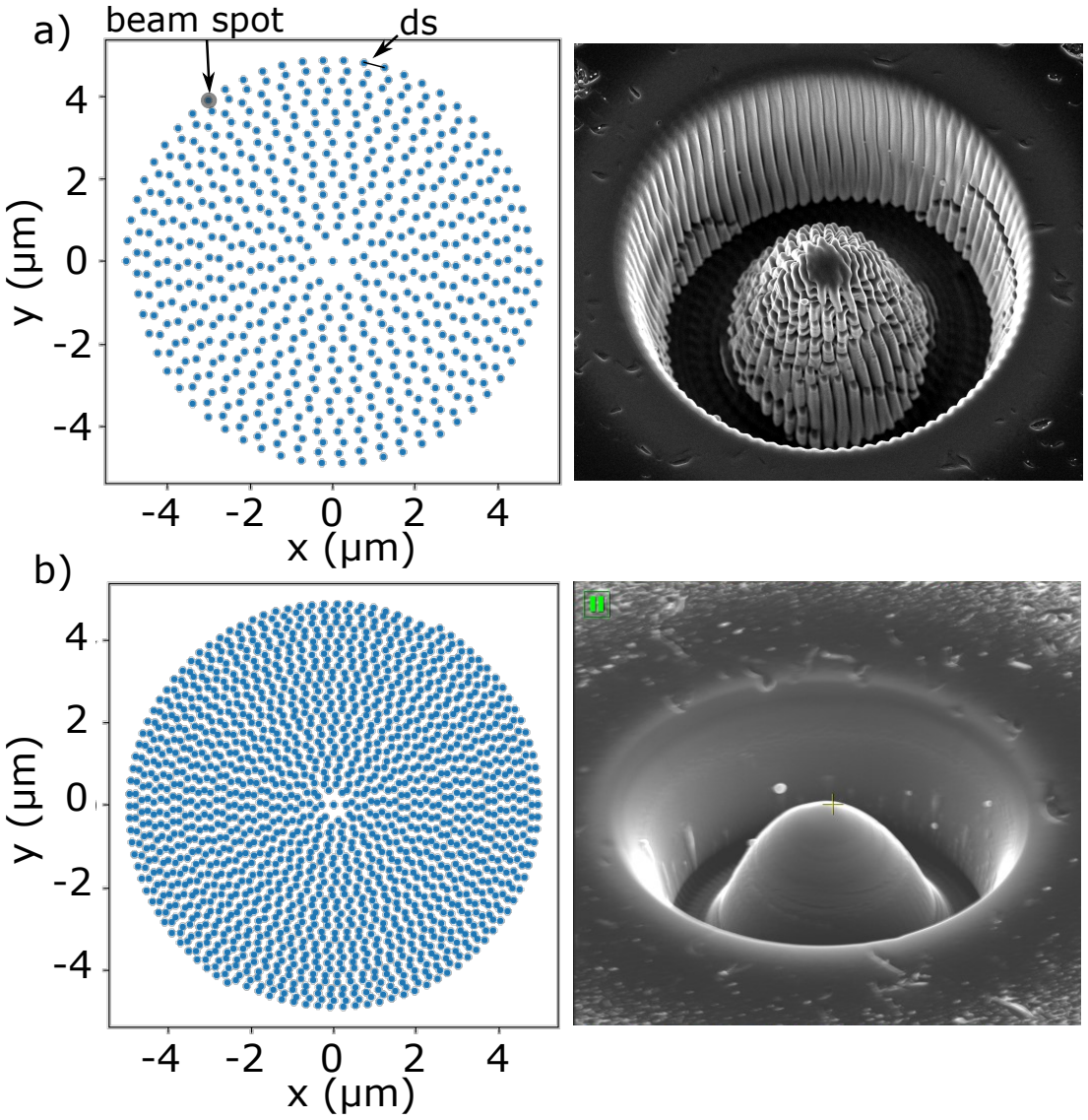

Figure 6.2: Effects of the current and step size in the milling process. a) When the distance between points is larger than the beam spot size (large dS compared to the current I), then there will be areas of the structure that aren't milled, creating a ripple artefact. When the points are too close then the structure might be over-milled. b) Careful optimisation is necessary for good structures.

The file that is read by the FIB system reads Cartesian x/y coordinates and a mill time. The coordinates follow the Archimedes spiral which is parameterised by the radius of the structure and the distance between adjacent points, dS. The depth is governed by the mill time and the current of the beam. The beam current in the FIB is created by an aperture system. Higher currents are generated by having the Gallium beam pass through larger apertures at the end of the accelerator. As a result, higher

currents increase the spot size of the beam and can be more difficult to focus into a small point (figure 6.2). Higher beam currents decrease then milling time substantially at the cost of structure resolution. It is important to select a beam current where the beam spot size is roughly the same as dS. This ensures that the beam is not milling empty regions between adjacent points, nor is it over milling the same region from overlapping points. Beam currents at 2.8 nA with a dS of about 50 nm create high quality structures that mill in a reasonable amount of time.

In addition to the beam current is the mill time, or the time the beam spends on each point. The method adopted for optimising the mill time is also from Jamali et al. [57]. In their work, the full depth of a structure is broken up into layers of depth dz. Breaking up the milling into layers helps mitigate the issues that arise from sputtering. During the milling process, the beam will etch away a small region of the diamond. The piece that is removed can go anywhere within the FIB chamber, including back onto the diamond in a sputtering process. Milling deep within the diamond increases the chance of sputtering as the etched material can more easily attach to the walls of a deep milled hole (figure 6.3). By milling relatively shallow layers (approximately 50 nm thick) then the etched material is more likely to be properly removed from the diamond sample.

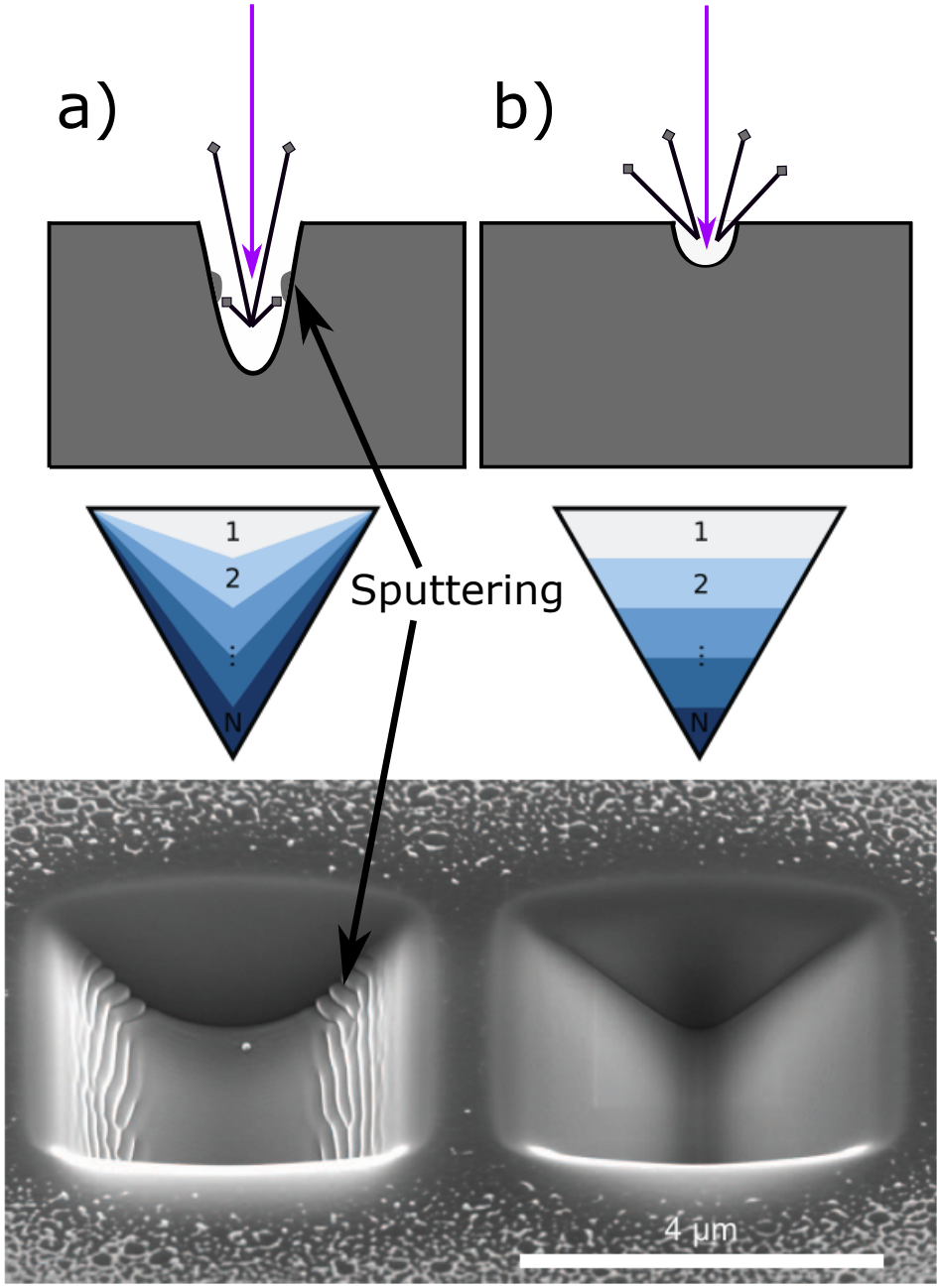

Figure 6.3: Illustration of the sputtering process in the FIB. In a), the mill time is long, creating a deep hole where etched material can land back onto the bulk diamond in the milling process. The images below show how the sputtering forms ripple layers in the structure that does not have the intended sharp wedge shape. In b) the milling is split into layers where each layer only mills to a shallow depth, allowing etched material to scatter away from the bulk diamond. The result is a smooth structure with much sharper edges at the corner of the wedge. Source for the bottom image: Jamali et al. [57].

All the structures were originally parameterised by the radius of the structure (SIL or parabola, R_s), the radius of the cone around the structure (R_c), dS, dz, and the beam current (I). The radius, R_s, along with the depth of the NV (or the parabola focal point depth, d_{NV}) together parameterise the structure with a particular height, h and parabola curvature, a. Subsequent iterations of the milling procedure included a flat region where the cone meets the structure (d_f) and a flat region over the top of the structure (d_t). The region where the cone meets the structure is a small corner where sputtering can occur as etched material connects to the side wall of the SIL or parabola. This creates a smooth buildup of material instead of a sharp corner which can affect the optical reflections, the flat region helps reduce this sputtering process. The flat region over the top of the structure helps ensure that the top of the structure isn't milled too deeply. The keeps the focal point of the structure where the NV is located as the milling process might make the structure shorter than intended and shift the focal point. Both the SILs and parabolic mirrors had a radius between 2-3 μm and a cone that was x2.5 larger than the radius of the structures (5-7.5 μm). The dS and dZ are both 50 nm and the current was optimised to 2.8 nA. Finally, the d_f term was set to 250 nm in diameter and the d_t term was set to 250 nm in width.

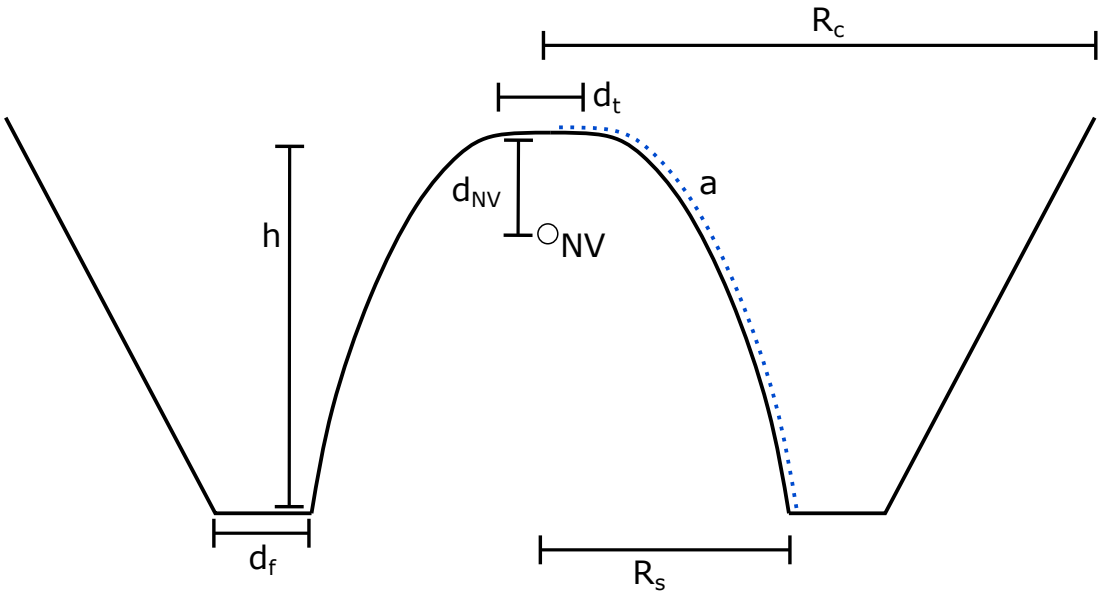

Figure 6.4: Simple diagram of a parabola with the FIB code parameters labelled upon it. These parameters define the size and shape of the structure. The parameters shown are for a parabola, but most of these parameters are used for the SIL as well with the exception of the SIL height (h) and curvature (a).

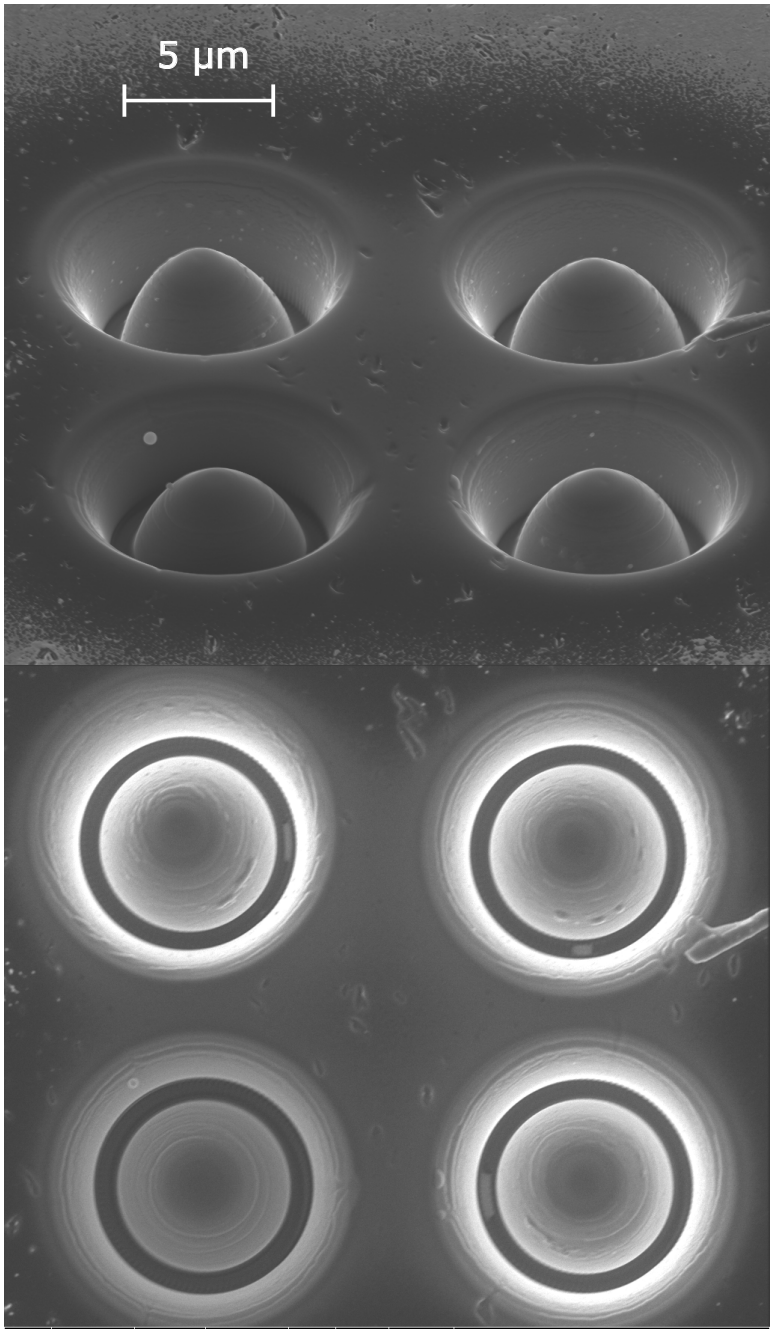

Figure 6.5: Example images of milled parabolas from a 52^o angle and 0^o top down angle milled with the parameters mentioned in this section. The parabolas qualitatively look good and the procedure is consistent, however some subtle asymmetries can be observed. Note that the flat top is not visible, indicating that the beam spot size is slightly larger than the dS factor, over-milling the structure by a small amount.

Figure 6.5 shows the overall results of an optimised parabola. Qualitatively the structures look accurate to what is needed, however, there are small asymmetries in

some of the structures and there are slight inconsistencies between the structures. One other thing to note is that the flat top in these particular images is not present, which is indicative of a beam spot size being larger than the dS length, causing some small over-milling.

There are characterisation tests that need to be made to confirm the structure quality before testing the optical collection efficiency. This includes quantitatively testing the accuracy of the milling procedure, finding the milling smoothness for optical characterisation and simulating the overall optical collection efficiency. The next section addresses all these concepts and includes an outline of the NV alignment procedures and how that affects optical collection efficiency.

6.3 Structure quality and Optical collection

Qualitatively, the structures made in the FIB process look parabolic in shape, however small errors in the structure that are hard to observe in SEM can have significant effects on the optical emissions. This can be broken down into three distinct areas: subtle changes in the parabola shape, surface roughness of the diamond and misalignment of the NV relative to the parabola focal point. The first two are structural issues; non-parabolic curves or rough surfaces can reflect the light in unexpected ways, affecting collection. NV misalignment is more difficult to understand, it cannot be observed at all using the SEM images shown in the previous section as the NV cannot be visualised. It is important to note that in this context, alignment refers to the position of the NV relative to the parabola focal point and does not consider the orientation of the NV in the diamond. As the NV is a dipole emitter, its radiative pattern is not necessarily symmetric with respect to its orientation. For a diamond with a [100] surface and an NV in the focal point of a parabola, all the four possible NV axes in the diamond lattice align to the optical axis such that all radiative patterns are symmetric to the parabola shape. This is not the case with a [110] surface in the diamond. For simplicity and the fact that most diamonds used in optical spectroscopy are made with a [100] surface, this work will only consider diamonds with a [100] surface and not consider the effects of NV orientation. In this section, the structure quality and resultant optical collection efficiency is measured using simulations. The structure quality and surface roughness is tested by fitting the data of a scanned parabola to a model structure and the alignment is tested by taking parabola data and modelling the optical collection efficiency with a simulated NV emitter source.

The first step in any of the characterisations is to obtain data from the parabolas for modelling. This is done using atomic force microscopy (AFM). With AFM, a nanoscopic tip is run along the surface of the diamond and the deflections in the tip due to nanoscopic changes in the diamond topography are measured. The deflections are used to re-create the diamond surface as a dense series of points. These points can then be uploaded into software for fitting or simulating optical emissions.

Data from the AFM can be fitted to a model parabola where the geometric parameters (radius, height, and curvature) are constant and set to the same parameters

of the parabolas designed in the code. The equation for the model is given by:

$$z - z_0 = \begin{cases} h - \left(R_s - \frac{R_s^2 - r^2}{a}\right) & r \leq \sqrt{-ad_f t + ah - aR_s + R_s^2} \\ d_t & r > \sqrt{-ad_t + ah - aR_s + R_s^2}. \end{cases} \tag{6.5}$$

In the Cartesian coordinates, the radius is converted: $r = \sqrt{(x - x_0)^2 + (y - y_0)^2}$ and the only fitting parameters are for the position of the model parabola to the FIB parabola: x_0, y_0 and z_0. This approach ensures that the parabolas milled are being compared to the exact same parabolas being designed in the code. After the fit, a Chi-squared analysis can be obtained to find the average deviation of points on the milled parabola compared to the model parabolic curve:

$$\chi^2 = \sum_{i=1}^{k} \frac{(x_i - m_i)^2}{m_i}, \tag{6.6}$$

where x_i is the point measured from the AFM parabola, m_i is the fit point from the model parabola and i indicates a sum over all the points in the structure up to k. The results of equation 6.6 encodes both the geometric alignment of the parabola to a model fit and predict the RMS difference between points, which is effectively the surface roughness of the structure.

Figure 6.6 shows an example of a parabolic mirror that has been milled in FIB, scanned in AFM and had the AFM data fitted to a model parabola which has the same parameters as the parabola curve intended in the milling code. The blue dots are the AFM parabola data and the smooth orange curve is the model fit. Qualitatively, the two data sets match each other reasonably well, however it is clear that there is a small asymmetry in the milled parabola, causing slight deviations compared to the model. By applying equation 6.6 we calculate that the average deviation of points to the model is 39 nm. To understand this value, we apply a formula for optical quality based on convention:

$$Q = \frac{\lambda}{4n}, \tag{6.7}$$

where λ is the wavelength of the optical emission and n is the diamond refractive index (2.4). Equation 6.7 gives a guideline of the minimum surface roughness required for perfect reflections, solving the equation with a value of the more common wavelength NV emission (700 nm) gives a surface roughness requirement of 73 nm. The solution to equation 6.6 shows the convolved geometric fit and the surface roughness, thus, the surface roughness cannot be more than 39 nm, much lower than the 73 nm minimum requirement for optical quality. These results imply that the FIB structures are smooth enough and close enough to our intended parabola to give the reflections required for the maximal optical collection, however, there is room for improvement by further optimising the parameters of the FIB process.

Even if the parabolic structure is perfect in shape and smoothness, the optical reflections can still be poor if the NV isn't in the focal point of the parabola. To

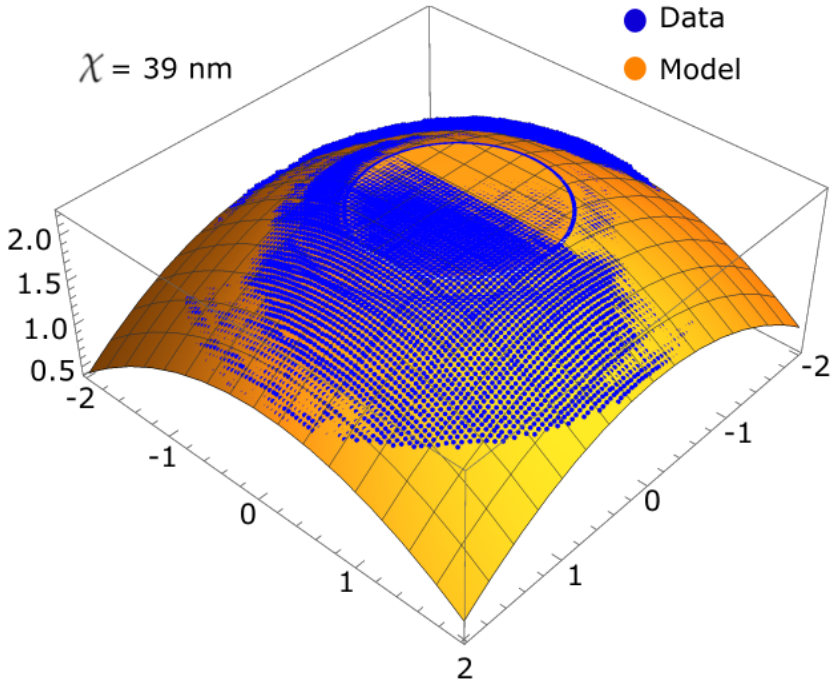

Figure 6.6: Image of the model fitting. The blue data are the points of a parabola made in FIB which has been measured and discretised into a series of data points using an AFM. The orange data is the model fit. Qualitatively the two data sets match quite well with some discrepancies. The results of a Chi-squared analysis shows quantitatively that the average deviation of points to the model fit is 39 nm.

understand this problem, we first need to understand how the NV is positioned within the parabola. The first step is to implant nitrogen ions into the diamond and anneal to create the NV centers, this can be achieved with high spatial certainty, ion straggle for 500 nm implantations can be as low as 50 nm [89]. After this, a marker system can be set up using the FIB, where a series of points are milled into the diamond. The etched markers can be viewed in a confocal system alongside the NVs so the position of the NVs can be made relative to the markers (figure 6.7). With the coordinates of the NVs relative to the markers obtained, the sample can be placed in the FIB and the parabolas can be milled around the expected position of the NV.

Whilst this system has been proven to assist with locating NVs for SIL fabrication [108], there are still issues with the method, especially when considering parabolas, where misalignment causes more serious effects on the optical collection efficiency. To understand this concept a simulation can be performed where a parabolic diamond mirror can be modelled around an NV emitter and the optical collection efficiency can be calculated for different NV positions within the parabola. The diamond parabola is simulated with a height of 5 μm, a base diameter of 6.32 μm, a smooth parabolic tip (no flat region) and a focal point depth at 0.5 μm. The NV emitter is modelled as a pair of dipole emitters that have a time-constant power (P_s) emission that emits at

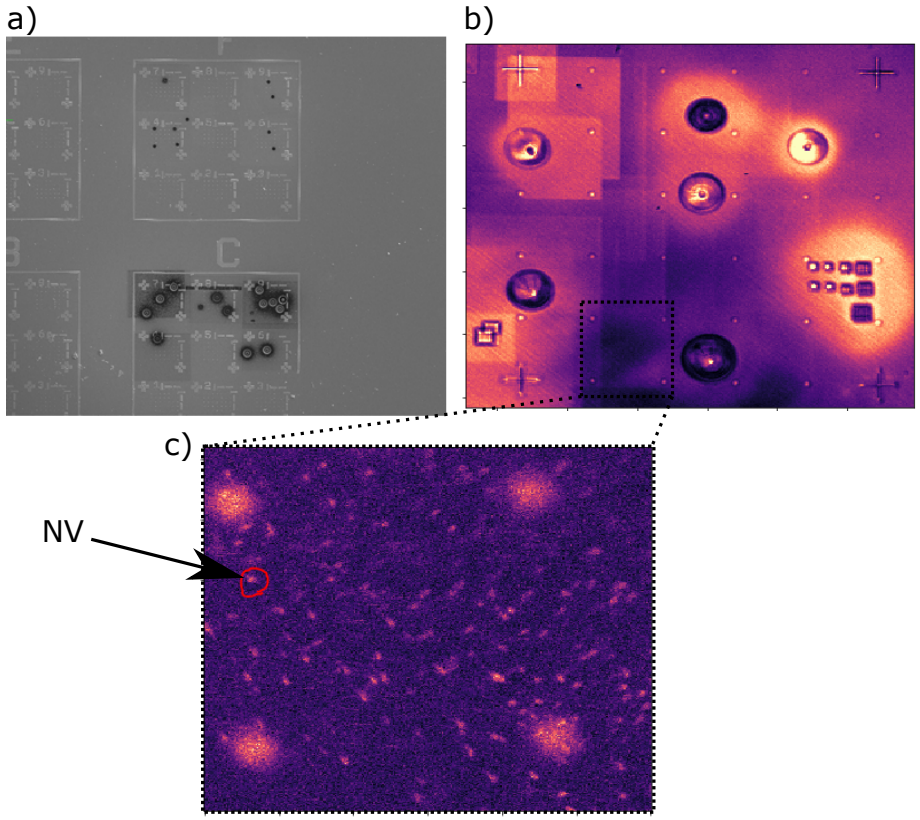

Figure 6.7: Images of the alignment protocol. In a), an SEM shows the etched markers with some structures milled into points on the grid where NVs would reside. These markers can be visualised along with some structures in confocal b), when zooming in on one of the small marker gridlines, the markers and the NVs can be visualised together in c). The markers are used as guiding points to create coordinates for where the NVs are which can be followed in an SEM for FIB milling.

wavelengths of 600-800 nm. The collected power (P_c) is calculated by integrating the solid angle of a cone expanding towards the detection system where the size of the solid angle is defined by the maximum angle that can be collected by an air objective lens with a NA of 0.95. The power itself is calculated in terms of the real part of the Poynting vector in the far-field:

$$P_c = 1/2\sqrt{\frac{\epsilon_0}{\mu_0}}\int_\theta\int_\phi \vec{E}^2 sin(\theta)d\theta d\phi, \tag{6.8}$$

where the optical collection efficiency then becomes $P_c/P_s \times 100\%$.

Figure 6.8 are simulation results of the optical collection efficiency where the NV emitter is displaced further and further away from the parabola focal point in both a lateral (figure 6.8a)) and vertical direction (figure 6.8a)). For zero displacement, the optical collection is very high (75%) and falls with distance. For lateral displacements,

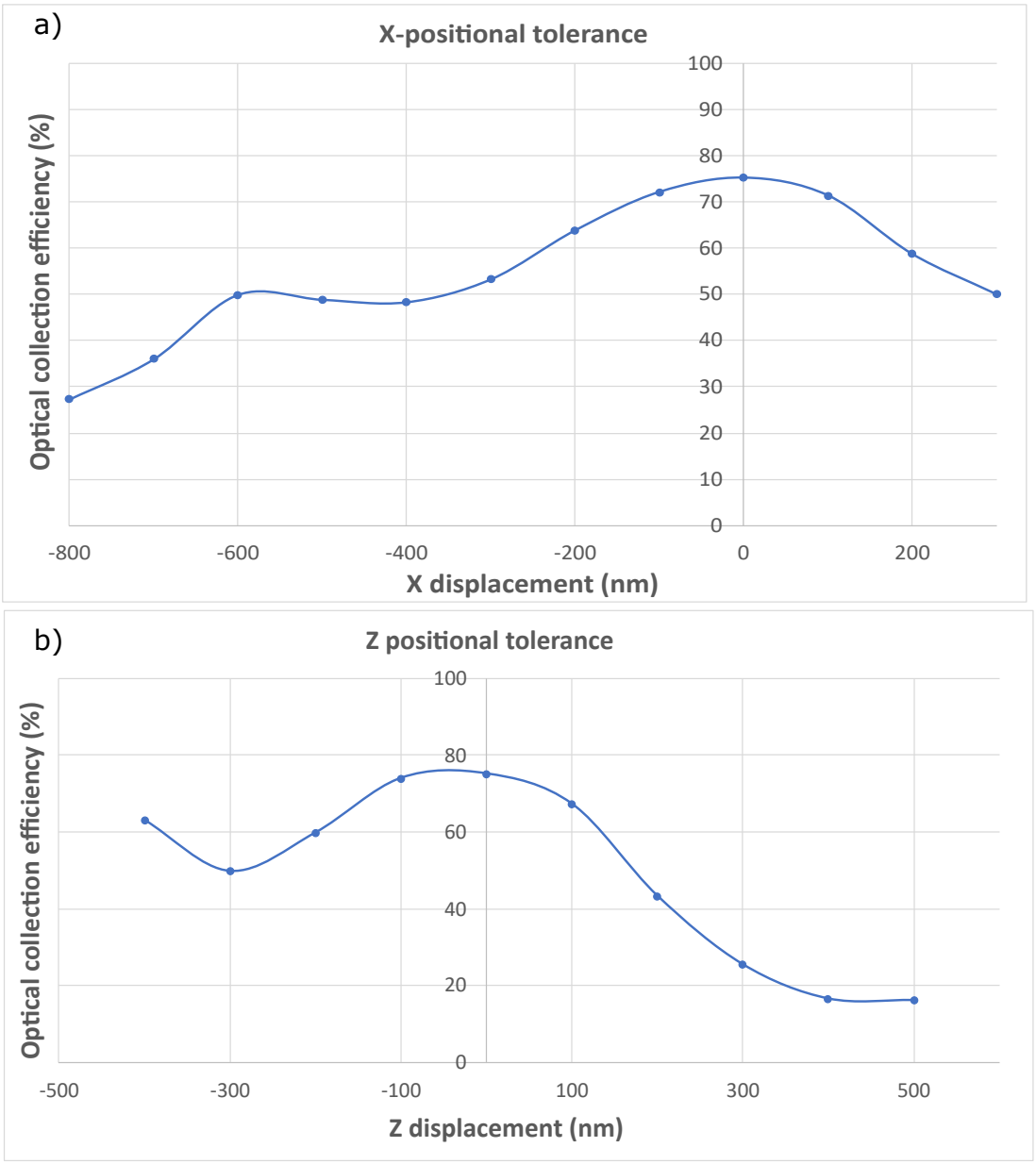

Figure 6.8: Plots of the optical collection efficiency as a function of NV displacement in the a) lateral direction and b) vertical direction where zero displacement indicates an NV exactly in the focal point of the parabola. With the NV in the focal point, the optical collection efficiency is simulated to be as high as 75% of the total emission. The plots indicate that the collection efficiency drops by a significant amount across the few hundred-nanometre distances with a more distinct drop for vertical displacements compared to lateral displacements.

the optical collection is more robust to displacements, only dropping by approximately 5% for 100 nm displacements, and 10% for 200 nm displacements. Vertical

displacements have a more significant effect on optical collection efficiency. Vertical changes of 100 nm drop the collection by as much as 10% and changes of 200 nm can drop the collection by up to 30% depending on the direction of the displacement. These values follow a similar trend when compared to simulations by Wan et al. [125], whilst their simulations are more robust to changes in the NV displacement within the parabola, a displacement of several hundred nanometres towards the parabola edge can result in the complete removal of the NV, as the NVs in their simulations are considerably closer to the parabola edge (100 nm), this makes the fabrication much more prone to full removal of the NVs.

When setting up the alignment of the NVs with the parabolas, the key step in the process is the confocal positioning of the NVs relative to the markers. Confocal positioning accuracy can be very high in confocal microscopy, much higher than the diffraction limit as the NVs and the markers can be accurately fitted to simple Gaussian functions. This can give positional errors which can be approximately 100 nm [79]. Whilst the spatial resolution is often worse in the z-direction, the consistency of the implantation [89] would mean that z-misalignment would be minimal, although still important as small errors produce much larger changes in optical collection efficiency. Laterally, displacements of 100 to 200 nm are possible simply due to the resolution of positioning in the confocal as well as smaller errors in the FIB system. Vertically, displacements due to positioning are likely to be smaller, which means that accurate milling of the parabola curvature and its focal point position would become the largest factor.

The other concept to consider is that whilst idealised optical collection efficiency is the ultimate goal, modest improvements can still have significant effects. If the parabola is misshapen or the NV is somewhat misaligned, it can still result in significant improvements compared to a completely unstructured diamond. For example, if there is a drop of optical collection efficiency from the ideal 70% made possible in simulations to 50% due to some errors, that would still produce results similar to Wan et al. for a 20-fold improvement to optical collection efficiency compared to unstructured diamond [125]. To the best of our knowledge, this is the largest improvement available in NV optical collection efficiency. In the next section, an overall discussion of the parabola milling process is undertaken and various means of improving the process are considered.

6.4 Discussion and future direction

The FIB process creates parabolic mirrors in diamond that are proven to be structurally very close to an ideal parabola. These ideal parabolas have low surface roughness, allowing for ideal optical reflections and also have high optical collection efficiencies proven with optical simulations. Additionally, the optical collection simulations suggest that the NV positioning in the parabola is essential, but misalignment of 100-200 nm can still produce optical collection efficiency that is equivalent to the best results currently in literature [125]. It is important to note that whilst the parabolas

are close to ideal, they are not perfect. There is still room to improve the quality of the parabolas, the two main areas of optimisation are the beam spot size compared to the step size ds and the depth optimisation, dz. These factors can still be further altered to create more optically perfect parabolic mirrors.

Another consideration is the optical collection efficiency simulations for these parabolas. The assumption in the previous section was that the Chi-squared analysis suggested that the parabolas made in FIB were close enough to perfect that the optical collection efficiency simulations of a perfectly designed parabola would be sufficient. Ideally, the data for the milled parabolas generated by AFM should be used in further optical collection efficiency simulations to confirm this assumption, this will be one of the simulations performed in future work. These simulations can also help understand purposefully made errors in the structure and their effect on optical collection efficiency. For example, the flat region, d_t, designed on the top of the parabola is expected to reduce optical collection efficiency as it creates an imperfect parabolic structure for reflections, but it is considered necessary for maintaining the focal point alignment to the NV. Future simulations of milled parabolas with different sized flat regions should be performed to understand how the milling alters the position of the focal point and its effect on the optical collection efficiency. The results might suggest that over-milling is less of an issue than previously thought when the milling parameters are optimised and the flat region can be removed altogether.

Ultimately, the true measure of this experiment would be the optical collection efficiency of an NV inside a milled parabola. In principle, this would be an easy thing to measure. The optical collection efficiency of an implanted NV in an unstructured diamond would be compared to an equivalent (or the same) NV milled inside a parabola and the difference in light collected would give the optical collection efficiency improvement. Further experiments can also be performed to understand how the increased optical collection improves NV sensitivity and spin readout fidelity. However, this approach limits the ability to perform an analysis if the optical collection efficiency is not as high as expected. Unusually low fluorescence might be due to a poorly milled structure, NV misalignment or perhaps an issue with reflection on the bottom of the diamond and the resultant detection pathway. Measuring the collection efficiency alone would not help understand where the error might be in the process. Matching the optical collection efficiency measured in experiment with the data from simulation would help remove some of this uncertainty, however an ideal approach would be to directly measure the fluorescence pattern of the NV far-field emission from the parabola. This would be achieved by replacing the single-photon counting photo-diode detector with a charge-coupled device (CCD) camera. The CCD camera would create an image of the NV emission rather than just count individual photon events. The image generated would depend on the interference of the emission light. In an ideal case, the light would be a single collimated mode which would generate a single spot of fluorescence on the CCD image. Various aberrations in the diamond would cause alternate reflections which would interfere with each other in the far-field, creating diffraction patterns in the CCD camera. These patterns can be matched with the results of various simulations to help diagnose problems in the parabolic mirror

design, allowing for further optimisations.

Finally, the last consideration that has been largely neglected in this chapter is the effect of the unstructured diamond at the bottom of the sample. Even if the parabolic mirror is perfect in design, there will still be reflections at the bottom of the diamond due to the processes outlined in section 6.2. Physically structuring the bottom of the diamond would be unfeasible as there are two light sources to optimise transmission: the collimated light from the parabolic reflection and the diverging light emanating directly from the NV (figure 6.1c)). So the best solution would be to reduce the refractive index mismatch of diamond to air by coating the diamond with other surfaces. Immersion oil is one such material that can be used or an anti-reflection coating that would create a much more smooth transition of light through different mediums. This is a major subject for future investigations.

Micro-optical structures for enhanced optical collection efficiency seems like a simple concept for improving NV performance. However, this chapter reveals that the process for improving optical fluorescence can be very complicated, with many variables to control and many approaches required to optimise and test the performance improvement. The improvement made by such structures is significant. The 20-fold improvement to optical collection efficiency created by a parabolic mirror is predicted to create a 4.5-fold improvement to DC sensitivity. Recall that the improvement to sensitivity predicted by the spin-to-charge conversion technique presented in chapter 5 was only 1.6. However, it is important to note that the two techniques aren't necessarily exclusive. One future pathway would be to create a parabolic mirror over the diamond and coat it in an electrode in order to perform the spin-to-charge conversion technique, allowing both improvements to operate together. This further motivates the development of both of these techniques as they can be used together to create a highly optimised NV device for a range of quantum applications.

Chapter 7

Quantum computing for neuroscience

In chapter 2, a method for sensing neurons in a network was developed using NV centers embedded in an array of diamond nanopillars. Whilst the potential for great improvements to neurosensing are shown in that chapter, further improvements to NV sensitivity were sought through the various works in chapters 3, 4, 5 and 6. All these chapters have great potential for a wide range of NV quantum applications, however, their specific application to the nanopillar-based neurosensing is limited. Yet, the improvements considered in this thesis are all applicable to improving NV spin-state readout for quantum computation. Whilst quantum computing and quantum sensing are different applications of the same NV device, it is possible that a quantum computer can be used to simulate neuron networks. Thus, the work of this chapter focuses on an alternative use of the NV in neurosensing, which is as a qubit for a quantum simulation of a large scale neuron network. In this way, the efforts to improve NV performance can be applied to neuroscience research for sensing and computation.

Quantum computers were theorised in the early 1980s as a means of solving problems intractable on a classical computer [24]. Since then, the research into quantum computing has increased dramatically with small scale quantum computing devices being manufactured using a number of different architectures including the NV [71, 77, 127]. However, along with the requirement for completely new hardware architectures to create the quantum computer, there is also a need for completely new software algorithms to solve problems utilising quantum technology. Many algorithms exist, such as factoring large numbers for cryptography, searching in large data sets and more direct simulations of quantum systems [75]. However, there are still many open questions on what sort of problems a quantum computer can solve and whether or not the quantum computer will perform better than a classical one for various tasks.

One potential application for quantum computing that has received surprisingly little attention is neuroscience. Extremely large scale projects have been undertaken over many years with the goal of simulating the human brain or parts of it using the worlds most powerful supercomputing infrastructure [4]. The main problem

to be overcome in this project is the extreme complexity of the human brain and the insufficient computational resources available to simulate it [36, 59]. On a basic level, neurons in the brain act remarkably similar to a computer network. Bits in a classical computer transmit information in a binary code, ones and zeroes, where large numbers of bits form a code that represents an action to be undertaken by the computer. A neuron will receive and transmit a signal in the same way. An AP pulse can be considered a binary system where 1 would represent an AP and zero would represent the lack of an AP. A string of pulses would act like a binary string which translates to actions undertaken by the brain and larger organism. Hypothetically, neurons could outpace classical computers in terms of speed and energy cost in computation due to two reasons. The first is that the connectivity of the neuron network would be larger, with many more connections, neuron networks allow for parallel computation in a way that is difficult if not impossible for a classical computer to match even with modern parallel core architectures like graphical processing units (GPU's). The second is the adaptability of the neuron network, neurons can grow and change connections to suit a changing environment, this affects the probability that a neuron will receive and transmit a signal and is called neuroplasticity [123]. One open question is whether these concepts can be modelled in a quantum computer. The high connectivity could be modelled with quantum entanglement and the neuroplasticity can be modelled by a conditional operation that would change the probability of other qubit flips during a readout based on a control qubits state [40].

Whilst the approach of modelling a single neuron with binary encoding by a single qubit is possible, it isn't at all practical when attempting to model large neuron networks. Single slices of cortical brains can have thousands of neurons and the entire human brain has as many as a hundred billion neurons with around 10^{15} neuron connections or synapses [61]. Modelling this effect would therefore require thousands to billions of entangling qubits which is very difficult, if not impossible to manufacture. Most attempts at modelling the human brain use mean-field approaches where many neurons in a population act on average in the same way.

In this chapter, a means of modelling this mean-field approach is conceptualised for a quantum computer. In section 7.1 a prominent theory of large scale neuron modelling is introduced which models large scale networks with a Fokker-Planck type equation. In section 7.2, the computational complexity of the Fokker-Planck model is briefly addressed which explains why classical computers struggle to solve such equations and motivates the use of quantum computers. A basic approach to quantum simulation of the neuron model is described, some simple means of encoding and computing the problem are addressed and the computational speedup is analysed.

The work presented in this chapter is not intended as a definite solution to neuroscience modelling using quantum computers. Such research would likely end up becoming a project of many years of dedicated research. The purpose of this work is to provide some of the first steps in this research as there does not appear to be any literature known that addresses this concept. The potential problems involved with such an undertaking are addressed which will motivate future study in this field. This research also ties in all the work of the previous chapters. The neurosensing work

required a detailed understanding of neuron biology and how they are modelled which is applied in this chapter. The other work in improving the NV as a viable qubit for quantum computing will directly allow any quantum neuron simulation to become realised with high-performance hardware. Thus, all the work in this thesis culminates into diamond quantum devices and their varied application to neuroscience.

7.1 Modelling large-scale neuron networks

The following is a derivation of a model for simulating mass neuron dynamics by Gerstner et al. [36], although many versions exist [1, 33, 81]. When modelling large scale neuron networks the same assumptions are often made. Consider a large network of interacting neurons, as signals travel from neuron to neuron, neurotransmitters are released at the synapse which can be excitatory or inhibitory, increasing or decreasing the chance that a neuron will transmit a signal when it receives one. The connections between neurons can also vary, one neuron can connect to one neuron in a line or it might connect to multiple neurons with multiple axons and dendrites such that it might receive a signal from multiple locations or transmit a signal to multiple locations. Mathematically this alters the parameters or weights that describe the probability of a neuron firing [3, 51, 61, 93]. In large scale neuron modelling, this concept is often simplified into neuron populations. Groups of neurons will often act synchronously, receiving an input, sending that input throughout the population and transmitting an amplified signal to a neighbouring population. Thus, the assumptions made in large scale neuron modelling are all based on the same concept of a mean-field theory. Across a single population of neurons, all the parameters that define individual neurons are the same or at least have the same mean value. This includes parameters such as the threshold for creating an AP (θ), the electrical resistance (R) in the neuron and the time constant of biological spiking (τ_m) among others. It is important to note that whilst parameters are the same in a single population, they can change across different populations. The second assumption is that the neuron signals, the AP's, are on average identical across the population. Whilst neuron signals have been known to change shape and size to some degree [19], on average, the signals in the network are the same. The final assumption is that the connectivity between neurons in a population is statistically homogeneous, this means that the weights made in synaptic connections that define the probability of passing a signal from one neuron to another are the same and stay the same through time. It also means that adding effects such as neuroplasticity with changing connection weights only occurs when dealing with changes from one population to another if at all [36].

Recall in chapter 2 the potential of a single neuron was studied as a function of time using the Hodgkin-Huxley equation:

$$C_m \frac{\partial V_m(t,z)}{\partial t} + I_\xi(r,z,t) + I_r(R,t) = 0, \tag{7.1}$$

where C_m is the membrane capacitance and $V_m(t,z)$ is the transmembrane potential. The $I_\xi(r,z,t)$, is an initial current that drives the system (e.g. from a clamp or a PSP).

The third term, $I_r(R,t)$, is the ionic current at the membrane radial boundary ($r = R$). This is the major source of the AP and it is caused by the opening and closing of ion channels along the membrane. The HH models the radial current in terms of the three most prominent ion channel types in a given neuron and their respective currents:

$$I_r(R,t) = I_{Na}(R,t) + I_K(R,t) + I_{Cl}(R,t), \tag{7.2}$$

where the subscripts indicate the three major ions crossing the membrane during an AP (sodium, potassium and chlorine respectively) and can be expressed with the following:

$$\begin{aligned} I_{Na}(R,t) =& g_{Na} m(t)^3 h(t)(V_m(t) - V_{Na}) + g_{NaL}(V_m(t) - V_{Na}) \\ I_K(R,t) =& g_K n(t)^4 (V_m(t) - V_K) + g_{KL}(V_m(t) - V_K) \\ I_{Cl}(R,t) =& g_{ClL}(V_m(t) - V_{Cl}). \end{aligned} \tag{7.3}$$

In mass neuron modelling, the dynamics of the population is described as the evolution of membrane potential densities in the same way that you would describe the evolution of a single neuron by its singular potential. Included in the model is the population firing rate, $A(t)$, (often called a population activity):

$$A(t) = lim_{\Delta t \to 0} \frac{1}{\Delta t} \frac{n_{act}(t \to t + \Delta t)}{N} = \frac{1}{N} \sum_{j=1}^{N} \sum_f \delta(t - t_j^f), \tag{7.4}$$

the population activity essentially describes all the AP's a neuron population will produce in a period of time. In a population of N neurons, the population activity is defined by counting the number of AP events, $n_{act}(t \to t + \Delta t)$ in a given interval, Δt, and dividing that number by N and Δt. It can also be described as the sum of all the firing times of a single neuron f, and the sum over all the neurons in the population up to N. In a large population of neurons with a time-dependent input and randomly fluctuating neuron signals, it is common to exchange the population activity with its expectation value, $< A(t) >$. In the limit of a population with infinite neurons, the fluctuations go to zero and the expectation value becomes the population activity.

To create a model of a large number of connected neurons, the common approach is to consider the dynamics of a single neuron and expand from there. To achieve this, the best place to start is the leaky integrate and fire for a single neuron:

$$\tau_m \frac{d}{dt} V_i = f(V_i) + R I_i(t), for V_i < \theta. \tag{7.5}$$

The leaky integrate and fire (LIF) model is a basic model of neuronal dynamics that almost all neuron models are derived from, including the Hodgkin-Huxley (HH) model. Like the HH model, the LIF is derived by considering the resistive and capacitive currents across a neuron membrane and using a circuit model with Kirchoff's laws to create the equations. The left-hand side of equation 7.5 is the capacitive current where τ_m is the time constant for membrane ion channels opening

and closing, the $I_i(t)$ is the input current that drives the system with the membrane resistance, R, and the $f(V_i)$ term is the resistive current which can be any number of different functions which model different effects in the neuron. The most common expression for the resistive current is a membrane potential difference term: $f(V_i) = V(t) - V_r$ where V_r is the resting potential of the neuron. However, there are many other expressions, such as more complicated ion channel currents like those found in the HH model, or adaptive coupled equations such as those found in neuroplastic models like the adaptive exponential model (AdExP) or the FitzHugh-Nagumo model [36]. The model can then be generalised to larger numbers of neurons by defining a potential density which is the number of neurons in the population at a given time with a given membrane potential:

$$lim_{N\to\infty} = \Big[\frac{neurons \quad with \quad V_0 < V_i(t) \leq V_0 + \Delta V}{N}\Big] = \int_{V_0}^{V_0+\Delta V} \rho(V,t)dV, \tag{7.6}$$

This can be normalised by saying that the number of neurons with a potential that lies in the full range of possible potentials must integrate to one:

$$\int_{-\infty}^{\theta} \rho(V,t)dV = 1, \tag{7.7}$$

where neurons can take low values but the potential is reset to the resting potential after a neuron reaches the threshold potential for an AP (θ). In the LIF model, AP's are considered as spikes that occur in a neuron but are not explicitly modelled like the HH model.

The aim now is to model the time evolution of the potential density and the associated population activity. Consider a population of neurons with potentials between V_0 and V_1. The fraction of neurons with a potential in this region can increase if individual neurons increase their potential from below the boundary V_0 or decrease from the upper boundary V_1. The crossing of these boundaries can be described as a flux, $J(V,t)$, where a positive flux increases the number of neurons in the boundary region (increasing the potential density) and a negative flux decreases that number. In a time Δt, the quantity $NJ(V,t)\Delta t$ describes the number of 'trajectories' crossing the arbitrary boundary V_0 from below minus the trajectories leaving the boundary from above V_1 (see figure 7.1).

These trajectories must be conserved in the same way the potential or ion concentrations are conserved:

$$\frac{\partial}{\partial t}\int_{V_0}^{V_1} \rho(V',t)dV' = J(V_0,t) - J(V_1,t), \tag{7.8}$$

taking a derivative with respect to the upper boundary removes the lower flux term and the integral on the left-hand side and creates the continuity equation. For

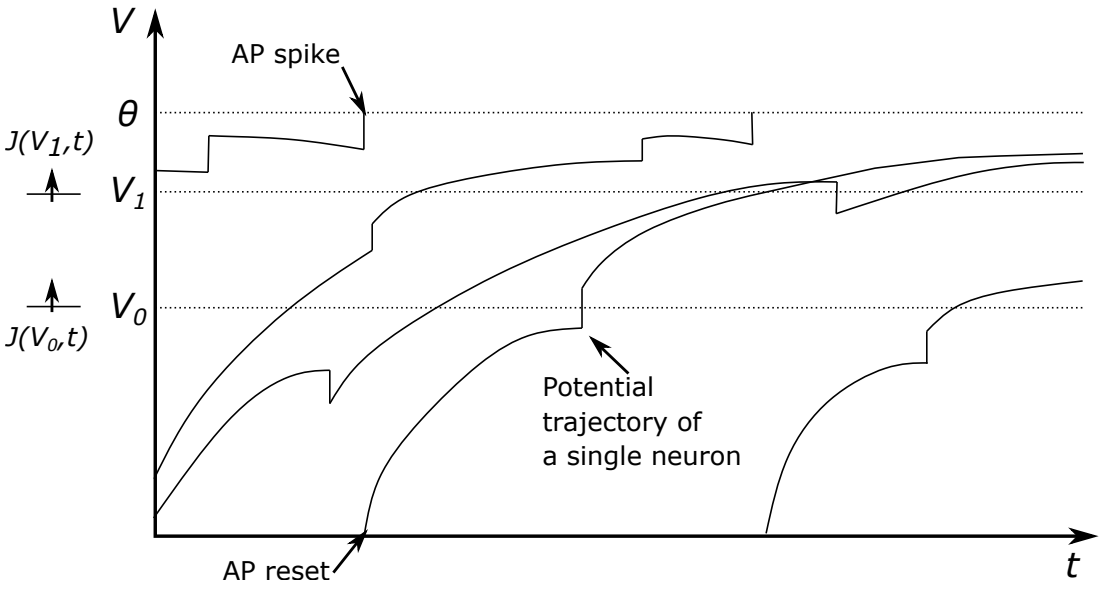

Figure 7.1: Image of the potential for arbitrary neurons evolving in time. The θ term is the threshold for neuron spiking where after a neuron reached this threshold, it undergoes an AP and is set to the reset potential or the resting potential. The region between V_0 and V_1 is the region that defines the potential density to be solved for. The specific placement of these regions is also arbitrary (e.g. it is common to set the upper threshold at the AP threshold θ). Electric potentials rising into the potential density region can be considered a positive flux of potential trajectories. Potentials rising high enough that they exit the density region can be considered a negative flux of potential trajectories. This flux model of neuron potentials allows for a useful approach to modelling the potential density and subsequently, a large population of interacting neurons. Image re-created from Gerstner et al. [36]

simplicity, V_1 is set to V:

$$\frac{\partial}{\partial t}\rho(V,t) = -\frac{\partial}{\partial V}J(V,t) for V \neq \theta, V_r. \tag{7.9}$$

This conserves the flux across the boundary V, however it is not complete as the threshold point and the reset point (resting potential) above and below V have the effect of completely removing or generating trajectories respectively. This is accounted for these by adding source and sink terms which are dependant on the population activity $A(t)$:

$$\frac{\partial}{\partial t}\rho(V,t) = -\frac{\partial}{\partial V}J(V,t) + A(t)\delta(V - V_r) - A(t)\delta(V - \theta), \tag{7.10}$$

thus, the density vanishes for all $V > \theta$. From continuity, the population activity

can be directly related to the flux through the threshold:

$$A(t) = J(\theta, t), \tag{7.11}$$

in other words, all the trajectories must come from the population activity in the first place. The next step in the derivation is a more explicit expression for the flux.

Consider the flux in a homogeneous population of integrate and fire neurons. They all have the same driving current, I, with AP changes in the potential, w_k, causing different effects. For example, an AP can cause a jump in the membrane potential, which can create excitatory or inhibitory effects in a neighbouring neuron with differing strengths. There is also an AP arrival rate for each type with mean spike arrival rates, ν_k, being identical for all neurons. Finally, there is the assumption that the actual AP spike trains at different neurons/synapses are independent of one another. From this there are two sources of flux, the AP spike arrivals causing a jump in the flux, or the driving current causing a slow drift:

$$J(V, t) = J_{drift}(V, t) + J_{jump}(V, t), \tag{7.12}$$

these terms need to be evaluated individually. For the J_{jump} term, consider an excitatory input $w_k > 0$. All neurons that have a potential V_i where $V_0 - w_k < V_i \leq V_0$ will experience a spike upon the arrival of the AP spike where V_0 is a reference potential. The time arrival of a specific AP event is not known, however from the assumption that the arrival rate of spikes, ν_k, is constant and the same across the neuron population, the total flux of spikes, $J_{jump}(V_0, t)$ can then be calculated as:

$$J_{jump}(V_0, t) = \sum_k \nu_k \int_{V_0 - w_k}^{V_0} \rho(V, t) dV, \tag{7.13}$$

where if the number of neurons in the population is large, the actual flux becomes very close to the expected flux. The drift term $J_{drift}(V, t)$ is defined as the potential density at a given reference potential and the reference potential multiplied by the rate of change of the potential with time, i.e. the density multiplied by the rate of change of the potential in that density:

$$J_{drift}(V_0, t) = \frac{d}{dt} V|_{V=V_0} \rho(V_0, t) = \frac{1}{\tau_m}(f(V_0) + RI_i(t))\rho(V_0, t), \tag{7.14}$$

where the right hand side of the equation comes from the LIF model equation 7.5. Note that current spikes are considered in $J_{jump}(V, t)$ and not in the drift equation. Current pulses that are not spike-like do need to be considered in $I_i(t)$.

The positive flux through the threshold, θ gives the population activity (equation 7.11). Since the APs can be generated by input spikes and the drift in the overall potential, the total flux (and therefore the population activity) can be defined as:

$$A(t) = J(\theta, t) = \sum_k \nu_k \int_{\theta - w_k}^{\theta} \rho(V, t) dV + \frac{1}{\tau_m}(f(\theta) + RI_i(t))\rho(\theta, t), \tag{7.15}$$

also, given that the potential vanishes at the threshold after a spike $V > \theta$, the sum over synapse types k can be restricted to excitatory synapses only. Substituting the flux terms into the continuity equation 7.10 gives:

$$\begin{aligned}\frac{\partial}{\partial t}\rho(V,t) = -\frac{1}{\tau_m}\frac{\partial}{\partial V}\Big((f(V)+RI_i(t))\rho(V,t)\Big) + \sum_k \nu_k(t)\rho(V-w_k,t) - \rho(V,t) \\ +A(t)\delta(V-V_r) - A(t)\delta(V-\theta),\end{aligned} \tag{7.16}$$

where the first term on the right-hand side accounts for the drift in potential density, the second account for the jumps by stochastic spike arrival and the final terms utilise the population activity to create new spikes and resets in the system. It is from the firing condition, that the potential density vanishes above the threshold: $\rho(V,t) = 0$ for $V > \theta$. Equations 7.15 and 7.16 can be coupled together to predict the population activity, $A(t)$ and the potential density, $\rho(t)$ in a population of integrate-and-fire neurons stimulated by an arbitrary common input, $I_i(t)$ [36].

In the limit of small jump amplitudes w_k, the potential density equation can be approximated by a diffusion equation. To achieve this, the far right hand side of equation 7.16 is expanded into a Taylor series up to second order in w_k. The result is a Fokker-Planck equation:

$$\begin{aligned}\tau_m\frac{\partial}{\partial t}\rho(V,t) = -\frac{\partial}{\partial V}\left(\Big(f(V)+RI_i(t)+\tau_m\sum_k \nu_k(t)w_k\Big)\rho(V,t)\right) + \\ \frac{1}{2}\Big(\tau_m\sum_k \nu_k(t)w_k^2\Big)\frac{\partial^2}{\partial V^2}\rho(V,t) \\ +\tau_m\big(A(t)\delta(V-V_r) - A(t)\delta(V-\theta)\big) + O(w_k^3),\end{aligned} \tag{7.17}$$

It is convenient to split this equation into a 'drive' and 'diffusion' term, where the drive is:

$$\mu(t) = RI_i(t) + \tau_m\sum_k \nu_k(t)w_k, \tag{7.18}$$

and the diffusion term is:

$$\sigma^2(t) = \tau_m\sum_k \nu_k(t)w_k^2, \tag{7.19}$$

thus creating the Fokker-Planck, drift-diffusion model of neuron dynamics, where the higher order terms are considered negligible due to the assumption of small jump

amplitudes:

$$\begin{aligned}\tau_m \frac{\partial}{\partial t}\rho(V,t) = -\frac{\partial}{\partial V}\Big(\big(f(V)+\mu(t)\big)\rho(V,t)\Big) + \\ \frac{1}{2}\sigma^2(t)\frac{\partial^2}{\partial V^2}\rho(V,t) \\ +\tau_m\big(A(t)\delta(V-V_r) - A(t)\delta(V-\theta)\big),\end{aligned} \tag{7.20}$$

Equation 7.20 and the population activity equation 7.15 are strictly all that is needed to solve any neuron population problem. Small changes allow for calculations of more specific versions of mass neuron problems. For example, coupling multiple populations where there isn't full connectivity might involve changing the spike arrival rate $\nu_k \to C_{n,k}A_k(t)$, where $A(t)$ remains the population activity, k is the index for one population, n is the index for another population and $C_{n,k}$ is a dimensionless constant that described the ratio of connectivity between the two populations. The same methodology can be applied to altering the spike weight, w_k, where the couplings can be deterministic or stochastic and as mentioned earlier in this section, $f(u)$ can be changed to include any sort of non-linear expression for the firing rate. One common strategy is to Taylor expand the population activity in w_k about $V = \theta$ to obtain the flux through the threshold specifically, this gives the same potential density equation 7.20 with a new population activity:

$$A(t) = \frac{-\sigma^2(t)}{2\tau_m}\frac{\partial\rho(V,t)}{\partial V}|_{V=\theta}, \tag{7.21}$$

which can be directly substituted into equation 7.20 for a single equation of neuron dynamics.

From this point, the idea is to alter the Fokker-Planck equation into a Schrodinger equation such that the evolution of the neuron dynamics modelled by the Fokker-Planck equation is simulated by the evolution of a quantum system. Section 7.2 is an attempt to achieve this using Hamiltonian based simulation.

7.2 Quantum computing for neuroscience

From the previous section, the two equations being solved in their most general forms are:

$$\begin{aligned}\tau_m \frac{\partial}{\partial t}\rho(V,t) = -\frac{\partial}{\partial V}\Big(\big(f(V)+\mu(t)\big)\rho(V,t)\Big) + \\ \frac{1}{2}\sigma^2(t)\frac{\partial^2}{\partial V^2}\rho(V,t) \\ +\tau_m\big(A(t)\delta(V-V_r) - A(t)\delta(V-\theta)\big),\end{aligned} \tag{7.22}$$

and:

$$A(t) = \sum_k \nu_k \int_{\theta - w_k}^{\theta} \rho(V,t)dV + \frac{1}{\tau_m}(f(\theta) + RI_i(t))\rho(\theta,t). \tag{7.23}$$

Whilst being a coupled set of partial integrodifferential equations, the model also scales in computational complexity with extra neuron populations as each new population represents another set of weights (w_k) and firing rates (ν_k) to couple into the system. This process becomes worse with added complexity; if the neuron firing function $f(V)$ has a non-linear variable for adaptation and/or the driving current $I(t)$ is complicated with a variable for time-dependent input noise then the multi-dimensional nature of the equations substantially increases computational complexity. Thus, these equations are not simple to solve in a classical system and researchers often solve these systems with approximations that only model very simple neuron systems [36, 100, 121].

To solve this equation on a quantum computer, the principal way is to apply a quantum simulation. In this process, an equation is cast into a form that is functionally similar to a Schrodinger equation, and the quantum system evolves to produce a solution that can then be mapped back into the original equation. Part of equation 7.22 can be re-cast in a Schrodinger form, beginning with the Schrodinger equation:

$$i\hbar \frac{d}{dt} |\Psi\rangle = \hat{H} |\Psi\rangle , \tag{7.24}$$

the potential density function $\rho(V,t)$ is mapped to the state of the quantum simulator $|\Psi\rangle$, the membrane time constant τ_m is mapped to $\hbar$, and by making the transformation $it \to \tau$, the Schrodinger equation is solved as a function of imaginary time. This means that the functions $\mu(t)$, $\sigma^2(t)$ and $A(t)$ will also have to be converted into a function of imaginary time as well as $f(V)$ if a time-dependent neuron firing function is considered. Whilst this is possible, it can be difficult depending on the type of neuron modelling being simulated. This also will mean that the Hamiltonian will have Hermitian and non-Hermitian terms. The following is a solution for the Hermitian terms and the non-Hermitian terms are left for future work, but in principle, they could be modelled as a diffusive noise component of a master equation. The Hamiltonian is expressed as:

$$\hat{H} = -\frac{\partial}{\partial V}\Big(f(V) + \mu(\tau)\Big) + \frac{1}{2}\sigma^2(\tau)\frac{\partial^2}{\partial V^2} + \tau_m\big(A(\tau)\delta(V - V_r) - A(\tau)\delta(V - \theta)\big), \tag{7.25}$$

what is missing in equation 7.25 is the associated population activity equation 7.23 which needs to be coupled into the system. Although if solving for the potential density around the spiking threshold θ, $A(\tau)$ can be added directly into the Hamiltonian with equation 7.21. Once the Fokker-Planck equation is converted into a suitable Hamiltonian, there are three main problems to address, the first is encoding the state $|\Psi\rangle$ so that it accurately represents the potential density. The second is encoding the

Hamiltonian so that it can be implemented on a quantum computer, and the last step is encoding the time evolution so that the state evolves in a way that accurately represents the neuron dynamics.

The first major problem is the encoding of the state. The quantum state $|\Psi\rangle$ is a binary system and the potential density is a continuous spectrum of values. One solution to this problem would be similar to the solution used in a classical computer where a value is represented by a string of bits. The potential would be discretized into a series of segments where each segment is represented by a unique state from a string of qubits, then the solution for a single neuron population and its associated potential density would be represented by a series of n qubits:

$$\rho(V,t) \approx \sum_j c_j(\tau) \left|V_j\right\rangle, \tag{7.26}$$

where $c_j(\tau)$ is a time-dependent coefficient of the quantum state and $\left|V_j\right\rangle$ is one n qubit state which represents a discrete value of the potential. Then the readout of the probability $|c_j(V_j,\tau)|^2$ can be directly related to $\rho^2(V,t)$. For example, in a three-qubit system, the string of qubits in the state $|000\rangle$ can represent resting potential, V_r. The state $|111\rangle$ can represent the threshold potential θ and each of the other qubit combinations can represent discrete values between V_r and θ. To achieve the level of values seen in a classical computer, the quantum system would need a similar number of qubits as bits used by classical computers to represent values, 16 to 64 qubits per neuron population, although most classical systems encode in 64-bit floating-point numbers for high accuracy. The more qubits used, the greater the accuracy at the cost of the hardware required to perform the computation.

The next major problem is converting the Hamiltonian into a form that can be implemented on the quantum computer. For example, the Hamiltonian must be altered so that the derivatives can be enacted on a discretized potential. There are many ways to achieve this; one example is the finite difference approach. In a classical simulation, the finite difference approach would be expressed as:

$$\frac{\partial}{\partial V}\rho(V,t) \approx \frac{\rho(V+\Delta,t)-\rho(V,t)}{\Delta}, \tag{7.27}$$

where Δ is a small, discrete change in V. The finite difference method is simply a means of approximating a derivative into a series of differences, each separated by a small increment. For a quantum state, the finite difference method can be equivalently written as:

$$\frac{\partial}{\partial V}\left|V_j\right\rangle \approx \frac{\left|V_{j+1}\right\rangle\left\langle V_{j+1}\right| - \left|V_j\right\rangle\left\langle V_j\right|}{\Delta}, \tag{7.28}$$

where $\Delta = l/2^n$, l is the full spectrum which is broken up into 2^n number of segments based on the number of qubits used to encode V. Note that from the Hamiltonian equation 7.25, the potential derivative acts on the potential density as well as function which are constant in V which need to be separated out and enacted separately. This is achievable but complicated if we choose a non-linear function $f(V)$.

Once the state is encoded and the Hamiltonian derived, the system can then be put into an initial state that represents a beginning state for the neuron population. The unitary gates then evolve the system in time which can be readout at different times, creating a dynamic solution that can be converted back into the solution for the neuron model. It is important to note that every time the solution is readout the wavefunction is collapsed so in order to obtain a full solution of the dynamics, the system must be initialised, evolved for a small period of time, readout, then re-initialised and evolved for a slightly longer period of time before readout. This process would then be repeated many times for increasingly longer evolution times until a full solution is obtained. The means of this evolution can vary depending on the quantum computing architecture. Most quantum computing approaches, including NV-based quantum computing, is performed digitally, where the changes to the quantum state are achieved using unitary gates. These gates in their simplest form are often represented as rotations on the Bloch sphere, where a number of these rotations performed one after another form a complicated operation that can approximate the Hamiltonian evolution being considered [76]. One common solution is to discretize time into a series of discrete, simple operations using the Trotter decomposition [76]. In a Schrodinger picture of quantum state evolution:

$$|\Psi(\tau)\rangle = e^{-i\hat{H}\tau} |\Psi(\tau = 0)\rangle , \tag{7.29}$$

the action of a time-varying Hamiltonian can be approximated by breaking down the evolution into short steps over which the Hamiltonian is approximately constant:

$$e^{-i\hat{H}\tau} \approx e^{-i\sum_m \hat{H}_m \tau_m} = \Pi_m e^{-i\hat{H}_m \tau_m}. \tag{7.30}$$

where the small operations, $e^{-iH_m\tau_m}$, are the unitary gates mentioned before which evolve the system in small discrete steps of τ_m. This approximation is the Trotter decomposition and is common in quantum computing [76]. The more gates, the more accurately the decomposition represents the actual dynamics at the cost of the computation time. However, the time of computation is limited by the coherence time of the qubits which are typically a fundamental property of the quantum computing architecture. The number of gates requires to fully capture the dynamics of a large scale neuron simulation is unclear, however, similar simulation on classical systems can give an idea of how rapidly the potential density changes over a set period of time which helps give an idea of how long we want to run a simulation for and how dense the time discretization must be to capture the change in the solution [36].

In summary, the goal is to cast the neuron problem into a Schrodinger equation where the evolution of the quantum states can be mapped to the evolution of the potential density in the neuron problem. This requires encoding the qubits so they accurately represent the potential density, approximating the Hamiltonian in a way that can be encoded as a set of simple gate operations and discretizing the time steps to apply the time evolution that matches the gate-based Hamiltonian.

As the computation time is set by the decoherence time, the final major question that needs to be addressed is: what is the benefit of the quantum computer? It

is well understood that current neuron models are too complicated for classical computers and simplifying approximations have limited usefulness [36, 59]. So the goal of the quantum computer algorithm is to either produce solutions to problems intractable on a classical computer or more accurate than those produced on a classical computer. This means that the effectiveness of the algorithm is heavily dependent on the hardware capabilities of the quantum computer running the algorithm. Quantum computers often describe performance as a function of circuit width and circuit depth. Circuit width describes the number of qubits and circuit depth describes the number of gates [6]. The computational resources required for this algorithm is large, each population will require at least 16 qubits and many gate operations acting on these qubits to perform the algorithm. Currently, the world record for the number of qubits in a quantum computer is 127 with a superconducting architecture from IBM [11], although the level of entanglement in these qubits is unclear. If the qubits could be fully entangled with high fidelity, then this could result in a simulation of almost 8 populations, which is on the smaller side of what is already being simulated on classical systems [36]. Similar superconducting computers have demonstrated circuit depths of over 20 gate operations [6, 128], which is likely not enough to simulate the dynamics accurately, although the number required is unclear.

The methods shown in this section are preliminary ideas that will need to be developed, however, other approaches could also be considered. One potential approach is to encode the potential density in the phase of the qubit rather than its state. A single qubit spin state can be represented as:

$$|\Psi\rangle = \frac{1}{\sqrt{2}}\left(|0\rangle + e^{i\phi(V,\tau)} |1\rangle \right) \tag{7.31}$$

where $\phi(V, \tau)$ is an associated phase. It is possible to map the potential density to $\phi(V, \tau)$ and perform interactions and readout of the phase using quantum phase estimation [76]. This would reduce the number of qubits required to represent values, but require greater control of the phase readout of the qubits themselves. Another possibility is encoding the Hamiltonian directly using an analogue simulation such as a quantum annealer, but this would only be applicable on analogue quantum simulators which are less common than digital ones.

The work presented in this chapter is merely an introduction to the possibility of quantum computing for neuroscience problems. The goal is to begin the research in this field, introducing the basic concepts and making a hypothesis that quantum computing can provide a unique set of solutions that can dramatically help computational neuroscience research. Whilst there is still a lot of work to be done and the possibility that the algorithm may not work at all, the potential benefits and possibilities help motivate future work.

Chapter 8

Conclusion

This thesis is an analysis of the nitrogen-vacancy (NV) center and its application to neuroscience. The key aspect of the work comprised of engineering the diamond containing NVs into a nano-pillar array for improved NV performance and neuron growth metrics. Whilst the results of this work showed the potential capabilities of the NV for neuron sensing, it prompted further work into the NV itself: how it can be engineered in various ways to improve its overall performance in both quantum sensing and quantum computation. These efforts included cryogenic spin to charge conversion (SCC) with an electrode, a study of NV singlet state spectroscopy, ambient SCC with an electrode, and the fabrication of micro-optical structures for enhanced optical collection. The largest improvement for these studies is in spin readout for quantum computation. The results of these studies lead to the consideration for NV quantum computing for neuroscience and the conceptualization of a quantum computing algorithm for simulating large scale neuron networks. As a result, the overall theme of the work is the engineering of diamond quantum devices and their application to neuroscience.

The neurosensing project in chapter 2 is the main work of this thesis. In this section the basic neuron anatomy and physiology is presented, the current imaging landscape is analysed along with the current methods of modelling neuron systems. The NV is then introduced as a sensor and a novel means of applying it to neurosensing is analysed in the form of a diamond nanopillar array. Unique theoretical modelling shows that the NV is not sensitive enough to measure neuron magnetic fields in the nano-pillar array, however it can measure the electric fields with high sensitivity as long as there is good contact between the neurons and the diamond nanopillars. In addition to the theoretical modelling, preliminary growth studies of neurons on nanopillar arrays suggests that neurons exhibit coordinated growth, connecting with the pillars as long as the distance between the pillars is optimal for neuron growth. These results motivate future work in both neuron modelling and neuron growth studies with the ultimate goal of actual neuron sensing. It also motivates future work in the various ways the NV can improve its capacity for neurosensing as well as other quantum applications.

One key method of improving NV performance lies in the optical contrast that is used to perform a spin readout. One established method of improving the optical contrast is with the SCC technique where the optical contrast is improved using

photoionization. This technique is improved upon in chapter 3 using theoretical modelling and the application of an electrode at cryogenic temperatures. Whilst this technique is restricted to cryogenic applications, the preliminary results suggest that the improvement to optical contrast and subsequent sensitivity is very substantial. Future work in this area would involve the actualisation of this experiment with an electrode over a near-surface NV and the SCC protocol tested.

From studies of SCC and photoionization in the NV comes a more general study of NV singlet state spectroscopy in chapter 4. Despite the extensive study of the NV from a variety of researchers, there are still mysteries in its electronic structure, in particular, the energy splitting of the singlet states relative to the triplet states and how that splitting affects the inter-system crossing (ISC). An experiment is designed which uses photoionization to understand this splitting and theoretical modelling is applied to understand the effects of electron-phonon broadening on the experiment. Whilst the experiment itself needs to be performed, the preliminary work helps ensure the quality and validity of the future results.

One main discovery that the singlet state spectroscopy experiment promises is an accurate measurement of the energy splitting of the lower singlet to the conduction band minimum. This energy splitting allows for an electrode-based SCC protocol at ambient temperatures studied in chapter 5. Theoretical modelling shows that this technique can significantly improve the optical contrast and sensitivity in the NV and whilst the improvement is not as large as that seen in the cryogenic SCC protocol, this method is has a wider application as it can be performed at ambient temperatures. Future work in this requires experimental realisation, however, this work also has many other interesting concepts to investigate, such as the effect of the electrode on NV charge state control and its effects on the optical collection and spin coherence.

The final area of investigation in NV performance lies in optical collection efficiency which is studied in chapter 6. Improving the amount of light collected from the NV arguably has the largest effect in improving the spin readout and overall performance in all quantum applications. The main method investigated in this thesis for improving optical collection efficiency is with the use of creating micro-optical structures in the diamond around the NV, particularly a parabolic mirror which reflects light to improve the amount of light reaching the detector. Parabolic mirrors were made using a focused ion beam (FIB) and their structural quality and optical capabilities were assessed using simulations. Preliminary results suggest that the parabolic mirrors perform as well as those made using other techniques but promise to be more resilient to fabrication errors. Future work will involve experimental measurements of NV optical collection efficiency in parabolic mirrors as well as assessing the improved optical collection efficiency for quantum applications.

Whilst all this work benefits NV readout and sensitivity in some way, their specific application to nanopillar-based neurosensing is limited. In chapter 3 the SCC protocol is only applicable at cryogenic temperatures, which is unsuitable for neurosensing. The photoionization experiment in chapter 4 is useful for a more general understanding of the NV but has no direct application to neurosensing. The ambient SCC protocol developed in chapter 5 is usable in a neurosensing experiment, however, applying

an electrode to a nanopillar array is a difficult task. The SCC protocol developed by Jaskula et al. [58] is a more viable candidate as it does not require electrodes that would be difficult to combine with the nanopillars. Finally, the parabolic diamond structure considered in chapter 6 is also applicable to neurosensing, however, the large structures with deep NV implantations are not suitable for neuron network growth or sensing where the NV should be as close as possible to the neuron signal source. The parabolic structures made in RIE by Wan et al. would be more suitable for nanopillars [125] as an array of thin, nanopillar-like parabolas could be developed in RIE, each with a near-surface NV. This analysis concludes that whilst these methods improve NV sensitivity they are not appropriate for the specific task of nanopillar-based sensing. However, all this work universally improves NV spin-state readout for quantum computation. Prompting research in an alternate means applying the NV to neuroscience.

This thesis ends with an analysis of quantum computation for neuroscience applications in chapter 7 and how the NV can be utilised in this field. Neuron networks are naturally suited for simulation in quantum computers as their networks operate as a binary encoding with information transfer that is probabilistic. An algorithm for simulating neuron networks using digital quantum simulation methods is conceptualised and its functionality is analysed. Future work would involve a more detailed analysis of this technique, how feasible it is and how it might perform against a purely classical network or even alternative quantum algorithms.

Understanding the human brain and its various neuron networks from a single neuron to its largest network in the brain is the key to understanding how we function as humans and how to understand and treat the myriad of neurological conditions that affect such a large portion of the human population. The nitrogen-vacancy (NV) center in diamond promises to unlock many of these mysteries, from both a sensing capacity in single neurons and large networks to the large scale simulation and understanding of neuron networks. Whilst a lot of this work is theoretical, it lays the groundwork for a large amount of future research in a variety of areas. Future experimental realisations of these projects can easily be utilised in a commercial setting, creating products and discoveries that could improve our understanding of concepts and conditions across many regions of neuroscience research.

Bibliography

1. L F Abbott and Carl Van Vreeswijk. Oscillators 02254. *Physical Review*, 48(2):1483–1490, 1993. (cited on page 167)

2. V. M. Acosta, A. Jarmola, E. Bauch, and D. Budker. Optical properties of the nitrogen-vacancy singlet levels in diamond. *Physical Review B - Condensed Matter and Materials Physics*, 82(20):2–5, 2010. (cited on page 126)

3. Bruce Alberts, Alexander Johnson, Julian Lewis, David Morgan, Martin Raff, Keith Roberts, and Peter Walter. *Molecular Biology of the Cell*. W.H Freeman, New York, 5th edition, 2008. (cited on pages xii, 17, 18, 19, 20, 21, 22, 23, 24, 25, 27, 28, and 167)

4. Katrin Amunts, Alois C Knoll, Thomas Lippert, Cyriel M A Pennartz, Philippe Ryvlin, Alain Destexhe, Viktor K Jirsa, Egidio D Angelo, and Jan G Bjaalie. The Human Brain Project — Synergy between neuroscience , computing , informatics , and brain-inspired technologies. *PLOS Biology*, 17(7):1–7, 2019. (cited on page 165)

5. Clay M. Armstrong and Bertil Hille. Voltage-gated ion channels and electrical excitability. *Neuron*, 20(3):371–380, 1998. (cited on pages xii and 22)

6. Frank Arute, Kunal Arya, Ryan Babbush, Dave Bacon, Joseph C. Bardin, Rami Barends, Rupak Biswas, Sergio Boixo, Fernando G.S.L. Brandao, David A. Buell, Brian Burkett, Yu Chen, Zijun Chen, Ben Chiaro, Roberto Collins, William Courtney, Andrew Dunsworth, Edward Farhi, Brooks Foxen, Austin Fowler, Craig Gidney, Marissa Giustina, Rob Graff, Keith Guerin, Steve Habegger, Matthew P. Harrigan, Michael J. Hartmann, Alan Ho, Markus Hoffmann, Trent Huang, Travis S. Humble, Sergei V. Isakov, Evan Jeffrey, Zhang Jiang, Dvir Kafri, Kostyantyn Kechedzhi, Julian Kelly, Paul V. Klimov, Sergey Knysh, Alexander Korotkov, Fedor Kostritsa, David Landhuis, Mike Lindmark, Erik Lucero, Dmitry Lyakh, Salvatore Mandrà, Jarrod R. McClean, Matthew McEwen, Anthony Megrant, Xiao Mi, Kristel Michielsen, Masoud Mohseni, Josh Mutus, Ofer Naaman, Matthew Neeley, Charles Neill, Murphy Yuezhen Niu, Eric Ostby, Andre Petukhov, John C. Platt, Chris Quintana, Eleanor G. Rieffel, Pedram Roushan, Nicholas C. Rubin, Daniel Sank, Kevin J. Satzinger, Vadim Smelyanskiy, Kevin J. Sung, Matthew D. Trevithick, Amit Vainsencher, Benjamin Villalonga, Theodore White, Z. Jamie Yao, Ping Yeh, Adam Zalcman, Hartmut Neven, and John M. Martinis. Quantum supremacy using a programmable superconducting processor. *Nature*, 574(7779):505–510, 2019. (cited on page 177)

7. N. Aslam, G. Waldherr, P. Neumann, F. Jelezko, and J. Wrachtrup. Photo-induced ionization dynamics of the nitrogen vacancy defect in diamond investigated by single-shot charge state detection. *New Journal of Physics*, 15:0–17, 2013. (cited on pages xviii, 80, 104, 110, 113, 130, and 141)

8. Thomas M. Babinec, Birgit J.M. Hausmann, Mughees Khan, Yinan Zhang, Jeronimo R. Maze, Philip R. Hemmer, and Marko Lončar. A diamond nanowire single-photon source. *Nature Nanotechnology*, 5(3):195–199, 2010. (cited on pages 3 and 74)

9. Bryce T. Bajar, Emily S. Wang, Shu Zhang, Michael Z. Lin, and Jun Chu. A guide to fluorescent protein FRET pairs. *Sensors (Switzerland)*, 16(9):1–24, 2016. (cited on pages 36 and 37)

10. Gopalakrishnan Balasubramanian, Philipp Neumann, Daniel Twitchen, Matthew Markham, Roman Kolesov, Norikazu Mizuochi, Junichi Isoya, Jocelyn Achard, Johannes Beck, Julia Tissler, Vincent Jacques, Philip R. Hemmer, Fedor Jelezko, and Jörg Wrachtrup. Ultralong spin coherence time in isotopically engineered diamond. *Nature Materials*, 8(5):383–387, 2009. (cited on page 122)

11. Philip Ball. First 100-qubit quantum computer enters crowded race. *Nature News & Views*, 599:542, 2021. (cited on page 177)

12. J F Barry, M J Turner, J M Schloss, D R Glenn, Y Song, M D Lukin, H Park, and R L Walsworth. Optical magnetic detection of single-neuron action potentials using quantum defects in diamond. *Proceedings of the National Academy of Sciences*, 113(49):14133–14138, 2016. (cited on pages 3, 15, 38, 39, and 64)

13. Michael S.J. Barson, Lachlan M. Oberg, Liam P. McGuinness, Andrej Denisenko, Neil B. Manson, Jörg Wrachtrup, and Marcus W. Doherty. Nanoscale Vector Electric Field Imaging Using a Single Electron Spin. *Nano Letters*, 21(7):2962–2967, 2021. (cited on page 99)

14. Michael S.J. Barson, Phani Peddibhotla, Preeti Ovartchaiyapong, Kumaravelu Ganesan, Richard L. Taylor, Matthew Gebert, Zoe Mielens, Berndt Koslowski, David A. Simpson, Liam P. McGuinness, Jeffrey McCallum, Steven Prawer, Shinobu Onoda, Takeshi Ohshima, Ania C. Bleszynski Jayich, Fedor Jelezko, Neil B. Manson, and Marcus W. Doherty. Nanomechanical Sensing Using Spins in Diamond. *Nano Letters*, 17(3):1496–1503, 2017. (cited on page 38)

15. D. A. Broadway, N. Dontschuk, A. Tsai, S. E. Lillie, C. T.K. Lew, J. C. McCallum, B. C. Johnson, M. W. Doherty, A. Stacey, L. C.L. Hollenberg, and J. P. Tetienne. Spatial mapping of band bending in semiconductor devices using in situ quantum sensors. *Nature Electronics*, 1(9):502–507, 9 2018. (cited on page 99)

16. Lilian Childress and Ronald Hanson. Diamond NV centers for quantum computing and quantum networks. *MRS Bulletin*, 38(2):134–138, 2013. (cited on page 6)

17. John Clark and Robert Plonsey. A MATHEMATICAL EVALUATION OF THE CORE CONDUCTOR MODEL. *Biophysical Journal*, 6(1):95–112, 1966. (cited on page 39)

18. Marlene R. Cohen and Adam Kohn. Measuring and interpreting neuronal correlations. *Nature Neuroscience*, 14(7):811–819, 2011. (cited on page 1)

19. Ben Corry, Serdar Kuyucak, and Shin-Ho Chung. Tests of Continuum Theories as Models of Ion Channels. II. Poisson–Nernst–Planck Theory versus Brownian Dynamics. *Biophysical Journal*, 78(5):2364–2381, 5 2000. (cited on pages 3, 40, 48, 51, and 167)

20. Gordon Davies. Vibronic spectra in diamond. *Journal of Physics C: Solid State Physics*, 7:3797–3809, 1974. (cited on pages 115 and 127)

21. Armando J. De Jesus, Noah Kastelowitz, and Hang Yin. Changes in lipid density induce membrane curvature. *RSC Advances*, 3(33):13622–13625, 2013. (cited on page 22)

22. Felipe Fávaro De Oliveira, Denis Antonov, Ya Wang, Philipp Neumann, Seyed Ali Momenzadeh, Timo Häußermann, Alberto Pasquarelli, Andrej Denisenko, and Jörg Wrachtrup. Tailoring spin defects in diamond by lattice charging. *Nature Communications*, 8(May), 2017. (cited on pages 65 and 82)

23. W. Denk, K. R. Delaney, A. Gelperin, D. Kleinfeld, B. W. Strowbridge, D. W. Tank, and R. Yuste. Anatomical and functional imaging of neurons using 2-photon laser scanning microscopy. *Journal of Neuroscience Methods*, 54(2):151–162, 1994. (cited on page 34)

24. David Deutsch. Th re e -state qu an tu m c ryptogr aph y. *Proceedings of the Royal Society of London. A. Mathematical and Physical Sciences*, 400(11):97–117, 1985. (cited on page 165)

25. Marcus W. Doherty, Neil B. Manson, Paul Delaney, Fedor Jelezko, Jörg Wrachtrup, and Lloyd C.L. Hollenberg. The nitrogen-vacancy colour centre in diamond. *Physics Reports*, 528(1):1–45, 2013. (cited on pages 7, 10, 104, 107, 115, 127, and 141)

26. Yuki Doi, Takahiro Fukui, Hiromitsu Kato, Toshiharu Makino, Satoshi Yamasaki, Toshiyuki Tashima, Hiroki Morishita, Shinji Miwa, Fedor Jelezko, Yoshishige Suzuki, and Norikazu Mizuochi. Pure negatively charged state of the NV center in n -type diamond. *Physical Review B*, 93(8):1–6, 2016. (cited on page 140)

27. F. Dolde, H. Fedder, M. W. Doherty, T. Nöbauer, F. Rempp, G. Balasubramanian, T. Wolf, F. Reinhard, L. C.L. Hollenberg, F. Jelezko, and J. Wrachtrup. Electric-field sensing using single diamond spins. *Nature Physics*, 7(6):459–463, 2011. (cited on pages xi, 3, 10, 11, 22, 38, and 68)

28. V. L. Feigin, R. V. Krishnamurthi, A. M. Theadom, A. A. Abajobir, S. R. Mishra, M. B. Ahmed, K. H. Abate, M. A. Mengistie, T. Wakayo, F. Abd-Allah, A. M. Abdulle, S. F. Abera, K. E. Mohammed, G. Y. Abyu, S. W. Asgedom, T. M. Atey, B. D. Betsu, H. B. Mezgebe, K. B. Tuem, M. A. Woldu, A. N. Aichour, I. Aichour, M. T. Aichour, R. O. Akinyemi, S. Alabed, R. Al-Raddadi, N. Alvis-Guzman, A. T. Amare, H. Ansari, P. Anwari, J. Ärnlöv, S. Fereshtehnejad, E. Weiderpass, R. Havmoeller, H. Asayesh, L. Avila-Burgos, E. F.G.A. Avokpaho, L. E.R.A.S. Afrique, M. R. Azarpazhooh, A. Barac, M. Barboza, S. L. Barker-Collo, T. Bärnighausen, M. S. Farvid, S. Mohammed, N. Bedi, E. Beghi, G. Giussani, D. A. Bennett, S. I. Hay, A. C. Goulart, I. S. Santos, I. M. Bensenor, P. A. Lotufo, A. Berhane, P. Jeemon, S. Bhaumik, L. Dandona, R. Dandona, G. A. Kumar, S. M. Birlik, S. Biryukov, D. Casey, K. J. Foreman, E. M. Goldberg, I. A. Khalil, H. H. Kyu, T. Manhertz, A. H. Mokdad, M. Naghavi, G. Nguyen, E. Nichols, M. Smith, C. J.L. Murray, G. A. Roth, J. D. Stanaway, T. Vos, R. G. Ellenbogen, M. Jakovljevic, D. L. Tirschwell, J. R. Zunt, D. J. Boneya, M. Hambisa, L. N.B. Bulto, H. Carabin, C. A. Castañeda-Orjuela, F. Catalá-López, R. Tabarés-Seisdedos, H. Chen, A. A. Chitheer, R. Chowdhury, H. Christensen, G. A. Deveber, S. D. Dharmaratne, H. P. Do, C. T. Nguyen, Q. L. Nguyen, T. H. Nguyen, V. M. Nong, K. Dokova, E. R. Dorsey, S. Eskandarieh, F. Fischer, A. Majeed, T. J. Steiner, S. Rawaf, R. Shakir, H. Shoman, J. M. Geleijnse, R. F. Gillum, P. N. Gona, H. C. Gugnani, R. Gupta, V. Hachinski, R. R. Hamadeh, G. J. Hankey, H. A. Hareri, P. Heydarpour, M. A. Sahraian, A. Kasaeian, R. Malekzadeh, G. Roshandel, S. G. Sepanlou, P. J. Hotez, M. Javanbakht, J. B. Jonas, Y. Kalkonde, A. Kandel, A. Karch, A. Kastor, M. Rahman, P. N. Keiyoro, Y. S. Khader, E. A. Khan, Y. Khang, A. T.A. Khoja, B. X. Tran, J. Khubchandani, D. Kim, Y. J. Kim, M. Kivimaki, Y. Kokubo, S. Kosen, M. Kravchenko, M. A. Piradov, Y. Y. Varakin, B. Kuate Defo, C. Kulkarni, R. Kumar, A. Larsson, P. M. Lavados, Y. Li, X. Liang, M. L. Liben, W. D. Lo, G. Logroscino, C. T. Loy, M. T. Mackay, A. Meretoja, C. E.I. Szoeke, H. Magdy Abd El Razek, L. G. Mantovani, J. Massano, M. Mazidi, C. McAlinden, S. Mehata, M. M. Mehndiratta, Z. A. Memish, W. Mendoza, G. A. Mensah, T. Wijeratne, T. R. Miller, N. Mohamed Ibrahim, A. Mohammadi, M. Moradi-Lakeh, I. Moreno Velasquez, K. I. Musa, J. W. Ngunjiri, D. N.A. Ningrum, B. Norrving, D. J. Stein, J. J.N. Noubiap, F. A. Ogbo, A. M.N. Renzaho, M. O. Owolabi, J. D. Pandian, P. G. Parmar, D. M. Pereira, M. Petzold, M. R. Phillips, R. G. Poulton, F. Pourmalek, M. Qorbani, A. Rafay, R. K. Rai, S. Rajsic, A. Ranta, M. S. Rezai, E. Rubagotti, P. Sachdev, S. Safiri, R. Sahathevan, A. M. Samy, P. Santalucia, B. Sartorius, M. Satpathy, M. Sawhney, M. I. Saylan, M. A. Shaikh, M. Shamsizadeh, K. N. Sheth, M. Shigematsu, D. A.S. Silva, E. Sobngwi, L. A. Sposato, L. J. Stovner, L. J. Stovner, R. Suliankatchi Abdulkader, D. Tanne, A. G. Thrift, R. Topor-Madry, T. Truelsen, K. N. Ukwaja, O. A. Uthman, T. Vasankari, N. Venketasubramanian, V. V. Vlassov, F. Wadilo, M. T. Wallin, R. Westerman, C. S. Wiysonge, C. D. Wolfe, D. Xavier, G. Xu, Y. Yano, H. H. Yimam, N. Yonemoto, C. Yu, Z. Zaidi, and M. E. Zaki. Global, regional, and national burden of neurological disorders during 1990–2015: a systematic analysis for the Global Burden of Disease Study 2015.

The Lancet Neurology, 16(11):877–897, 2017. (cited on page 1)

29. Mark Fox. *Quantum optics: an introduction*. Oxford University Press, Oxford, 6th edition, 2009. (cited on page 123)

30. K. Franze. The mechanical control of nervous system development. *Development*, 140(15):3069–3077, 2013. (cited on pages 69 and 70)

31. Peter Fromherz, Gerd Hübener, Bernd Kuhn, and Marlon J. Hinner. ANNINE-6plus, a voltage-sensitive dye with good solubility, strong membrane binding and high sensitivity. *European Biophysics Journal*, 37(4):509–514, 2008. (cited on pages xiii, 32, and 33)

32. Kai Mei C. Fu, Charles Santori, Paul E. Barclay, Lachlan J. Rogers, Neil B. Manson, and Raymond G. Beausoleil. Observation of the dynamic Jahn-Teller effect in the excited states of nitrogen-vacancy centers in diamond. *Physical Review Letters*, 103(25):1–4, 2009. (cited on pages xx, 128, 135, and 136)

33. Stefano Fusi and Maurizio Mattia. Collective behavior of networks with linear (VLSI) integrate-and-fire neurons. *Neural Computation*, 11(3):633–652, 1999. (cited on page 167)

34. María A. Gandini, Alejandro Sandoval, and Ricardo Felix. Patch-clamp recording of voltage-sensitive Ca2+ channels. *Cold Spring Harbor Protocols*, 2014(4):329–335, 2014. (cited on pages xiii, 31, and 32)

35. Vini Gautam, Shagufta Naureen, Naeem Shahid, Qian Gao, Yi Wang, David Nisbet, Chennupati Jagadish, and Vincent R. Daria. Engineering Highly Interconnected Neuronal Networks on Nanowire Scaffolds. *Nano Letters*, 17(6):3369–3375, 2017. (cited on pages 3, 4, 70, 71, and 74)

36. Wulfram Gerstner, Werner M. Kistler, Richard Naud, and Liam Paninski. *Neuronal dynamics: From single neurons to networks and models of cognition*. Cambridge University Press, 2014. (cited on pages xxiii, 6, 13, 166, 167, 169, 170, 172, 174, 176, and 177)

37. M. L. Goldman, A. Sipahigil, M. W. Doherty, N. Y. Yao, S. D. Bennett, M. Markham, D. J. Twitchen, N. B. Manson, A. Kubanek, and M. D. Lukin. Phonon-induced population dynamics and intersystem crossing in nitrogen-vacancy centers. *Physical Review Letters*, 114(14):1–6, 2015. (cited on pages 80, 105, and 107)

38. Yiyang Gong, Cheng Huang, Jin Zhong Li, Benjamin F. Grewe, Yanping Zhang, Stephan Eismann, and Mark J. Schnitzer. High-speed recording of neural spikes in awake mice and flies with a fluorescent voltage sensor. *Science*, 350(6266):1361–1366, 2015. (cited on pages xiii, 36, and 37)

39. Christine Grienberger and Arthur Konnerth. Imaging Calcium in Neurons. *Neuron*, 73(5):862–885, 2012. (cited on pages xiii, 34, and 35)

40. Lov. K Grover. A fast quantum mechanical algorithm for database search. *Association for computing machinery*, pages 212–219, 1996. (cited on page 166)

41. Michal Gulka, Daniel Wirtitsch, Viktor Ivády, Jelle Vodnik, Jaroslav Hruby, Goele Magchiels, Emilie Bourgeois, Adam Gali, Michael Trupke, and Milos Nesladek. Room-temperature control and electrical readout of individual nitrogen-vacancy nuclear spins. *Nature Communications*, 12(4421):1–8, 2021. (cited on page 80)

42. J P Hadden, J P Harrison, A. C. Stanley-Clarke, L Marseglia, Y. L D Ho, B R Patton, J. L. O'Brien, and J. G. Rarity. Strongly enhanced photon collection from diamond defect centers under microfabricated integrated solid immersion lenses. *Applied Physics Letters*, 97(24), 2010. (cited on page 146)

43. Aviad Hai, Ada Dormann, Joseph Shappir, Shlomo Yitzchaik, Carmen Bartic, Gustaaf Borghs, J. P.M. Langedijk, and Micha E. Spira. Spine-shaped gold protrusions improve the adherence and electrical coupling of neurons with the surface of micro-electronic devices. *Journal of the Royal Society Interface*, 6(41):1153–1165, 2009. (cited on pages xiii, 4, 38, and 76)

44. Aviad Hai, Joseph Shappir, and Micha E. Spira. In-cell recordings by extracellular microelectrodes. *Nature Methods*, 7(3):200–202, 2010. (cited on pages 4, 37, and 76)

45. L. T. Hall, D. A. Simpson, and L. C.L. Hollenberg. Nanoscale sensing and imaging in biology using the nitrogen-vacancy center in diamond. *MRS Bulletin*, 38(2):162–167, 2013. (cited on page 3)

46. Owen P Hamill. Patch-Clamp Technique. *John Wiley and Sons*, pages 1–14, 2014. (cited on page 31)

47. Liam Hanlon, Vini Gautam, James D. A. Wood, Prithvi Reddy, Michael S. J. Barson, Marika Niihori, Alexander R. J. Silalahi, Ben Corry, Jörg Wrachtrup, Matthew J. Sellars, Vincent R. Daria, Patrick Maletinsky, Gregory J. Stuart, and Marcus W. Doherty. Diamond nanopillar arrays for quantum microscopy of neuronal signals. *Neurophotonics*, 7(03):1, 2020. (cited on page 39)

48. Lindsey Hanson, Ziliang Carter Lin, Chong Xie, Yi Cui, and Bianxiao Cui. Characterization of the cell-nanopillar interface by transmission electron microscopy. *Nano Letters*, 12(11):5815–5820, 2012. (cited on page 74)

49. D. K. Hartline and D. R. Colman. Rapid Conduction and the Evolution of Giant Axons and Myelinated Fibers. *Current Biology*, 17(1):29–35, 2007. (cited on page 28)

50. E. D. Herbschleb, H. Kato, Y. Maruyama, T. Danjo, T. Makino, S. Yamasaki, I. Ohki, K. Hayashi, H. Morishita, M. Fujiwara, and N. Mizuochi. Ultra-long coherence times amongst room-temperature solid-state spins. *Nature Communications*, 10(1):8–13, 2019. (cited on page 141)

51. Bertil Hille. *Ion Channels of Excitable Membranes*. Sinauer Associates Inc., Sunderland, 2nd edition, 2001. (cited on pages 4, 17, 23, 24, 25, 27, 28, 29, 51, 52, 56, and 167)

52. A. L. Hodgkin and A. F. Huxley. A Quantitative description of membrane current and its application to conduction and excitation in nerve. *Journal of Physiology*, 4(117):500–544, 1952. (cited on pages 47, 48, and 56)

53. David A. Hopper, Richard R. Grote, Annemarie L. Exarhos, and Lee C. Bassett. Near-infrared-assisted charge control and spin readout of the nitrogen-vacancy center in diamond. *Physical Review B*, 94(24):1–5, 2016. (cited on pages 121, 122, and 133)

54. David A. Hopper, Joseph D. Lauigan, Tzu Yung Huang, and Lee C. Bassett. Real-Time Charge Initialization of Diamond Nitrogen-Vacancy Centers for Enhanced Spin Readout. *Physical Review Applied*, 13(2):1, 2020. (cited on page 125)

55. KUN HUANG and AVRIL RHYS. Theory of light absorption and non-radiative transitions in F-centres. *Royal Society*, 204(1078):74–92, 1950. (cited on pages 115 and 127)

56. Tzu Yung Huang, Richard R. Grote, Sander A. Mann, David A. Hopper, Annemarie L. Exarhos, Gerald G. Lopez, Garrett R. Kaighn, Erik C. Garnett, and Lee C. Bassett. A monolithic immersion metalens for imaging solid-state quantum emitters. *Nature Communications*, 10(1):1–8, 2019. (cited on page 146)

57. Mohammad Jamali, Ilja Gerhardt, Mohammad Rezai, Karsten Frenner, Helmut Fedder, and Jörg Wrachtrup. Microscopic diamond solid-immersion-lenses fabricated around single defect centers by focused ion beam milling. *Review of Scientific Instruments*, 85(12), 2014. (cited on pages xxii, 6, 145, 146, 150, 152, and 153)

58. J. C. Jaskula, B. J. Shields, E. Bauch, M. D. Lukin, A. S. Trifonov, and R. L. Walsworth. Improved Quantum Sensing with a Single Solid-State Spin via Spin-to-Charge Conversion. *Physical Review Applied*, 11(6):1, 2019. (cited on pages xvi, 5, 12, 77, 80, 81, 102, 105, 120, 122, 132, 134, 136, and 181)

59. Jakob Jordan, Tammo Ippen, Moritz Helias, Itaru Kitayama, Mitsuhisa Sato, Jun Igarashi, Markus Diesmann, and Susanne Kunkel. Extremely scalable spiking neuronal network simulation code: From laptops to exascale computers. *Frontiers in Neuroinformatics*, 12(February), 2018. (cited on pages 166 and 177)

60. N. Kalb, P. C. Humphreys, J. J. Slim, and R. Hanson. Dephasing mechanisms of diamond-based nuclear-spin memories for quantum networks. *Physical Review A*, 97(6):1–10, 2018. (cited on page 126)

61. Eric Kandel, James Schwartz, and Thomas Jessell. *Principles of Neural science*. McGraw-Hill Companies, 5th edition, 2000. (cited on pages 17, 22, 166, and 167)

62. Sinan Karaveli, Ophir Gaathon, Abraham Wolcott, Reyu Sakakibara, Or A. Shemesh, Darcy S. Peterka, Edward S. Boyden, Jonathan S. Owen, Rafael Yuste, and Dirk Englund. Modulation of nitrogen vacancy charge state and fluorescence in nanodiamonds using electrochemical potential. *Proceedings of the National Academy of Sciences*, 113(15):3938–3943, 2016. (cited on pages 3 and 38)

63. P. Kehayias, M. W. Doherty, D. English, R. Fischer, A. Jarmola, K. Jensen, N. Leefer, P. Hemmer, N. B. Manson, and D. Budker. Infrared absorption band and vibronic structure of the nitrogen-vacancy center in diamond. *Physical Review B - Condensed Matter and Materials Physics*, 88(16):1–5, 2013. (cited on pages 116 and 127)

64. Bernd Kuhn and Peter Fromherz. Anellated Hemicyanine Dyes in a Neuron Membrane: Molecular Stark Effect and Optical Voltage Recording. *The Journal of Physical Chemistry B*, 107(31):7903–7913, 2003. (cited on pages 32 and 33)

65. T.C. Lee, R.L. Kashyap, and C.N. Chu. Building Skeleton Models via 3-D Medial Surface Axis Thinning Algorithms. *Graphical Models and Image Processing*, 56(6):462–478, 1994. (cited on page 71)

66. Daniel Liewald, Robert Miller, Nikos Logothetis, Hans Joachim Wagner, and Almut Schüz. Distribution of axon diameters in cortical white matter: an electron-microscopic study on three human brains and a macaque. *Biological Cybernetics*, 108(5):541–557, 2014. (cited on page 59)

67. Courtney L Lopreore, Thomas M Bartol, Jay S Coggan, Daniel X Keller, Gina E Sosinsky, Mark H Ellisman, and Terrence J Sejnowski. Computational modeling of three-dimensional electrodiffusion in biological systems: Application to the node of Ranvier. *Biophysical Journal*, 95(6):2624–2635, 2008. (cited on pages 3, 40, 51, 52, 55, 56, 57, and 59)

68. Artur Lozovoi, Harishankar Jayakumar, Damon Daw, Gyorgy Vizkelethy, Edward Bielejec, Marcus W. Doherty, Johannes Flick, and Carlos A. Meriles. Optical activation and detection of charge transport between individual colour centres in diamond. *Nature Electronics*, 4(10):717–724, 2021. (cited on page 141)

69. Neil B. Manson, Morgan Hedges, Michael S.J. Barson, Rose Ahlefeldt, Marcus W. Doherty, Hiroshi Abe, Takeshi Ohshima, and Matthew J. Sellars. NV–N+ pair centre in 1b diamond. *New Journal of Physics*, 20(11), 2018. (cited on page 104)

70. Paolo Massobrio, Jacopo Tessadori, Michela Chiappalone, and Mirella Ghirardi. In vitro studies of neuronal networks and synaptic plasticity in invertebrates and in mammals using multielectrode arrays. *Neural Plasticity*, 2015, 2015. (cited on page 2)

71. Peter C. Maurer, Georg Kucsko, Christian Latta, Liang Jiang, Norman Y. Yao, Steven D. Bennett, Fernando Pastawski, David Hunger, Nicholas Chisholm, Matthew Markham, Daniel J. Twitchen, J. Ignacio Cirac, and Mikhail D. Lukin.

Room-temperature quantum bit memory exceeding one second. *Optics InfoBase Conference Papers*, 336(6086):1283–1287, 2012. (cited on page 165)

72. P. W. May, E. M. Regan, A. Taylor, J. Uney, A. D. Dick, and J. McGeehan. Spatially controlling neuronal adhesion on CVD diamond. *Diamond and Related Materials*, 23:100–104, 2012. (cited on page 3)

73. Daniel J. McCloskey, Nikolai Dontschuk, David A. Broadway, Athavan Nadarajah, Alastair Stacey, Jean Philippe Tetienne, Lloyd C.L. Hollenberg, Steven Prawer, and David A. Simpson. Enhanced Widefield Quantum Sensing with Nitrogen-Vacancy Ensembles Using Diamond Nanopillar Arrays. *ACS Applied Materials and Interfaces*, 12(11):13421–13427, 3 2020. (cited on page 3)

74. S Ali Momenzadeh, Rainer J Stöhr, Felipe Favaro De Oliveira, Andreas Brunner, Andrej Denisenko, Sen Yang, Friedemann Reinhard, and Jörg Wrachtrup. Nanoengineered Diamond Waveguide as a Robust Bright Platform for Nanomagnetometry Using Shallow Nitrogen Vacancy Centers. *Nano Letters*, 23(1):100–104, 2015. (cited on pages 3, 4, 6, 65, 71, 74, and 146)

75. Ashley Montanaro. Quantum algorithms: An overview. *npj Quantum Information*, 2(1):1–8, 2016. (cited on page 165)

76. Micheal A. Nielsen and Isaac L. Chuang. *Quantum computation and Quantum information*. Cambridge University Press, Cambridge, 10th anniv edition, 2010. (cited on pages 176 and 177)

77. A. P. Nizovtsev, S. Ya Kilin., F. Jelezko, T. Gaebal, I. Popa, A. Gruber, and J. Wrachtrup. A quantum computer based on NV centers in diamond: Optically detected nutations of single electron and nuclear spins. *Optics and Spectroscopy (English translation of Optika i Spektroskopiya)*, 99(2):233–244, 2005. (cited on page 165)

78. Pavel Novak, Julia Gorelik, Umesh Vivekananda, Andrew I. Shevchuk, Yaroslav S. Ermolyuk, Russell J. Bailey, Andrew J. Bushby, Guy W.J. Moss, Dmitri A. Rusakov, David Klenerman, Dimitri M. Kullmann, Kirill E. Volynski, and Yuri E. Korchev. Nanoscale-Targeted Patch-Clamp Recordings of Functional Presynaptic Ion Channels. *Neuron*, 79(6):1067–1077, 2013. (cited on pages 1, 2, and 31)

79. Lukas Novotny and Bert Hecht. *Principles of Nano-optics*. Cambridge University Press, New York, 1st edition, 2006. (cited on pages 145, 149, 150, and 161)

80. R. W. Nunes and Xavier Gonze. Berry-phase treatment of the homogeneous electric field perturbation in insulators. *Physical Review B - Condensed Matter and Materials Physics*, 63(15):1551071–15510722, 2001. (cited on page 141)

81. Duane Q. Nykamp and Daniel Tranchina. A population density approach that facilitates large-scale modeling of neural networks: Extension to slow inhibitory synapses. *Neural Computation*, 13(3):511–546, 2001. (cited on page 167)

82. L. M. Oberg, M. O. De Vries, L. Hanlon, K. Strazdins, M. S.J. Barson, M. W. Doherty, and J. Wrachtrup. Solution to Electric Field Screening in Diamond Quantum Electrometers. *Physical Review Applied*, 14(1):1, 2020. (cited on pages xvii, 99, and 100)

83. Lachlan M. Oberg, Eric Huang, Prithvi M. Reddy, Audrius Alkauskas, Andrew D. Greentree, Jared H. Cole, Neil B. Manson, Carlos A. Meriles, and Marcus W. Doherty. Spin coherent quantum transport of electrons between defects in diamond. *Nanophotonics*, 8(11):1975–1984, 2019. (cited on pages 5, 82, 90, and 102)

84. Marie Engelene J. Obien, Kosmas Deligkaris, Torsten Bullmann, Douglas J. Bakkum, and Urs Frey. Revealing neuronal function through microelectrode array recordings. *Frontiers in Neuroscience*, 9(JAN):423, 2015. (cited on pages 37 and 38)

85. J. O. Orwa, C. Santori, K. M.C. Fu, B. Gibson, D. Simpson, I. Aharonovich, A. Stacey, A. Cimmino, P. Balog, M. Markham, D. Twitchen, A. D. Greentree, R. G. Beausoleil, and S. Prawer. Engineering of nitrogen-vacancy color centers in high purity diamond by ion implantation and annealing. *Journal of Applied Physics*, 109(8), 2011. (cited on page 7)

86. Dina Y. Otify, EmanA. Youssef, Naglaa B. Nagy, Mona K. Marei, and Magda I. Youssif. Transdifferentiation of Bone Marrow Mesenchymal Stem Cells into Neural Cells via Cerebrospinal Fluid. *Biomedicine and Biotechnology*, 2(4):66–79, 2014. (cited on pages xi and 18)

87. Amelie Perron, Hiroki Mutoh, Walther Akemann, Sunita Ghimire Gautam, Dimitar Dimitrov, Yuka Iwamoto, and Thomas Knöpfel. Second and third generation voltage-sensitive fl uorescent proteins for monitoring membrane potential. *Frontiers in Molecular Neuroscience*, 2(June):1–8, 2009. (cited on page 2)

88. Darcy S. Peterka, Hiroto Takahashi, and Rafael Yuste. Imaging Voltage in Neurons. *Neuron*, 69(1):9–21, 2011. (cited on pages 1, 2, 29, 30, 31, 32, 33, 34, 35, and 37)

89. S. Pezzagna, B. Naydenov, F. Jelezko, J. Wrachtrup, and J. Meijer. Creation efficiency of nitrogen-vacancy centres in diamond. *New Journal of Physics*, 12, 2010. (cited on pages 158 and 161)

90. Sébastien Pezzagna and Jan Meijer. Quantum computer based on color centers in diamond. *Applied Physics Reviews*, 8(1), 2021. (cited on page 6)

91. Jurgis Pods, Johannes Schönke, and Peter Bastian. Electrodiffusion models of neurons and extracellular space using the poisson-nernst-planck equations - Numerical simulation of the intra- and extracellular potential for an axon model. *Biophysical Journal*, 105(1):242–254, 2013. (cited on pages 3, 29, 40, and 51)

92. Marko A Popovic, Nicholas Carnevale, Balazs Rozsa, and Dejan Zecevic. Electrical behaviour of dendritic spines as revealed by voltage imaging. *Nature Communications*, 6:1–12, 2015. (cited on page 2)

93. Dale Purves, George J Augustine, David Fitzpatrick, William C Hall, Anthony-Samuel LaMantia, James O McNamara, and Mark S Williams. *Neuroscience*. Sinauer Associates, Inc., Sunderland, Massachusetts, 3rd edition, 2004. (cited on pages xii, xxv, 17, 24, 26, 27, 30, and 167)

94. Wilfrid Rall. Core Conductor Theory and Cable Properties of Neurons. *Comprehensive Physiology*, 2011. (cited on page 39)

95. Lukas Razinkovas, Marcus W. Doherty, Neil B. Manson, Chris G. Van De Walle, and Audrius Alkauskas. Vibrational and vibronic structure of isolated point defects: The nitrogen-vacancy center in diamond. *Physical Review B*, 104(4):1–19, 2021. (cited on pages xviii, 104, 114, 115, 116, and 127)

96. Magnus J.E. Richardson and Gilad Silberberg. Measurement and analysis of postsynaptic potentials using a novel voltage-deconvolution method. *Journal of Neurophysiology*, 99(2):1020–1031, 2008. (cited on page 2)

97. Brian K. Ridley. *Quantum processes in Semiconductors*. Oxford University Press, Oxford, 3rd edition, 2013. (cited on pages 4, 50, and 51)

98. Brian K. Ridley. *Quantum Processes in Semiconductors*. Oxford University Press, Oxford, 5th edition, 2014. (cited on page 29)

99. L Rondin, J-P Tetienne, T Hignant, J-F Roch, P Maletinsky, and V Jacques. Magnetometry with nitrogen-vacancy centers in diamond. *Reports on Progress in Physics*, 77(5):056503, 2014. (cited on pages xi, 3, 9, 10, 11, 38, 65, 136, and 145)

100. Robert Rosenbaum. A diffusion approximation and numerical methods for adaptive neuron models with stochastic inputs. *Frontiers in Computational Neuroscience*, 10(APR):1–20, 2016. (cited on page 174)

101. B.J Roth and John P. Wikswo. The magnetic field of a single axon. A comparison of theory and experiment. *Biophysical Journal1*, 48(1):93–109, 1985. (cited on pages xiv, 39, 44, 45, and 46)

102. E. Samson, J. Marchand, and K. A. Snyder. Calculation of ionic diffusion coefficients on the basis of migration test results. *Materials and Structures/Materiaux et Constructions*, 36(257):156–165, 2003. (cited on page 59)

103. Michael Samuel and James Barson. *The mechanical and thermal properties of the nitrogen-vacancy centre in diamond*. PhD thesis, Australian National University, 2018. (cited on pages xi and 8)

104. Yosuke Sasama, Taisuke Kageura, Katsuyoshi Komatsu, Satoshi Moriyama, Jun Ichi Inoue, Masataka Imura, Kenji Watanabe, Takashi Taniguchi, Takashi Uchihashi, and Yamaguchi Takahide. Charge-carrier mobility in hydrogen-terminated diamond field-effect transistors. *Journal of Applied Physics*, 127(18), 2020. (cited on page 92)

105. Leonid P Savtchenko, Mu Ming Poo, and Dmitri A Rusakov. Electrodiffusion phenomena in neuroscience: A neglected companion. *Nature Reviews Neuroscience*, 18(10):598–612, 2017. (cited on pages 2, 4, 31, and 63)

106. Romana Schirhagl, Kevin Chang, Michael Loretz, and Christian L. Degen. Nitrogen-Vacancy Centers in Diamond: Nanoscale Sensors for Physics and Biology. *Annual Review of Physical Chemistry*, 65(1):83–105, 2014. (cited on page 38)

107. Charles P. Silchter. *Principles of magnetic resonance*. Springer, Heidelberg, 3rd edition, 1996. (cited on page 93)

108. P Siyushev, F Kaiser, V Jacques, I Gerhardt, S Bischof, H Fedder, J Dodson, M Markham, D Twitchen, F Jelezko, and J Wrachtrup. Monolithic diamond optics for single photon detection. *Applied Physics Letters*, 97(24):1–4, 2010. (cited on pages 146 and 158)

109. Petr Siyushev, Milos Nesladek, Emilie Bourgeois, Michal Gulka, Jaroslav Hruby, Takashi Yamamoto, Michael Trupke, Tokuyuki Teraji, Junichi Isoya, and Fedor Jelezko. Photoelectrical imaging and coherent spin-state readout of single nitrogen-vacancy centers in diamond. *Science*, 363(6428):728–731, 2019. (cited on pages 5, 80, and 102)

110. Christian G. Specht, Oliver A. Williams, Richard B. Jackman, and Ralf Schoepfer. Ordered growth of neurons on diamond. *Biomaterials*, 25(18):4073–4078, 2004. (cited on pages 4 and 70)

111. Micha E Spira and Aviad Hai. Microelectrodes get on your nerves Multi-electrode array technologies for neuroscience and cardiology. *Nature nanotechnology*, 8(2):83–94, 2013. (cited on pages 2, 4, and 37)

112. Greg Stuart, Jackie Schiller, and Bert Sakmann. Action potential initiation and propagation in rat neocortical pyramidal neurons. *Journal of Physiology*, 505(3):617–632, 1997. (cited on page 53)

113. Eva Syková and Charles Nicholson. Diffusion in Brain Extracellular Space. *Physiological Reviews*, 88(4):1277–1340, 2009. (cited on pages 4 and 29)

114. Attila Szabo and Neil S. Ostlund. *Modern quantum chemistry : introduction to advanced electronic structure theory*. Dover Publications, Mineola, N.Y, 1st edition, 1996. (cited on pages 5, 108, and 110)

115. Mayumi Tada, Atsuya Takeuchi, Miki Hashizume, Kazuo Kitamura, and Masanobu Kano. A highly sensitive fluorescent indicator dye for calcium imaging of neural activity in vitro and in vivo. *European Journal of Neuroscience*, 39(11):1720–1728, 2014. (cited on page 34)

116. J. M. Taylor, P. Cappellaro, L. Childress, L. Jiang, D. Budker, P. R. Hemmer, A. Yacoby, R. Walsworth, and M. D. Lukin. High-sensitivity diamond magnetometer with nanoscale resolution. *Nature Physics*, 4(10):810–816, 2008. (cited on page 3)

117. J. P. Tetienne, L. Rondin, P. Spinicelli, M. Chipaux, T. Debuisschert, J. F. Roch, and V. Jacques. Magnetic-field-dependent photodynamics of single NV defects in diamond: An application to qualitative all-optical magnetic imaging. *New Journal of Physics*, 14, 2012. (cited on page 126)

118. Agnes Thalhammer, Robert J. Edgington, Lorenzo A. Cingolani, Ralf Schoepfer, and Richard B. Jackman. The use of nanodiamond monolayer coatings to promote the formation of functional neuronal networks. *Biomaterials*, 31(8):2097–2104, 2010. (cited on pages 3 and 4)

119. Ronald Ulbricht and Zhi Heng Loh. Excited-state lifetime of the N V- infrared transition in diamond. *Physical Review B*, 98(9):98–101, 2018. (cited on page 124)

120. M. Vainio and L. Halonen. Mid-infrared optical parametric oscillators and frequency combs for molecular spectroscopy. *Physical Chemistry Chemical Physics*, 18(6):4266–4294, 2016. (cited on page 111)

121. Sebastian Vellmer and Benjamin Lindner. Fokker–Planck approach to neural networks and to decision problems: A unique method for stochastic models in computational and cognitive neuroscience. *European Physical Journal: Special Topics*, 230(14-15):2929–2949, 2021. (cited on page 174)

122. I. I. Vlasov, V. G. Ralchenko, A. V. Khomich, S. V. Nistor, D. Shoemaker, and R. A. Khmelnitskii. Relative abundance of single and vacancy-bonded substitutional nitrogen in CVD diamond. *Physica Status Solidi (A) Applied Research*, 181(1):83–90, 2000. (cited on page 7)

123. Patrice Voss, Maryse E. Thomas, J. Miguel Cisneros-Franco, and Étienne de Villers-Sidani. Dynamic brains and the changing rules of neuroplasticity: Implications for learning and recovery. *Frontiers in Psychology*, 8(OCT):1–11, 2017. (cited on page 166)

124. G. Waldherr, J. Beck, M. Steiner, P. Neumann, A. Gali, T. H. Frauenheim, F. Jelezko, and J. Wrachtrup. Dark states of single nitrogen-vacancy centers in diamond unraveled by single shot NMR. *Physical Review Letters*, 106(15):1–4, 2011. (cited on page 124)

125. Noel H Wan, Brendan J Shields, Donggyu Kim, Sara Mouradian, Benjamin Lienhard, Michael Walsh, Hassaram Bakhru, Tim Schröder, and Dirk Englund.

Efficient Extraction of Light from a Nitrogen-Vacancy Center in a Diamond Parabolic Reflector. *Nano Letters*, 18(5):2787–2793, 2018. (cited on pages 6, 146, 147, 161, and 181)

126. James K. Woosley, Bradley J. Roth, and John P. Wikswo. The magnetic field of a single axon: A volume conductor model. *Mathematical Biosciences*, 76(1):1–36, 1985. (cited on pages xiv, xv, 2, 39, 40, 41, 44, 45, 46, 58, 60, 63, and 64)

127. Yang Wu, Ya Wang, Xi Qin, Xing Rong, and Jiangfeng Du. A programmable two-qubit solid-state quantum processor under ambient conditions. *npj Quantum Information*, 5(1), 2019. (cited on page 165)

128. Yulin Wu, Wan Su Bao, Sirui Cao, Fusheng Chen, Ming Cheng Chen, Xiawei Chen, Tung Hsun Chung, Hui Deng, Yajie Du, Daojin Fan, Ming Gong, Cheng Guo, Chu Guo, Shaojun Guo, Lianchen Han, Linyin Hong, He Liang Huang, Yong Heng Huo, Liping Li, Na Li, Shaowei Li, Yuan Li, Futian Liang, Chun Lin, Jin Lin, Haoran Qian, Dan Qiao, Hao Rong, Hong Su, Lihua Sun, Liangyuan Wang, Shiyu Wang, Dachao Wu, Yu Xu, Kai Yan, Weifeng Yang, Yang Yang, Yangsen Ye, Jianghan Yin, Chong Ying, Jiale Yu, Chen Zha, Cha Zhang, Haibin Zhang, Kaili Zhang, Yiming Zhang, Han Zhao, Youwei Zhao, Liang Zhou, Qingling Zhu, Chao Yang Lu, Cheng Zhi Peng, Xiaobo Zhu, and Jian Wei Pan. Strong Quantum Computational Advantage Using a Superconducting Quantum Processor. *Physical Review Letters*, 127(18):180501, 2021. (cited on page 177)

129. Ying Xu, Ya Jia, Mengyan Ge, Lulu Lu, Lijian Yang, and Xuan Zhan. Effects of ion channel blocks on electrical activity of stochastic Hodgkin–Huxley neural network under electromagnetic induction. *Neurocomputing*, 283:196–204, 2018. (cited on page 1)

130. Bas Jan Zandt, Bennie ten Haken, J. Gert van Dijk, and Michel J A M van Putten. Neural dynamics during anoxia and the "wave of death". *PLoS ONE*, 6(7):3–8, 2011. (cited on pages 56, 57, and 59)

131. Qi Zhang, Yuhang Guo, Wentao Ji, Mengqi Wang, Jun Yin, Fei Kong, Yiheng Lin, Chunming Yin, Fazhan Shi, Ya Wang, and Jiangfeng Du. High-fidelity single-shot readout of single electron spin in diamond with spin-to-charge conversion. *Nature Communications*, 12(1):1–6, 2021. (cited on pages 5 and 80)